Title

Modeling the Development and Transmission of Slip Bands in Polycrystalline Materials

Author

Ahmadikia, Behnam

Publication Date

2023

University of California
Santa Barbara

Modeling the Development and Transmission of Slip Bands in Polycrystalline Materials

A dissertation submitted in partial satisfaction
of the requirements for the degree

Doctor of Philosophy
in
Mechanical Engineering

by

Behnam Ahmadikia

Committee in charge:

Professor Irene Beyerlein, Chair
Professor Samantha Daly
Professor Christos Thrampoulidis
Doctor Mariyappan Arul Kumar

September 2023

The Dissertation of Behnam Ahmadikia is approved.

Professor Samantha Daly

Professor Christos Thrampoulidis

Doctor Mariyappan Arul Kumar

Professor Irene Beyerlein, Committee Chair

August 2023

Modeling the Development and Transmission of Slip Bands in Polycrystalline Materials

by

Behnam Ahmadikia

To Kian Pirfalak

who would have made a great scientist had they let him...

Acknowledgements

I would like to take this opportunity to express my sincere gratitude to individuals who have been instrumental in the completion of this dissertation. I owe my deepest gratitude to my parents for their boundless love, sacrifices, and unwavering support, the foundation upon which I have built my academic achievements. I would not be writing this if they had not instilled in me the importance of education and provided me with the tools and opportunities to pursue my goals. My heartfelt appreciation also goes to my beloved wife, Setareh, for her love, patience, and steadfast support. Her belief in me, even during the most challenging times, has been a constant source of inspiration. I would like to thank her for standing by me, providing a shoulder to lean on, and understanding the demands of this journey. I am forever grateful to have her as my partner in life. Finally, I would like to express my wholehearted gratitude to my advisor, Professor Irene Beyerlein, to whom I am eternally indebted. Her guidance, continued support, and unwavering commitment to my academic growth have been indispensable to my PhD journey. Her genuine and passionate interest in science has had a profound impact, not only helping the development of this dissertation but also molding me into a better researcher and individual. I am deeply grateful for her devotion to every aspect of my education and for believing in my potential, even when I doubted myself.

Curriculum Vitæ

Behnam Ahmadikia

Education

2017-2023	Ph.D. in Mechanical Engineering, University of California, Santa Barbara.
2014-2017	M.Sc. in Mechanical Engineering, Sharif University of Technology.
2010-2014	B.Sc. in Mechanical Engineering, Isfahan University of Technology.

Publications

B. Ahmadikia, M. Arul Kumar, I. J. Beyerlein, “Effect of Neighboring Grain Orientation on Strain Localization in Slip Bands in HCP Materials”, *International Journal of Plasticity*, 144, 103026, 2021.

B. Ahmadikia, L. Wang, M. Arul Kumar, I. J. Beyerlein, “Grain Boundary Slip–Twin Transmission in Titanium”, *Acta Materialia*, 244, 118556, 2022.

B. Ahmadikia, O. Paraskevas, W. Van Hyning, J. Hestroffer, I. J. Beyerlein, C. Thrampoulidis, “Data-driven texture design for reducing elastic and plastic anisotropy in titanium alloys”, *Acta Materialia* (in revision).

B. Ahmadikia, D. Shadle, J. C. Stinville, K. E. Nygren, M. Arul Kumar, T. M. Pollock, M. P. Miller, I. J. Beyerlein, “Role of Microstructure on the Development of Microvolumes in Polycrystals”, *International Journal of Plasticity* (in revision).

B. Ahmadikia, A. L. Beyerlein, M. Arul Kumar, I. J. Beyerlein, “Designing Ti-6Al-4V Microstructure for Strain Delocalization Using Neural Networks”, *Materials Theory* (in review).

B. Ahmadikia, J. C. Stinville, M. Arul Kumar, T. M. Pollock, I. J. Beyerlein, “Stronger Materials Localize Faster”, *Nature Communications* (in preparation).

Abstract

Modeling the Development and Transmission of Slip Bands in Polycrystalline Materials

by

Behnam Ahmadikia

Polycrystalline materials are characterized by complex microstructures, which present significant challenges in accurately predicting their overall properties. Among the critical factors complicating the prediction of mechanical properties is the heterogeneous nature of plastic deformation, manifested as localized slip bands in these materials. Microscopic slip within slip bands has been shown to govern macro-scale material properties, such as strength and toughness. Yet, our understanding of the spatial heterogeneity associated with slip remains surprisingly limited.

While ductility in polycrystalline materials stems from slip accumulation, localized slip is also implicated in crack initiation, propagation, and ultimate material failure. Recent experimental investigations have revealed that the observed trade-off between strength and toughness is attributed to the localized slip occurring within slip bands at the microscopic level. Over the past few decades, significant advancements in microscopy and characterization techniques have enabled researchers to capture slip bands and associated microstructural phenomena in polycrystals. However, these techniques are often expensive, challenging to interpret, and time-consuming to explore the multifaceted localization behavior under different conditions. Despite the breakthroughs in experimental capabilities, our computational capacity to model the development and implications of slip bands in polycrystalline solids have remained limited.

Motivated by recent advancements in slip band characterization and the growing demand for a numerical method to complement the experiments, this dissertation aims to develop a crystal plasticity-based computational framework to explicitly model slip bands and heterogeneous micromechanical fields associated with them. Slip bands are treated as discrete microstructural entities, enabling the computation of associated stress and strain fields. The proposed model is validated against a wide range of experimental results and subsequently applied to multiple microstructure settings to elucidate micro- and macro-scale phenomena observed in various polycrystalline materials. These phenomena include neighbor-affected slip band localization, the role of slip bands in triggering subsequent slip or twin bands or orientation deviation zones in the neighboring grain, and the link between macroscopic strength and microscopic slip in polycrystalline materials, to name a few. Explicit slip band modeling is, furthermore, combined with machine learning and data-driven approaches to design materials with superior, targeted properties, such as reduced anisotropy or strain delocalization in titanium alloys.

Integration of the framework developed here with novel experimental techniques holds immense potential to significantly advance our capabilities in predicting material properties. This transformative combination will bridge existing gaps in our understanding and enable more efficient and effective materials development, ultimately leading to improved material performance.

Contents

List of Figures

List of Tables

Chapter 1

Introduction

1.1 Motivation

In response to rapidly evolving economic and technological factors, there is a pressing need to enhance the performance, safety, and reliability of advanced engineering systems. These systems heavily rely on polycrystalline materials, rendering metals as the backbone of many critical industries including energy, defense, and aerospace. Predicting the behavior of metallic materials is vital for identification of potential failure modes and enhancing structural integrity, however, it requires a thorough understanding of the processing–microstructure–property relationships.

Polycrystalline materials often possess complex, multi-scale, hierarchical microstructures that have long posed challenges in predicting their overall properties. Advanced manufacturing techniques, such as additive manufacturing, have only added to these complexities [22]. Particularly, a key factor contributing to the intricacies of mechanical properties prediction is the complex, heterogeneous nature of plastic deformation in these materials. Microscopic crystallographic slip processes have been evidenced to govern macro-scale material properties, such as strength and toughness. Yet, our understanding of the spatial heterogeneity associated with slip is still surprisingly limited.

One of the main attributes of slip is its localized, as opposed to homogeneous, distribution within deforming crystals. The localized regions of crystallographic slip are commonly referred to as *slip bands*. Although the formation of slip bands is the main underlying mechanism warranting polycrystalline materials' ductility and formability, it is also believed to be responsible for crack initiation and propagation and, ultimately, the failure of the material. While several theories have been proposed to elucidate the trade-off between strength and toughness, a recent experimental study encompassing a diverse array of polycrystalline materials, featuring multiple crystal structures, found that the observed trade-off is in part attributed to the localized slip occurring within slip bands at the microscopic level [3]. Specifically, it was observed that materials with higher yield strengths, indicative of greater overall strength, exhibit a heightened propensity for accumulating slip within highly localized slip bands. It was further found that the normalized fatigue strength decreases with the material's yield strength increasing. Many studies have linked intense slip bands to micro-scale phenomena that serve as precursors for crack formation [4, 23, 24, 25, 26, 27]. As an illustration, a titanium alloy loaded to merely 65% of its yield strength, developed only two intense slip bands across more than 20,000 crystals. Nevertheless, these rare slip bands were subsequently observed to be the nucleation site for fatigue cracks due to the continued increase in their localization intensity [27]. Altogether, experimental observations highlight slip bands as micros-scale events that contribute to crack initiation, the first step in compromising material toughness.

Especially over the past two decades, the advancements in microscopy and characterization techniques have enabled researchers to capture slip bands and microstructural phenomena associated with them in a vast range of material systems. Among these tools are high-resolution Heaviside digital image correlation (HR Heaviside-DIC) and scanning electron microscopy combined with electron backscatter diffraction (SEM-EBSD). Furthermore, associated phenomena include slip-slip and slip-twin transmissions, long-range chain of localization, and intragranular zones of orientation deviation. Despite these breakthroughs, our computational capacities to model the development and implication of slip bands in polycrystalline solids have remained limited. An extensive number of studies have been dedicated to modeling slip, mostly using crystal plasticity (CP) based models, such as finite element (FE) [28, 29, 30, 31, 32, 33, 34, 35] and fast Fourier transforms (FFT) [36, 37] calculations. Nevertheless, the effects of grain properties and its neighborhood on slip band development and role of slip bands in triggering another slip band/twin, creating an orientation deviation zone in the neighboring grain, or overall material properties have remained unaddressed by these studies. This shortcoming is due partly to these models failing to model slip bands explicitly as discrete microstructural entities and, therefore, missing the stress/strain fields associated with them.

While experimental tools have provided new insights into slip localization in polycrystalline solids, they are often costly, hard to interpret, and time-consuming to efficiently explore localization behavior of materials under different conditions. Motivated by recent advancements in characterization of slip bands and the emerging need for a computational framework to integrate with that, this work aims to develop a crystal plasticity-based numerical tool to explicitly model slip bands and the heterogeneous stress/strain fields associated with them. We will validate our model against various experimental results, and then apply it to multiple microstructure settings to explain micro- and macro-scale phenomena observed in a wide range of polycrystalline materials.

As it will be unfolded in the next seven chapters, the integration of the model developed here alongside the novel experimental techniques significantly advance our capabilities of predicting material properties. We believe this transformative combination has the potential to bridge the existing gaps in our understanding and enable more efficient and effective materials development, ultimately leading to improved material performance and meeting the demands of rapidly evolving industrial needs.

1.2 Plastic deformation in HCP and FCC polycrystalline materials

Plastic deformation in most polycrystalline materials including hexagonal close-packed (HCP) and face-centered cubic (FCC) metals is commonly understood to occur heterogeneously [3, 5, 22, 38, 39, 40, 41, 42, 43]. The amount of slip can vary not only among grains within the same polycrystal, but also vary significantly within an individual grain. The intragranular heterogeneity in plastic deformation can manifest in different ways, such as by slip localization in intense slip bands or kink bands, deformation twinning, and lattice reorientation gradients, to name a few [4, 44, 45, 46, 47, 48, 49]. Within a plastically strained crystal, slip occurs via dislocation glide on specific crystallographic planes, shown in Figure 1.1a and b, respectively for HCP and FCC crystal structures. When intense glide happens predominantly on a particular plane or closely spaced parallel planes, intense slip bands, may form. Such intense slip bands within one grain can transmit into a neighboring grain [50, 51, 10], initiate twinning [5, 10, 52, 50], trigger a chain of bands across the polycrystal [4, 53], create an orientation deviation zone in the neighbor [9, 23], or serve as precursors for voids or cracks formation [54, 55].

In recent years and thanks to the advancements in experimental techniques, heterogeneous slip occurring in individual crystals and even throughout a 3D subset of polycrystals has been characterized. A recent article [22] reviews the methods used for quantification of slip localization including high-resolution digital image correlation (HR-DIC), electron channeling contrast imaging (ECCI), solid-state scanning transmission electron microscopy (STEM), and scanning electron microscopy coupled with electron backscatter

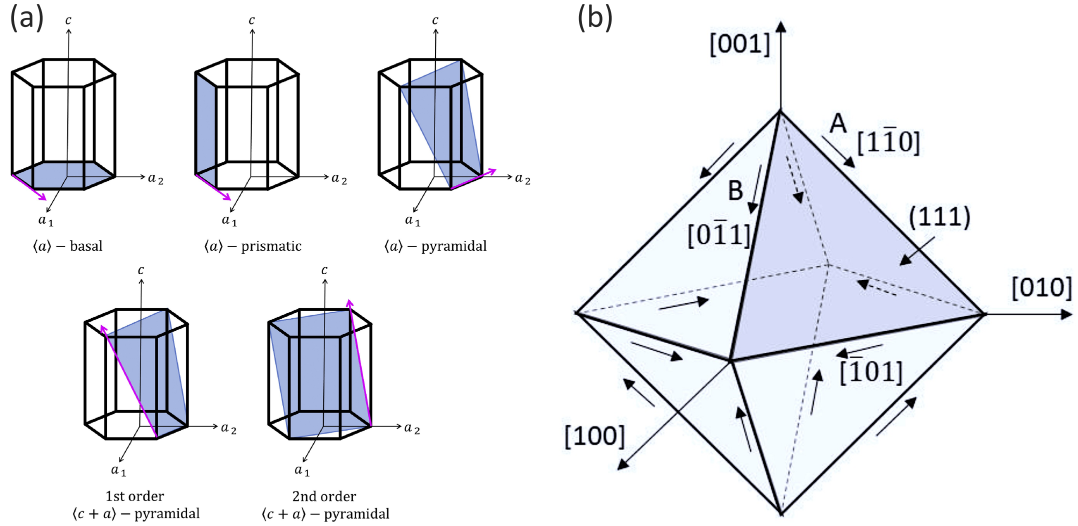

Figure 1.1: (a) Crystallographic slip systems of HCP metals [1]. Three basal, three prismatic, and twelve 1^{st} order $< c + a >$ pyramidal slip systems are implemented in the crystal plasticity simulations in this work. (b) The slip system octahedron for FCC metals with the octahedron (111) slips planes and $< 110 >$ slip directions [2].

diffraction (SEM-EBSD). In the following, we briefly present a few of these studies. A combination of EBSD and HR-DIC was employed to characterize slip bands in a wide range of BCC, FCC, and HCP materials to reveal that, regardless of crystal structure, a material with a higher yield strength tends to have larger amplitudes of slip localized within slip bands with wider spacings [3] (Figure 1.2a). The development of intense slip bands in deformed Ti-6Al-4V titanium alloy was studied, utilizing an *in-situ* SEM-DIC technique [4]. Slip bands formed primarily on the prismatic and basal planes and at strain levels lower than macroscopic yield strain. They showed that such bands successively transmitted from one grain to another, spanning as many as 21 grains (Figure 1.2b). Using SEM-EBSD in commercially pure titanium (CP-Ti), it was observed that prismatic slip bands form in the crystallographically softer grains, connected to $\{10\bar{1}2\} < \bar{1}011 >$ tensile twins in the neighboring grain across the grain boundary [5] (Figure 1.2c).

Localized plasticity in intense slip bands in a grain does not always transmit to slip or twinning in the neighboring grain. Researchers in [6] investigated the mechanisms of slip

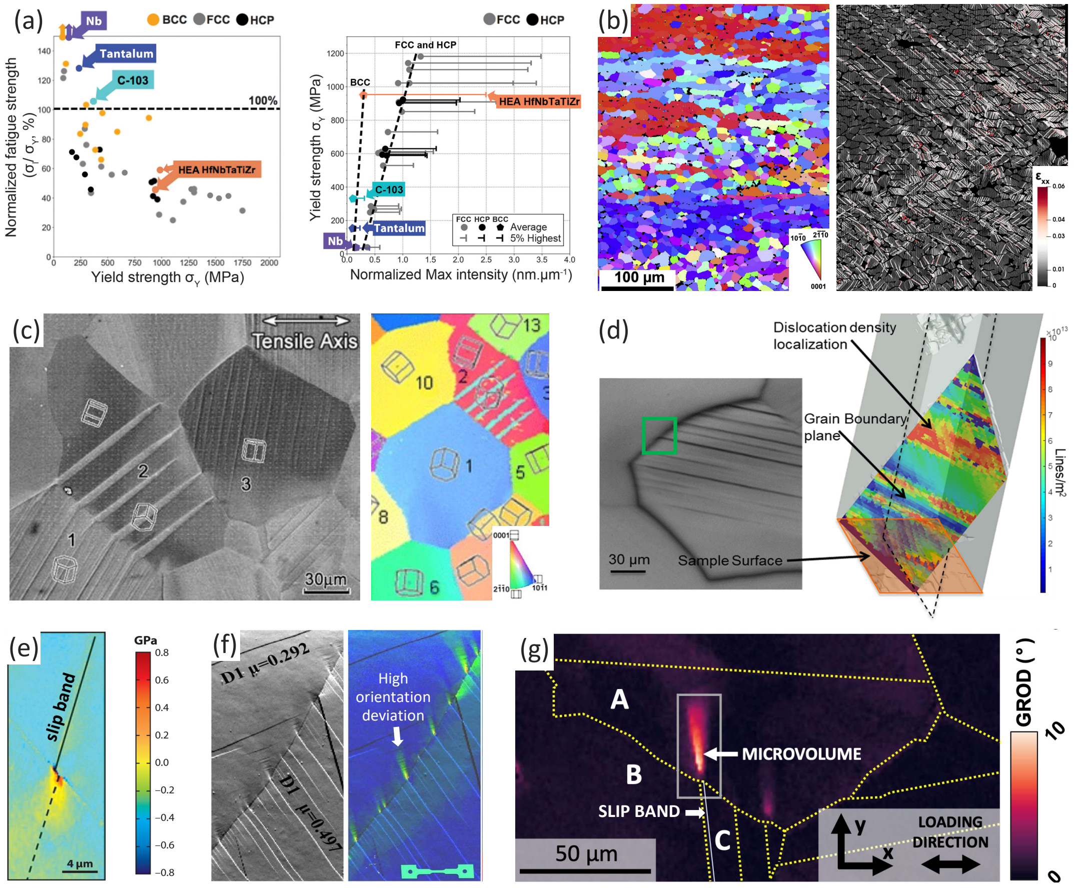

Figure 1.2: (a) Fatigue strength reported as a percentage of the yield strength and slip intensity at 0.2% macroscopic plastic strain as a function of the yield strength for various metals [3]. (b) Strain map at 1.0% strain shows long-range slip localization in Ti-6Al-4V titanium alloy [4]. (c) SEM-EBSD images show how deformation twins in Grain 2 appear to have been nucleated at the grain boundary, due to slip bands localizing in Grain 1 [5]. (d) A slice taken of the grain boundary plane indicates the localization of geometrically necessary dislocations (GNDs) where intense slip bands intersect the grain boundary plane in titanium [6]. (e) HR-EBSD map from a blocked slip band in titanium reveals a localized stress concentration ahead of the slip band/grain boundary intersection [7]. (f) Intense slip bands trigger local zones of high orientation deviation where they intersect the grain boundary in a nickel-based superalloy [8]. (g) Distribution of the grain reference orientation deviation (GROD) reveals the formation of a local high GROD zone at the slip band/grain boundary junction in the nickel-based superalloy Inconel 718 [9].

transfer in Ti through calculation of the density of geometrically necessary dislocations (GNDs) and found that when the grain neighbor does not provide an easy path for dislocation transmission, it is more likely that a dislocation pile-up forms inside the slipping grain at the grain boundary rather than slip transfers occurs at the boundary (Figure 1.2d). By measuring the residual shear stress ahead of a slip band blocked at the grain boundary in pure magnesium and titanium, it was verified that a stress concentration at the band tip in the neighboring grain may form due to the development of slip bands in the parent grain and their interaction with the grain boundary [56, 7] (Figure 1.2e).

In addition to triggering a localized deformation mode in the neighbor, recent microstructure characterizations have revealed events in which intense slip bands in one grain creates within the neighboring grain intragranular zones with orientations different from that of the rest of the grain [9, 8, 23] (Figure 1.2f, g). Critically, it has been observed that micro-cracks tend to initiate in these zones and further develop towards the interior of the grain or along the grain boundary, eventually leading to macroscopic failure of the material [9, 8].

Having established the paramount role that slip bands play in plastic deformation and overall mechanical properties of materials, in the next section, we will propose a number of key objectives to pursue in this dissertation.

1.3 Research objectives

The overarching goal of this dissertation is to improve our understanding of the development and consequences of slip localization within slip bands in polycrystalline materials. we propose a mesoscale explicit slip band modeling tool built on the elasto-viscoplastic fast Fourier transforms model to calculate the micromechanical fields that emerge within, around, and ahead of developing slip bands. The calculated stress, strain, and orientation fields will provide new insights into microstructure-property relationships in metallic materials. In support of this, the following key objectives are proposed:

1. To identify the effects of material properties and grain neighborhood on the development of slip bands, particularly in HCP metals, and to elucidate the key factors that govern their transmission across the grain boundaries by studying neighborhood-induced slip/twin localization.
2. To interpret experimental observations of slip localization and its implications on macroscopic material properties, through a one-to-one comparison between simulation and experimental results.
3. To identify the key microstructural features involved in strain localization in polycrystalline materials, and to design an optimal microstructure featuring strain delocalization, via exploiting the explicit slip band model integrated with machine learning approaches.
4. To design an optimal texture for reducing elastic and plastic anisotropy in HCP materials through a combination of micromechanical modeling and data-driven optimization.

1.4 Dissertation organization

The dissertation is structured as follows. In Chapter 2, we describe in detail the computational framework, called SB-FFT, we have developed for explicit modeling of slip bands in crystalline materials. In Chapter 3, we utilize this model to simulate the evolution of a discrete slip band within HCP materials, aiming to identify the effect of grain neighbor orientation on slip band development, as well as its potential transmission into the neighboring grain. Chapter 4 is dedicated to examining the grain neighborhood-induced slip or twin localization in pure titanium, using a combination of SB-FFT and Twin-FFT crystal plasticity modeling tools. The results presented in this chapter elucidate the key factors that govern the transmission of slip and twin bands across grain boundaries. Next, in Chapter 5, applying the SB-FFT model to a wide range of FCC and HCP materials and comparing our results with experimental results, we provide unprecedented insights into the underlying nature of slip localization in polycrystalline materials. Chapter 6 aims to identify the fundamental factors that contribute to the formation of microvolumes, intragranular zones with orientations significantly different from that of the rest of the grain, in polycrystals. We achieve this goal by modeling a discrete slip band in the nickel-based superalloy Inconel 718 and investigating the micromechanical fields, such as orientation and slip, associated with that. In Chapter 7, we start incorporating machine learning and data-driven approaches into our micromechanical simulations, to design materials with targeted, superior properties. Particularly, this chapter intends to identify the microstructural features that would minimize strain localization in Ti-6Al-4V titanium alloy. We combine SB-FFT simulations on 3D polycrystals with neural network models to design an optimal microstructure featuring strain delocalization. Slightly digressing from slip bands, in Chapter 8, we exploit a new data-driven optimization method that integrates a combinatorial optimization formulation and a 3D crystal plasticity model to discover microstructural textures that would reduce anisotropy in elastic and plastic properties of titanium alloys. Finally in Chapter 9, we will draw the key conclusions from this dissertation, concluding with some recommendations for future studies.

Chapter 2

Explicit slip band modeling

2.1 Introduction

In this chapter, the computational tool we have developed to explicitly model slip bands in polycrystalline solids is described in detail. First, we briefly review the geometric factors and modeling techniques that have been proposed to date to explain the development and transmission of slip bands. Then, the fundamentals of the elasto-viscoplastic fast Fourier transforms approach are presented. Finally, we describe the slip band fast Fourier transforms model developed to specifically model slip localization in polycrystals.

To this date, numerous studies have been carried out aiming to identify a criterion to explain slip transmission phenomenon in crystalline materials. In the beginning, the likelihood that slip transmission occurs from one slip system to another has been quantified by geometric parameters. Livingston and Chalmers [57] were the first to consider a geometric factor, N, to gauge the likelihood transmission would occur between a slip system in one grain and another slip system in the neighboring grain. Their N is given by:

$$\mathrm{N} = (\mathbf{n}_{\mathrm{i}}.\mathbf{n}_{\mathrm{o}})(\mathbf{b}_{\mathrm{i}}.\mathbf{b}_{\mathrm{o}}) + (\mathbf{n}_{\mathrm{i}}.\mathbf{b}_{\mathrm{o}})(\mathbf{b}_{\mathrm{i}}.\mathbf{n}_{\mathrm{o}}), \tag{2.1}$$

where the unit vectors $\mathbf{n}$ and $\mathbf{b}$ respectively represent the slip plane normal and Burgers vector (i.e., slip direction) of incoming and outgoing systems, which are denoted by the subscripts i and o, respectively. Later, Luster and Morris [14] noted that this factor would suggest a non-intuitive transmission for two slip systems with mutually perpendicular slip directions. To circumvent this problem, they modified N by removing the second term in (2.1) and leaving the following,

$$\mathrm{m}' = (\mathbf{n}_{\mathrm{i}}.\mathbf{n}_{\mathrm{o}})(\mathbf{b}_{\mathrm{i}}.\mathbf{b}_{\mathrm{o}}). \tag{2.2}$$

Attractive in its simplicity, m' has since been widely used in the literature to either anticipate or explain slip transmission. Yet still, it has not been uniformly applicable across many different conditions, such as material, slip system orientation, and grain boundary angle. In efforts to improve it, other geometric slip transmission indicators have been proposed that account for different microstructural measures, such as grain boundary orientation [58] and residual Burgers vector [59]. Lee et al. [60] conducted an in situ TEM analysis of the interaction of gliding dislocations with the grain boundaries in HCP metals and proposed three conditions for slip transmission:

1. The misalignment between the traces on the grain boundary plane made by the incoming and the outgoing slip planes should be minimized.
2. The magnitude of the Burgers vector of the residual dislocations left at the grain boundary after slip transmission has occurred should be small.

3. The magnitude of the Burgers vector of the residual dislocations left at the grain boundary after slip transmission has occurred should be small.

They devised what is known today as the LRB criterion [59, 60]. This transmission indicator did not, however, explicitly incorporate the third condition, the RSS on the outgoing slip system. Candidate outgoing systems were instead represented by the Schmid factor and considered as a separate condition. An in situ EBSD on a duplex titanium alloy subjected to tensile tests suggested that the Schmid factor may serve as a relevant parameter to predict the transmitted slip system on the condition that it can be activated [61]. In a study on CP-Ti, it was found that among the six available $\{10\bar{1}2\} < \bar{1}011 >$ tensile twinning variants, the observed slip-stimulated twin lamellae had the highest m' value, while the Schmid factor based on the global stress state was a less significant indicator of twin activity [5]. In a similar study on slip-induced tensile twinning in a Mg-Y alloy, it was identified that the classical m' cannot explain the transmission, and it is the microscopic deformation that controls slip-to-twin transmission occurrences [10]. Examining experimental characterization of slip transmission in several alloys, including HCPs, resulted in the conclusion that different materials appear to have different dependencies on geometrical features, like slip directions, slip planes, and angle of the intersection of slip plane trace on the grain boundary plane [62]. Since then, several criteria that account for weighted sum of these three conditions have been proposed [62].

Apart from geometric criteria, a number of computational techniques have been built to model strain localization via intense slip bands. Most of them involved a local strain softening mechanism to formulate heterogeneous deformations. Bréchet et al. [63] were among the first to propose that heterogeneous plastic deformation in the form of slip bands is due to a local softening mechanism caused by the destruction of short-range order. This softening-based model has since been used to simulate strain localization in shear banding, dislocation channeling, and persistent slip bands in cubic materials using a finite element (FE) framework [31, 32, 64, 65, 66]. Zhang et al. [33] developed a shear-enhanced crystal plasticity constitutive relationship that reduced the slip resistance to account for the slip softening due to breakdown of the short-range order. Using this constitutive model within a 2D crystal plasticity FE framework, they have simulated strain localization in a duplex Ti alloy. Notably, their simulated slip band structure was in qualitative agreement with experiments. An exponential decay in slip resistance implemented within a crystal plasticity Fast Fourier Transform (FFT) solver was employed to capture strain localization in 2D and 3D polycrystal simulations [36]. Through a systematic analysis of strain localization modes, slip and kink bands were distinguished and the evolution in their volume fractions was simulated. These simulations were carried out for an isotropic material with hypothetical parameters.

The localized plasticity via slip bands in a given grain would cause stress concentrations in its neighboring grain. From these slip band models, not studied in much detail is the stress field generated within, around, and ahead of these localized slip bands. They also mainly focused on BCC and FCC metals and, for HCPs, only the basal systems were considered. Further, the effects of parent and possibly nearest neighboring grain orientation on slip band development and the possibility of blunting, triggering another slip band/twin, or creating an orientation deviation zone in the neighboring grain were not addressed. In what follows, we describe a framework for explicit modeling of slip bands, and the heterogeneous stress/strain fields associated with them, that will be used to explain several micro- and macro-scale experimental observations in a wide range of polycrystalline materials.

2.2 Elasto-viscoplastic fast Fourier transforms approach

In this work, we extend a crystal plasticity model to simulate the development of an intragranular slip band in a polycrystal. The model builds upon the infinitesimal-strain formulation of the elasto-viscoplastic (EVP) fast Fourier transform (FFT) method developed by Lebensohn et al. [67] to simulate heterogeneous deformation in polycrystals. EVP-FFT computes the spatially resolved intragranular micromechanical fields and macroscopic mechanical behavior of polycrystalline materials. This methodology can treat any number of intragranular heterogeneities with a given morphology and volume fraction, and these heterogeneous domains can adopt any crystallographic orientation and constitutive response distinct from the rest of the grain. As its name suggests, the EVP-FFT approach employs an elastic-viscoplastic constitutive potential for the material. The material model is discretized into a regular 3D grid of points, each at the center of a voxel. The solution procedure involves iteratively adjusting a compatible strain field and an equilibrated stress field until its constitutive potential minimizes the average local work at every material point in the model. Fourier transforms are used to perform simple products in Fourier space instead of solving convolution integrals in real space.

Many prior computational studies have employed the EVP-FFT framework to investigate the deformation behavior of polycrystalline materials [68, 69, 70, 71, 72, 73, 74, 75, 76]. In close relation to the work here, recently, EVP-FFT has been employed to treat discrete twin lamellae or cracks within crystals. In the case of a twin, a planar twin lamella is the heterogeneous domain, defined by a predetermined set of voxels that are crystallographically reoriented to the orientation of the twin variant and within which the characteristic twin shear of the twin variant is imposed [77]. The model was, for instance, used to study the effect of local stress fields on twin growth and transmission across grain boundaries in HCP materials [78]. To investigate the influence of microstructure variability on short crack growth, the EVP-FFT approach was used to model an elliptic crack by assigning void properties, i.e., infinite compliance, to a set of voxels inside a grain within an FCC Ni-based superalloy [79].

We first briefly review the portion of the formulation of the EVP-FFT model concerned with the constitutive law. A full presentation of EVP-FFT can be found in the original work [67]. The stress in an elasto-viscoplastic material at point $\mathbf{x}$ is given by Hooke's law:

$$\boldsymbol{\sigma}(\mathbf{x}) = \mathbf{C}(\mathbf{x}) : \boldsymbol{\varepsilon}^{\mathrm{e}}(\mathbf{x}) = \mathbf{C}(\mathbf{x}) : (\boldsymbol{\varepsilon}(\mathbf{x}) - \boldsymbol{\varepsilon}^{\mathrm{p}}(\mathbf{x})) \tag{2.3}$$

where $\boldsymbol{\sigma}(\mathbf{x})$ is the Cauchy stress tensor, $\mathbf{C}(\mathbf{x})$ contains material's anisotropic elastic constants, and $\boldsymbol{\varepsilon}(\mathbf{x})$, $\boldsymbol{\varepsilon}^{\mathrm{e}}(\mathbf{x})$, and $\boldsymbol{\varepsilon}^{\mathrm{p}}(\mathbf{x})$ are respectively the total, elastic, and plastic strain tensors, calculated at any material point $\mathbf{x}$. Applying an appropriate implicit time discretization scheme provides the following for the stress at $\mathbf{x}$ at time $t + \Delta t$,

$$\boldsymbol{\sigma}^{\mathrm{t+\Delta t}}(\mathbf{x}) = \mathbf{C}(\mathbf{x}) : \left(\boldsymbol{\varepsilon}^{\mathrm{t+\Delta t}}(\mathbf{x}) - \boldsymbol{\varepsilon}^{\mathrm{p,t}}(\mathbf{x}) - \dot{\boldsymbol{\varepsilon}}^{\mathrm{p,t+\Delta t}}\left(\mathbf{x}, \boldsymbol{\sigma}^{\mathrm{t+\Delta t}}\right) \Delta \mathrm{t}\right) \tag{2.4}$$

where $\dot{\boldsymbol{\varepsilon}}^{\mathrm{p}}(\mathbf{x})$ is the viscoplastic strain-rate tensor. A viscoplastic flow rule is used to relate $\dot{\boldsymbol{\varepsilon}}^{\mathrm{p}}(\mathbf{x})$ to the stress tensor and all active slip systems at the same point, i.e.,

$$\dot{\boldsymbol{\varepsilon}}^{\mathrm{p}}(\mathbf{x}) = \sum_{\mathrm{s=1}}^{\mathrm{N}} \mathbf{m}^{\mathrm{s}}(\mathbf{x}) \dot{\gamma}^{\mathrm{s}}(\mathbf{x}) = \dot{\gamma}_0 \sum_{\mathrm{s=1}}^{\mathrm{N}} \mathbf{m}^{\mathrm{s}}(\mathbf{x}) \left(\frac{|\mathbf{m}^{\mathrm{s}}(\mathbf{x}) : \boldsymbol{\sigma}(\mathbf{x})|}{\tau_{\mathrm{c}}^{\mathrm{s}}(\mathbf{x})}\right)^{\mathrm{n}} \mathrm{sgn}\left(\mathbf{m}^{\mathrm{s}}(\mathbf{x}) : \boldsymbol{\sigma}(\mathbf{x})\right) \tag{2.5}$$

where N_s is the number of slip systems made available to the material, and $\mathbf{m}^{\mathrm{s}} = (1/2)(\mathbf{b}^{\mathrm{s}} \otimes \mathbf{n}^{\mathrm{s}} + \mathbf{n}^{\mathrm{s}} \otimes \mathbf{b}^{\mathrm{s}})$ is the symmetric part of the Schmid tensor of slip system s. Here, $\mathbf{b}^{\mathrm{s}}$ and $\mathbf{n}^{\mathrm{s}}$ respectively represent the Burgers vector and plane normal of slip system s. The scalars $\dot{\gamma}^{\mathrm{s}}(\mathbf{x})$ and $\tau_{\mathrm{c}}^{\mathrm{s}}(\mathbf{x})$ are the shear rate and the slip strength (SS) or the critical resolved shear stress (CRSS), associated with slip system s at point $\mathbf{x}$, respectively. $\dot{\gamma}_0$ is a reference strain rate, and n is the stress exponent. In (2.5), the term $\operatorname{sgn}\left(\mathbf{m}^{\mathrm{s}}(\mathbf{x}) : \boldsymbol{\sigma}(\mathbf{x})\right)$ enforces the slip rate direction to align with the glide direction.

2.3 Slip band fast Fourier transforms (SB-FFT)

In the model developed here, a slip band is considered a heterogeneity with a different constitutive law within the EVP-FFT model. Similar to a crack or twin lamella, an intense slip band formed within a grain is a planar heterogeneity that bears a higher amount of shear. Furthermore, like a twin lamella, slip bands develop on crystallographic planes and in a particular crystallographic direction. However, unlike a twin lamella, the amount of reorientation and shear associated with a slip band is not limited to or precisely defined by the atomic structure. Further, in a slip band, the amount of shear evolves with strain (or time) depending on the deformation history and local microstructure.

That being said, the slip band is treated as a region in which the resistance to slip, $\tau_{\mathrm{c}}^{\mathrm{s}}$, decays at a rate proportional to the rate of slip [80, 81]. Although the origins of such localized softening have yet to be clarified, the conventional argument is that it emerges due to a rise in local temperature generated by concentrated slip on a single slip system or slip plane [82, 83, 84]. Regardless of its origin, significant number of experimental studies correlate intense slip bands with a low or negative work hardening in the material [85, 86, 87, 88, 89, 90, 91, 92, 93, 94, 95]. For instance, a study of HCP crystals reported that strain localization was accompanied by a reduction in stress levels within the slip band [95]. Cyclic softening was observed in the Ti-Al single crystal deformed by single and/or double prismatic slip [92, 93, 94]. Cleared channels of slip bands were correlated with the defect removal mechanism or local relaxation in copper crystals [90]. Accordingly, extensive crystal plasticity modeling studies treat slip bands as regions experiencing material softening, a decay in the slip resistance with strain [63, 28, 29, 30, 31, 32, 33, 34, 36, 37, 96, 97]. Zhang et al. [33], for instance, used an evolution law allowing increased plastic strain rates to soften slip resistance on the basal and prismatic planes within the primary α-phase of a Ti–6Al–4V alloy. An exponential decay of the critical resolved shear stress, with a 20% maximum softening, was used to capture strain localization in HCPs [36].

In the model developed here, at each material point $\mathbf{x}$ located within the pre-selected slip band domain, the slip strength (τ_c^{s}) for slip system s decreases proportionally with the rate of plastic strain ($\dot{\gamma}^{\mathrm{s}}$) on that system. The slip resistance in the surrounding parent matrix and all other grain(s) remains constant or follows a hardening law, depending on the material being studied. To model materials that show significant hardening, we elect to use an extended Voce hardening law [98, 99, 100]. The following expressions respectively describe the evolution of slip resistance within the slip band domain, and outside of it without and with strain hardening:

$$\tau_c^{\mathrm{s,t+\Delta t}}(\mathbf{x}) = \begin{cases} \tau_c^{\mathrm{s,t}}(\mathbf{x}) - D_0 \tau_c^{\mathrm{s,t}}(\mathbf{x}) \left|\dot{\gamma}^{\mathrm{s,t}}(\mathbf{x})\right| \Delta t & : \ \mathbf{x} \in \mathrm{SB} \\ \tau_c^{\mathrm{s,t}}(\mathbf{x}) = \tau_c^{\mathrm{s}}(\mathbf{x})|_{\gamma^{\mathrm{s}}(\mathbf{x})=0} & : \ \mathbf{x} \notin \mathrm{SB} \\ \tau_c^{\mathrm{s,0}}(\mathbf{x}) + (\tau_1^{\mathrm{s}} + \theta_1^{\mathrm{s}} \sum_s \gamma^{\mathrm{s,t}}(\mathbf{x}))\left[1 - exp(-(\sum_s \gamma^{\mathrm{s,t}}(\mathbf{x}))\theta_0^{\mathrm{s}}/\tau_1^{\mathrm{s}})\right] & : \ \mathbf{x} \notin \mathrm{SB} \end{cases} \tag{2.6}$$

where the coefficient D_0 is a material constant to regulate the rate of softening. Due to its relationship to slip, it will likely depend on the applied temperature and strain rate. It is suggested to calibrate the model using experimental results to obtain an accurate measure for D_0. However, when relevant experimental data is not available, this constant can be numerically determined so that the slip band fully develops within the prescribed applied strain. $\tau_c^{\mathrm{s,0}}$ and θ_0^{s} are respectively the initial CRSS and hardening rate, while

τ_1^s and θ_1^s determine the asymptotic characteristics of the hardening. Finally, to avoid numerical instabilities, a lower limit for τ_c^s is set for all slip systems.

Chapter 3

Role of grain neighbor orientation on slip localization in HCP materials

3.1 Introduction

This chapter aims to identify the effect of grain neighbor orientation on slip band development, as well as its potential transmission into the neighboring grain. To this end, we employ the explicit slip band model SB-FFT introduced in Chapter 2 to simulate the evolution of a discrete crystallographic slip band within an HCP crystal. The slip band is treated as a planar heterogeneity with a softening rate constitutive law distinct from the rest of the grain. The SB-FFT simulations focus on calculations of the local stress and strain fields and activated slip modes both within the parent grain and ahead of the band in the neighboring grain. We validate the model predictions by comparisons with previously reported experimental observations on CP-Ti, Mg-Y, and Ti64 alloys.

3.2 Model set-up and material parameters

Figure 3.1 shows bicrystal model set up comprised of a parent grain, containing an explicit, discrete slip band, adjoined by its neighboring grain, without a slip band. The model uses periodic boundary conditions in all three directions. The model set up shown is the $y - z$ plane of the periodic simulation cell. Within this plane, the parent and neighboring grains are similarly discretized into 100 × 200 voxels in the $y - z$ directions, respectively. The simulation cell in the $x-$direction is three voxels thick. As shown, the bicrystal is surrounded by a 20-voxel-thick homogeneous layer with uniformly distributed crystal orientations, intended to represent the average bulk response from the surrounding polycrystal. As will be discussed shortly, this value is determined to be sufficiently large such that the spatially resolved micromechanical fields are unaffected by the periodic nature of the imposed boundary conditions. In this example set up, for convenience, the slip band is made to lie at a 45° angle with respect to $y-$axis. Each crystal can take on any crystallographic orientation. The orientation of the parent grain is assigned such that the Burgers vector and slip plane normal of the slip band system lie in the $y - z$ plane and respectively along the vectors $\mathbf{b}$ and $\mathbf{n}$ shown in Figure 3.1. Accordingly, the parent grain orientation, when using Euler angles in Bunge convention, is (90°, 90°, 45°) when the slip band lies on a prismatic plane, and (0°, 45°, 30°) when it lies on a basal plane.

A preselected slip band with a given thickness w is embedded in the parent grain with its plane lying 45° with respect to $y-$axis, in which material can soften with application of a far-field strain based on the constitutive law described in (2.6). The crystallographic orientation of the parent crystal corresponding to a band, lying either on the basal plane or the prismatic plane, is shown using HCP crystal frames in Figure 3.1. The orientation of the neighboring grain can vary. Uni-axial tension is applied along the $y-$direction,

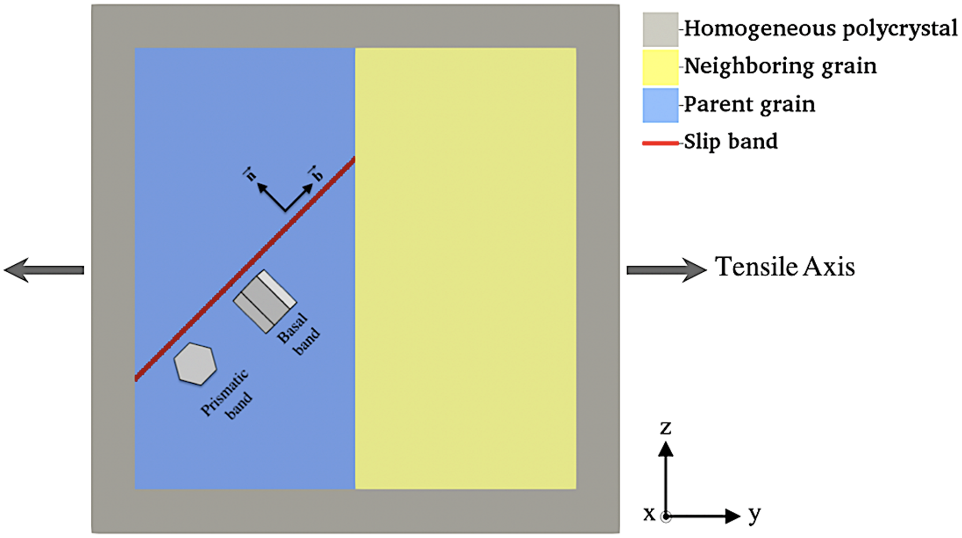

Figure 3.1: Schematic of the bicrystal unit cell under uniaxial tension in the $y-$direction. A two-voxel-thick ($w = 2$) slip band is shown in red embedded in parent grain. The hexagonal structures show the orientations of the parent HCP crystal corresponding to a prismatic or a basal slip band. The vectors **b** and **n** are, respectively, the Burgers vector and slip plane normal of the slip system on which the slip band localization occur.

while the normal stress components in $x-$ and $z-$ directions are enforced to be, on average, zero. This state of stress would yield a Schmid factor of 0.5 for the slip system chosen for the slip band in the parent crystal.

For most of this study, the SB-FFT calculations focus on slip bands in magnesium and commercially pure titanium. In Section 4, for validating the model with experimental studies, we additionally apply the model to an Mg-Y alloy and a Ti-6Al-4V alloy. Table 3.1 presents the properties of these four materials at room temperature, which includes the coefficient D_0 in (2.6), the anisotropic elastic constants, c/a ratio, potential slip systems, and their strengths (SS). For most of the studied materials, the order of magnitude of D_0 was determined so that the slip band would fully develop in the range of these materials within an applied strain of 1%. For the Ti-6Al-4V alloy, however, with high-resolution local strain measurements available, this coefficient was rigorously determined through a calibration process, as explained in Section 4.3. The stress exponent n

appeared in (2.5) is set to 10 for all of the simulations carried out in this work. A short study of the effect of the stress exponent on degree of localization is presented in Appendix A. The elastic and plastic properties of Mg and CP-Ti are significantly different. As a measure of elastic anisotropy, we employ the universal measure of anisotropy A^L applicable to all crystalline materials [101], where the ideal case of elastic isotropy corresponds to A^L being zero. The anisotropy index of CP-Ti is $A^L = 0.075$, which is higher than the index of Mg, which is $A^L = 0.012$. Concerning plastic behavior, Mg is more plastically anisotropic than Ti, with ratio of SS values for the easiest to hardest slip mode of 1:11:26 (basal:prismatic:pyramidal) for Mg against roughly 1:2:3 (prismatic:basal:pyramidal) for Ti. For Mg, the easiest mode is basal with a very low SS, followed by prismatic, and finally pyramidal, which is the hardest. For Ti, however, the easiest mode is prismatic, followed by moderately harder basal, and then pyramidal as the hardest system.

Table 3.1: Elastic constants [16], c/a ratio [17], softening coefficient D_0, and CRSS values for different deformation modes for Mg [18], CP-Ti [15], Mg-Y [19], and Ti-6Al-4V [20]. Note that only slip modes are employed to accommodate plastic deformation in the calculations

Material	Elastic constants (GPa)					c/a	D_0	CRSS values for deformation modes (MPa)			
	C_{11}	C_{22}	C_{13}	C_{33}	C_{44}	ratio		basal $< a >$	prismatic $< a >$	pyramidal I $< c + a >$	Twin $\{10\bar{1}2\}$
Mg	59.8	23.2	21.7	61.7	16.4	1.624	10	3.3	35.7	86.2	20
CP-Ti	162.4	92.0	69.0	180.7	46.7	1.588	10	128	69	180	225
Mg-Y	59.8	23.2	21.7	61.7	16.4	1.624	30	22	85	90	13
Ti-6Al-4V	162.4	92.0	69.0	180.7	46.7	1.588	64	420	370	590	-

3.2.1 Band thickness (w) effects

Cooperative, as opposed to independent, movement of dislocations on collective glide planes that are spatially correlated implies that several parallel glide planes with less than 10 nm spacing are congregated to form a single slip band [102]. Significant number of experimental studies have reported a finite thickness for observed slip bands, ranging from 0.1 μm to 2 μm [85, 92, 93, 103, 104, 105, 106]. For instance, the average thickness of slip bands in quench-hardened gold single crystals subjected to uniaxial tension was reported to be about 0.16 μm or equivalent to 850 consecutive $\{111\}$ parallel planes [85]. From the atomic force microscopy (AFM) measurements of 83 slip bands within 12 grains in polycrystalline nickel, a wide spectrum of band thicknesses (150-1150 nm) and step heights (2-25 nm) was found [106]. While the slip band thickness varies in these studies depending on the material and loading conditions, a common observation is that slip bands manifest finite thicknesses that are much smaller than the overall grain size. Therefore, for modelling slip bands, we need to choose a thickness that provides a localization effect while remains substantially thinner than its parent grain. Figure 3.1 shows the slip band within a crystal, as represented by a planar domain of thickness w, described by two parallel boundaries, each of which represents the glide plane projected on $y-z$ plane. Several simulations were conducted for a wide range of w from $w=1$ to $w=22$ voxels to identify an appropriate value. For the present calculations, we aim for a uniform region of slip along the band and across its thickness and to select the same thickness for all calculations hereinafter. A thickness of $w=1$ is found unsuitable since the band develops discontinuously along its length, in stark contrast to experimental observations. For all bands with $w>1$, localized slip eventually develops along the band. For $w>2$, the fields within the band vary across the thickness of the band to a degree that depends on w. While the variation could have physical significance, this effect is not the phenomenon under investigation. In what follows, we use a slip band domain with $w=2$, which produces uniform behavior across the width of the domain.

3.2.2 Cell thickness effects

The model microstructure is constant in the out-of-plane, $x-$direction, and therefore represents a columnar structure through thickness. To seek out any sensitivity in the results to the simulation cell thickness, calculations were repeated over a range of thicknesses from three to 100 voxels. Figure 3.2a shows the bicrystal model cell that is 100 voxels thick, surrounded by a 20-voxel-thick buffer layer in $y-$ and $z-$directions. The orientation of the parent grain is assigned such that the tilting plane on which the deformation is expected to be localized is a prismatic plane. The orientation of the neighboring grain is (20°, 151°, 92°). A tensile strain is applied in the $y-$axis. Figure 3.2b show the contours of the projected resolved shear stress on the slip band system (SB-RSS) at the point when the $y-$axis uniaxial strain is 1% when the unit cell is three voxels thick. As the strain is gradually applied along the $y-$axis, the stress and strain build in the buffer layer and two crystals and slip occurs. At some larger strain level, such as at the applied 1% shown, the slip band begins to develop more strain than its surrounding parent crystal. Around the band, the stress becomes heterogeneous, with localized stress field building in the neighboring crystal. Concomitantly, the stress reduces within and in the vicinity of the slip band. The same contours at the mid-plane of the bicrystals with the 50 and 100 voxel thick unit cells are shown in Figure 3.2c and d, respectively. In all cases, the SB-RSS is lower in the band region, due to the localized softening, and heightened in the neighboring crystal. Comparing the SB-RSS distributions among these three cell thicknesses finds their differences to be negligible. This consistency can be expected due to the fact that both Burgers vector and slip plane normal of the favored system with strain localization rest in the $y-z$ plane and have no out-of-plane component. For computational efficiency, a cell thickness of three voxels is used for all calculations in this work.

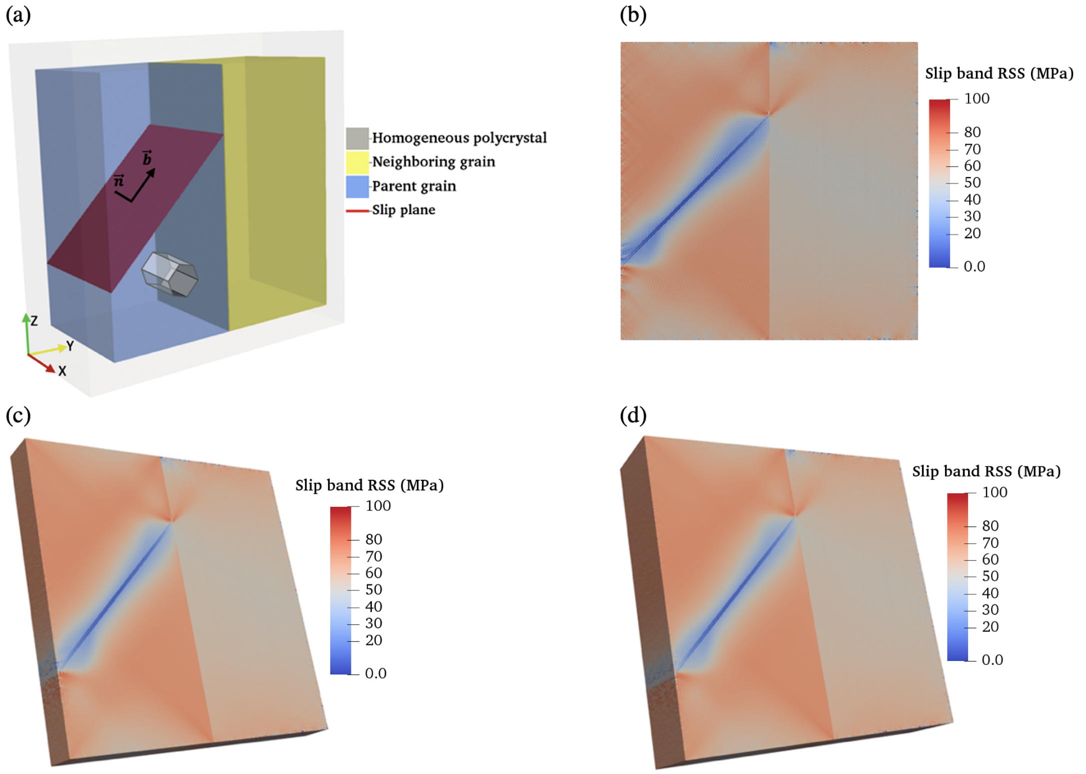

Figure 3.2: (a) Schematic of a bicrystal setup for a 100-voxel thick along the $x-$axis subjected to uniaxial tension in $y-$direction. The slip plane consists of two voxels through thickness ($w = 2$). Orientation of the parent crystal with a prismatic slip band is shown by an HCP crystal frame. Calculated distributions of the projected slip band resolved shear stress (SB-RSS) in CP-Ti for three different out-of-plane thicknesses along the $x-$axis: (b) three, (c) 50, and (d) 100 voxels. In (c, d), the stress contours are shown at the mid-planes of the cells. The surrounding homogeneous layer of polycrystal has been removed from the image in (b)-(d).

3.3 Grain neighbor-affected slip localization

3.3.1 Development of slip localization

We begin by studying the development of a prismatic slip band in CP-Ti under continued straining. The crystal is initially free of a slip band before application of the applied strain. In other words, while a domain is preselected within the parent crystal for the slip band to develop in, all material points in the parent crystal are strain-free before application of the far-field strain. The parent crystal has an orientation of (90°, 90°, 45°) and the neighboring grain orientation is (152°, 128°, 136°). As the far-field strain is applied, a slip band on a prismatic slip plane develops in the parent grain. At yield, the crystals begin to activate slip on one or more slip systems throughout the grain and in the slip band. Figure 3.3 tracks the slip accumulated just on the prismatic slip system corresponding to the slip band, as averaged over the parent grain ($\bar{\varepsilon}_{\mathrm{M}}$) and also averaged solely across the slip band domain ($\bar{\varepsilon}_{\mathrm{SB}}$) as the applied strain increases. At a critical value of applied strain, 0.2% in this case, $\bar{\varepsilon}_{\mathrm{M}}$ and $\bar{\varepsilon}_{\mathrm{SB}}$ become non-zero, signifying that both the band and the matrix begin to slip. At a higher far-field strain, the slip band begins to accumulate more shear strain than its parent, as indicated by the $\bar{\varepsilon}_{\mathrm{M}}$ and $\bar{\varepsilon}_{\mathrm{SB}}$ curves splitting as the rate of accumulated slip within the slip band increases (see inset). At 0.63% macroscopic strain, the slip band accumulates three times more shear strain, on average, as its parent (i.e., $\bar{\varepsilon}_{\mathrm{SB}} > 3\bar{\varepsilon}_{\mathrm{M}}$). This situation, when a small fraction of the grain volume (here, ∼1%) begins to sustain much more strain than its parent, represents the onset of localization. As the applied strain increases, the slip band shear $\bar{\varepsilon}_{\mathrm{SB}}$ rapidly increases further, growing to be several times $\bar{\varepsilon}_{\mathrm{M}}$.

Next, the simulation is repeated with the same parent and slip band but two other grain neighbor orientations. One grain neighbor orientation creates a higher misorientation (∼89°) with the parent than the earlier example. Its orientation could also be

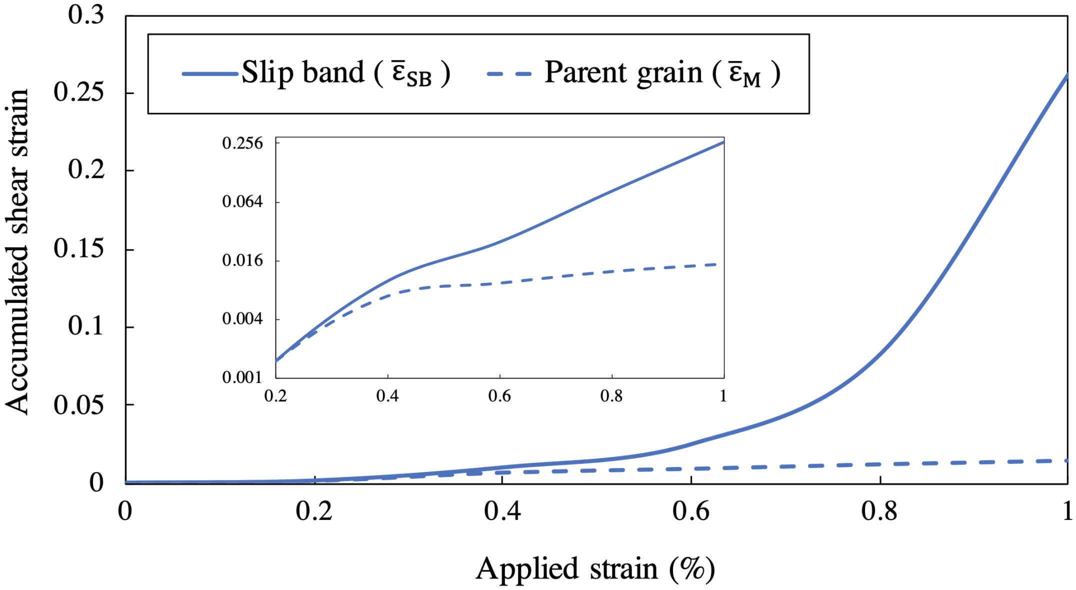

Figure 3.3: Evolution of $\bar{\varepsilon}_{\mathrm{SB}}$, the average accumulated plastic strain on the prismatic slip band system within the band domain, and of $\bar{\varepsilon}_{\mathrm{M}}$ outside the band in the parent grain in CP-Ti. Inset: semi-log plot is shown for a strain range of 0.2-1% focusing on the accumulated slip in the parent, as well as the separation in the evolution of accumulated slip within the slip band from that in parent, as the applied strain increases.

considered a soft orientation, being more suitably oriented for prismatic slip with respect to the applied load. The second orientation has a similar misorientation (~64°) as the earlier example. But it is a relatively hard one, being even less suitably oriented for prismatic slip than the other two orientations. Here, we adopt an ad hoc conservative definition for 'soft' and 'hard' orientations, keeping in mind that there is in fact a spectrum of geometric hardness ranging from soft to hard. In particular, a 'soft' or 'hard' orientation respectively indicates a 'low' or 'high' geometric hardness for the easiest slip mode in that orientation. Quantitatively, it is measured by the maximum Schmid factor m_s among the slip systems of the easiest slip mode, which can range from 0 to 0.5. Between the two grain neighbors mentioned earlier, the soft neighbor has $m_s = 0.48$, while hard neighbor has $m_s = 0.09$. The properties of grain neighbor orientations for these two additional cases are also listed in Table 3.2.

Table 3.2: Euler angles in Bunge convention, misorientation between the parent and nearest neighbor grain, and maximum Schmid factor among the systems of the easiest slip mode in CP-Ti and Mg bicrystals.

Material	Easiest system	Neighboring grain orientation	Euler angles (degrees)			Maximum Schmid factor of the easiest system in the neighboring grain	Misorientation (degrees)
			ϕ_1	Φ	ϕ_2		
CP-Ti	Prismatic	Soft	353	174	254	0.48	89.3
		Moderate	152	128	136	0.24	68.3
		Hard	26	88	163	0.09	64.0
Mg	Basal	Soft	352	146	223	0.46	78.8
		Moderate	138	160	66	0.23	32.4
		Hard	93	81	259	0.05	85.8

Figure 3.4a compares the evolution of $\bar{\varepsilon}_{\mathrm{M}}$ and $\bar{\varepsilon}_{\mathrm{SB}}$ in the same slip band/parent grain for the three grain neighbor orientations. Regardless of grain neighbor orientation, the evolution of $\bar{\varepsilon}_{\mathrm{M}}$ and $\bar{\varepsilon}_{\mathrm{SB}}$ manifest in a similar manner. A finite amount of strain is required for slip to initiate in the parent and band, and with more strain, slip is seen to accumulate much faster in the band. If we, as before, consider as a measure of localization $\varepsilon_{\mathrm{loc}}$, the

macroscopic strain at which $\bar{\varepsilon}_{\mathrm{SB}} > 3\bar{\varepsilon}_{\mathrm{M}}$, we find that the nearest neighbor orientation affects how quickly the slip band accumulates shear strain. The higher misorientation neighbor, with the geometrically softer orientation has a localization strain $\varepsilon_{\mathrm{loc}}$ of 0.72%, while the neighbor with a similar misorientation as the earlier example, but with a harder orientation has a lower localization strain $\varepsilon_{\mathrm{loc}}$ of 0.56%. In another view, at the same applied strain of 0.72%, in the latter case the slip band would have nearly 10 times more shear strain than the parent, while in the former case, the slip band would have only three times more. At least in these three cases, the crystallographically harder neighboring grain promotes faster slip band localization. To demonstrate strain heterogeneity between the slip band and the parent grain as well as between the two crystals, contours of equivalent plastic strain in these three cases are presented in Appendix A.

3.3.2 Stress fields associated with a slip band

As more shear strain localizes in the slip band, the stresses locally in a zone ahead of the slip band are expected to rise concomitantly. In the present bicrystal configuration, the slip band tip plastic zone lies in the neighboring grain at the slip band/GB junction. Figure 3.5a plots the development of average von Mises stress in a small slip band tip volume of 6×6×3 voxels (2-3 times in size than the band thickness) in the neighboring grain with applied strain. Alongside these curves, the evolution of the average von Mises stress for the entire neighboring grain are also plotted. In all cases, the stress in the slip band tip zone increases with applied strain, while the stress in the grain eventually softens in some cases. A stress concentration caused by the strain localization in the band can be identified by the amount the von Mises stress in the slip band tip zone at the slip band/GB junction exceeds the grain average. For CP-Ti, the stress concentration due to the slip band in all three neighbors increases as the applied strain increases beyond $\varepsilon_{\mathrm{loc}}$,

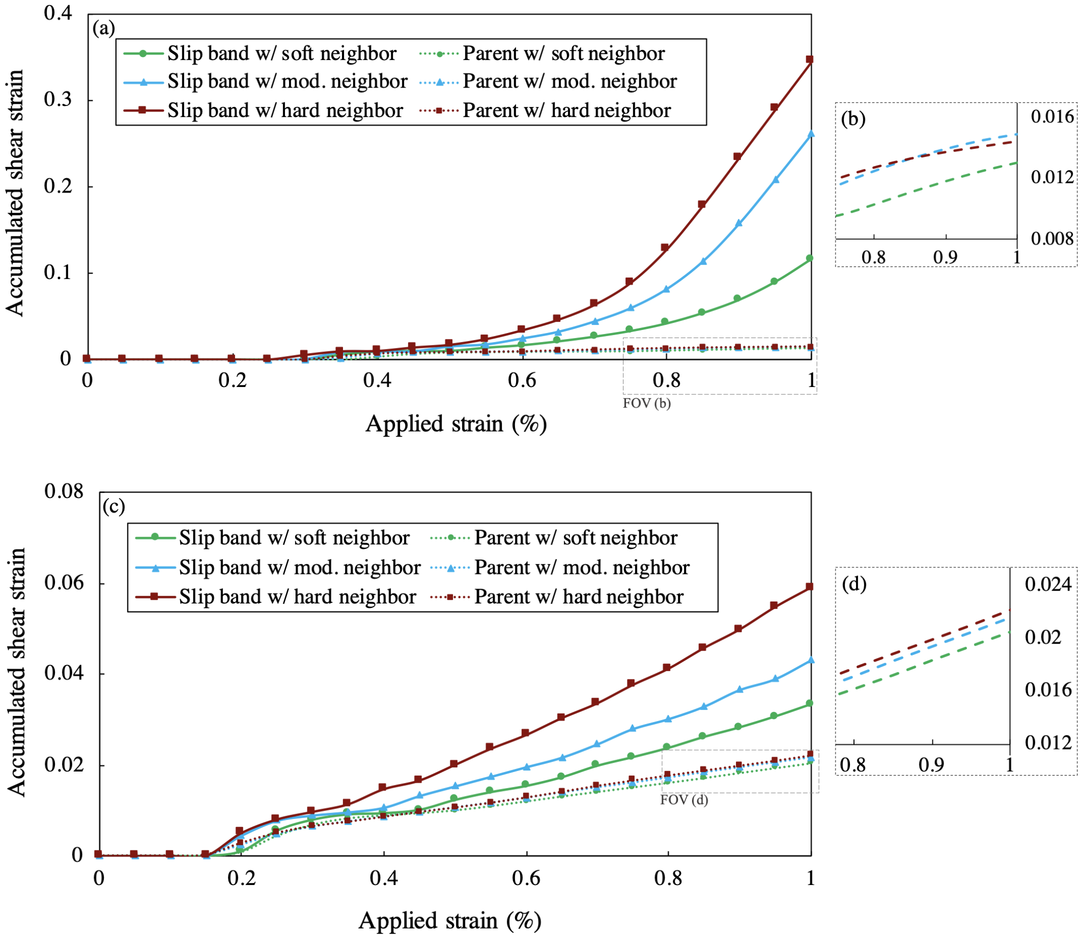

Figure 3.4: Evolution of accumulated plastic strain on the slip band system within the band domain and in the parent matrix in three typical situations of soft, moderate, and hard neighboring grains for the (a) CP-Ti and (c) Mg with a prismatic and a basal slip band, respectively. (b) and (d) Selected enlarged views in (a) and (c), respectively, show the average plastic strain in the parent grain.

when the slip band has accumulated intense shear. The reason for the moderate neighbor developing lower von Mises stress than the soft neighbor is found to be that the second easiest slip mode (i.e., basal slip) in the soft neighbor is not favorable with respect to the applied load, while in the moderate neighbor, it is extremely favorable ($m_s = 0.5$). This might have contributed to the overall softness of the 'moderate' grain and caused lower stress levels.

At the same time, the slip band and the parent grain in vicinity of the band develops a reaction stress, called a *back-stress*, that acts against slip. The back-stress is responsible for a decay in the total stress in the parent grain in the vicinity of the band as more strain is applied. Figure 3.6a shows the evolution of the resolved shear stress on the slip band system (SB-RSS) within the vicinity of the band in the parent matrix, as well as in the entire parent grain, as the applied strain on a CP-Ti sample increases up to 1%. The RSS in the slip band vicinity is averaged over two parallel bands above and below the slip band domain, each with thickness of two voxels. Development of the back-stress is evident by the reduction in stress at the areas surrounding the band as the far-field strain rises beyond the localization strain $\varepsilon_{\mathrm{loc}}$. These three cases indicate signs that the harder the neighbor is to deform, the more shear strain accumulates in the band, and the higher back-stress is experienced by the parent grain around the slip band.

Next, we consider the same analysis but in another HCP metal, Mg. Compared to CP-Ti, Mg is a weaker material, wherein the SS values to activate slip in any of the slip systems in Mg are lower than those in CP-Ti (see Table 3.1). As another key difference, the preferred basal slip system in Mg is approximately ten times easier than the next easiest slip system, prismatic slip, whereas in CP-Ti the SS for prismatic slip is only half that of basal slip. In simulation, the Mg parent crystal orientation is (0°, 45°, 30°). As in CP-Ti, for Mg, three different neighboring grain orientations are considered, representing either a geometrically hard, moderate, and soft orientation. These are defined by their

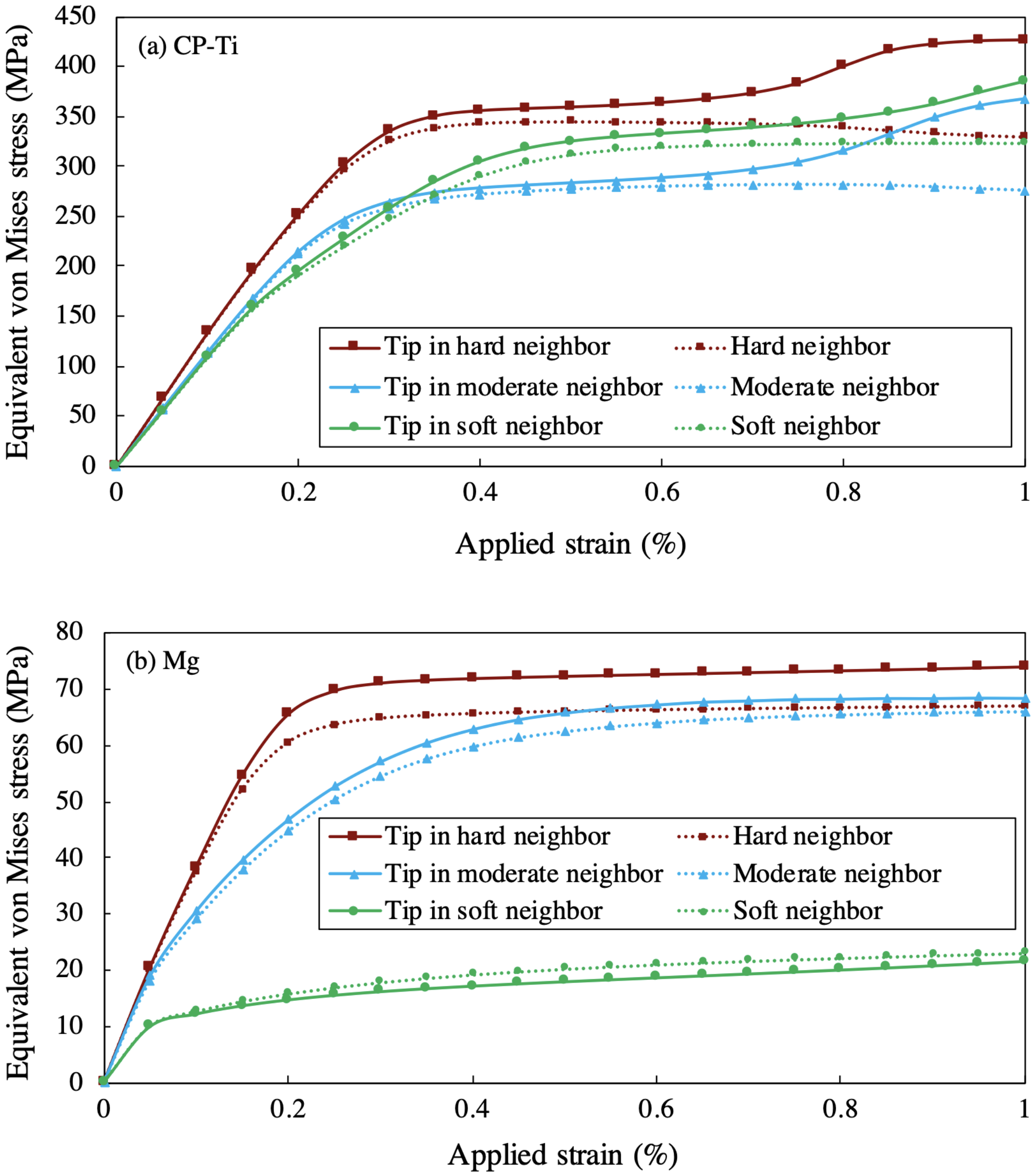

Figure 3.5: Evolution of the equivalent von Mises stress in a small zone ahead of the slip band tip and in the interior of the neighboring grain for representative soft, moderate, and hard neighboring grains for the (a) CP-Ti with a prismatic and (b) Mg with a basal slip band, respectively.

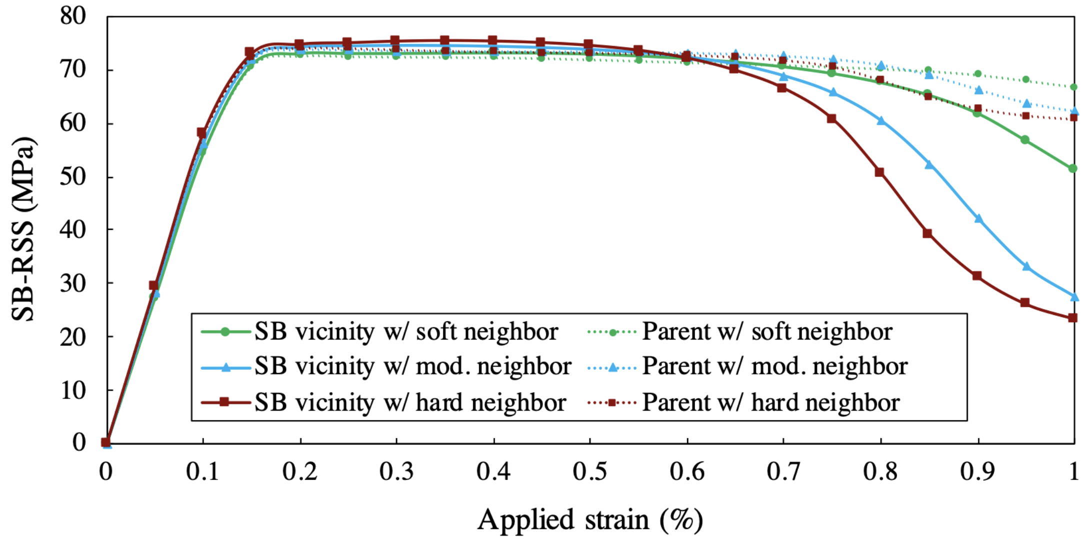
(a) CP-Ti

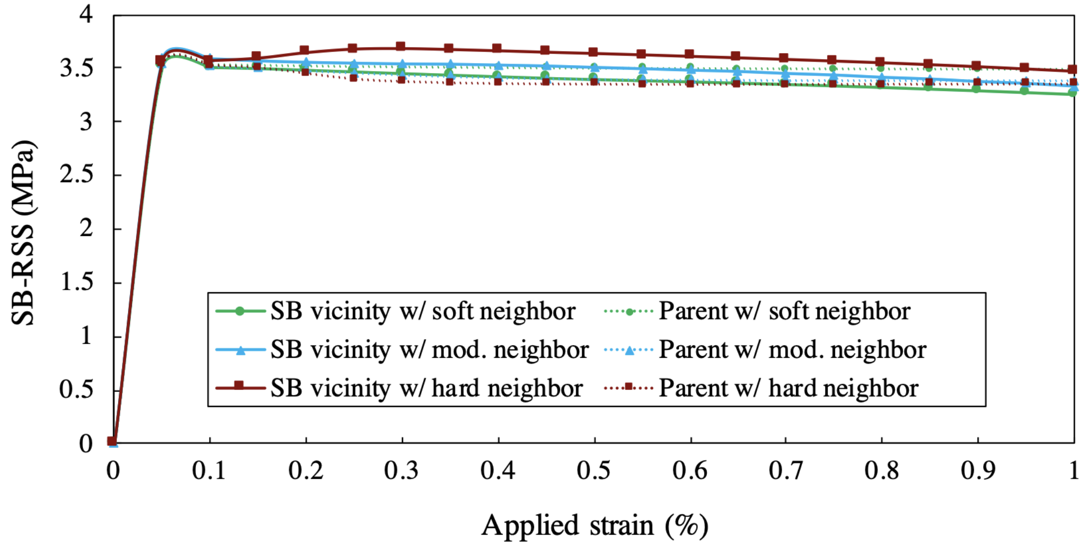
(b) Mg

Figure 3.6: Evolution of the resolved shear stress on the slip band system (SB-RSS) in the vicinity of the slip band domain and parent matrix in three typical situations of soft, moderate, and hard neighboring grains for (a) CP-Ti and (b) Mg with a prismatic and a basal slip band, respectively.

suitability to activate basal slip with respect to the applied load. Their maximum Schmid factor among the basal slip systems is $m_s = 0.05$, 0.23, and 0.46. Table 3.2 summarizes the geometrical parameters for these three cases. Figure 3.4c shows the evolution of the accumulated plastic strain on the slip band system within the slip band domain ($\bar{\varepsilon}_{\mathrm{SB}}$) and in the parent grain ($\bar{\varepsilon}_{\mathrm{M}}$) in Mg. Plasticity initiates earlier in all three cases in Mg compare to those in CP-Ti, a confirmation of the greater ease to activate basal slip in Mg than any of the slip systems in CP-Ti. The neighbor orientation has a similar effect on localization, with relatively harder neighbors causing the slip band to localize strain much faster than the softer neighbor. The noticeable difference, however, is that compared to CP-Ti, in Mg, the $\bar{\varepsilon}_{\mathrm{SB}}$ is lower and the needed $\varepsilon_{\mathrm{loc}}$ for the onset of localization is larger. The associated development of and rise in von Mises stress in the zone ahead of the slip band tip in the neighboring grain are shown in Figure 3.5b. As seen in CP-Ti, the von Mises stresses generated by the slip band are the highest for the hardest neighbor. However, the stresses in the slip band tip zone do not necessarily lead to stress concentrations. In the hardest neighbor, the zone stresses are clearly above those of the average stress in the neighboring grain, signaling the development of stress concentrations, but, in the softest neighbor, the average stress in the grain are higher than in the zone, signifying no stress concentration. As an assessment of back-stress development in the parent grain, for Mg, Figure 3.6b shows evolution of the SB-RSS in the vicinity of slip band domain and in the parent grain as the applied strain increases up to 1%. Minimal back-stress development, or none in some cases, is observed. Comparing the amounts of reductions in Figure 3.6a with b indicates that, regardless of grain neighbor orientation, CP-Ti is developing larger back-stresses than Mg. Higher back-stress development is a consequence of the larger strains that localize within the bands in CP-Ti, as seen in Figure 3.4.

3.3.3 Role of neighboring grain

The few cases analyzed above suggest that the misorientation angle between two crystals has little effect on slip localization within the band, while the Schmid factor m_s of the easiest system in the neighboring grain has a much greater effect. To determine whether this effect is prevalent, the calculations are broadened to include several grain neighbor orientations, spanning the full range of possible grain boundary misorientations and levels of plastic hardness for CP-Ti and Mg. Figure 3.7 presents the accumulated slip band strain $\bar{\varepsilon}_{\mathrm{SB}}$ at uniaxial strain of 1% and the macroscopic strain $\varepsilon_{\mathrm{loc}}$ needed for the onset of localization ($\bar{\varepsilon}_{\mathrm{SB}} > 3\bar{\varepsilon}_{\mathrm{M}}$) for 33 distinct grain neighbor orientations. Here, $\bar{\varepsilon}_{\mathrm{SB}}$ is normalized by $\bar{\varepsilon}_{\mathrm{M}}$ in the parent grain, and the neighboring grain hardness is classified by the maximum Schmid factor of its easiest slip mode (prismatic slip for CP-Ti and basal slip for Mg). Figure 3.7a reveals a correlation between the accumulated shear strain in the slip band and the hardness of the neighboring grain orientation for both metals. The plastically harder the neighboring grain (lower m_s), the faster the shear strain within the slip band intensifies. Figure 3.7b shows that, concomitantly, the macroscopic localization strain $\varepsilon_{\mathrm{loc}}$ decreases for the harder grain neighbor. For some grain neighbor orientations in Mg, in both low and high Schmid factor domains, the onset of localization did not occur within the 1% applied strain. In other words, even at 1% macroscopic strain, the accumulated slip in the band $\bar{\varepsilon}_{\mathrm{SB}}$ did not exceed $3\bar{\varepsilon}_{\mathrm{M}}$. Accordingly, those orientations are not presented in Figure 3.7b as a localization strain was not obtained for them. Furthermore, it should be stated that, despite its appearance in Figure 3.7b due to the exclusion of some orientations, the localization strain $\varepsilon_{\mathrm{loc}}$ for a basal slip band in Mg does not involve a greater sensitivity to neighbor orientation than a prismatic slip band in CP-Ti. Comparing the two materials, the weaker material, Mg, generally accumulates less strain in its slip band than the stronger material, CP-Ti, and requires more strain $\varepsilon_{\mathrm{loc}}$

for the onset of localization. It is also found that the stronger elastic anisotropy in CP-Ti, compared to that in Mg, is a contributing parameter to the observation that CP-Ti accumulates more strain in its band (further details on the effect of elastic anisotropy on localization in slip bands can be found in Appendix A). Finally, the accumulated shear strain in the prismatic slip bands in CP-Ti exhibits a greater sensitivity to neighbor orientation than that in the basal slip bands in Mg.

Through the foregoing calculations and analysis, we have, thus far, identified a *neighbor-affected slip band localization* phenomenon. Regardless of material and slip band crystallography, a hard neighbor accelerates the development of the band localization in the parent grain and intensifies slip localization within it. In these cases, as the slip band intensifies, it will affect the deformation of the neighboring grain in a small zone ahead of the slip band. It should be noted, however, that these calculations assume slip band localization process is permitted to proceed continuously without disruption by another dissipation mechanism, such as void formation, grain boundary sliding, fracture, twinning, and formation of another slip band, particularly before the ε_{loc} is reached.

Another assumption that the calculations in this work are based on is that no strain-hardening is induced by local slip activities during the development of a slip band. This assumption may be justified as following. Shear stress-shear strain behavior in most ductile single crystals, such as cubic structures, manifests a three-stage pattern where easy glide in stage I is followed by a strong linear hardening in stage II, due to the secondary slip intersecting the primary system, and finally leads to stage III in which hardening is exhausted. In HCP crystals, on the other hand, due to incapability of secondary slip caused by deficiency of available slip systems, an extended stage I is typically observed which does not lead to the strong hardening of stage II. Instead, a stage B associated with twinning is expected which creates much less hardening than stage II in cubic crystals [107]. In a relevant study on Mg single crystals [108], the shear stress-strain curve was

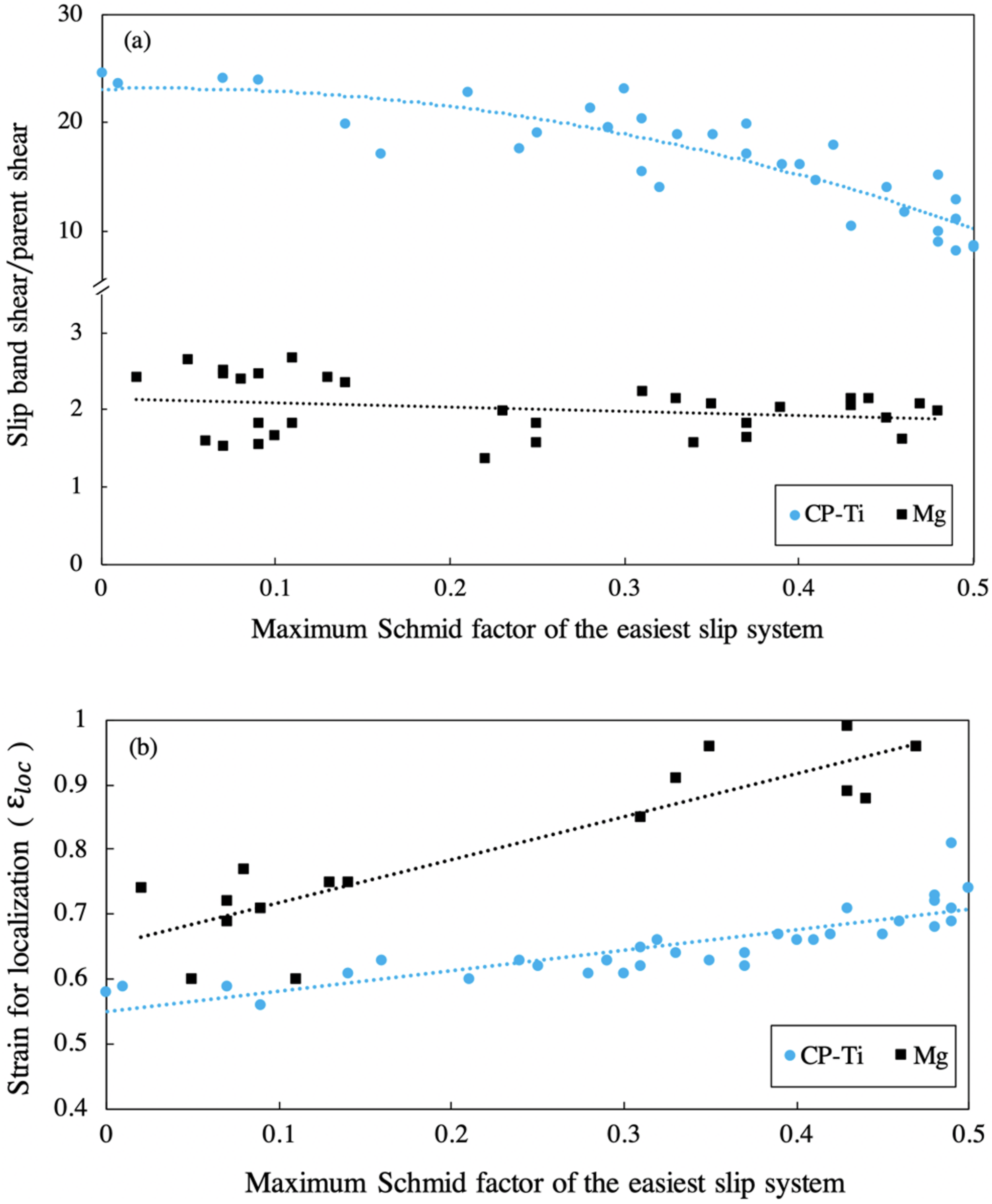

Figure 3.7: (a) Average accumulated plastic strain on the slip band system within the slip band normalized by that in the parent grain for both CP-Ti and Mg at 1% macroscopic applied strain for a broad range of grain neighbor orientations, (b) Variations of the localization strain ($\varepsilon_{\mathrm{loc}}$) with grain neighbor orientation for both CP-Ti and Mg. It is apparent that $\varepsilon_{\mathrm{loc}}$ for Mg bicrystals are relatively higher than Ti, which can imply that slip bands develop earlier in Ti than they do in Mg. Note that some grain neighbor orientations in Mg for which the onset of localization did not occur within the 1% applied strain range are excluded in part (b). As a result, sensitivity of $\varepsilon_{\mathrm{loc}}$ for a basal slip band in Mg to neighbor orientation, as exhibited, may not be accurately comparable with that for a prismatic slip band in CP-Ti.

into two stages; stage A in which the work hardening associated with the easy glide can be very low, and stage B where twin nucleation or secondary slip creates a higher work hardening. It was also reported that, particularly for Mg, stage A extends over 50%-250% shear strain and the low hardening rate in this very long stage is due mainly to interactions between dislocations on the same (basal) slip plane. Therefore, specifically in HCP crystals, noticeable hardening in the slip bands due to nucleation of twins and secondary slip and their intersection with the primary dislocations will not happen in early stages of deformation. In our simulations, the extent of secondary slip within the band domain is negligible (see Appendix A for more details). That being considered, with the strain levels applied in this work, the strain-hardening associated by secondary slip may be excluded. Furthermore, since the grain neighbor orientation effect merely depends on the relative orientation of the easy (low SS) and hard (high SS) slip systems with respect to the applied loading, and as the strain-hardening will not change the slip strength ratio between the easy and hard slip systems, it is not expected that the results presented in this work qualitatively depend on the incorporation of strain-hardening.

3.4 Identifying transmitted slip system

As seen in Figure 3.5, for some grain neighbor orientations, the slip band can generate a concentration in stress in the neighboring grain. In these calculations, this stress is generally accommodated by a combination of elasticity and visco-plasticity by a number of slip systems, which can easily belong to different modes. The calculated slip activity is that which is energetically favorable for accommodating the shear contributed by the slip band and applied load. In this section, for a few neighbor orientations, we probe the state of stress in a zone ahead of a slip band and the slip system(s) it could activate.

Figure 3.8a presents the equivalent von Mises stress distribution at 1% macroscopic strain in a CP-Ti bi-crystal comprised of a neighboring grain with orientation (130°, 147°, 93°), adjacent to a parent grain with a prismatic band. A zone of stress concentration is observed to develop where the slip band is terminated by the grain boundary. The interior of the neighboring grain distant from its boundaries experiences a lower state of stress.

To identify the slip systems that could be activated with further straining, the stresses are projected onto various candidate slip systems. Figure 3.8b-d show the contours of the projected RSS onto a slip system from each slip mode: prismatic, basal, and pyramidal. The slip system shown developed the highest RSS in its mode. Each contour map is colored such that blue shades represent values below the critical resolved shear stress (CRSS) and red shades above. The neighboring grain in this particular case is favorably oriented with respect to the applied load for prismatic slip. From the prismatic RSS map in Figure 3.8b, prismatic slip is already active in this grain, as indicated by the RSS equaling the SS for most of the grain. This is also confirmed by the accumulated slip contours found in Appendix A. At the slip band/GB junction, the projected RSS exceeds the SS, signifying a favorability to continue slip in this slip system at this site. The RSS map for basal slip in Figure 3.8c suggests that basal slip could be triggered at the slip band/GB junction where the RSS exceeds the SS. Basal slip is, however, not active elsewhere in the grain, and, therefore, any basal activity would be localized and solely a consequence of the slip band. This outcome is also consistent with the accumulated slip contours (see Appendix A). Finally, as shown in the RSS map for pyramidal slip in Figure 3.8d, pyramidal slip is not active in the neighboring grain or near the slip band/GB site. For this nearest neighbor orientation, the slip band is likely not to transfer new slip onto a pyramidal slip system.

Any stress concentrations that develop in the neighboring grain where the slip band meets the boundary can potentially result in the “transmission” of slip across the GB

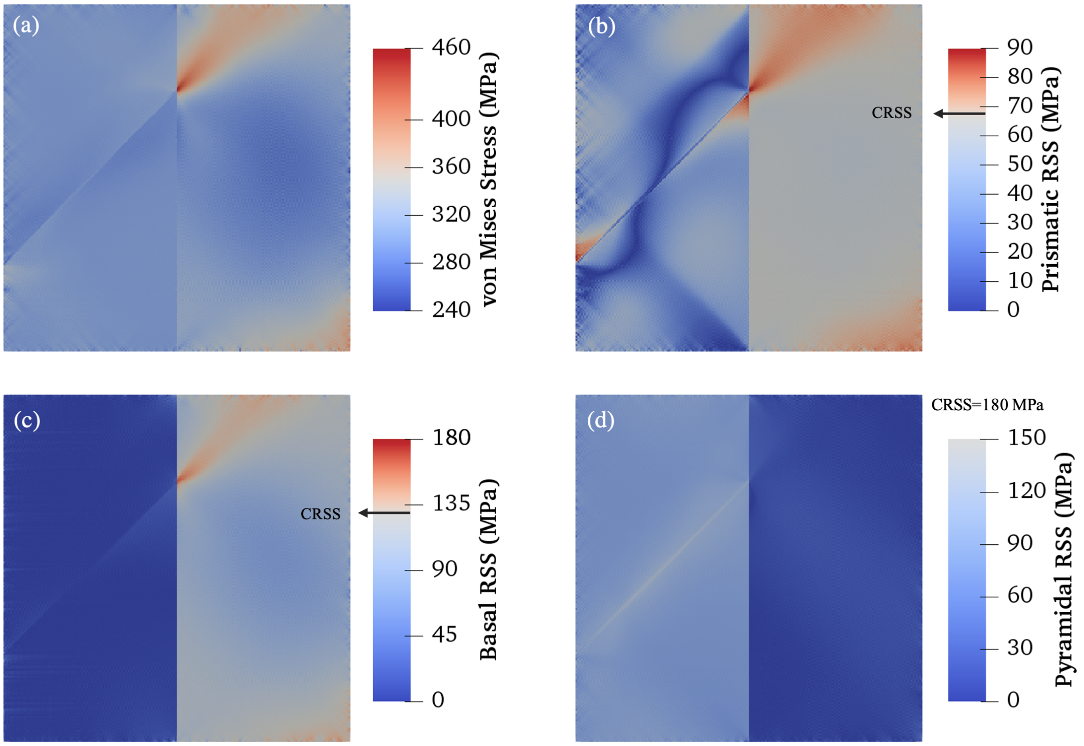

Figure 3.8: In CP-Ti, (a) distribution of the von Mises stress in the parent grain containing a prismatic slip band and in its neighbor. The crystals are under one percent uniaxial strain. Development of a forward-stress is apparent, (b) Contour of the resolved shear stress (RSS) on a prismatic slip band system, (c) Distribution of the RSS on a basal slip system. The intense forward-stress at the tip implies the propensity of the basal activity in the neighboring grain despite the fact that it is not favorably oriented with respect to the applied load for basal slip, (d) The RSS distribution on a pyramidal plane shows no intensifying effect from slip band development. Note that the homogeneous surrounding layer has been removed from all images.

via the formation of another slip band in the neighboring grain at the slip band/GB intersection. Should this occur, the new slip band would select a certain slip plane in the neighboring grain on which to form, one that is presumably energetically favorable and leads to maximum rate of energy dissipation. As mentioned in the introduction, the viability of transmission and likely transmission system have conventionally been identified based on maximum geometric alignment of the incoming and outgoing slip systems, such as m' in (2.2) [14]. It has further been proposed that the question of transmission ought to additionally consider the RSS or Schmid factor (m_s) of the outgoing slip system with respect to the applied loading state [59, 60]. For the bicrystal orientations considered in Figure 3.8, the prismatic-prismatic transmission has the highest m_s (0.36) but low m' (0.03), whereas the prismatic-basal transmission has the highest m' (0.62) but a low m_s (0.17). The forecasted activity in the slip band tip zone in Figure 3.8b-c, however, suggests that either a prismatic-prismatic or prismatic-basal transmission are likely.

In Figure 3.9, we examine, for a few more neighbor orientations, the slip system(s) that the slip band could activate in the neighboring grain based on the stress concentration developed at the band tip, and how they compare to expectations based on m' in (2.2), Schmid factor m_s, and the N parameter in (2.1). Table 3.3 summarizes the neighboring orientations, selected slip systems, and associated values of m_s, m', and N for two CP-Ti (Figure 3.9a-b) and two Mg (Figure 3.9c-d) examples. It should be noted that the selected slip systems shown in Figure 3.9 are not necessarily those with the highest RSS. Instead, they are selected in a way that best manifest the consistency or inconsistency between the predictions by our model and geometric factors. Figure 3.9a shows the pyramidal RSS map in a grain neighbor, which has a high c-axis misorientation with the parent grain, after uniaxial deformation of 1% strain. In this case the outgoing slip system studied has a high m_s, m', and N. Consistent with these geometric factors, the slip band tip zone generates a zone of high RSS that is intense and aligned with this system. Therefore, both the geometric factors and local stress fields indicate a possibility for prismatic-pyramidal slip transmission in CP-Ti. For a different neighbor orientation, Figure 3.9b presents the basal RSS map also after 1% strain, wherein m_s, m', and N are all low, for the selected basal system in neighboring grain. In contrast to these factors being low, the stress concentration ahead of the band on the selected basal plane is intense, suggesting that a prismatic to basal transmission is still likely in this case.

The basal RSS map in Figure 3.9c considers a basal slip band in Mg with a neighboring grain orientation that, according to the high m_s, m', and N, is well suited for a basal-basal slip transmission based on ideal alignment. However, the RSS maps suggest that the slip band tip zone would not support this transmission, despite the nearly perfect alignment. Finally, Figure 3.9d shows the prismatic RSS map to probe a potential basal-prismatic transmission in Mg. The stress concentrations suggest that such a transmission is supported by the local stress state, consistent with the high m_s and N and in spite of the zero m'. Taken together, these four examples demonstrate that geometric alignment (N, m'), slip-band-tip stresses, and grain orientation (m_s) do not suggest the same outcome on slip transmission. Ultimately, comparisons with experiments would identify which indicator or indicators are useful. To this end, in the next section, we compare the SB-FFT model calculations with some observations reported in the literature.

Table 3.3: Neighboring grain orientation, c-axis misorientation between the two crystals, and geometric factors associated with slip systems shown in Figure 3.9 for HCP bicrystals.

Material	Band type	Part	Neighboring grain Euler angles (ϕ_1, Φ, ϕ_2)	c-axis misorientation (degrees)	Selected slip system	Schmid factor	m'	N
CP-Ti	Prismatic	(a)	$(22, 92, 307)$	68.0	Pyramidal $(\bar{1}101)$ $[1\bar{2}13]$	0.43	0.93	0.88
		(b)	$(263, 95, 259)$	8.6	Basal (0001) $[11\bar{2}0]$	0.09	0.15	0.15
Mg	Basal	(c)	$(207, 137, 112)$	18.8	Basal (0001) $[\bar{2}110]$	0.48	0.89	0.87
		(d)	$(266, 85, 198)$	89.3	Prismatic $(10\bar{1}0)$ $[\bar{1}2\bar{1}0]$	0.49	0	0.99

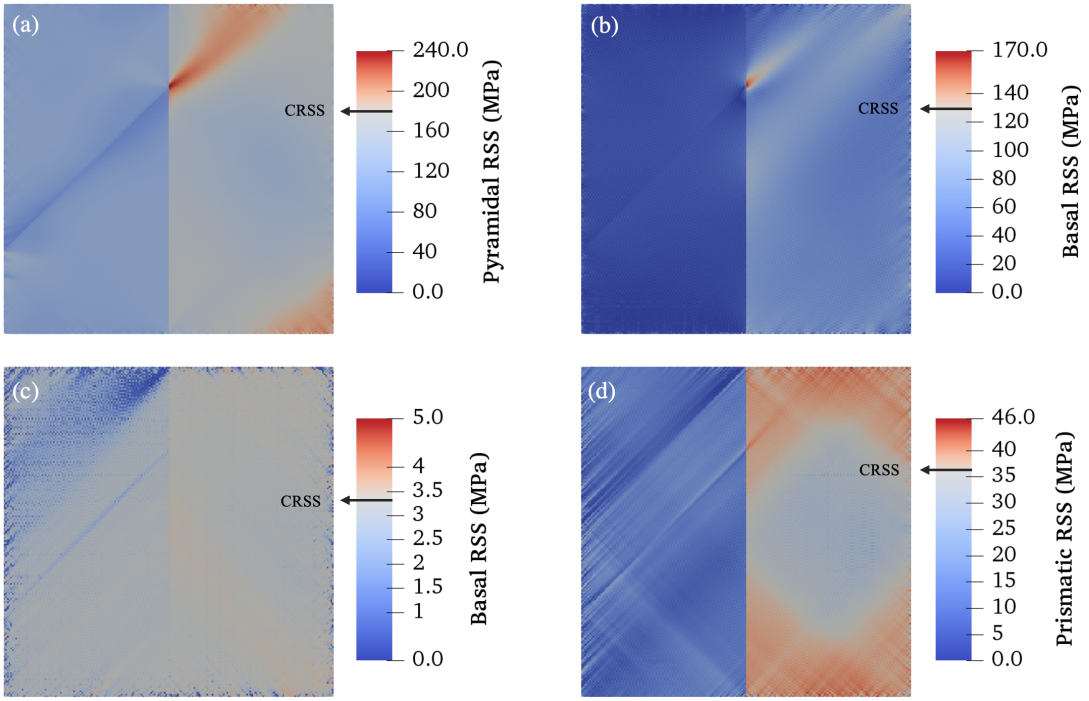

Figure 3.9: Distribution of the resolved shear stress (RSS) on certain systems for different grain neighbor orientations (a-b) CP-Ti with a prismatic slip band and (c-d) Mg with a basal slip band: (a) Stress concentration developed ahead of the slip band is consistent with the incoming prismatic slip system and outgoing pyramidal slip system being well-aligned as suggested by m', (b) An intense forward-stress on the basal slip system is developed despite of the low values of geometric factors for this prismatic slip to basal slip transmission, (c) There is no considerable forward-stress at the slip band tip zone, while the outgoing basal slip system is perfectly aligned with the slip band system, (d) A slip band tip zone developing on the basal slip system develops despite the $m' = 0$ for a basal slip to prismatic slip transmission. Note that the homogeneous surrounding layer has been removed from all images.

3.5 Interpretation of experimental observations

Slip band transmission has been studied experimentally in a variety of HCP alloys and in a variety of ways. Next, we apply the slip band stress model (SB-FFT) to these cases. In doing so, we consider other materials, apart from CP-Ti and Mg, and other microstructural configurations, mirroring the experimental ones. It should be noted that there are numerous parameters that play a role in an experimental setting, such as sample free surface, second nearest neighbors, etc., and the idealized bicrystal setup used in this work contains only a few of those parameters. For instance, the morphology of the slip bands and orientation of grain boundaries with respect to the load direction are preserved in the simulation setups. Furthermore, the homogeneous layer with uniform distribution of crystal orientations surrounded the bicrystal is implemented to represent the average bulk response from the surrounding polycrystal. In other words, the bi-crystal setup can be viewed as two neighboring grains with a significantly finer mesh embedded in a coarsely meshed polycrystal.

3.5.1 Simulation of slip-stimulated twinning in CP-Ti

Transmission across the grain boundaries of slip to twin was studied in CP-Ti deformed in bending [5]. Using electron back-scattered diffraction (EBSD), a few instances were identified in which prismatic slip bands and $\{10\bar{1}2\} < \bar{1}011 >$ twin variants were connected across a grain boundary. Figure 3.10a presents a SEM image showing the development of $(1\bar{1}02)[\bar{1}101]$ twin lamellae in a relatively small grain (Grain 52), which is contiguous to a crystal with several parallel intense prismatic slip bands (Grain 51). It appeared that the slip bands triggered the twins in the neighboring grain. The interesting questions are then why did prismatic bands not form and why did twins form instead, and with the particular V6 variant (see Table 3.4 for crystallographic information of dif-

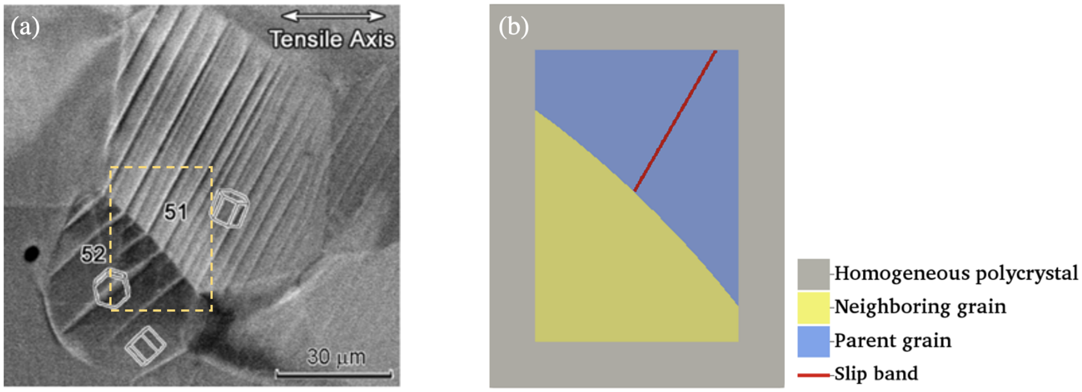

Figure 3.10: (a) SEM image of the surface tensile areas in a CP-Ti sample deformed in bending shows that prismatic slip in one grain has caused $\{10\bar{1}2\}$ twinning in the neighboring grain through a slip-twin transmission process [5], (b) The bicrystal unit cell with the preserved morphology of the grain boundary employed to validate the slip band model by simulating slip-twin transmission case shown in part (a). The image in (a) is taken with permission from [5].

ferent variants seen experimentally). Considering Schmid factors only would suggest that this neighboring grain is not well oriented for twinning since the variant with the highest Schmid factor, V6, has a low value of $m_s = 0.23$. A Schmid factor analysis would also suggest that it is not well oriented for prismatic slip since the highest value is $m_s = 0.26$. However, according to the m' factor in (2.2), it was better oriented for the observed prismatic-twin transmission (with $m' = 0.89$), than a hypothetical prismatic-prismatic transmission (maximum $m' = 0.47$).

Figure 3.10b shows our model of these same two crystals surrounded by a homogeneous polycrystalline layer. The morphology of the prismatic band, grain boundary, and crystallographic orientations with respect to the load direction are preserved in the simulation setup. As in the experiment, the model microstructure is subjected to a far-field applied strain in the horizontal direction of the image, that starts at zero and is incremented quasi-statically to a maximum level of 2%, the level corresponding to the SEM image.

Figure 3.11a shows the evolution with applied strain of the resolved shear stress (RSS) on a prismatic slip system and $(1\bar{1}02)[\bar{1}101]$ twin system in the neighboring grain averaged over two regions: a finite-sized (6×6×3 voxel) region near the tip of the slip band, and the entire neighboring grain volume. The prismatic slip system shown is identified as the one with the highest calculated average RSS of all three prismatic slip systems in the tip region and likewise, the selected twin system, as the one with the highest calculated RSS among the six possible. The evolution of the RSS on the most favored prismatic slip system finds that the RSS increases with strain, but eventually the RSS is slightly higher on average in the grain than at the tip of the slip band. This implies that prismatic slip is favored less at the slip band tip region than elsewhere in the neighboring grain. In contrast, the results in Figure 3.11a show that, unlike the average RSS in the grain, the twin RSS intensifies with strain at the tip of the slip band.

Figure 3.11b shows the calculated distribution of the twin plane RSS for the variant $(1\bar{1}02)[\bar{1}101]$, the one seen experimentally and denoted as 'V6'. Consistent with the observation, we see that an intense stress concentration region develops ahead of the slip band for this twin variant. All the other variants had a lower calculated RSS, and thus, the calculation would suggest that this variant would be the most favored among the six. To summarize, the calculations explain why a prismatic slip band did not form and the twin variant that is actually seen experimentally did. They further suggest that it would not have been selected without the slip band, as indicated by the calculations.

3.5.2 Simulation of slip-slip and slip-twinning transmissions in Mg-Y alloys

Recently, Zhou et al. [10] used in situ SEM/EBSD on the Mg-5 wt% Y alloy to observe slip-slip and slip-twin transmission across a number of grain boundaries. Figure 3.12a and c show a few micrographs from their work. For Figure 3.12a at 5% uniaxial

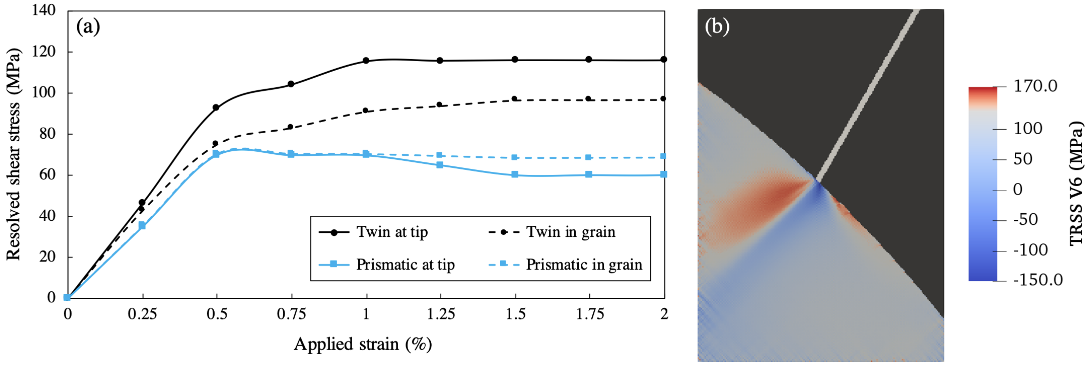

Figure 3.11: (a) Evolution of the resolved shear stress on the prismatic and $\{10\bar{1}2\}$ twin planes as the macroscopic strain increases. The curves are shown for both the average RSS in the slip band tip zone only and in the entire neighboring grain, (b) Distribution of the twin plane resolved shear stress (TRSS) for the $(1\bar{1}02)[\bar{1}101]$ tensile twin variant (V6) at 2% macroscopic strain. The surrounding homogeneous layer has been removed from the image.

strain, they reported that basal slip band from G1 initiated a $(01\bar{1}2)[0\bar{1}11]$ tensile twin in neighboring grain G2. In Figure 3.12c, at 2.5% strain, they found that the basal slip band in G3 resulted in another basal slip band and a $(1\bar{1}02)[\bar{1}101]$ twin in G4. These two twin variants could be considered non-Schmid twins, since their Schmid factors were exceedingly low, just 0.005 (G2) and 0.23 (G4). The m' transmission factor was also low for some of these systems (see Table 3.4). Evidently, in these cases, the basal slip band led to twin formation, but the reason behind the variant selection is not clear. To determine if slip band tip stresses could provide an explanation, models of bicrystals embedded in a homogeneous medium are constructed, with the same crystal orientations and grain boundary orientation as the experiment, as shown in Figure 3.12b for the G1/G2 pair and Figure 3.12d for the G3/G4 pair. In each model, the parent grain contains a region for which a basal slip band belonging to the slip system identified in the experiment can evolve with strain. In simulations, the strains are applied in tension in the same orientation with respect the microstructure up to a strain level of 5%. Properties of the Mg-Y alloy used in the calculations are presented in Table 3.1. To identify the likely

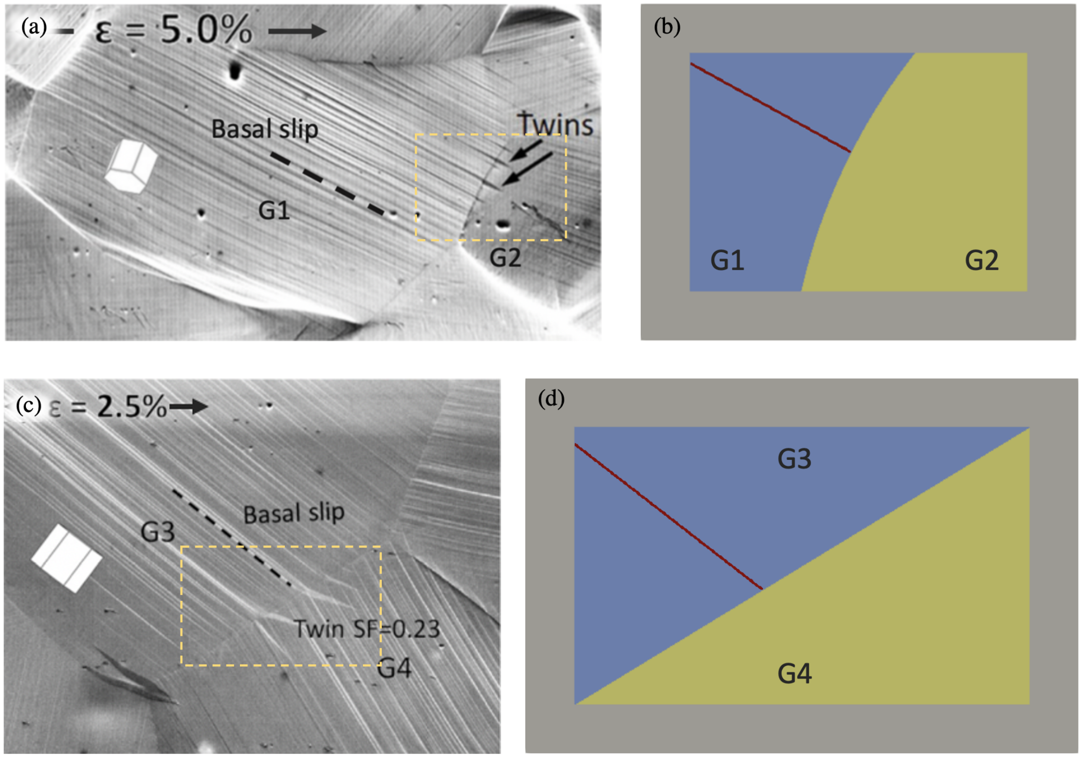

Figure 3.12: SEM image of two pairs of grains at the surface of an Mg-Y sample subjected to uniaxial strain of (a) 5%, and (c) 2.5%. In each case, the basal slip in one grain is linked to $\{10\bar{1}2\}$ twins and/or another basal slip band in the neighboring grain [10], (b, d) Bicrystal setups with preserved morphology of the grain boundary used to model two slip transmission cases shown in parts (a) and (c). The images in (a) and (c) are taken with permission from [10].

twin or slip system to be activated in the neighboring grains, we analyze in Table 3.4 the calculated RSS/SS ahead of the slip band for all six $\{10\bar{1}2\}$ twinning variants, as well as the basal, prismatic, and pyramidal $< c + a >$ system with the highest RSS. Although twinning is not considered as a dissipative mechanism in our crystal plasticity calculations, as a reference, some previously characterized estimates for a critical resolved shear stress for tensile twinning on $\{10\bar{1}2\}$ planes are included in Table 3.1.

The calculated ratios acquired at 5% strain for the G1/G2 bicrystal predict that among the six twin variants, the $(01\bar{1}2)[0\bar{1}11]$ twin variant (V2) has the highest resolved shear stress and, therefore, will be activated first. This is the same variant as seen experimentally. The RSS/SS ratio for all of the slip systems are lower than 1.0, indicating that the stress state generated by the slip band would not especially result in slip in the neighboring grain. Figure 3.13a shows the evolution of the RSS/SS ratios for the basal, prismatic, and pyramidal system with the highest RSS at the slip band tip as well as the twin RSS for the twin variant V2 in grain G2, as the macroscopic strain increases. Over the straining period, not only are the RSS/SS ratios for all slip systems lower than 1.0, but they are less at the band tip than in the neighboring grain on average. The calculations imply that the slip band stress state selected this variant.

Likewise, in the bicrystal modeled for G3/G4 pair, as presented in Table 3.4, calculations show that among all twin variants, the $(1\bar{1}02)[\bar{1}101]$ variant (V6) has the highest propensity for activation. The RSS/SS ratio for the basal slip is higher than 1.0, suggesting also the likelihood of activating basal slip in grain G4 at the grain boundary. Calculations of the evolution of the RSS/SS in Figure 3.13b indicate that although the overall stress in the grain is sufficient to activate both the V6 twin variant and basal slip, the band intensifies the RSS values for these two deformation modes at the boundary. These variants are the same as those seen experimentally.

Table 3.4: Schmid factor, m', and ratios of RSS/SS averaged at the band tip and over the entire grain associated with $\{10\bar{1}2\}$ twin variants as well as basal, prismatic, and pyramidal slip systems in grains G2 and G4 shown in Figure 3.12.

		Tensile twinning						Slip modes		
		V1	V2	V3	V4	V5	V6	Basal	Prismatic	Pyramidal
	Slip/twin plane normal	$(10\bar{1}2)$	$(01\bar{1}2)$	$(\bar{1}102)$	$(\bar{1}012)$	$(0\bar{1}12)$	$(1\bar{1}02)$	(0001)	$(10\bar{1}0)$	$\{10\bar{1}1\}$[a]
	Slip/twin direction	$[\bar{1}011]$	$[0\bar{1}11]$	$[1\bar{1}01]$	$[10\bar{1}1]$	$[01\bar{1}1]$	$[\bar{1}101]$	$[\bar{2}110]$	$[\bar{1}2\bar{1}0]$	$< \bar{2}113 >$
G1 → G2	Schmid factor	−0.21	0.005[b]	−0.41	−0.24	−0.01	−0.38	0.22	0.47	0.49
	m'	0.62	0.20[b]	−0.35	−0.17	0.002	0.24	0.74	0.14	0.07
	RSS/SS at tip	0.6	2.2[b]	1.0	0.6	2.2	1.3	0.93	0.92	0.90
	RSS/SS in grain	−4.1	−0.1[b]	−5.7	−4.3	−0.1	−5.5	0.96	0.98	0.92
G3 → G4	Schmid factor	0.24	0.33	0.17	0.19	0.33	0.23[b]	0.47	0.15	0.44
	m'	0.62	0.07	−0.16	−0.16	0.29	0.83[b]	0.85	0.10	0.001
	RSS/SS at tip	4.41	3.26	4.75	4.39	3.29	4.94[b]	1.24	0.27	0.55
	RSS/SS in grain	2.25	3.64	2.42	2.08	3.74	2.67[b]	1.07	0.21	0.52

[a] Presented data corresponds to $(1\bar{1}01)[\bar{2}113]$ and $(\bar{1}101)[1\bar{2}13]$ first order pyramidal $< c + a >$ slip in G2 and G4, respectively.

[b] Operating twin variant.

3.5.3 Simulation of serial slip transmissions in microtextured Ti-6Al-4V titanium

Utilizing an *in situ* high resolution scanning electron microscope digital image correlation (SEM DIC) technique, Echlin et al. [4] studied the long-range plastic strain localization in a microtextured Ti-6Al-4V sample. A microtextured region within the sample refers to a broad mm-scale band of grains that are closely oriented, typically with misorientations from 5° to 30°. They reported that not only could slip bands develop at strains lower than macroscopic yielding in the microtextured region, but they also successively transmitted from one slip mode in one grain to the same mode to its neighboring

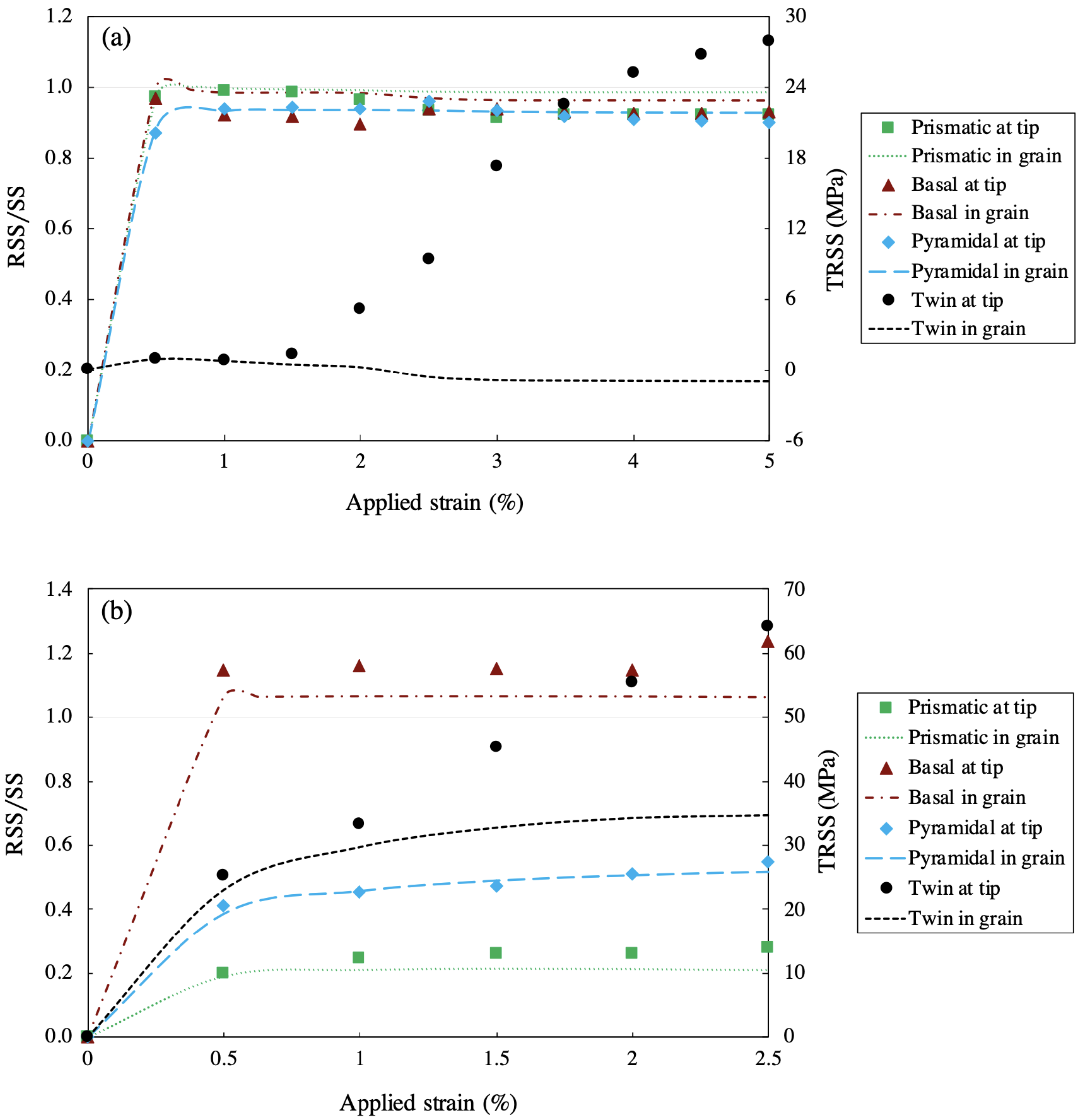

Figure 3.13: Evolution of the ratio of the resolved shear stress (RSS) to slip strength (SS) for different slip modes and the twin plane resolved shear stress (TRSS) for the most favored $\{10\bar{1}2\}$ twin variant as the applied strain increases, for (a) G1→ G2 and (b) G3 → G4 transmission cases shown in Figure 3.12. The datapoints represent the average RSS in the band tip domain while dashed curves show that in the entire neighboring grains G2 and G4.

grain. Long chains of prismatic-to-prismatic, as well as basal-to-basal slip transmissions developed across the deformed sample. Such a chain of slip bands transmitting from one grain to another within regions where neighboring grains were closely oriented, was also observed in another Ti alloy in [61].

The bicrystal configuration shown in Figure 3.1 is used to model the slip band development and the resulting stress concentration in Ti-6Al-4V tensile samples, for which the material properties are presented in Table 3.1. To represent a typical pair of grains in the microtextured region, the orientation of the parent grain is assigned, so that either prismatic or basal slip is favorable and that of the neighboring grain makes an angle of 30° or less with the c-axis of the parent. We find that for a softening coefficient D_0 of 64, the strain levels in the slip band and the parent grain for a range of neighboring orientations are, on average, comparable to the experimentally measured values. Figure 3.14 shows one such case where the DIC measurement of the normal strain along the loading direction at 0.77% macroscopic strain are compared with the same component calculated in the parent matrix and slip band at the same macroscopic strain (the surrounding simulated material is removed from the image). The neighboring orientation in this case is (262°, 104°, 86°).

Figure 3.15a shows the measured normal strain along the loading direction at 0.86% macroscopic strain level [4]. The microstructure shown contains both strongly textured microtextured regions separated by regions of low texture. The slip bands seen in grains across the microstructure exhibit a range of intensities. As validation, slip band calculations are repeated for three different nearest neighbor grain orientations, that span the likely c-axis misorientations, 12°, 72°, and 89°, seen in Figure 3.15a. Figure 3.15b-d presents the calculated strain fields in the slip band at the same 0.86% macroscopic strain. By only changing the grain neighbor orientation, a similar range of band strains as seen experimentally is achieved.

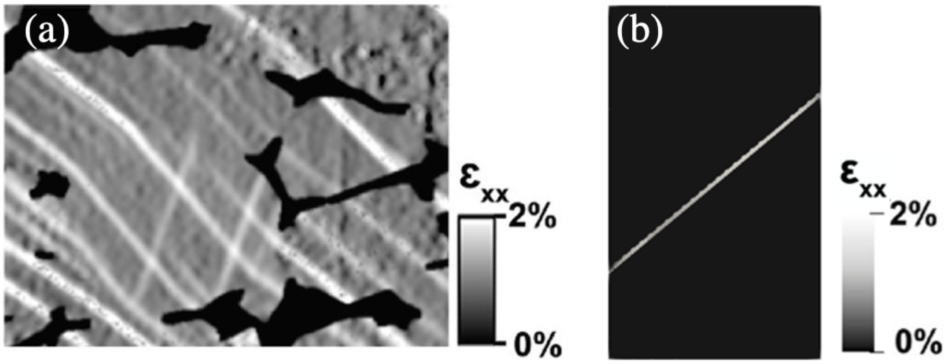

Figure 3.14: DIC measurement [4] (a), and calculated (b) distribution of the normal strain along the loading direction in the prismatic slip band and the parent matrix, at 0.77% macroscopic strain. The surrounding homogeneous layer and the neighboring crystal have been removed from the image in (b). The image in (a) is taken with permission from [4].

To identify the role that the localized slip band tip stresses in the neighboring grain could play in transmission, calculations were carried out for a number of grain orientations spanning distinct c-axis misorientations from 0° to 30°. Figure 3.15e maps the accumulated slip on the dominant system (i.e., the most stressed system) in the slip band tip zone versus the c-axis misorientation. In most cases, we find that only one or at most two slip systems are activated ahead of the band. The map shows that for any c-axis misorientation of less than 30°, a prismatic slip band is anticipated to transmit onto a prismatic slip system in the neighboring grain. Likewise, for the parent grains with a basal band, a high propensity of a basal-basal transmission is expected. However, when the misorientation approaches 30º, either several slip systems with nearly equal accumulated slip are activated, or in rare cases, a basal to non-basal slip transmission is indicated. The interpretation here is that either a basal or prismatic slip band could have triggered a same-slip transmission across grain boundaries with $< 30°$ c-axis misorientations.

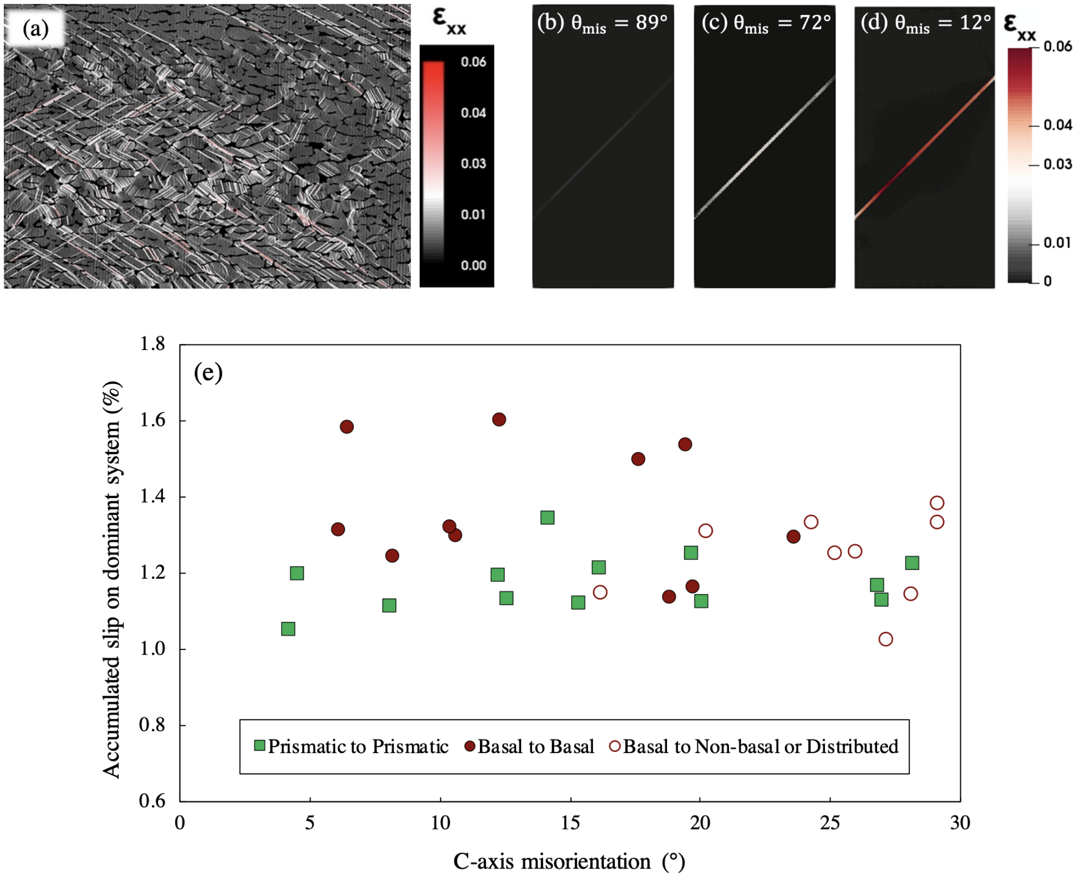

Figure 3.15: (a) SEM DIC measurement of the normal strain along the loading direction for a Ti-6Al-V4 tensile sample at 0.86% macroscopic strain [4], (b-d) Simulated distributions of the normal strain along the loading direction in the parent grain at 0.86% macroscopic strain from three representative parent/grain neighbor pairs show a same range of strain localization within the band compared to experimental data, (e) Accumulated slip on the dominant system in the slip band tip zone against the c-axis misorientation of two adjacent crystals. Both prismatic and basal slip bands are predicted to transmit onto a slip system of the same mode in the neighboring grain for low misorientations. In (b)-(d), the surrounding homogeneous layer and the neighboring crystal have been removed from the image. The image in (a) is taken with permission from [4].

3.6 Assessing the propensity of slip transmission from a slip band

To date, criteria for slip transmission and the transmission pathways have been based solely on the relative orientations of the incoming and outgoing slip systems in question and Schmid factors based on the applied state of stress but not on properties of the material or local stress generated by the slip band. As we have shown here, in some cases, depending on the neighboring orientation, slip or twin activity that is distinct from that in the rest of the grain can occur. As a final study, we employ the model to identify situations in which slip transmission from a slip band into a neighboring grain is likely and the slip system(s) to which the transmission event occurs. Using the calculations, we link these conditions with the slip activity generated ahead of slip band in the neighboring grain.

The slip activity triggered in the neighboring grain at the tip of a slip band can either labeled as *concentrated* or *distributed*. Concentrated slip corresponds to only one or at most two activated systems. Any slip system with the projected RSS/SS ratio greater than one is considered as an *activated system* by slip band. The RSS/SS of the second activated system could be equal or close to the highest one, within 90% of the ratio for the first system. Concentrated slip is considered here as a signature of slip transmission and the activated slip system(s) the selected ones for transmission. Distributed slip, on the other hand, occurs when there are three or more activated systems and is usually associated with plasticity dispersed more or less equally on many slip planes.

Considering again a pair of CP-Ti crystals within a polycrystal, we investigate the effect of neighboring grain orientation on the likelihood of slip transmission from a prismatic slip band into a neighboring grain and the slip system(s) to which the transmission event occurs. A broad range of orientations, including 50 distinct neighbor orientations are considered in the calculations. Figure 3.16 presents the c-axis misorientations that lead to one of three cases, concentrated slip on a slip system belonging to the same slip family as the slip band, concentrated slip on a system belong to a different family, or distributed slip. Similar to other geometric factors, such as m' and Schmid factor, no strong correlation between the c-axis misorientation and the propensity of slip transmission is detected. However, the type of slip system onto which incoming slip band is anticipated to transmit correlates with the misorientation angle. In particular, it is apparent from Figure 3.16a that for a prismatic incoming band in CP-Ti, slip in parent grain transmits to a prismatic system in the neighbor grain when the misorientation is small. For high misorientations on the other end, transmission to a different family of slip systems, such as basal or pyramidal, is expected. Lastly, for the moderate misorientation angles, likely systems for transmission are combined of a prismatic and a basal plane.

Basal slip bands may also develop in certain grains of CP-Ti and, in Figure 3.16b, we present the slip transmission map from a similar set of calculations for a basal slip band. Since the slip resistance on prismatic planes in CP-Ti is the lowest among all deformation modes, basal to prismatic transmissions are evident in a broad range of misorientations. Moreover, due to the fact that pyramidal $< c + a >$ slip has the highest strength, among all bars representing 'basal or pyramidal' in Figure 3.16a and 'prismatic or pyramidal' in Figure 3.16b, only a few correspond to the pyramidal slip.

Figure 3.17a and b maps the concentrated vs distributed slip activity against the c-axis misorientation between two adjacent grains for basal and prismatic slip bands in Mg, respectively. The same trends as what explained for CP-Ti are realized for Mg, except for a few distinctions. Firstly, since pure Mg has a high plastic anisotropy, i.e., the difference between the strength of different slip modes is significantly large, pyramidal slip – the hardest slip mode – is not activated in any misorientation angle. Moreover, numerous instances of the easy basal slip are identified as basal to basal transmissions

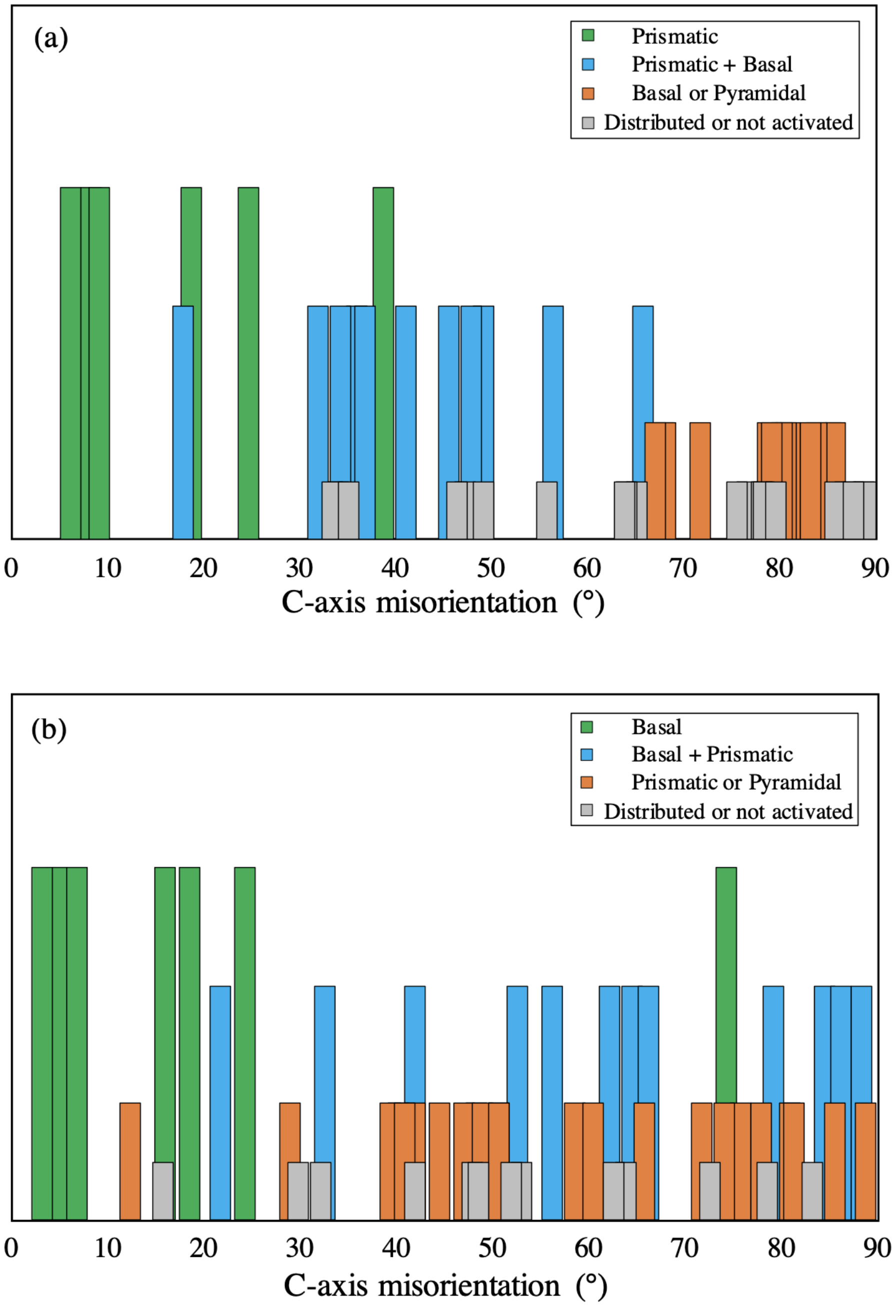

Figure 3.16: Slip activity generated ahead of the slip band in the neighboring grain against the c-axis misorientation between two adjacent crystals for (a) prismatic, and (b) basal band type in CP-Ti. Presented data suggests that when the misorientation is small, transmission to a like system is expected, while for high misorientations slip in the parent grain is predicted to transmit onto an unlike system in the grain neighbor. Note that most of the orange bars represent either a basal or a prismatic slip and only a few correspond to the pyramidal slip.

shown ubiquitously in any misorientation angle in Figure 3.17a and as prismatic to basal transmissions shown in moderate-high misorientations in Figure 3.17b.

Considering the maps for different band types and materials presented in Figure 3.16 and Figure 3.17, exclusive transmission to the same slip family as the incoming band at small misorientation angles is prevalent. This implication was also presented earlier for Ti-6Al-4V titanium alloy in previous section, where the model was validated against an experimental study reported in [4]. In addition to that, occurrences of prismatic to prismatic slip transmission at low misorientation angles are recognized in another study that investigated the slip transfer mechanisms across low-angle grain boundaries in a deformed titanium sample [109].

We have shown that the slip band tip stress-based criterion proposed in this work can be utilized for identifying the nearest neighbor orientations in which slip band transmission is possible and the likely slip system for which it occurs. Additionally, there are other areas where the slip band model and the stress-based criterion can be useful. For instance, in a post-mortem analysis of a slip transmission across the grain boundary, it might not be easy to recognize the grain in which slip bands have formed first and then initiated the slip (or twin) in the neighboring grain. By studying the local stress fields and possible stress concentrations at the band tip, the sequence of events can be identified. The local stress fields at the band tip predicted by SB-FFT model can also be measured experimentally. Using the high-resolution electron backscatter diffraction (HR-EBSD) technique, the resolved shear stresses on specific slip systems ahead of the slip bands in CP-Ti were measured [95, 104]. In a different series of studies [13, 110, 111], using high resolution *ex-situ* digital image correlation (DIC) and EBSD techniques, researchers measured plastic strain accumulation with sub-grain level spatial resolution in a nickel-based polycrystal. In particular, with the combination of crystallographic orientation data and plastic strain measurements, the resolved shear strains on individual slip

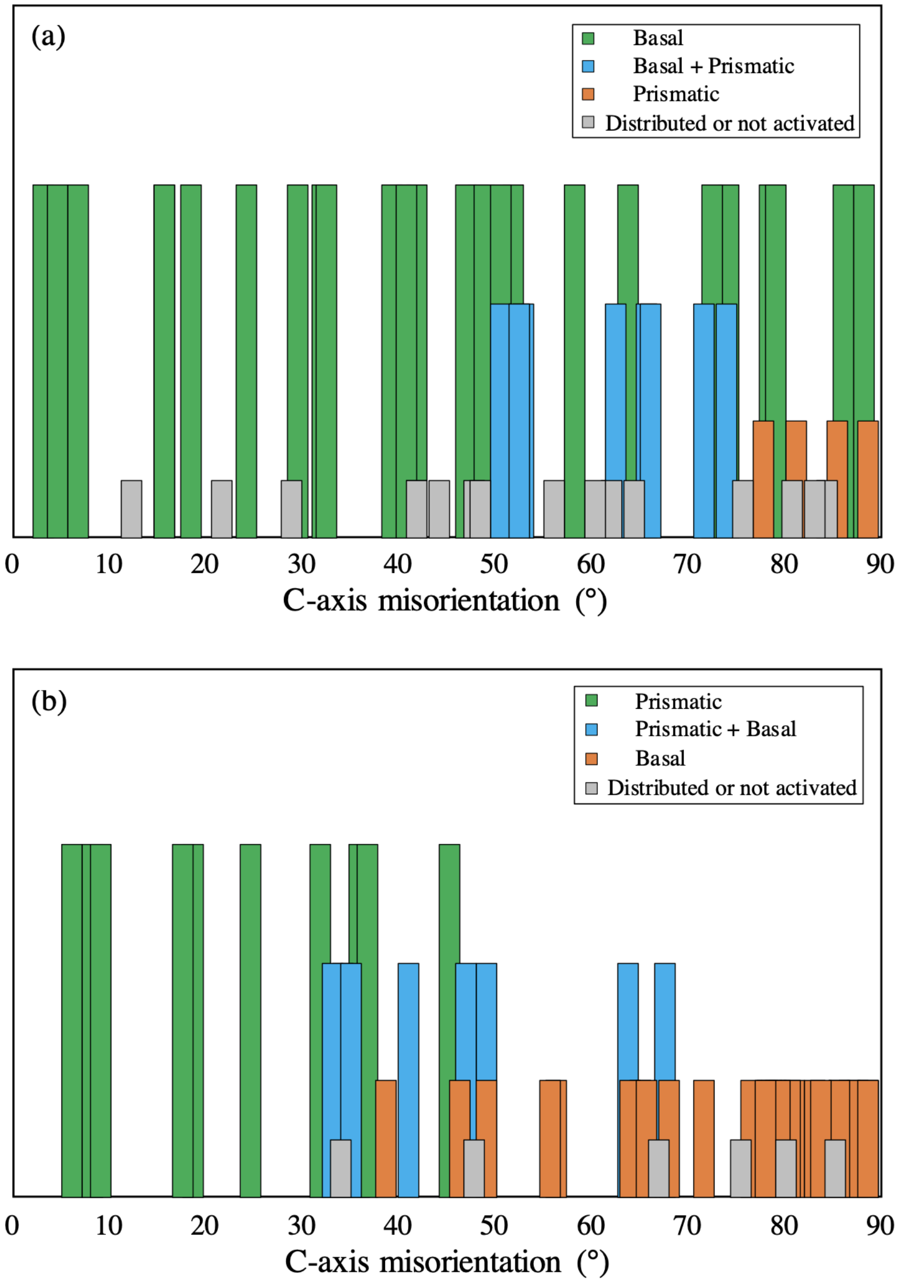

Figure 3.17: Slip activity generated ahead of the slip band in the neighboring grain against the c-axis misorientation between two adjacent crystals for (a) basal, and (b) prismatic band type in Mg. Presented data suggests that when the misorientation is small, transmission to a like system is expected, while for high misorientations slip in the parent grain is predicted to transmit onto an unlike system in the grain neighbor.

systems were spatially calculated across a substantial region of interest. Plastic strain localization on individual slip systems on either side of the grain boundary was measured and it was identified how these fields can be associated to the observed slip transfer [110]. It is noted that our criterion is based on the local stress fields at the band tip, and not the strain fields. However, the condition of RSS/SS>1.0 considered in the criterion to identify 'activated' systems at the band tip confirms the plastic strain accumulation for those systems. Moreover, the concept of labeling slip activities at the band tip as 'concentrated' or 'distributed' can still be utilized if the shear strain on individual slip systems were available, instead of the resolved shear stresses.

3.7 Conclusion

In summary, we present a model built from the crystal plasticity FFT-based elasto-viscoplastic model to simulate the development of a crystallographic slip band spanning an HCP crystal. The technique, called SB-FFT, is employed to simulate the process of localization in a slip band. We consider intragranular slip bands that accumulate strain on either prismatic or basal slip planes and intersect the grain boundaries. The calculations include a full range of neighboring grain lattice orientations and a number of different HCP materials. In every case, the local stress fields that develop around and ahead of the slip band in the neighboring grain are analyzed. The main conclusions of this study are as follows:

- In HCP crystals, the lattice orientation of the nearest neighbor strongly affects the amount of plastic strain that localizes in the slip band.
- We show that neighbor orientations that respond to the slip band by activating plastically hard deformation modes facilitate slip band strain localization.

- Regardless of nearest neighbor orientation and crystallographic of the slip band, the levels of accumulated plastic strain in slip bands of the stronger CP-Ti are substantially greater than those in slip bands in Mg.

- A slip band tip stress-based criterion is proposed for identifying the nearest neighbor orientations in which slip band transmission is possible and the likely slip system for which it occurs.

- Analysis of previously reported observations of slip to twin transmission suggest a local slip band tip stress-concentration criterion is a better indicator of a cross-GB transmission and the transmitted slip or twin system than conventionally used geometry-based factors.

- We show that for low GB misorientations, the slip band is likely to transmit into another slip band of the same type in the neighbor grain, while for high GB misorientations, it is likely to transmit into one of a different type or to not transmit at all.

Chapter 4

Grain boundary slip-twin transmission in titanium

4.1 Introduction

Commercially pure titanium (CP-Ti) and its alloys have been widely used in industry due to their superior mechanical properties, such as high specific strength, excellent corrosion resistance, and biocompatibility [112, 113, 114, 115, 116]. However, their plastic behavior can be highly anisotropic and strongly dependent on temperature and strain rate [117, 118, 119, 120]. The complexity is due in part to the activation of two distinct deformation mechanisms–slip and twinning. Both heterogeneously shear the grain on crystallographic planes [121, 122, 123, 124, 125], and can grow in intensity in the form of bands that extend partly or fully across the grain [119, 5, 126, 127, 128]. Localized slip bands (SBs) and twin bands play a significant role in the deformation of Ti since they accommodate a large share of the parent grain's deformation while only occupying a small fraction of the grain's volume. These localized bands generate intense stress fields in the regions where the band terminates, whether inside the grain or at the grain boundary

(GB). The latter is the more frequently observed case and, importantly, the situation that permits them to affect deformation mechanisms in the neighboring grains. They can, for instance, act as a potential site for strain localization and void nucleation [54, 55]. They have also been seen to "transmit" and propagate across the GBs, potentially leading to long twin or SB chains that percolate across the grain structure [4, 129, 130, 131]. To what extent localized SBs or twins can alter deformation mechanisms in neighboring grains and the variables determining the propensity of such transmissions have long been key questions of interest.

Over the last few decades, several experimental studies have employed imaging techniques to study twin and SB transmissions across GBs in polycrystalline Ti alloys, as well as other structural hexagonal close-packed (HCP) metals [5, 126, 95, 6, 132, 133, 52, 134, 135]. In the post-mortem surface techniques, microscopic signatures of the slip or twin transmission are "co-located" pairs, a term that refers to a pair of slip and/or twin bands, each embedded in a different grain, intersecting the shared GB at nearly the same location. Slip-band pairs, twin pairs, or mixed slip/twin pairs have all been reported to occur frequently, suggesting that they are a non-negligible contributor to plastic deformation [119, 5, 132, 133, 52, 136]. Significantly, another study demonstrated that such co-located pairs were not a surface effect and occurred subsurface as well [126].

To understand the conditions for transmissions, a geometric factor, $\mathrm{m}' = (\mathbf{n}_\mathrm{i}.\mathbf{n}_\mathrm{o})(\mathbf{b}_\mathrm{i}.\mathbf{b}_\mathrm{o})$ is often used. The m' gauges the alignment of the planes, with normal vectors of $\mathbf{n}$, and the shear directions, denoted by $\mathbf{b}$, of the incoming (i) and outgoing (o) slip or twin systems in question [14]. It helps to identify the most likely SB system or twin variant that would form in the neighboring grain, should a transmission event occur. It tends to suggest that transmissions are more favored the lower GB misorientation, a tendency that indeed is generally observed [137, 62].

While easy to use, several studies have demonstrated that additional variables, not accounted for in m', must also govern slip and twin transmissions [133, 52, 134, 10, 138, 139, 140, 141]. Using post-mortem electron back-scattered diffraction (EBSD), Wang et al. reported a correlation in location across the GB between prismatic SBs in geometrically soft grains and $\{10\bar{1}2\} < \bar{1}011 >$ tensile twins in geometrically hard neighboring grains [5]. They found that m' of the observed co-located slip-twin pairs do not always correspond to the highest m' value possible between the pair of grains. High-resolution EBSD and differential aperture X-ray Laue micro-diffraction analyses of localized SBs in CP-Ti further showed that a high value of m' is not necessarily associated with SB transmission across the GB [95, 6]. A study on HCP Mg-Y alloy also found that m' cannot explain some of the observed slip-to-twin transmissions across GBs [10]. A machine learning model, using only grain orientations, failed to predict twins resulting from twin-twin transmissions at both low-angle and high-angle GBs [141]. Finally, a recent study in CP-Ti revealed that the morphology of the GB influences slip transmission across the GB [134]. They used electron channeling contrast imaging (ECCI) coupled with controlled surface removal to investigate the interaction of SBs with the GB as a function of depth. The slip system onto which incoming SBs transmit across the same GB was found to vary at different depths due to the fact that the orientation of the GB with respect to the incoming SBs varies between the surface and subsurface levels.

In addition to microstructural variables, it has been suggested that local stress fields produced by the bands themselves promote transmission and can determine the twin variant or SB system that will subsequently form on the other side of the GB [126]. Slip or twin bands can generate intense stress fields in the neighboring grains at the band/grain boundary junction. The intensity and character of these fields can differ from the grain average stresses in the neighboring grain and potentially promote slip or twinning activity that would not otherwise occur. One way of resolving such stress fields within a group of HCP grains is to utilize spatially resolved micromechanical techniques that can model localized intragranular bands and their interactions with GBs. In recent years, a few theoretical approaches [96, 63], as well as several numerical methods, ranging from finite element (FE) method [28, 29, 30, 31, 32, 33, 34, 142, 143] to phase-field models [144, 145, 146, 147] to fast Fourier transform (FFT) calculations [77, 51, 36, 37, 69, 148, 78], have been developed to model discrete SBs or twin lamellae within a grain and the stress fields ahead of them. Most of them were based on crystal plasticity, which enables deformation via anisotropic elasticity and multiple slip modes of the HCP crystal. In previous chapter, we implemented SB-FFT formulation to study the shear localization for a range of HCP metals, including CP-Ti, and concluded that neighboring grain orientations influence SB intensification. Also, the type of band (prismatic or basal) in one grain was found to substantially alter the active deformation modes in the neighboring grain within the vicinity of the GB. A few more studies performed explicit twinning simulations using crystal plasticity-based models to calculate stress fields ahead of twin/GB junctions relevant for understanding twin-twin transmissions [77, 70, 149]. Most of these studies only address the formation of a slip or twin band, and in cases where the localized stress fields ahead of the band is studied, only the transmission between two SBs or between two twin bands were considered, leaving the transmission between a SB and a twin uninvestigated.

This chapter examines the grain neighborhood-induced twin or slip localization in CP-Ti. Combining scanning electron microscopy (SEM) analysis and crystal plasticity FFT modeling, we aim to elucidate the key factors that govern the transmission of slip and twin bands across the GBs. The model employed here features both discrete intragranular SBs and twin lamellae in the same microstructure. Different deformation modes are characterized in CP-Ti samples subjected to four-point bending. Prevalent at several GBs are co-located pairs of prismatic SBs and $\{10\bar{1}2\} < \bar{1}011 >$ tensile twins connected across a GB. Many of these pairs are analyzed via SEM and represented directly in simulations, with retention of the actual GB morphology and the orientation of the twin/slip band with respect to the GB and loading direction. In many cases, the geometric m' fails to rationalize them. We demonstrate how calculation of the local stress fields helps to explain the occurrence of slip vs. twin transmission or the lack of transmission, and the selection of outgoing slip system or twin variant. It also helps to identify the transmission pathway (i.e., slip $\rightarrow$ twin or twin $\rightarrow$ slip) for the experimentally observed co-located pairs. The results indicate that the deformation mechanisms in one grain can be strongly affected by those of its neighboring grains, and the transmitted mechanism does not necessarily match the slip/twin system active in those grains.

4.2 Mechanical testing and characterization[1]

To characterize the transmission of slip/twin bands across the GBs, a rolled and recrystallized grade 1 commercially pure titanium (CP-Ti) is selected and subjected to four-point bending. The initial and deformed microstructures were characterized using a JEOL 6500 SEM equipped with an orientation imaging microscopy (OIM) system (EDAX/ TSL, Draper, UT). The mechanical test and a few initial microstructural characterizations have been previously carried out and are described in [5, 119]. Some of the microscopy data from that experiment are newly presented here. So that the chapter is self-contained, a brief description of the testing and characterization methods is given here.

Table 4.1 provides the chemical composition of the selected material system. To prepare the material for the four-point bend test, a 25 mm-long specimen with a rectangular cross-section of 3 mm × 2.5 mm was cut such that the bulk of the grains have their c-axes oriented approximately 45° from the tensile axis of the bending sample. The specimen

---

[1] The experimental part of this study was conducted by Leyun Wang.

surface (25 mm × 3 mm) was mechanically polished before deformation. For high quality, visibly scratch-free surface, a final polishing was performed with a colloidal silica suspension. EBSD analysis in an area of 5 mm×3 mm in the center of the surface of the specimen prior to deformation was performed. The initial material had a typical basal texture with an intensity of 6 multiples of random distribution with a grain size of 80 μm. The specimen was then subjected to a four-point bending test so that the central region of its surface experienced uniform tensile stress along the sample longitudinal direction [150]. A surface tensile strain of approximately 2% was applied to ensure enough of the grains in the sample were plastically deformed. Post-mortem EBSD investigations were conducted in the same 5 mm × 3 mm region located in the center of the surface, using the same imaging parameters. Intense SBs and twins on the surface were characterized via trace analysis and using the EBSD maps.

Table 4.1: Composition of grade 1 CP-Ti. All measurements are in wt. %.

Element	O	Fe	Al	Cu	C	Ni	Cr	S	N	Ti
wt. %	0.169	0.049	0.017	0.017	0.015	0.013	0.011	0.011	0.004	bal.

4.3 Modeling discrete twin/slip bands

An infinitesimal-strain crystal plasticity (CP) model based on fast Fourier transform (FFT) is employed in the present study. This full-field computational scheme, originally developed by Lebensohn et al. [67], has been advanced to capture intergranular heterogeneity in the form of intense SBs [51, 36, 37] and deformation twinning [77, 69, 151] in separate studies. Here we combine these two techniques to simulate heterogeneous elasto-viscoplastic deformation in CP-Ti crystals in which both intense SBs and deformation twins exist. Since the implementation of twinning requires some alterations in the constitutive laws previously described in Chapter 2, we briefly review the FFT framework used for modeling discrete twins in the following.

As previously mentioned, in the CP-FFT approach, a compatible strain field is adjusted to an equilibrated stress field by minimizing the average local work at each discretization point in several iterations [67]. The stress-strain relationship of an elasto-viscoplastic material with shear transformation is given by,

$$\boldsymbol{\sigma}(\mathbf{x}) = \mathbf{C}(\mathbf{x}) : \boldsymbol{\varepsilon}^{\mathrm{e}}(\mathbf{x}) = \mathbf{C}(\mathbf{x}) : \big(\boldsymbol{\varepsilon}(\mathbf{x}) - \boldsymbol{\varepsilon}^{\mathrm{p}}(\mathbf{x}) - \boldsymbol{\varepsilon}^{\mathrm{tr}}(\mathbf{x})\big) \tag{4.1}$$

where $\boldsymbol{\sigma}(\mathbf{x})$ is the Cauchy stress tensor, $\mathbf{C}(\mathbf{x})$ contains material's anisotropic elastic constants, and $\boldsymbol{\varepsilon}(\mathbf{x})$, $\boldsymbol{\varepsilon}^{\mathrm{e}}(\mathbf{x})$, $\boldsymbol{\varepsilon}^{\mathrm{p}}(\mathbf{x})$, and $\boldsymbol{\varepsilon}^{\mathrm{tr}}(\mathbf{x})$ are respectively the total, elastic, plastic, and transformation strain tensors, calculated at any material point $\mathbf{x}$. Twinning is modeled as a strain transformation process and the associated transformation strain $\boldsymbol{\varepsilon}^{\mathrm{tr}}(\mathbf{x})$ applies only to points within the twin domain [77, 69, 151]. This shear transformation tensor is null in all points outside of the twin domains, including those associated with SBs. Using a semi-implicit time discretization scheme, the stress state in the material point $\mathbf{x}$ at time $t + \Delta t$ can be written as,

$$\boldsymbol{\sigma}^{\mathrm{t+\Delta t}}(\mathbf{x}) = \mathbf{C}(\mathbf{x}) : \big(\boldsymbol{\varepsilon}^{\mathrm{t+\Delta t}}(\mathbf{x}) - \boldsymbol{\varepsilon}^{\mathrm{p,t}}(\mathbf{x}) - \dot{\boldsymbol{\varepsilon}}^{\mathrm{p,t+\Delta t}}\big(\mathbf{x}, \boldsymbol{\sigma}^{\mathrm{t+\Delta t}}\big)\,\Delta\mathrm{t} - \boldsymbol{\varepsilon}^{\mathrm{tr,t}}(\mathbf{x}) - \Delta\boldsymbol{\varepsilon}^{\mathrm{tr,t+\Delta t}}(\mathbf{x})\big) \tag{4.2}$$

The viscoplastic strain-rate tensor at material point $\mathbf{x}$ is constitutively calculated from the stress tensor through a sum over the N available slip systems, as follows:

$$\dot{\boldsymbol{\varepsilon}}^{\mathrm{p}}(\mathbf{x}) = \sum_{\mathrm{s=1}}^{\mathrm{N}} \mathbf{m}^{\mathrm{s}}(\mathbf{x})\dot{\gamma}^{\mathrm{s}}(\mathbf{x}) = \dot{\gamma}_0 \sum_{\mathrm{s=1}}^{\mathrm{N}} \mathbf{m}^{\mathrm{s}}(\mathbf{x}) \left(\frac{|\mathbf{m}^{\mathrm{s}}(\mathbf{x}) : \boldsymbol{\sigma}(\mathbf{x})|}{\tau_{\mathrm{c}}^{\mathrm{s}}(\mathbf{x})}\right)^{\mathrm{n}} \mathrm{sgn}\left(\mathbf{m}^{\mathrm{s}}(\mathbf{x}) : \boldsymbol{\sigma}(\mathbf{x})\right) \tag{4.3}$$

The change in transformation strain during the twinning process is specified as,

$$\Delta\boldsymbol{\varepsilon}^{\mathrm{tr}}(\mathbf{x}) = \mathbf{m}^{\mathrm{tw}}(\mathbf{x})\Delta\gamma^{\mathrm{tw}}(\mathbf{x}),\ \ \Delta\gamma^{\mathrm{tw}}(\mathbf{x}) = \mathrm{S}^{\mathrm{tw}}/\mathrm{N}^{\mathrm{tw-inc}} \tag{4.4}$$

In (4.3), $\dot{\gamma}^{\mathrm{s}}(\mathbf{x})$ and $\tau_{\mathrm{c}}^{\mathrm{s}}(\mathbf{x})$ are respectively the shear rate and the critical resolved shear stress (CRSS), associated with slip system s at point $\mathbf{x}$. Furthermore, $\dot{\gamma}_0$ is a normalization factor and n is the stress exponent. $\mathbf{m}^{\mathrm{s}} = (\mathbf{b}^{\mathrm{s}} \otimes \mathbf{n}^{\mathrm{s}} + \mathbf{n}^{\mathrm{s}} \otimes \mathbf{b}^{\mathrm{s}})/2$ and $\mathbf{m}^{\mathrm{tw}} = (\mathbf{b}^{\mathrm{tw}} \otimes \mathbf{n}^{\mathrm{tw}} + \mathbf{n}^{\mathrm{tw}} \otimes \mathbf{b}^{\mathrm{tw}})/2$ are the Schmid tensors associated with the slip system s and the twinning system, respectively. Unit vectors $\mathbf{b}^{\mathrm{s}}$ ($\mathbf{b}^{\mathrm{tw}}$) and $\mathbf{n}^{\mathrm{s}}$ ($\mathbf{n}^{\mathrm{tw}}$) are aligned with the slip (twinning) shear direction, and slip (twin) plane normal. Finally, in (4.4), $\mathrm{N}^{\mathrm{tw-inc}}$ is the number of increments by which the shear strain in the twin domain, $\Delta\gamma^{\mathrm{tw}}$, reaches the characteristic twin shear, S^{tw}.

For material points corresponding to SBs, the SB-FFT model described in Chapter 2 is employed. The coefficient D_0 in (2.6) is numerically determined so that the experimentally observed SBs fully develop within the prescribed applied strain. To avoid numerical instabilities, a lower limit of $\tau_c^{\mathrm{s}} = 2$ MPa is set for all slip systems.

4.3.1 Material parameters and model setup

Material parameters used in the calculations include the single-crystal elastic constants at room temperature, available slip systems, and their critical resolved shear stress (CRSS) values, the lattice constant (c/a ratio), and the coefficient D_0 in (2.6). These are presented for CP-Ti in Table 4.2. CP-Ti has an anisotropy index of $A^L = 0.075$, where the ideal case of perfect isotropy yields zero [101], showing more elastic anisotropy than many common HCP metals, like Mg ($A^L = 0.012$) and Zr ($A^L = 0.046$). We made available to the calculation the dominant slip systems reported in experimental studies [5, 133, 136, 21]. These are prismatic $< a >$, basal $< a >$, and pyramidal

$\{10\bar{1}1\} < 11\bar{2}3 >$ slip. Considering plastic deformation, the easiest slip mode in Ti is prismatic slip, followed by moderately harder basal slip, and then pyramidal $< c + a >$ as the hardest mode [21]. For comparison, a reported CRSS value for $\{10\bar{1}2\}$ tensile twinning is also given in Table 4.2, although it is not used or needed in the calculations.

Table 4.2: Elastic constants [16], c/a ratio [17], softening coefficient D_0, and critical resolved shear stress (CRSS) values [21] for different deformation modes available for CP-Ti. Note that only slip modes are allowed to accommodate plastic deformation in the calculations.

Material	Elastic constants (GPa)					c/a	D_0	CRSS values for deformation modes (MPa)			
	C_{11}	C_{22}	C_{13}	C_{33}	C_{44}	ratio		prismatic $< a >$	basal $< a >$	pyramidal I $< c + a >$	Twin $\{10\bar{1}2\}$
CP-Ti	162.4	92.0	69.0	180.7	46.7	1.588	50	96	127	240	225

Crystalline microstructures are modeled here that mirror those observed experimentally, both previously published [119, 5] and newly presented data, including material points associated with discrete twin lamellae and SBs. Figure 4.1 shows an example comprising a grain with many prismatic SBs neighboring a grain with a few twin lamellae. The box with dashed lines in Figure 4.1(a) shows the frame from which the bicrystals are created for the calculations. Figure 4.1(b) and (c) show the microstructure models used for the corresponding SB and twin band, respectively. The decomposition of a co-located pair into uncoupled, independent simulations of SB and twin band allows the analysis of the local stress fields ahead of each band and helps to identify whether the pair developed via a directional "path-dependent transmission" or an independent "co-formation" event. The bicrystals in Figure 4.1(b) and (c) are discretized into 250×300 voxels in the $y-$ and $x-$direction, respectively. A SB domain is preselected within the banded grain to mirror the SEM image. The actual imaged domain corresponds to the intersection of the dominant glide plane with the viewing $x - y$ plane. For all SBs modeled here, two voxels span the SB thickness. This thickness is sufficiently fine to enable a uniform shear through the thickness of the band, as argued in previous chapter. To model the discrete twin bands in all calculations, a six-voxel-thick twin domain is embedded in its parent crystal, as shown in Figure 4.1(c). The out-of-plane thickness of the bicrystals spans three voxels in all calculations. It was shown in previous chapter that greater (by two orders of magnitude) simulation cell thicknesses do not change the calculated micromechanical fields. All simulation cells are surrounded by a 40-voxel-thick layer in both in-plane directions with properties of a randomly oriented CP-Ti polycrystal. The thickness of this layer is sufficiently large to render spatially resolved micromechanical fields insensitive to the image forces due to the considered periodic boundary condition.

The CPFFT simulation cells are subjected to uniaxial tension along the $y-$direction, up to 2% strain, consistent with the actual experimental condition. Normal stress components in the other two directions are enforced to be zero. Modeling slip banding and twinning are performed sequentially. In the SB simulations, the constitutive law stated in (2.6) is applied to the material points inside/outside the band domain, and no shear transformation or reorientation is involved. Macroscopic strain is set to evolve in increments of 0.01% per time step and the time steps are specified to be small enough to ensure convergence. When modeling the twin lamella, the same level of uniaxial strain is first applied to the simulation cell without the twin. Subsequently, the lattice of the twin domain is reoriented following the twin/matrix orientation relationship, and the characteristic twin shear is built incrementally and homogeneously over $\mathrm{N}^{\mathrm{tw-inc}} = 2000$ increments, according to (4.4). Considering that twinning occurs on much faster time scales than slip, we model slip as a rate sensitive process, in which plasticity develops in time with strain, and twinning as a relatively instantaneous process. We insert the twin at a fixed time step, rather than modeling its growth over time. Thus, the incremental implementation of the twin shear is only to ensure numerical convergence and occurs at a fixed macroscopic strain level, signifying the instantaneity of twinning relative to slip. Although not an inherent limitation of the present formulation, hardening in the

CRSS values for basal and prismatic slip are not included for the sake of simplicity in the calculations. The competition between these two modes is not expected to change significantly within the few percent of applied strain.

In all calculations, as in Figure 4.1, we consider the actual GB plane morphology and crystal orientations. The shear tractions calculated along the boundary because of local GB curvature or inclination with respect to macroscopic load are expected to contribute to the local stresses and potentially play a role in the propensity for band transmission. To elucidate the GB morphology effect, we repeat some calculations for a simplified geometry consisting of two equal-sized grains sharing a planar GB, as seen in Figure 4.2(c). For both actual and planar GBs, two sets of simulations are conducted, one with and the other without the slip/twin band modeled in their parent grain. The calculated local stresses ahead of the band, at the GB junction within the neighboring grain, particularly over a region that is several times the thickness of the band, as indicated in Figure 4.1(b) and (c) with dashed black boxes are compared. To identify the deformation mode and system onto which a transmission from an experimentally observed slip/twin system is more likely to happen, when explicitly modeling either a discrete SB or twin, the system of the modeled band or twin corresponds to the experimentally observed system. However, in any material point outside of the band domain, all slip systems are available for activation. Further, we consider all 18 slip systems and six variants of $\{10\bar{1}2\}$ tensile twinning, when identifying candidate slip/twin system in the neighboring grain for transmission. For instance, to determine the slip system onto which a twin transmits across the GB, we compare slip activity on all 18 systems at the twin tip and identify those with the highest activity as potential outgoing systems in a twin-to-slip transmission.

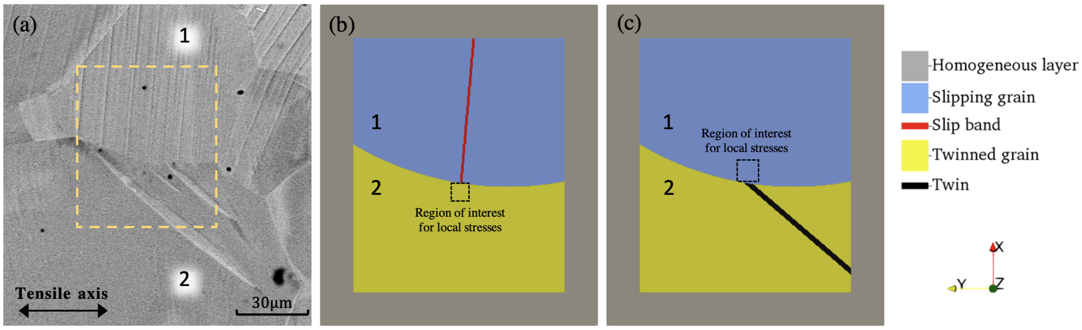

Figure 4.1: (a) SEM image showing intense prismatic SBs in Grain 1 and $\{10\bar{1}2\}$ twin lamellae in Grain 2. Dashed lines indicate the border of the simulation cell. (b) Schematic of the bicrystal unit cell subjected to the SB constitutive law to examine potential slip-twin transmission. A 2-voxel-thick ($w_s = 2$) SB is embedded in the top grain, impinged at the curved GB. (c) The bicrystal unit cell simulated with the twinning constitutive law to study potential twin-slip transmission. A 6-voxel-thick ($w_t = 6$) black domain in the bottom grain shows the preselected area for twinning. In both (b) and (c), the dashed black box shows the region of interest in which the local stresses at the tip of the slip/twin band are assessed. The SEM image corresponds to pair P4 of Table 4.3.

4.4 Experimental characterization of co-located slip-twin pairs

Results from the current microstructural characterization of the deformed material along with detailed descriptions of some parts of the dataset that were previously published in [5] are presented here. Consistent with those descriptions in [5], trace analysis across the investigated surface area revealed that prismatic slip was prevalent in many grains in the part of the dataset newly presented here. The analysis also reveals the activation of substantial number of grains with T1:$\{10\bar{1}2\}$ tensile twins. Considering the twin volume fraction and the relatively low characteristic twin shear for T1 twins in CP-Ti, no more than approximately 4% of the total strain was accommodated via deformation twinning [5]. SEM image analysis shows a strong correlation between the twin lamellae and prismatic SBs in the grain neighbor in nearly one-third of the twinned grains. Table 4.3 presents the crystallographic and geometric information obtained from the SEM/EBSD analysis for four pairs of twinned grains and "banded grains" (grains containing SBs) in which the SBs and twins (S ↔ T) were co-located, as well as two cases of co-located SBs on either side of the boundary (S ↔ S). For comparison, we include the same information for a grain containing lone SBs, blocked at the GB (S ⊣ 0). Grain orientations are given by Euler angles in Bunge convention in a coordinate system with x = transverse, y = tensile axis, and z = sample normal. In some cases, several SB/twin co-located pairs were observed across the same boundary, and for these cases, the number of SBs or twins identified in each grain is included. Before performing micromechanical calculations, a geometric analysis is performed for all the observed cases. Table 4.3 lists the Schmid factor for the observed slip (m_s) or twin (m_t) band system. The underlined Schmid factor entries, whether m_s or twinning m_t, indicate when the active SB or twinning variant is preferred, compared to all other slip or T1 twinning systems, by their parent orientation alone. Table 4.3 also offers the geometric factor m' associated with the transmission. An underlined m' value means that, according to the m' criterion, the transmission is most favorable (i.e., has the highest m') among all prismatic slip – T1 twinning pairing in S ↔ T cases, or slip – slip pairing in S ↔ S cases. Crystallographic information about different variants of prismatic slip and tensile twinning is presented in Table 4.4.

Table 4.3: Orientation of the SB and twinned grains as well as the Schmid factors for the active systems and the geometric factor m' associated with the transmission. The deformation modes in all banded and twinned grains are prismatic slip (except for P6) and $\{10\bar{1}2\}$ tensile twin (T1), respectively. Refer to Table 4.4 for the variant's crystallographic details.

		Banded grain						Twinned / banded grain						
	Pair	Euler angles			Observed prismatic SB			Euler angles			Observed T1 twinning / SB			m'
		ϕ_1	Φ	ϕ_2	variant	Number of bands	m_s	ϕ_1	Φ	ϕ_2	variant	Number of bands	m_t or m_s	
$S \leftrightarrow T$	P1	77	65	288	2	27	0.48	159	87	196	1	5	0.43[b]	0.93
	P2	68	74	291	2	17	0.44	313	93	131	6	6	0.23	0.89
	P3	93	123	356	3	21	0.47	20	105	348	2	3	0.38	0.88
	P4	91	80	281	2	23	0.50	26	83	339	2	3	0.39	0.79
$S \leftrightarrow S$	P5	59	78	295	2	5	0.37	67	84	292	1	5	0.27	0.27
	P6	82	80	257	3	31	0.49	147	63	76	<c+a>[a]	8	0.41	0.03
S - 0	P7	95	75	68	3	10	0.49	12	82	143	–	0	–	–

[a] Observed slip mode is $(\bar{1}011)[2\bar{1}\bar{1}3] < c + a >$ pyramidal slip system.

[b] Both twin variants 1 and 5 have the highest Schmid factor in the twinned grain.

Table 4.4: Crystallographic information about different variants of prismatic slip and $\{10\bar{1}2\}$ tensile twinning.

	Prismatic slip			$\{10\bar{1}2\}$ tensile twinning					
Variant	1	2	3	1	2	3	4	5	6
Shear direction	$[2\bar{1}\bar{1}0]$	$[\bar{1}2\bar{1}0]$	$[11\bar{2}0]$	$[\bar{1}011]$	$[0\bar{1}11]$	$[1\bar{1}01]$	$[10\bar{1}1]$	$[01\bar{1}1]$	$[\bar{1}101]$
Plane normal	$(01\bar{1}0)$	$(10\bar{1}0)$	$(1\bar{1}00)$	$(10\bar{1}2)$	$(01\bar{1}2)$	$(\bar{1}102)$	$(\bar{1}012)$	$(0\bar{1}12)$	$(1\bar{1}02)$

One can obtain some quick insight from assessing these geometric factors. First, it is evident that the observed SB prismatic system in the banded grains in S $\leftrightarrow$ T cases has the highest Schmid factor between the three possible prismatic systems. The same conclusion, however, cannot be made for twinned grains as there are several grains in which the operating twin variant is not associated with the highest Schmid factor twin variant. When considering the combinations of prismatic SBs and twins, we find that the geometric factor m' becomes the better geometric predictor than the Schmid factor. A previous study [5] came to a similar conclusion, suggesting that grain with a twinning system that makes a high m' with respect to the incoming SBs is more likely to display slip-stimulated twinning. However, neither the Schmid factor nor m' indicates whether observed transmitted pairs were accomplished via co-formation or path-dependent transmission. Alternatively, analysis of the local stress field can indicate not only if the band transmits, but whether these pairs resulted from co-formation or path-dependent transmission and the sense of direction taken. To this end, in the calculations that follow, we decompose co-located pairs into two problems, each of which with just one slip or twin band, and analyze the stress field ahead of it in the neighboring grain.

4.5 Role of grain boundary morphology on local stress fields

Since local stress states are important for the analysis, we first investigate the effect of GB morphology, its curvature and orientation with respect to loading axis, on the local stress state, by comparing the GB shear traction developed for the actual morphology with that for a planar boundary. Figure 4.2(a) shows a SEM image from pair P3 with prismatic SBs in Grain 1 connected to twin lamellae in Grain 2 across the GB. Bicrystals with the actual and planar GB morphology are shown in Figure 4.2(b) and (c), respectively. Both models are subjected to 2% applied strain along the y-direction, consistent with the experiments. Furthermore, to evaluate how SBs affect the GB shear traction, simulations are repeated with no active SB in Grain 1. Figure 4.3(a-d) shows the distributions of the GB shear traction (τ_{GB}), on the Grain 1 side of the boundary, for both actual and planar boundaries with and without a SB. The GB shear traction at each point near the boundary is calculated given the full stress tensor and the orientation of the GB at that point. Figure 4.3 reveals a significant distinction between the GB shear tractions, signaling the imperative role GB orientation and curvature play. The cases containing a SB in Figure 4.3(b, d) further demonstrate the discontinuity in the shear traction along the boundary at the band/GB junction caused by the SB. The shear traction varies significantly along the GB, a phenomenon that would have been missed if the actual morphology of the GB was not modeled. Finally, Figure 4.3(e) compares the shear traction profiles between the actual GB morphology and the planar one. While in both cases the SB locally alters the stress fields, particularly at the SB/GB junction, the alteration is more substantial when the actual morphology of the GB is considered. The results thus far quantitatively reveal a significant role of GB morphology on GB shear traction, a quantity that could contribute to slip transmission across the GB. This notion is consistent with prior studies [134, 152]. An experimental investigation of the interaction of SBs with the GB as a function of depth in CP-Ti revealed that the slip system onto which incoming SBs transmit across the same GB can alter at different depths, only because the orientation of the GB with respect to the incoming SBs changes between two depths [134]. Furthermore, a molecular dynamics (MD) study [152] found that the resolved shear stress (RSS) contribution from the GB tractions either helps or hinders the emission of dislocations, depending on their direction with respect to the RSS contribution from the applied loading. Accordingly, the actual morphology and orientation of GBs, as well as the orientation of SBs or twin domains, with respect to applied loading are preserved in all calculations that follow.

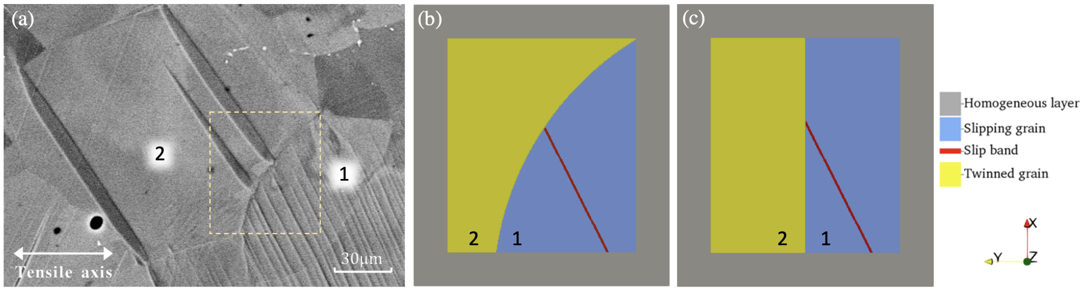

Figure 4.2: (a) SEM image reveals pair P3 with slip ↔ twin transmission across the GB in a CP-Ti sample subjected to 2% uniaxial strain along the $y-$axis. The box with dashed lines shows the frame from which computational models are built. Models constructed with (b) an actual or (c) a planar GB morphology for the pair of grains in (a). In both models (b-c), a 2-voxel-thick SB is embedded in Grain 1.

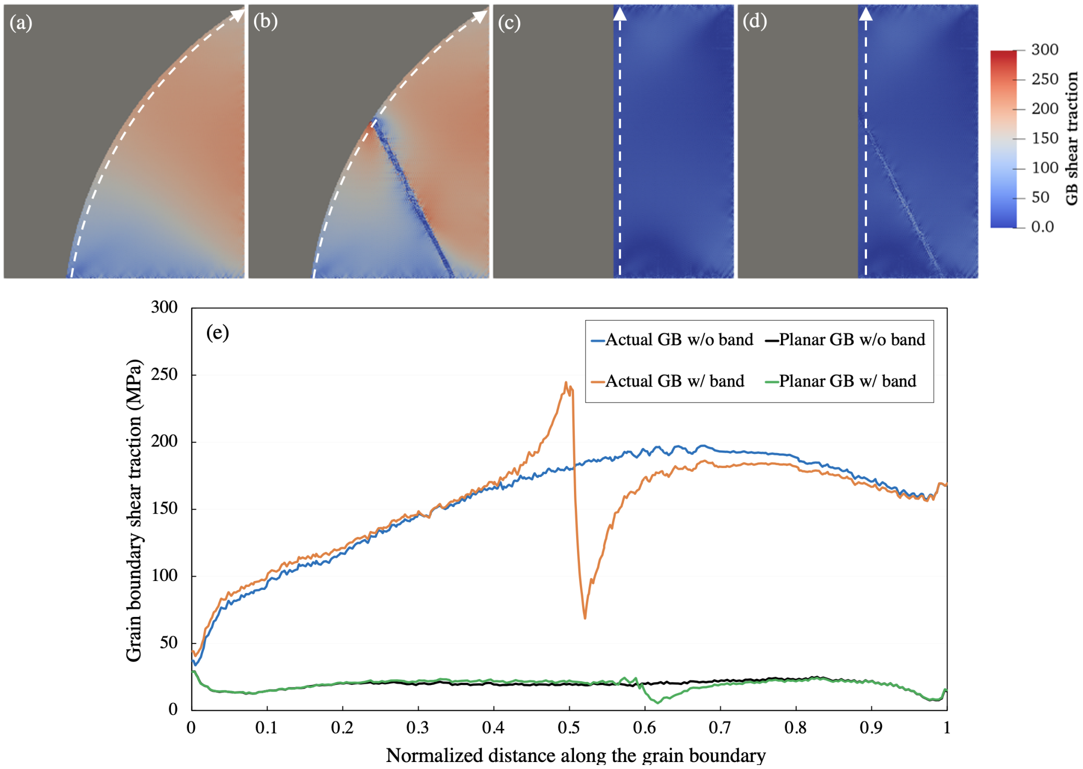

Figure 4.3: Distribution of the GB shear traction in Grain 1 at 2% macroscopic strain for the bicrystal with the actual GB morphology (a) without and (b) with an intense SB and (c-d) for the same bicrystal but with a planar GB (c) without and (d) with an intense SB, (e) Variation of the GB shear traction at 2% macroscopic strain calculated along the paths shown with white dashed lines in parts (a) through (d). The sudden drop in the two GB profiles with a SB corresponds to the location where the SB is crossed and is associated with the softening in the band. Distance along the GB is normalized by the length of the GB. Grain 2 is colored grey in parts (a-d) to help emphasize the fields in the Grain 1 side of the GB.

4.6 Simulation of slip-to-twin transmissions

In this section, we investigate a few cases to study the stress field developed at the tip of a SB inside the neighboring grain to identify whether they assist or prevent slip-to-twin transmission across the GB. Figure 4.4(a) shows a SEM image of pair P2 in which parallel prismatic SBs in Grain 1 are spatially correlated with $(1\bar{1}02)[\bar{1}101]$ twin lamellae in a relatively small neighboring Grain 2 at 2% applied strain. Activated prismatic slip in Grain 1 has a high Schmid factor of $m_s = 0.44$, suggesting the possibility for the independent activation of SBs in this grain. In Grain 2, on the other hand, the Schmid factor for the most favorable twin variant (V6), which is the same as the observed variant, is only $m_t = 0.23$, signifying that this grain is not well oriented for twinning. Twin nucleation in small grains is particularly unlikely when the Schmid factor is low [153], further highlighting the role that SB localization in Grain 1 could play in twin nucleation in Grain 2, but not the other way around. Due to the fact that the m' factor associated with the prismatic SBs in Grain 1 and observed twin variant in Grain 2 ($m' = 0.89$) is the highest among all other twin variants, it was previously conjectured that twin nucleation might have happened as a result of a local change in the stress fields at the GB caused by the prismatic slip activity localized in Grain 1 [5]. However, the noteworthy questions are why easy prismatic slip with a slightly higher Schmid factor ($m_s = 0.26$) did not form in Grain 2 and why twins, with this variant, formed instead?

These questions can be addressed by investigating local stress fields at the SB tip for both mechanisms. Figure 4.4(b) shows the bicrystal model used to study local stress fields at the tip of the prismatic SBs in Grain 1. The other nearest and next nearest neighbors are not explicitly modeled, but rather the effect of the surrounding neighbors is represented by a homogeneous medium. In Appendix B, we demonstrate for this pair that explicitly resolving more neighboring grains than in the current bicrystal model does not significantly affect the local stress fields in and around the slip band tip. Figure 4.4(c) and (d) respectively represent the distribution of the twin resolved shear stress (TRSS) for variant V6 $(1\bar{1}02)[\bar{1}101]$ seen in Grain 2, for a simulation model with and without a SB in Grain 1, both for 2% applied strain. In either case, we first find that the stress field in the two grains is heterogeneous and unlike the far-field macroscopic stress, signifying the effect of the surrounding homogeneous medium on local stress distribution within these grains. Without a SB, the TRSS is uniformly distributed and low, suggesting twinning is not favored in Grain 2 under the imposed 2% strain. With a SB, however, intense TRSS develops in Grain 2 at the SB tip. The TRSS maps for the other five $\{10\bar{1}2\}$ twin variants find that variant V6 shown in Figure 4.4 and seen experimentally, experiences the greatest intensity, which explains why V6 was selected. The difference in stress fields between the cases with and without a slip localization supports the idea that the enhanced stress field at the SB tip is responsible for the twins seen in Grain 2. Since slip competes with twinning, the driving forces for prismatic slip are also compared for these two cases to determine whether SB formation would have been favored over twinning. Evaluation of the prismatic slip system resolved shear stress fields in Grain 2 indicates that the maximum RSS intensity at the SB tip is weakened by 18% with the SB than without. These calculations, therefore, suggest that the intense prismatic SBs in Grain 1 initiated the twins in Grain 2 despite the low Schmid factor of this variant, determining this co-located pair as a case of path-dependent transmission. In this case, the choice of deformation mechanisms, slip or twinning, of Grain 2 was significantly influenced by the deformation behavior, particularly the localized SBs within neighboring Grain 1.

To demonstrate a case in which SBs do not affect the stress fields in the grain neighbor, the pair P4 shown in Figure 4.1 is considered. In P4, Grain 1 contains several parallel prismatic SBs, whereas $(01\bar{1}2)[0\bar{1}11]$ twin (variant 2) is activated in Grain 2. Grain 1 is perfectly oriented for prismatic slip with $m_s = 0.5$ while the Schmid factor for the

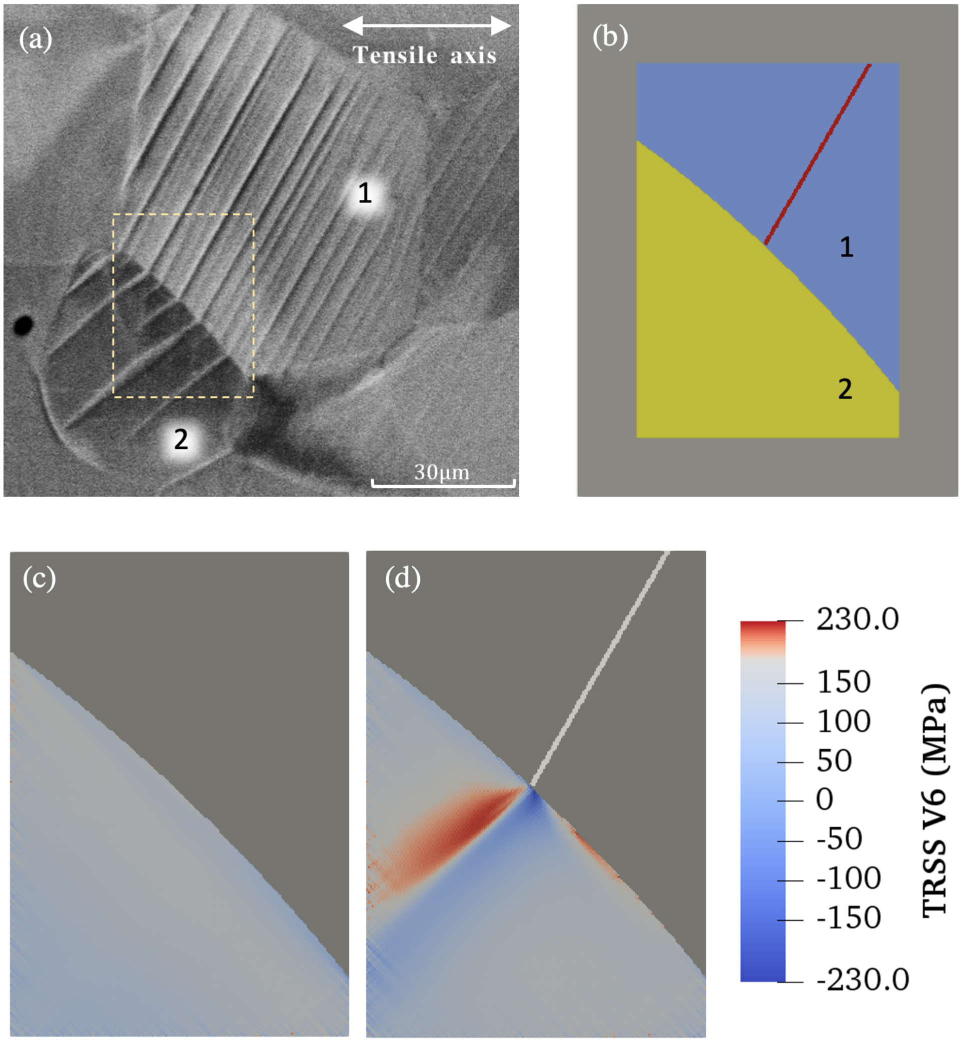

Figure 4.4: (a) SEM image at 2% macroscopic strain for pair P2 revealing a possible transmission between intense prismatic SBs in Grain 1 and $(1\bar{1}02)[\bar{1}101]$ tensile twin (variant 6) in Grain 2 [5], (b) Bicrystal model for the pair P2 shown in (a), calculated field at 2% macroscopic strain of the twin plane resolved shear stress (TRSS) for the $(1\bar{1}02)[\bar{1}101]$ tensile twin variant (V6), (c) without and (d) with an intense SB in Grain 1.

observed twin variant in Grain 2 ($m_t = 0.39$) as well as the transmission factor ($m' = 0.79$) are relatively high. Since the twin lamellae in Grain 2 have terminated in the middle of the grain, we can argue that they initiated at the common GB of Grain 1 and 2 and at locations where the SBs intersected it. However, whether SBs in Grain 1 and twins in Grain 2 were accomplished via co-formation or path-dependent transmission cannot be determined from the SEM image. To gain insight into the sequence of events, contours of the TRSS for the operating twin variant (V2) after 2% applied strain are shown in Figure 4.5(a) and (b), respectively, for a model without and with a SB embedded in Grain 1. First, it is evident that the SB in Grain 1 has no effect on the V2 TRSS field in Grain 2. Second, analyzing the other variant TRSS fields finds that the SB would not serve as a driving force for any other twin variant. Last, the TRSS for the V2 variant is the highest value, the same variant as seen experimentally. Thus, this variant selection is unaffected by the activity of SBs in Grain 1. Taken together, it may be conjectured that either the prismatic slip in Grain 1 and tensile twinning in Grain 2 formed independently, a co-formation event, or twin lamellae in Grain 2 initiated SBs in Grain 1. To see if the latter is possible, we simulate the reversed transmission, in which the twins in Grain 2 formed first. The result reveals intensified local stresses on the prismatic system at the twin tip inside Grain 1, suggesting that a path-dependent twin-to-slip transmission is more likely than the co-formation event.

4.7 Simulation of twin-to-slip transmissions

Figure 4.2 shows the SEM image of pair P3 containing prismatic SBs in Grain 1 connected to two $(01\bar{1}2)[0\bar{1}11]$ twin lamellae (V2) in Grain 2, and the bicrystal models used to calculate stress fields in these two grains. The Schmid factor for the prismatic slip in Grain 1, twin in Grain 2, and the transmission factor are, respectively, $m_s = 0.47$,

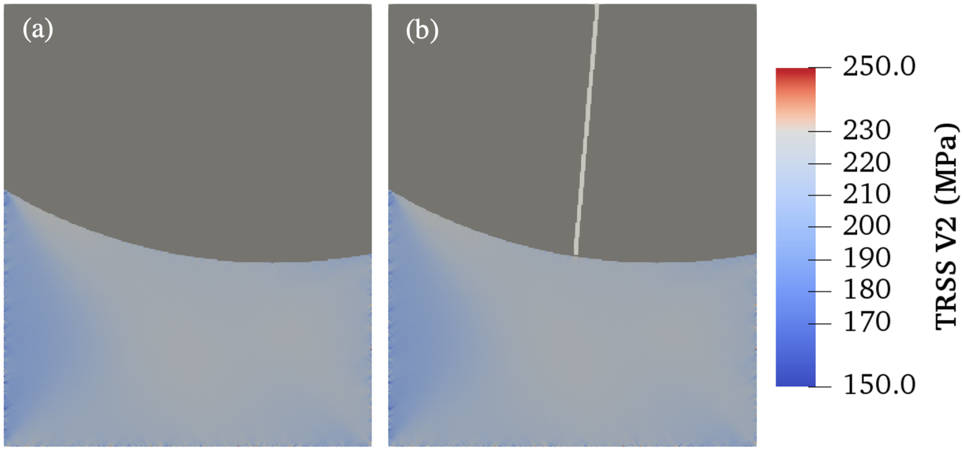

Figure 4.5: Calculated twin plane resolved shear stress (TRSS) fields for the $(01\bar{1}2)[0\bar{1}11]$ tensile twin variant (V2) at 2% macroscopic strain (a) without and (b) with an intense SB in Grain 1. It is evident that the SB in this case does not affect the local driving stress for twinning at the tip.

$m_t = 0.38$, $m' = 0.88$. Figure 4.6(a) presents the distribution of the TRSS for the operating twin variant (V2) in Grain 2, after 2% applied strain, without a SB. Even without the SB, the TRSS is not uniformly distributed neither within Grain 2 nor along its GB with Grain 1. Remarkably, the location along the GB at which the TRSS is heightened, predicted by calculations, corresponds to the location of two twin lamellae formed at the GB (see Figure 4.2(a)). This would suggest that twinning in Grain 2 is already favored to form at the observed site in the GB without a need for SBs in Grain 1. Since the actual morphology of the GB appears to make a defining role, we show in Figure 4.6(c) the contour of TRSS for the operating twin variant in Grain 2 from a bicrystal model with a planar GB and without a SB in Grain 1. For the planar GB, twinning in Grain 2 is most likely to form at the triple junction at the top segment of the boundary, in stark contrast to experimental observations. A comparison between Figure 4.6(a) and (c) implies that the morphology of the GB can influence local stress fields along the GB (through its effect on the GB shear traction) to the extent that it can control slip transmission events across the GB. It is also possible that the SB in Grain 1

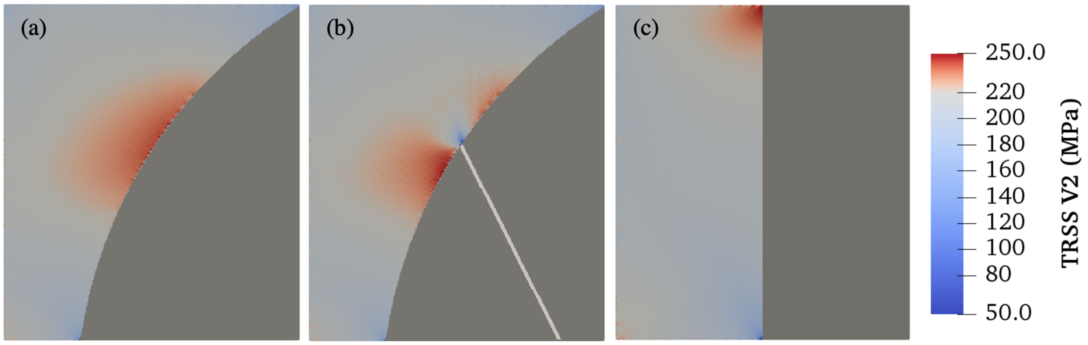

Figure 4.6: Calculated distribution of the twin plane resolved shear stress (TRSS) in pair P3 for the $(01\bar{1}2)[0\bar{1}11]$ tensile twin variant (V2) at 2% macroscopic strain, with the actual GB morphology, and (a) without and (b) with a SB embedded in Grain 1. Perhaps counterintuitively, the SB has decreased the TRSS in the vicinity of the SB, and thus reduces the possibility of slip to twin transmission across the boundary. (c) TRSS distribution in Grain 2, for a planar GB without a SB, elucidating the effect of GB morphology on the local stress fields at the boundary.

participated in choosing the observed V2. Figure 4.6(b) shows the V2 TRSS field due to the SB in Grain 1. Perhaps counterintuitively, a local reduction occurs at the tip of the band. Not only would a SB in one grain not generate stress concentrations that promote twinning, but it would also hinder slip → twin transmission. Evidently, SBs in Grain 1 do not contribute to twinning in Grain 2.

To be complete, V2 twins in Grain 2 could have caused SBs in Grain 1. The bicrystal model shown in Figure 4.7(a) is used to calculate the resolved shear stress (RSS) fields for $(1\bar{1}00)[11\bar{2}0]$ prismatic slip corresponding to the observed SB. Figure 4.7(b) and (c) respectively show the contours without and with the V2 twin. Comparing these two RSS maps reveals that the twin in Grain 2 maximizes the RSS in Grain 1 ahead of the twin tip but lowers it elsewhere. Among all three prismatic slip variants, the active slip system, shown in Figure 4.7(b, c), has the highest RSS, explaining the selection of the active slip system observed experimentally. This co-located pair likely occurred via transmission of V2 twins in Grain 2 into prismatic SBs in Grain 1.

Next, we present simulation results for the likely slip ↔ twin transmission event in

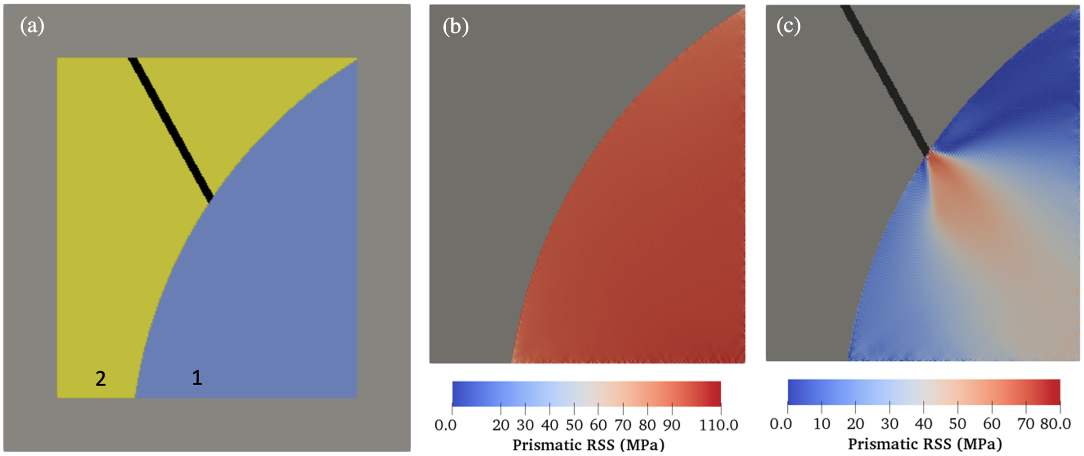

Figure 4.7: (a) Bicrystal model for pair P3 shown in Figure 4.2(a), with a twin lamella in black, (b-c) Calculated distribution of the resolved shear stress (RSS) for the prismatic slip system in Grain 1, in which intense prismatic SBs are observed, at 2% strain, and (b) without the twin, and (c) with the twin.

pair P1, as shown in Figure 4.8(a). High Schmid factors for the prismatic slip in Grain 1 ($m_s = 0.48$), twin in Grain 2 ($m_t = 0.43$), and the transmission factor ($m' = 0.93$) suggest that these two mechanisms are independently favored to activate under the macroscopic load. The bicrystal setup created to model this pair of grains is displayed in Figure 4.8(b). Figure 4.8(c) and (d) show the amount of shear accumulated on the prismatic slip system, the one observed experimentally, without and with the twin, respectively. The calculations suggest that under an applied strain of 2%, the prismatic slip system becomes uniformly activated within Grain 1, due to the Grain 1 crystal orientation with respect to loading. With the twin in Grain 2, the slip activity in Grain 1 escalates exclusively at the twin/GB junction. Calculations considering the reverse path, with the SB in Grain 1 and Grain 2 twin free, reveal a stress concentration inside Grain 2 at the SB/GB junction, for all six twin variants. Since both prismatic slip in Grain 1 and $(10\bar{1}2)[\bar{1}011]$ tensile twinning in Grain 2 are already favored due to the parent grain orientations, the intense SBs in Grain 1 and twins in Grain 2 affected their location and less so their systems.

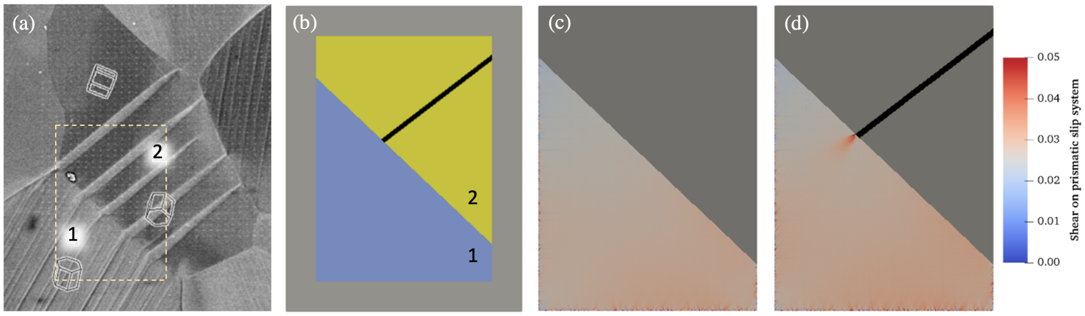

Figure 4.8: (a) SEM image reveals pair P1 with slip ↔ twin transmission across the GB after 2% uniaxial strain [5]. (b) Bicrystal model for pair P1 with a twin lamella in black. (c-d) Calculated distribution of the accumulated shear on the active prismatic system in Grain 1 from pair P1 at 2% strain (c) without the twin and (d) with the twin.

4.8 Simulation of slip-to-slip transmissions and blocked slip bands

Other common observations include one SB or a pair of co-located SBs at GBs, signifying slip-to-slip transmission or a blocked SB. The SEM image in Figure 4.9(a) shows the pair P5 with prismatic SBs in Grain 1 and Grain 2 correlated across a GB. In Grain 1, SBs are localized on the most favorable prismatic system, S2:$(10\bar{1}0)[\bar{1}2\bar{1}0]$, with a Schmid factor of $m_{s2} = 0.37$. In Grain 2 SBs correspond to the prismatic system S1:$(01\bar{1}0)[2\bar{1}\bar{1}0]$, which has a lower Schmid factor of $m_{s1} = 0.27$. The transmission factor associated with these two slip systems is $m' = 0.27$. Based on this geometric analysis alone, activation of the system S1 in Grain 2 is counterintuitive since another prismatic slip system had a higher Schmid factor ($m_{s2} = 0.42$) and correspondingly higher m' value ($m' = 0.98$) with S2 in Grain 1. To understand why slip transmission involved an unsuitably oriented slip system, two bicrystal models were simulated, each of which contains a SB in one of the grains. Figure 4.9(b) shows the model with a SB in Grain 1, with which the local stress fields at the band tip inside Grain 2 are evaluated. Figure 4.9(c) presents the distribution of shear accumulated on the active prismatic slip system in Grain 2 (S1) at 2% applied strain. While the areas in the interior of the Grain 2 do not accommodate any shear strain on system S1, the localized slip activity on this system at the SB tip is intense, implying that SBs in Grain 2 were initiated due to prismatic SBs in Grain 1. Transmission from Grain 1 to Grain 2 was further supported by repeating the calculation for the contrary situation, SB transmission from Grain 2 to Grain 1. The SB in Grain 2 showed no impact on local fields at the band tip inside Grain 1 and therefore this pathway is unlikely. To compare how local stress fields encourage slip activity on these two systems in Grain 2, resolved shear stress (RSS) on prismatic systems S1 and S2 are presented in Figure 4.9(d), as the far-field strain increases. Notably, while the RSS for system S2 is higher than that for S1 in the interior of the grain, activity of SBs in Grain 1 intensifies the RSS for system S1 at the band tip to a level higher than the local value of RSS on system S2 at the GB. In contrast to the stress states inside the grain, SBs in Grain 1 encourage S1 activity, the one observed experimentally, while suppressing S2 activity at the GB.

Figure 4.10 for pair P6 shows a likely transmission between $(1\bar{1}00)[11\bar{2}0]$ prismatic SB in Grain 1 with a Schmid factor of $m_1 = 0.49$ and $(\bar{1}011)[2\bar{1}\bar{1}3]$ pyramidal $< c + a >$ SB in Grain 2 with a Schmid factor of $m_2 = 0.41$. The interesting aspect about this transmission is its extremely low $m' = 0.03$. The question is then why this transmission with pyramidal slip is observed instead of one involving the easier basal slip system that is more favorably oriented for activation ($m_s = 0.49$) and for transmission ($m' = 0.65$). To address this question, Figure 4.10(c) shows the distribution of shear strain accumulated on the active pyramidal slip system in Grain 2. The presented contour is obtained at 4% far-field strain since no activity at the band tip was found for any slip system at 2% strain. The calculations successfully predict activation of the hard pyramidal slip system at the band tip in Grain 2, despite the very low m' value for the observed transmission. Analysis of RSS maps for the favorably oriented basal slip system further reveals that

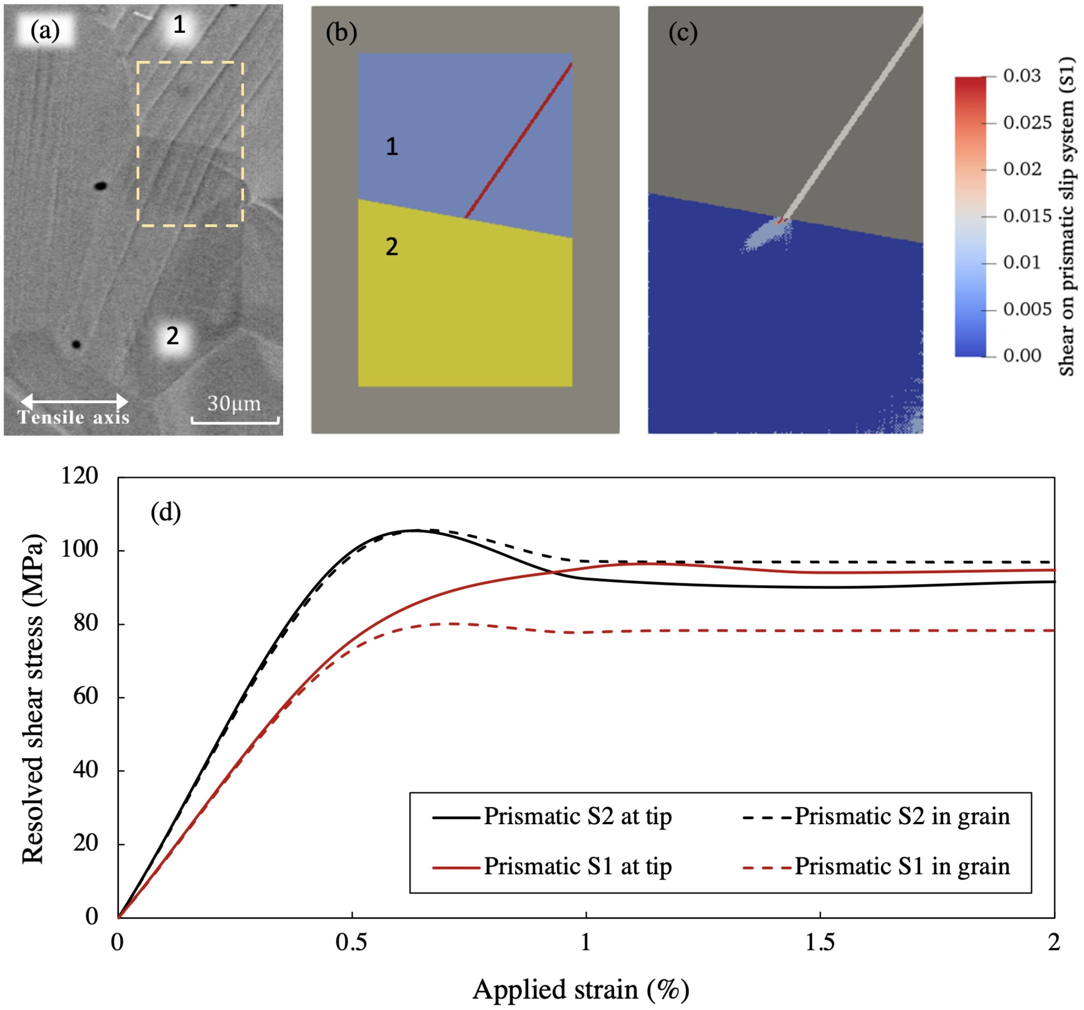

Figure 4.9: (a) SEM image of pair P5 revealing transmission between $(10\bar{1}0)[\bar{1}2\bar{1}0]$ prismatic slip (S2) in Grain 1 and $(01\bar{1}0)[2\bar{1}\bar{1}0]$ prismatic slip (S1) in Grain 2, at 2% macroscopic strain, (b) Bicrystal model subjected to the SB constitutive law for the pair of grains shown in (a), (c) Calculated distribution of shear accumulated on the S1 prismatic system in Grain 2 confirms the effect of SBs in Grain 1 on the selection of system onto which they transmit in Grain 2, (d) Evolution of the resolved shear stress on two prismatic slip systems denoted by “S1” and “S2”, as the macroscopic strain increases. The curves are shown for both the average RSS in the SB tip zone only and in the entire Grain 2.

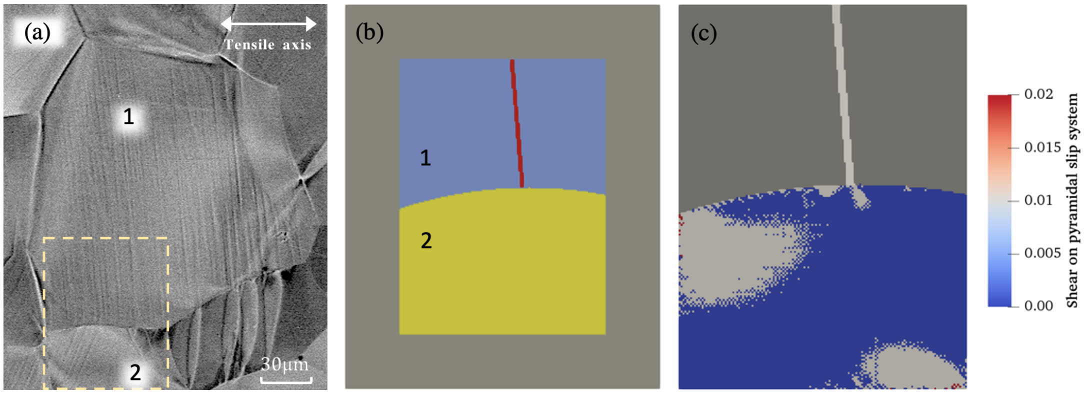

Figure 4.10: (a) SEM image of pair P6 revealing transmission between $(1\bar{1}00)[11\bar{2}0]$ prismatic slip (S3) in Grain 1 and $(\bar{1}011)[2\bar{1}\bar{1}3]$ pyramidal slip in Grain 2, at 2% macroscopic strain, (b) Bicrystal model subjected to the SB constitutive law for the pair of grains shown in (a), (c) Distribution of shear accumulated on the pyramidal system in Grain 2 at 4% applied strain.

the SB in Grain 1 does not promote activation of basal slip at the GB. Simulation of the reversed transmission, in which the pyramidal SB in Grain 2 formed first, reveals that the local fields at the pyramidal band tip generated inside Grain 1 would not favor the activation of the prismatic slip system corresponding to the observed SBs. Prismatic SBs formed first and not the other way around.

Finally, an example of blocked SBs by the GB (P7) is shown in the SEM image in Figure 4.11(a), where intense prismatic SBs in Grain 1 were not transmitted into Grain 2. The bicrystal model used to study stress fields at the band tip is also shown in Figure 4.11(b). While Grain 2 experienced homogeneous deformation, or no deformation at all, calculations indicate multiple slip and twinning modes in this grain that are favored by the far-field loading orientation and are well-aligned with prismatic SBs in Grain 1. The most likely slip system in Grain 2 for a slip-to-slip transmission is $(01\bar{1}1)[1\bar{2}13]$ pyramidal slip with $m_s = 0.49$ and $m' = 0.74$, while the most likely twin variant for a slip-to-twin transmission is $(\bar{1}102)[1\bar{1}01]$ twin variant (V3) with $m_t = 0.46$ and $m' = 0.98$. Calculations reveal no intensifying or weakening effect from the SB in Grain 1 on the

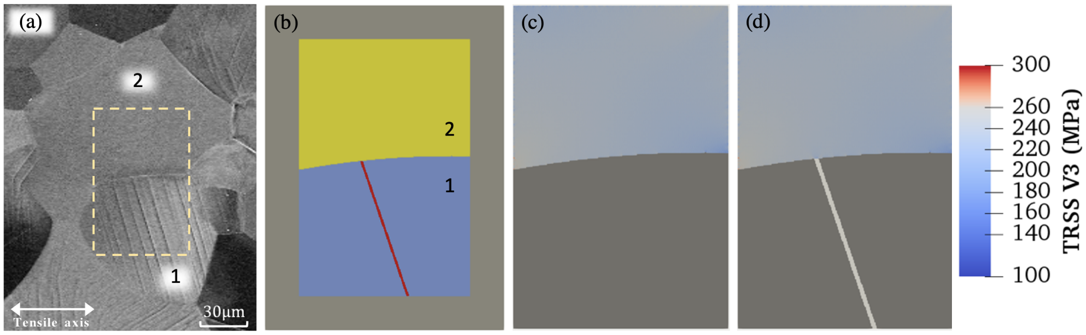

Figure 4.11: (a) SEM image for pair P7 showing prismatic SBs in Grain 1 blocked at the GB at 2% macroscopic strain, while some twin variants in Grain 2 are perfectly aligned with the incoming slip, geometrically making the slip → twin transmission more likely to occur, (b) Bicrystal model for pair P7 shown in (a), Calculated distribution of the twin plane resolved shear stress (TRSS) at 2% macroscopic strain for the $(\bar{1}102)[1\bar{1}01]$ twin variant (V3) that has the highest value of $m' = 0.98$ associated with a slip → twin transmission, for the simulations (c) without and (d) with an intense SB in Grain 1. It is noted that despite the perfect alignment between the incoming slip system and the outgoing twin variant, the band is blocked at the boundary and creates no impact on the local stress fields at the tip.

local stress fields at the GB for any slip system or twin variant. Contours of the TRSS for the $(\bar{1}102)[1\bar{1}01]$ twin variant (V3) at 2% macroscopic strain are shown in Figure 4.11(c) and (d), respectively, for models without and with a SB in Grain 1. These explain why the SBs did not promote twin variant V3 in the neighboring Grain 2. The resolved shear stresses for all slip and twinning modes at any point inside Grain 2 are below their applicable critical value. Consequently, the accumulated shear strain on all slip systems is zero, indicating that Grain 2 accommodated no strain at all. Despite high values of m' and m_s, not all SBs will transmit SBs or trigger twins across a boundary and those that are blocked can be identified because they do not generate driving forces.

4.9 Discussion

It was previously reported in [152] that the contribution of the GB shear traction to the overall resolved shear stress developed at the GB can affect whether the GB assists or inhibits the emission of dislocations at the GB, a phenomenon directly associated with slip transmission across the GB. It can be envisioned that GB morphology could be included in GB engineering to control deformation mechanisms within the grains and inhibit or promote their transmissions across the GBs. As suggested by the TRSS fields in Figure 4.6(c, e), a curved GB, especially the segments of it that make a 45° angle with the loading axis, promotes twin formation from the boundary more than a planar boundary would. This finding is in agreement with the effect of GB orientation on slip activity in CP-Ti reported in an experimental study [134], where it was found that a change in the orientation of the GB with respect to loading direction necessitates the activation of secondary slip systems in proximity to the grain boundaries. It is also demonstrated here that GB/band junction stress fields can help to identify the transmission path, that is, which mechanism initiated the transmission and which one completed it. Contrary to previous speculations that most twins in the studied CP-Ti sample were formed via a slip-stimulated twin nucleation mechanism [5], we reveal the reverse, in which some of the co-located slip and twin bands in CP-Ti manifest first as twins, which then stimulated a SB in the grain neighbor. Table 4.5 summarizes simulation and experimental results for each studied pair. Depending on the calculated stress fields around the co-located pairs, each transmission case is classified as one of the followings; $\mathrm{S} \rightarrow \mathrm{T}$ for slip-to-twin transmission, $\mathrm{T} \rightarrow \mathrm{S}$ for twin-to-slip transmission, $\mathrm{S} \rightarrow \mathrm{S}$ for slip-to-slip transmission, and $\mathrm{S} \dashv 0$ for SBs that are blocked at the GB. Many studies have reported various effective techniques, such as grain size refinement and adding solid solution or precipitates, for inhibiting twinning in titanium [154, 155, 156, 157, 158]. Thus, the direction of the transmission path taken can have implications on the effectiveness of such techniques. Particularly, if most SBs are activated by the twin bands, inhibiting the formation of twins may cause reduced formability in the material associated with the lower extent of slip.

Table 4.5: Twin variants observed in transmission instances, the Schmid factors for the incoming and outgoing systems, and the geometric factor m' associated with the transmission. To compare simulation results with experimental observations, the deformation mode in the neighbor with the highest RSS value and the slip/twin band effect on the local stress state at the band tip are also presented for each pair. The slip mode where intense SBs are detected is prismatic slip (except for P6). See Table 4.4 for crystallographic information about different variants of prismatic slip and tensile twinning.

	Pair	Observed SB		Observed twin / SB		m'	Deformation mode with highest RSS at the tip	SB effect on stress at the tip	Prismatic variant with highest RSS at the tip	Twin/SB effect on stress at the tip	Transmission classification
		Prismatic variant	m_s	variant	m_t or m_s						
$S \leftrightarrow T$	P1	2	0.48	1	0.43	0.94	6, 3	Intensifying	3, 2	Intensifying	$T \rightarrow S$
	P2	2	0.44	6	0.23	0.89	6	Intensifying	–	–	$S \rightarrow T$
	P3	3	0.47	2	0.38	0.88	1, 4	Weakening	3, 1	Intensifying	$T \rightarrow S$
	P4	2	0.50	2	0.39	0.79	2, 5	No effect	2, 1	Intensifying	$T \rightarrow S$
$S \leftrightarrow S$	P5	2	0.37	1	0.27	0.27	1, 2	Intensifying	2, 1	No effect	$S2 \rightarrow S1$
	P6	3	0.49	<c+a>[a]	0.41	0.03	<c+a>[a]	Intensifying	3	No effect	$S3 \rightarrow$ <c+a>
$S \dashv 0$	P7	3	0.49	–	–	–	–	No effect	–	–	$S \dashv 0$

[a] Observed slip mode is $(\bar{1}011)[2\bar{1}\bar{1}3] < c + a >$ pyramidal slip system.

Several cases presented here demonstrate that simple geometric parameters, such as Schmid factor and m', that have been widely used to forecast active deformation mechanisms and their potential transmission across boundaries are not consistently reliable. First, while undoubtedly beneficial for quickly identifying the most favorable pair for transmission, they do not identify whether this transmission happens in the first place. Second, they clearly do not account for differences in deformation mechanisms at the GB junction from the rest of the grain or for the GB morphology. This conclusion supports several experimental studies that have reported many instances in which m' was not effective in explaining why the observed transmission occurred or a potential transmission did not [95, 6, 10]. While requiring more computation, an intragranular stress-based criterion, such as the one presented in this work, provides a better prediction and accounts for these features. In fact, it has been established that, in addition to good alignment between two slip systems, as indicated by m', the outgoing system needs to have a sufficiently large resolved shear stress level from the dislocation pile-up stress field before a transmission can occur [60]. While the notion is acceptable, identifying the variables that affect these local RSS has not been straightforward. As demonstrated here, these driving stresses are localized and depend on the properties of both the band that impinges on the GB and the GB itself. For instance, local stresses explain the activation of a prismatic slip system despite its low Schmid factor and low m', in favor of other prismatic systems with higher values of m_s and m'. Similarly, local stresses developing at the GB/SB junction explain the observed transmission to a hard pyramidal $< c + a >$ slip system despite its nearly zero m'. Last, local stresses explain why a SB would become blocked despite many potential pathways with high m'. Finally, we remark that many current constitutive models for HCP materials that deform by slip and twinning do not consider the exchange of deformation mechanisms into and out of a grain from its neighborhood. Most modeling techniques predict deformation mechanisms in the grain based on the stress field calculated using grain properties and constraints of neighboring grains [67, 159, 160]. Three-dimensional, spatially resolved crystal plasticity models, for instance, consider the influence of the stress and deformation response of grain neighborhoods under compatibility constraints [136, 161, 162, 163]. Local stress fields can be generated at the GBs or triple junctions that differ from the stress field in the interior of the grain as a result. Invariably, the slip and twin activity and orientations in these regions would differ as well [164, 165, 166, 167]. Yet still, in these models, deformation mechanisms are not transmitted, and the dependence on the neighborhood is indirect. Analysis of local band/GB junctions of many co-located pairs studied here shows that the slip or twin happened in one grain only because it was passed from its neighboring grain. The event in Figure 4.4, for instance, exemplifies tensile twins activated in the neighboring grain caused by stress concentrations from the SBs in the parent grain. The tensile twins superseded prismatic slip, which would have been expected or predicted in that grain based on its properties. While including deformation "fluxes" in such models is numerically challenging, a part of the roadblock has been the lack in understanding the direction of transmission and which slip system or twin variant are involved. The present results provide guidance on selecting the participating direction and crystallographic pathway.

4.10 Conclusions

Consistent with the report previously published in [5] on a part of the deformed microstructure, experimental observations from the newly presented data in this work show that the plastic deformation in CP-Ti is mainly realized via strong localized crystallographic bands, either $\{10\bar{1}2\} < \bar{1}011 >$ twins or prismatic SBs. These localized bands are typically seen to intersect at the parent grain boundaries, having initiated or terminated there. In some instances, SBs or twins terminating in the interior of the grain were also observed. In either case, many GBs show a clear correlation in location for slip/twin bands on two sides of the boundary, forming co-located pairs. What is not clear from SEM images, however, is whether these co-located pairs were achieved via a directional, path-dependent transmission or independently via a co-formation event. To address this question, we present a crystal plasticity fast Fourier transform model that uniquely treats both discrete SBs and twin lamellae. Unlike most modeling techniques that predict deformation in each grain based on the grain properties, the present model directly incorporates grain neighbor properties into the prediction of deformation mechanisms in the parent grain. The model is applied to bicrystal unit cells that replicated a pair of grain with transmission from SEM images. Studying local stress field caused by a slip or twin band at the GB/band junction, we investigate the propensity for a new slip/twin band to form in the grain neighbor, and hence identify the transmission path taken. We show that the local stress field calculated by discrete slip and twin band model can determine not only if a transmission has occurred in an observed co-located pair, but also the direction of the transmission, an insight that geometric criteria, such as m', cannot provide. We further reveal that retaining the actual morphology of the GB when modeling a set of grains can heavily influence local stress fields developed near the boundary, and consequently, the slip/twin transmission across the GB. Such influence ensues from the effect of GB morphology on the intensity of the sudden disruption in the GB shear traction that occurs at the discrete slip or twin band/GB junction and contributes to the local back-stress and stress concentration developed on either side of the boundary.

Chapter 5

Modeling slip localization in metals for mechanical properties prediction

5.1 Introduction

Strong relations exist for metallic materials between macroscopic mechanical properties and the localization of plasticity. Materials that deform by slip produce intense plastic localization events referred to as slip localization that originate from the constraint glide of dislocations. The characteristics of these events depend on the chemistry, structure, and microstructure of the metallic materials and infer some of the macroscopic mechanical properties. Understanding these characteristics allows identification of the metallic materials' structure and multi-scale microstructure effects and, ultimately, an accurate prediction of macroscopic mechanical properties.

For instance, the connectivity of the slip localization events in titanium alloys has been observed to affect their yield strength significantly [4, 168, 53]. Slip localization events, usually constrained in one or a few crystallographic grains, can connect over long-range in titanium alloys due to the presence of micro-textured regions. Consequently, a continuous route that favors the unrestrained motion of dislocations is achieved across the entire specimen section leading to early macroscopic yield [4, 169]. More recently, the intensity of the slip localization was observed to inform the fatigue strength of metallic materials [3]. Metallic materials that promote intense slip localization during loading were observed to have poor efficiency in fatigue [3]. The intensity of the slip localization is also observed to relate at room temperature in face-centered cubic (FCC), and hexagonal close-packed (HCP) materials to their yield strength [51, 3]. Materials with high yield strength manifest larger amplitudes of slip localization with fewer slip events than materials with low yield strength. In addition, the characteristics of the interaction of slip localization events within the microstructure and between them control the hardening behavior of metallic materials [170].

While slip localization events can be rapidly captured and characterized experimentally by innovative measurements such as high-resolution digital image correlation [3, 43, 171, 172, 22], a significant effort remains to model these events and their evolution as a function of the microstructure. Molecular dynamics (MD) and discrete dislocation dynamics (DDD) simulations capture dislocation motion that leads to slip localization. For instance, DDD simulations [173, 174, 175] demonstrate the combined effect of dislocation obstacle strength and density and distribution of obstacles on the yield strength of the materials. These simulations show the yield strength of a wide range of metallic materials scales with predictions by continuum dislocation pileup models, demonstrating why strong materials tend to produce a high amplitude of slip localization. In parallel, MD simulations revealed complex interactions of slip localization and the characteristics of the grain boundaries in metallic materials [176, 177, 178, 179]. Grain boundaries are observed to have different energy barriers that promote or prevent the transmission of slip, significantly changing the characteristics of the slip localization and the macroscopic mechanical properties. DDD and MD simulations show the critical role of metallic materials' grain structure, structure, and fine-scale microstructure. However, the complexity of the multi-scale microstructure of metallic materials and computational power limitation prevent such simulations over representative microstructure areas for an accurate prediction of the mechanical properties.

Crystal plasticity (CP) simulations are the preferred method to capture the complexity of the grain structure. These simulations are performed on representative microstructure volumes/surfaces that encompass the variety of grain configurations of metallic materials. However, they usually used a homogenization framework that prevents explicitly quantifying slip localization events. Recent efforts are now made to introduce the explicit description of slip localization within these simulations [51, 50, 36, 37, 33] that open new avenues to explore the role of the multi-scale microstructure of metallic materials. This approach combines material deformation (slip localization) and mechanistic (stress distribution) considerations. Capturing the complexity of the microstructure and the explicit description of slip localization may allow accurate prediction of the deformation behavior of metallic material.

In this chapter, CP simulations with an explicit description of the slip localization are used for various FCC and HCP materials. The characteristics of the slip localization are obtained through these simulations, and a one-to-one comparison with experimental results is performed. The model demonstrates the complex effect of the microstructure on slip localization. Interestingly, it is revealed that slip localization introduces a resistance against subsequent slip in their vicinity. This resistance originates from a local stress field, termed reaction stress, produced by a slip event in its vicinity. Reaction stress depends on the grain configuration and intrinsic properties of the material. The local stress field produced by an initial slip localization event controls the behavior of the subsequent slip events. This finding highlight a substantial mechanistic effect of the interaction between the cumulative motion of dislocation and grain structure that results in slip localization.

Such significant findings allow capturing the impact of the multi-scale microstructure on the plastic localization in metallic materials.

5.2 Mechanical testing and characterization

5.2.1 In-situ mechanical testing

Flat dogbone-shaped specimens with a gauge section of 1x3 mm^2 were used for tensile testing on a custom in-situ ± 5000 N stage within a FEI Versa3D microscope with a field-emission gun. In-situ strain gauges and fiducial markers at both ends of the specimen were used to measure the macroscopic strain. High resolution digital image correlation (HR-DIC) measurements were performed at macroscopic plastic stains from 0.02% to 1.2% after pausing the tensile testing. Monotonic tensile tests were performed at strain rates of $10^{-4}s^{-1}$.

5.2.2 High-resolution digital image correlation measurement

Before the mechanical testing is done all the samples were polished first with SiC papers up to 1200 grit followed by polishing with 6 μm diamond suspension and finally a 0.05 μm colloidal silica was used for 12 hours of chemo-mechanical polishing. Two methods were used to make nano-scale speckle patterns that are used for HR-DIC measurements: (1) Following the procedure of Kammers et al. [180] gold nanoparticles with an average size of 60 nm were deposited onto the surface; (2) following the work of Montgomery et al. [181] a 10 nm thin silver coating sputtered via magnetron on the surface was reconfigured to produce speckle patterns with an average particle size of 60 nm. 1 x 1 mm^2 regions were examined and images were taken in 10x10 grid before and after mechanical deformation with an overlap of 15% . DIC calculations were then performed on the images, and the resulting fields were stitched using a pixel resolution merging procedure. A typical subset size of 31 x 31 pixels (1044 nm x 1044 nm) with a step size of 3 pixels (101 nm) were used for the HR-DIC measurements. SEM image sets were acquired before loading and under load following the guidelines of Kammers and Daly [182] and Stinville et al. [183]. A National Instruments$^{\text{TM}}$ scan controller and acquisition system (DAQ) were used to control beam scanning in the FEI microscope. This custom beam scanner removes the SEM beam scanning defects associated with some microscope scan generators [183, 184].

5.2.3 Heaviside digital image correlation

When considering displacement fields that involve discontinuous displacement, like those produced by slip or fracture phenomena, one can no longer use the hypothesis of continuous displacement fields that is inherent to the conventional DIC methodology [185]. Heaviside-DIC was developed to address and improve conventional DIC's shortfalls when dealing with discontinuous displacements. Heaviside-DIC adds a jump/step function to the algorithm to capture the discontinuity within each sampled subset. If no discontinuity occurs then the jump function returns zero allowing for the standard algorithm to converge. The Heaviside-DIC also provides higher displacement resolutions below 10 nm considering the present sample preparation, imaging conditions and DIC parameters, and the ability to find multiple discontinuities within a subset. The method also enables the direct measurement of the amplitudes and direction of the physical displacements induced by a slip event. More information is provided elsewhere [186, 187].

5.2.4 Data merging and analysis

Microstructure characterization was performed by Electron Backscatter Diffraction (EBSD) measurements with an EDAX OIM-Hikari XM4 EBSD detector using step sizes around 0.5 micron. Diffraction patterns were typically acquired using an accelerating voltage of 30 kV, a 4 × 4 binning and a beam current of 0.2 nA. EBSD maps were acquired prior and after deformation. For each material, EBSD data was aligned into the HR-DIC measurements, which is subject to the least spatial distortion. Sub-pixel spatial registration between the HR-DIC and EBSD measurements is done using pairs of control points as described in reference [188]. It provides accurate registration between the microstructure at the surface of the specimen and HR-DIC data. Each single slip trace over the investigated regions (more than 2000 per materials) was manually segmented from HR-DIC data. The profile of the intensity of the in-plane displacement (in-plane slip amplitude) induced along each slip event was automatically extracted and fitted. The maximum and average value of the fit along the profile are extracted for analysis. The maximum slip intensity for each single slip event is normalized by the square root of the length of the slip event to make comparisons among materials with different grain structure and sizes. Slip trace spacing between two slip traces is defined as the minimum distance between them. The distance is defined on sets of similar slip bands: same active slip system(s) within the same microstructure entities (grain, parent grain, twin or region delimited by high angle boundaries). More information is provided elsewhere [188, 3].

5.3 Material parameters and model setup

5.3.1 Computational framework: SB-FFT formulation

Presumably due to a raise in local temperature caused by localized slip on a single slip plane or the multiplication of mobile dislocations destructing the short-range order and providing an easy path for subsequent dislocation glide, slip bands are commonly treated as regions in which the resistance to slip decays as more slip is localized within them [80, 81, 82, 83, 84].

To simulate intense slip bands observed in studied materials in this work, the SB-FFT model described in Chapter 2 is applied to a vast range of FCC and HCP metals. For the interest of this work, the coefficient D_0 in (2.6) for HCP and FCC metals is specified to be, respectively, 30 and 70, remaining fixed across all simulations for each crystal structure. The reason for this invariance is to isolate the effects of microstructure geometric constraint and slip strengths across each crystal structure. Furthermore, to avoid numerical instabilities, maximum softening in the SB available region is limited to 90% of the initial CRSS, i.e., $\min_t \tau_{\mathrm{c}}^{\mathrm{s,t}}(\mathbf{x}) = 0.1\tau_{\mathrm{c}}^{\mathrm{s,t}}(\mathbf{x})|_{\mathrm{t=0}}$.

5.3.2 Material parameters and model setup

Material parameters, including the single crystal elastic constants at room temperature, active slip systems and their critical resolved shear stress (CRSS) values, as well as the c/a ratio (for HCPs) and Zener ratio (for FCCs), are listed in Table 5.1 for eight FCC and three HCP materials simulated in this work. The CRSS values for the three slip modes in HCP materials are taken from the literature. For each FCC material, however, the CRSS value is determined via simulation of a homogeneous polycrystal and fitting the resulted stress-strain curve against that measured experimentally. Simulated engineering stress-strain curves along with the experimental curves are shown in Figure 5.4 for all studied materials. The computational framework described in previous section is applied to a bicrystal setup shown in Figure 5.5a. The parent and neighboring grains are similarly discretized into 100×200 ($y \times z$) voxels while the thickness of the simulation cell in the x-direction is three voxels. The two crystals are surrounded by a 20-voxel-thick homogeneous layer with random orientations which represents the bulk response from the surrounding polycrystal. A SB available region with the thickness of two voxels is preselected in the parent grain, making a 45^{o} angle with respect to the y-axis. The bicrystal setup is then strained along the y-axis, up to 2.5% far-field strain. Normal stress components in the other two directions are enforced to be zero. The SB available region is subjected to a softening law, according to (2.6). Slip resistance in the rest of the parent crystal, as well as all other material points in the neighboring grain and the surrounding homogeneous layer, remains fixed (in HCPs) or can be hardened based on Voce law (in FCCs), as the far-field strain increases. In simulation of HCP materials, orientation of the parent crystal is (90°, 90°, 45°) when the slip band lies on a prismatic plane, and (0°, 45°, 30°) when it localizes on a basal plane. Furthermore, when simulating FCC materials, orientation of the parent grain is (204.2°, 84.7°, 24.2°). Finally, orientation of the neighboring grain can vary across different simulations. Figure 5.5b and c respectively shows four orientations used for the neighboring grain in FCC bicrystals, and 20 orientations used for modeling each slip band type in HCP bicrystals.

Table 5.1: Elastic constants, c/a ratio (HCPs), Zener ratio (FCCs), and critical resolved shear stress (CRSS) values for different slip modes in investigated materials.

Crystal structure	Material	Ratio	Elastic constants (GPa)					Ref.	CRSS values for slip modes (MPa)			Ref.
		Zener	C_{11}	C_{12}			C_{44}		$\{1\bar{1}1\} < 110 >$			
FCC	René 88DT	2.23	267.1	170.5			107.6	[189]	525			–
	Inconel 718 (precipitation strengthened)	2.72	259.6	179.0			109.6	[190]	495			–
	René 65	2.23	267.1	170.5			107.6	[189]	390			–
	CoNi-SB	3.13	236.4	150.9			133.9	[191]	320			–
	Stainless steel 316L (additive manufactured)	2.31	247.5	140.3			123.7	[192]	230			–
	Inconel 718 (solid-solution strengthened)	2.72	259.6	179.0			109.6	[190]	134			–
	Stainless steel 316L (forged plate)	2.31	247.5	140.3			123.7	[192]	120			–
	Copper	3.27	166.1	119.9			75.6	[193]	14			–
		c/a	C_{11}	C_{12}	C_{13}	C_{33}	C_{44}		Prismatic $< a >$	Basal $< a >$	Pyramidal I $< c + a >$	
HCP	Titanium Ti-6Al-4V	1.588	162	92	69	181	47	[193, 194]	370	420	590	[195]
	Titanium Grade 4								244	363	444	[196]
	Titanium Ti-7Al								220	245	388	[197]

5.4 Experimentally observed link between macroscale strength and microscale localization[1]

Solid datapoints in Figure 5.1 show the amplitude of slip localized within the SBs in twelve FCC and three HCP materials, measured at two different strain levels, 0.2% and 1.0% plastic strain. Slip amplitude in each SB in a given alloy was first characterized using the HR-DIC technique and then normalized by the SB length, to nullify the dependency of

---

[1] The experimental part of this study was conducted by Jean-Charles Stinville and published in [3].

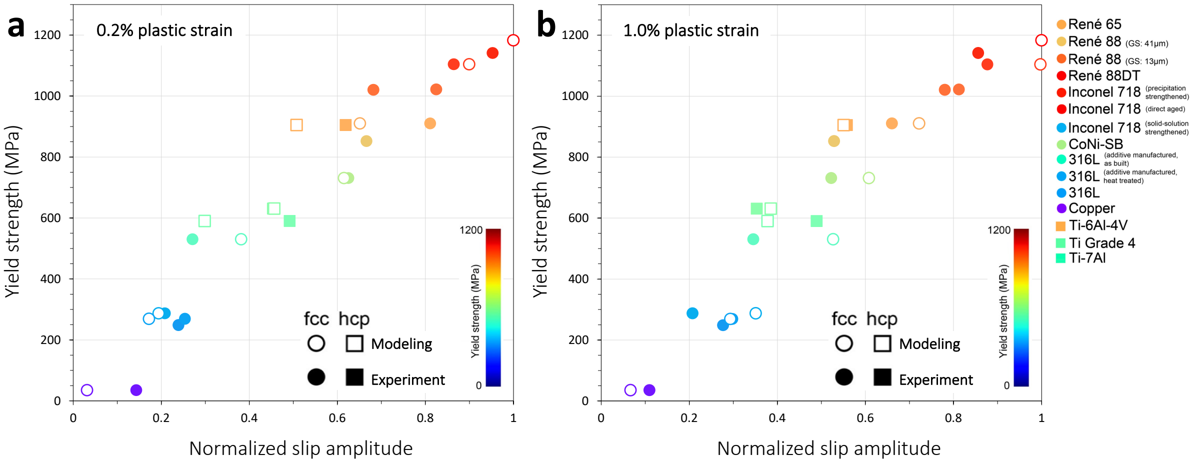

Figure 5.1: Experimental and numerical results for the amplitude of slip localization within the slip bands in different alloys and their relationship with material yield strength. (a) At 0.2% plastic strain. (b) At 1.0% plastic strain. Slip amplitudes are normalized by their largest value.

slip localization on SB length. Reported data in Figure 5.1 are the average slip amplitude among all SBs characterized in each material. Regardless of the level of plastic strain applied, amplitude of slip localization is revealed to be proportional to material yield strength. Furthermore, this relationship is not limited to materials within the same crystal structure. That is to say, between two alloys selected from the wide range of FCC and HCP metals investigated, a material that is macroscopically stronger with a higher yield strength tends to localize more slip within its SBs, with the ratio of slip amplitudes being linearly proportional to their yield strengths. Considering the extremes, HR-DIC measurements reveal a low tendency to localize slip in copper, while in René 88DT, slip is highly localized within the SBs, rather than being homogeneously accommodated by the grain.

Next, Figure 5.2 shows the average SB spacing measured in the investigated FCC and HCP metals. To obtain the SB spacing for each alloy, the distance between any two adjacent SBs in each grain is measured and the average over all pairs of SBs in the alloy is calculated. The absolute values of SB spacing vary from ~ 1 μm to ~ 6 μm, with the minimum and maximum values corresponding to copper and René 88DT, respectively. Furthermore, consistently across all alloys, the average SB spacing decreases as the macroscopic strain increases, signifying the formation of new SBs in each grain at higher strain levels. Similar to the behavior of slip amplitude, SB spacing is revealed to have a positive correlation with the material yield strength. Again, comparing two alloys with either an FCC or an HCP crystal structure, the stronger material tends to localize slip within SBs that form farther away from each other.

So far, the HR-DIC measurements in Figure 5.1 and Figure 5.2 reveal that, regardless of crystal structure, a material with a higher yield strength manifests larger amplitudes of slip localized within SBs with wider spacings. The important question is now why a macroscopically stronger material has a stronger tendency to accumulate slip in localized SBs, rather than homogeneously accumulating slip across the grain, and why it localizes slip in fewer number of bands with larger spacing between them. In what follows, we address these questions by micromechanical modeling of slip localization in FCC and HCP metals investigated experimentally.

5.5 Model validation

To understand the role of material strength on localization, a crystal plasticity (CP) model within a 3D spatially resolved replication of the microstructure has been built that permits localization in a domain that is subjected to a rate-dependent softening constitutive law. The narrow domain designated for the SB, called *SB available domain*, is distinctive from the rest of material in that it is permitted to soften, while the rest hardens with the macroscopic load increasing. Initially, each slip system has the same slip resistance or critical resolved shear stress (CRSS) in all material points within a given mi-

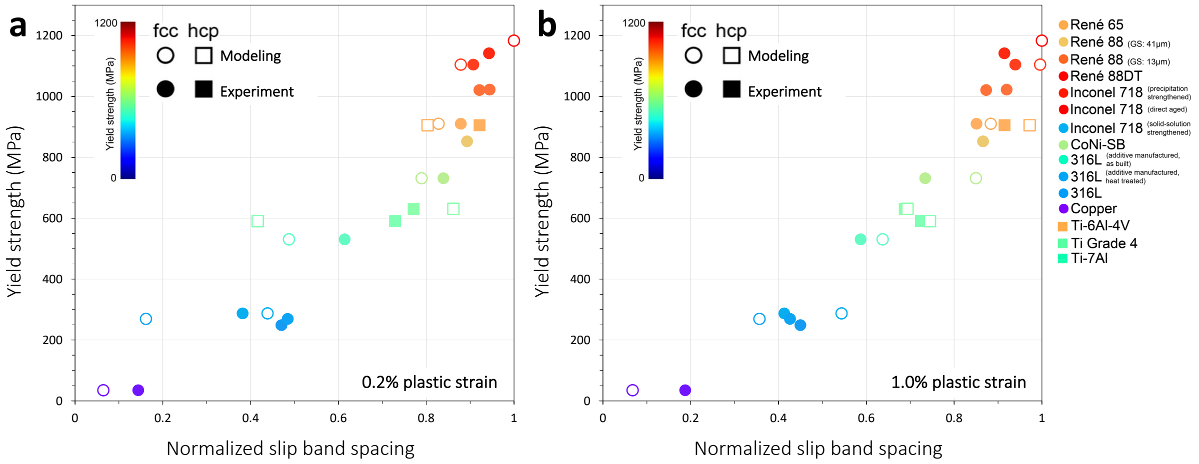

Figure 5.2: Experimental and numerical results for slip band spacing in different alloys and their relationship with material yield strength. (a) At 0.2% plastic strain. (b) At 1.0% plastic strain. Slip band spacings are normalized by their largest value.

crostructure. In the material points within the SB available domain, applied constitutive response is such that slip activation leads to the decay of the CRSS. From the physical point of view, slip in this domain gradually removes any obstacles, making it easier for subsequent dislocations behind it to glide. Such material softening is presumably due to a raise in local temperature caused by localized slip on a single slip plane or the multiplication of mobile dislocations destructing the short-range order and providing an easy path for subsequent dislocation glide, as argued in several works [80, 81, 82, 83, 84]. It should be noted that the prior designation of a domain for the SB in our model does not necessarily signify the band formation. There are cases in which no localization occurs in the SB available domain, despite the softening constitutive response applied to it. Instead, formation of a SB is distinguished by the amount of slip it localizes compared to its parent crystal. We predict the applied strain needed for localization, how intense slip in the band domain grows, and what implications slip banding has on the local stress and strain fields in a heterogeneously deforming crystal.

First, we validate our model by comparing the profile of accumulated slip along the

SB predicted by the model with those measured experimentally in nickel-based Inconel 718 precipitation strengthened alloy at 0.61% macroscopic plastic strain. Figure 5.3a shows an EBSD graph from a region of interest within the microstructure that include a number of grains containing intense SBs. The map of strain along the loading direction at 0.61% applied plastic strain shown in Figure 5.3b evidences the localization of plastic deformation within intense SBs, particularly in grains G1, G2, and G3. The strain along the loading direction accommodated within these bands grow to levels as high as 4X of the applied far-field strain. The amplitude of slip localized on the SB system for these SBs are shown in Figure 5.3c. This slip map reveals that not only do the SBs, even those contained in a single grain, localize different amplitudes of slip, but also the slip amplitude can vary along a single SB. Figure 5.3d shows the microstructure created to replicate the region of interest shown in Figure 5.3a. Orientation of each grain in the microstructure is assigned according to the EBSD data. This grain structure is surrounded by a homogeneous layer with random orientation that is intended to render the bulk response from the rest of the polycrystal and make the micromechanical fields spatially resolved in region of interest insensitive to the applied periodic boundary conditions. A SB available domain is designated within grain G2 in a way that matches with the EBSD graph. The microstructure is then subjected to 0.61% plastic strain and the intensification of slip within the discrete SB available domain is examined. Figure 5.3e shows the model prediction for the profile of slip amplitude along the SB length, starting from the G2/G3 grain boundary, and how it compares with that measured experimentally. Overall, an acceptable agreement is evident between the numerical and experimental results. The deviation at the left end of the profile, which corresponds to regions within grain G2 near the G2/G3 grain boundary, is conjectured to ensue from local grain boundary events, such as slip transmission from grain G2 to G3, which is observed experimentally but not implemented in the model. Regardless, the agreement between the profiles indicates the

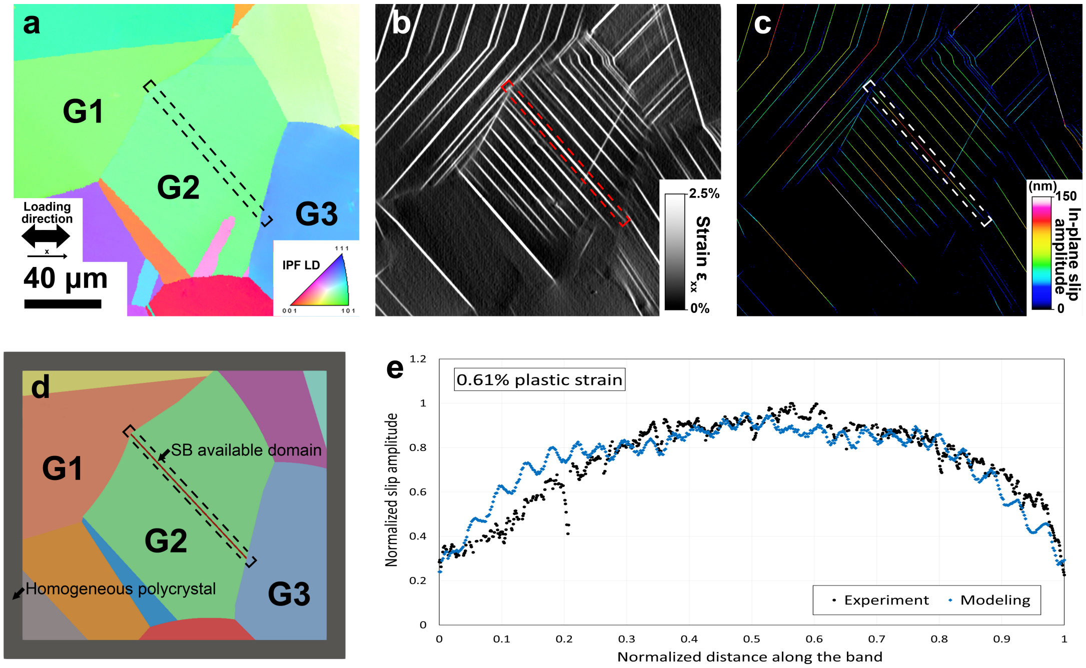

Figure 5.3: Experimental and numerical results of slip localization for a nickel-based superalloy deformed at 0.61% plastic deformation. (a) Grain structure obtained form electron backscatter diffraction for a region of interest. (b) Associated strain map along the loading direction after 0.61% applied plastic deformation. Concentrated strain bands are evidence of slip events. (c) Quantitative measurement of the in-plane displacement induced by slip events: in-plane slip amplitude. (d) Microstructure setup created to model deformation in the region of interest shown in part (a). The SB available domain is indicated by a narrow red region designated in grain G2. (e) Comparison of the normalized slip amplitude obtained form experimental and numerical results after 0.61% applied plastic deformation.

applicability of our model to slip localization within SBs.

Next, we apply the explicit SB model to a wide range of FCC and HCP materials studied experimentally to examine the role of material strength on slip localization. To do that, we begin by identifying material parameters for each alloy through the direct comparison between the macroscopic response obtained by the model and that characterized experimentally. The dashed lines in Figure 5.4 show the measured stress-strain curves for different materials up to 2.5% far-field engineering strain, indicating that most of the materials experience strain hardening. To obtain the bulk hardening response,

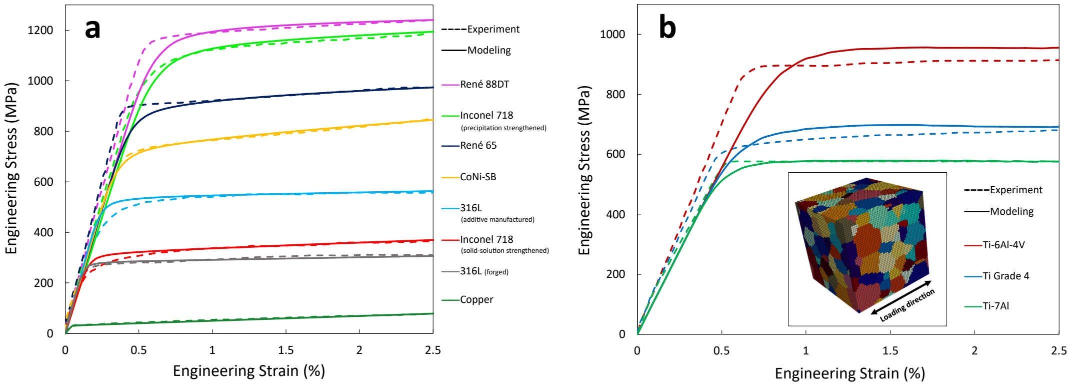

Figure 5.4: Experimental and numerical stress-strain curves for alloys deformed up to 2.5% engineering strain. (a) Stress-strain curves for FCC materials show that most of the materials experience strain hardening. Curve-fitting is performed to identify material parameters, including the CRSS value and hardening parameters. (b) Stress-strain curves for three HCP materials. The CRSS values for different slip modes in these metals are obtained from the literature. Inset shows the representative polycrystal used for modeling the macroscopic response of these materials.

a ploycrystal model, shown as an inset in Figure 5.4b, is subjected to 2.5% uniaxial strain for each material and macroscopic stress-strain curves are fitted to the experimental curves. Fitted material parameters, such as CRSS value and hardening parameters, are then determined. Due to activation of several slip modes in HCPs, the CRSS values for different slip modes in the three HCP metals studied here are obtained from the literature.

With the material parameters identified, we apply the explicit SB model to an idealized microstructure to study how the material strength govern slip localization. This idealized setup is purposely designed to isolate the SB micromechanical fields and is not a limitation of our explicit SB model. Figure 5.5a shows the bicrystal setup, surrounded by a homogeneous polycrystalline layer. A SB available domain is designated within the parent grain, impinging on the grain boundary with its neighbor. As shown by the crystal frames in Figure 5.5a, the orientation of the parent grain is assigned such that the slip direction and slip plane normal for the SB system align with vectors $\boldsymbol{b}$ and $\boldsymbol{n}$,

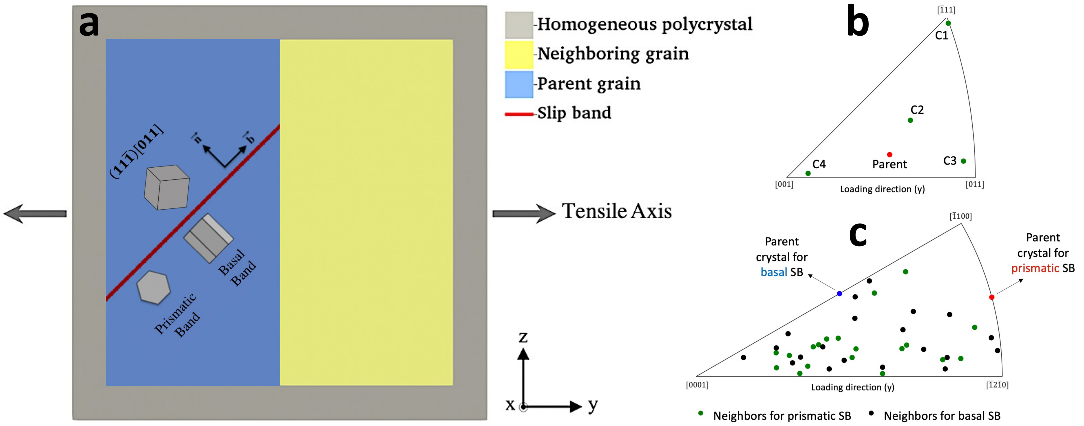

Figure 5.5: (a) Schematic of the bicrystal unit cell surrounded by a homogeneous polycrystalline layer, undergoing uniaxial tension. A 2-voxel-thick SB available domain is designated in the parent crystal for the slip band to develop. Hexagonal frames show the orientation of the parent crystal for a slip band on prismatic and basal planes in an HCP material. Likewise, the cube shows how parent crystal is oriented for a slip band to develop on its primary slip plane. Vectors ***b*** and ***n*** are respectively along the shear direction and slip plane normal of the system on which localization may occur. (b) Four orientations assigned to the neighboring grain in FCC simulations. (c) 20 orientations assigned to the neighboring grain in HCP simulations with a prismatic and a basal SB.

respectively. Experimental observations in HCP metals reveal that prismatic and basal SBs generally form within the applied levels of strain. Accordingly, both prismatic and basal SBs are modeled for HCP alloys. As concluded in Chapter 3, the orientation of grain neighbors can significantly influence slip localization within the SB in the grain. Furthermore, as mentioned earlier, our experimental results present the slip amplitude and SB spacing in an average sense over a microstructure region that contains many grains. To nullify the effect of grain neighbor orientation and follow the experiments, several simulations are performed for each material and SB type, each of which with a distinct grain neighbor orientation, and the results are averaged over all simulations. Figure 5.5b,c show the orientation of grain neighbors for modeling FCCs and HCPs, respectively. For all materials and band types, the bicrystal model is subjected to 2.5% plastic strain along the $y-$direction.

5.6 Interpretation of the link between macroscale strength and microscale localization

We begin the results by presenting the micromechanical fields within the SB in a weak FCC metal, copper, and how it compares with them in a strong material, Inconel 718 precipitation strengthened. For these two materials, Figure 5.6 shows the map of strain along the loading direction when 1.0% macroscopic plastic strain is applied. To isolate the role of material strength on localization, grain neighbor orientation is the same in both cases. Consistent with the experimental observations, comparison of these strain fields verifies that the stronger material localizes more slip within its SBs. In other words, Figure 5.6 suggests that copper manifests a weak slip banding phenomenon where slip tends to accumulate rather uniformly across the grain, instead of being accumulated in localized SBs. Deformation accommodation in Inconel 718 precipitation strengthened, on the other hand, is mainly realized by instances of strong, localized SBs. The extent of slip localization within SBs as predicted by the explicit SB model for all investigated FCC and HCP metals are presented in Figure 5.1 for macroscopic plastic strains of 0.2% and 1.0%. In both strain levels, modeling results reveal a positive correlation between the slip amplitude and materials yield strength, following the trend observed experimentally. Again, this relationship is not limited to a particular crystal structure and slip localization and its relationship with the macroscopic yield strength can be explained by a single characteristic line for both FCC and HCP alloys.

To uncover why a stronger material localize more slip, we investigate slip localization in these alloys from an energy point of view. Considering the general formula $U = \int_t \int_V \sigma_{ij}(\boldsymbol{x},t)\dot{\epsilon}_{ij}(\boldsymbol{x},t)\, dV\, dt$ for the strain energy, we calculate the amount of energy required for deforming the parent grain via slip accumulation on its primary slip system at

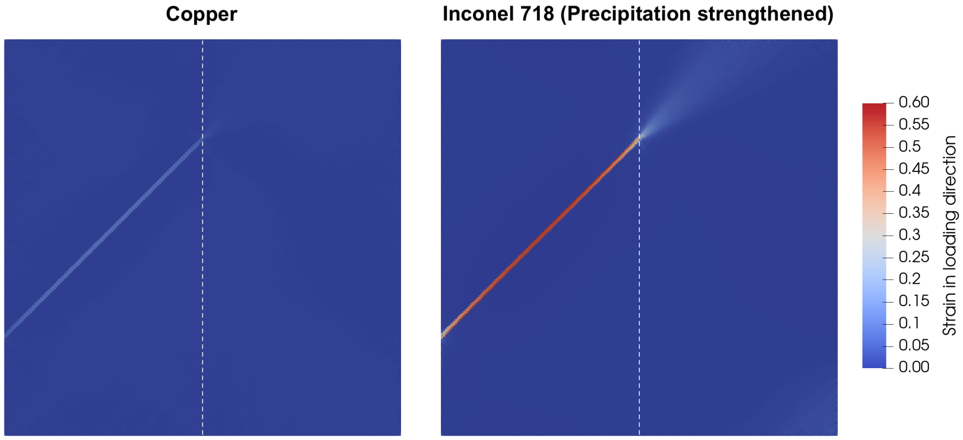

Figure 5.6: Distribution of strain along the loading direction for copper and Inconel 718 precipitation strengthened at 1.0% macroscopic plastic strain, both with the same neighboring grain orientation. Higher intensity of slip localization within the SB in Inconel 718 confirms the positive correlation between the material strength and amplitude of slip localization as revealed by the experiments.

different macroscopic strain levels by calculating $U^* = \int_0^T \int_{V_{parent}} \tau_{SB}(\boldsymbol{x}, t)\dot{\gamma}_{SB}(\boldsymbol{x}, t)\, dV\, dt$. In this equation, τ_{SB} and $\dot{\gamma}_{SB}$ are respectively the resolved shear stress (RSS) and the rate of slip accumulated on the SB system at any point $\boldsymbol{x}$ within the parent grain at time t. The integration involves all voxels in the parent grain including both the SB available domain and the parent matrix. We consider two cases of homogeneous deformation, in which no discrete SB is modeled in the parent grain, and localized deformation, in which slip is allowed to localize within the SB available domain if the material chooses to. In the case of homogeneous deformation, both τ_{SB} and $\dot{\gamma}_{SB}$ are expected to be fairly uniform within the parent grain. In case of localized deformation, however, with slip accumulating within the SB domain, the slip resistance in this domain is allowed to decrease according to the softening law in (2.6). On the other hand, the parent matrix is subjected to strain hardening as it accommodates slip. Considering the disparity in the amount of slip accumulated in these two domains, their energy levels can be quite different. Nevertheless, they add up to the amount of energy required for deforming the grain heterogeneously. Figure 5.7a shows the energy required to deform the parent grain, either homogeneously or heterogeneously, in the weak copper and strong Inconel 718 precipitation strengthened, as well as the intermediate stainless steel 316L additive manufactured. The divergence of curves after some incipient slip at around 0.2% plastic strain indicates that, for all three materials, a lower amount of energy is needed to deform the grain via localized slip, compared to that via a homogeneous state of slip. This is consistent with the experimental observation of localized SBs in all alloys investigated in this work. However, what distinguishes a weak material, such as copper, from a stronger material, like Inconel 718, is the disparity between the levels of energy for homogeneous and heterogeneous deformations. In copper, slip localization within SBs is barely energetically favorable over accumulating it uniformly across the entire grain volume, hence the weak slip banding observed in this material. With the material yield strength increasing, however, the energy gap widens such that localizing slip within a small domain becomes more energetically favorable over accumulating it uniformly within a larger volume. Intense, localized SBs observed in Inconel 718 can then be explained by the large difference between the energy levels that signifies a strong preference, from an energy point of view, for localizing slip. In Figure 5.7b, we extend the energy analysis to all investigated alloys and average the results over all grain neighbor orientations. Respectively for 0.2% and 1.0% macroscopic plastic strains, the hollow and solid data-points show the relationship between the energy required for the homogeneous deformation of the grain and that for the heterogeneous deformation which involves slip localization within the SB. Figure 5.7b reveals that at both strain levels —more pronounced at the larger strain of 1.0%— the deviation of the energy relationship from the line of equality intensifies in favor of the heterogeneous deformation, as the material yield strength increases. Therefore, it is concluded that, regardless of the crystal structure, a material with a higher yield strength tends to form localized SBs with intense slip amplitudes since it is much more energet-

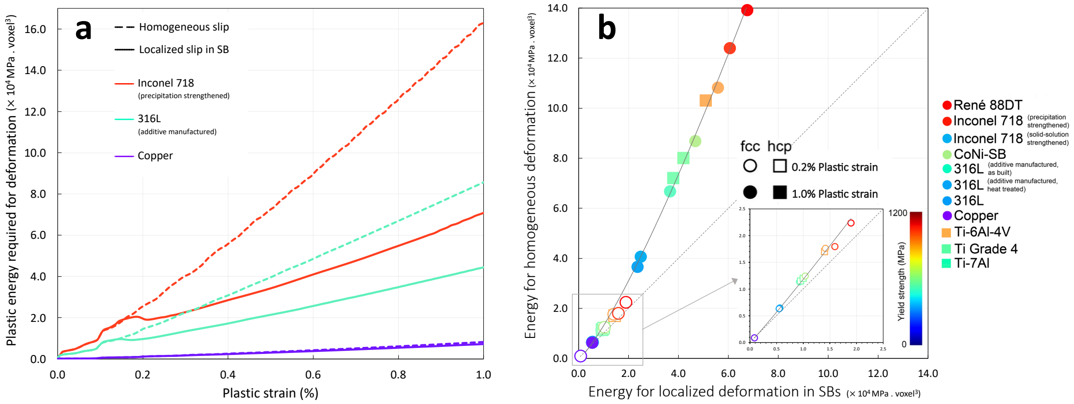

Figure 5.7: (a) Energy required for deforming the grain homogeneously and heterogeneously via localized SBs at different macroscopic loading up to 1.0% plastic strain, for three different FCC metals with low (copper), moderate (stainless steel 316L), and high (Inconel 718) yield strength. (b) Relationship between energy required for homogeneous and heterogeneous deformation of the grain at 0.2% and 1.0% plastic strains for all investigated alloys. The disparity between two energy quantities intensifies as the material becomes macroscopically stronger.

ically favorable, compared to a situation where it deforms via uniform slip across the entirety of the grain.

Next, we address the observation that macroscopically stronger materials manifest wider SB spacings. Although the idealized microstructure presented in Figure 5.5a contains only a single SB in its parent grain, prediction of SB spacing is still viable through investigation of the stress field around the developing discrete SB. Concurrent with slip localization within the SB, areas in the vicinity of the band within the parent grain develop a heterogeneous stress field. This heterogeneity involves a reduction in stress levels in the affected areas, lowering the driving force required for slip on the SB system. We refer to this heterogeneous stress state around the band as the *reaction-stress*, implying that it resists further slip accumulation around the band. Figure 5.8 shows the distribution of the resolved shear stress (RSS) on the SB system for three FCC metals; copper, stainless steel 316L additive manufactured, and Inconel 718 precipitation strengthened. To isolate the role of strength, grain neighbor orientation is the same in all three cases

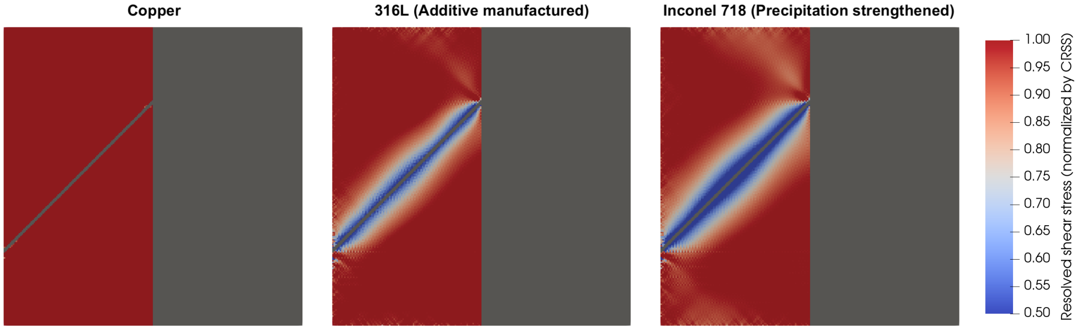

Figure 5.8: Distribution of the resolved shear stress (RSS) on the SB system for copper, 316L additive manufactured, and Inconel 718 precipitation strengthened at 1.0% macroscopic plastic strain, all with the same neighboring grain orientation. The fields in the neighboring grain and SB domain are colored gray as the emphasis is on the reaction-stress developed around the band in the parent grain. RSS values are normalized by the initial CRSS in each material.

and the RSS values are normalized by the initial CRSS value for each material. Starting with copper, the RSS map shows a homogeneous distribution for the stress within the parent grain, indicating that the entire parent grain is highly stressed for slip accumulation and no reaction-stress is developed in this case. In the case of stainless steel 316L, however, the RSS map shows high stresses everywhere in the parent grain, except for the areas near the band in which the stress is significantly decreased to levels lower than the slip resistance on the SB system, i.e., the CRSS. Finally, in Inconel 718, both the intensity and the extent of the reaction-stress increase, leaving more areas in the parent grain affected by a stress reduction.

The reaction-stress developed around a localizing SB hinders further slip accumulation in these areas. To understand the extent of such resistance against slip, Figure 5.9 shows the map of slip rate on the SB system at 1.0% plastic strain for four FCC metals with different yield strength, all with the same grain neighbor orientation. Consistent with the reaction-stress distribution in Figure 5.8, the rate of slip is reduced around the SB, with the reduction being more significant in a stronger material. We now define the *no activity zone* as the area around the SB in which rate of slip is lower than 5% of that in

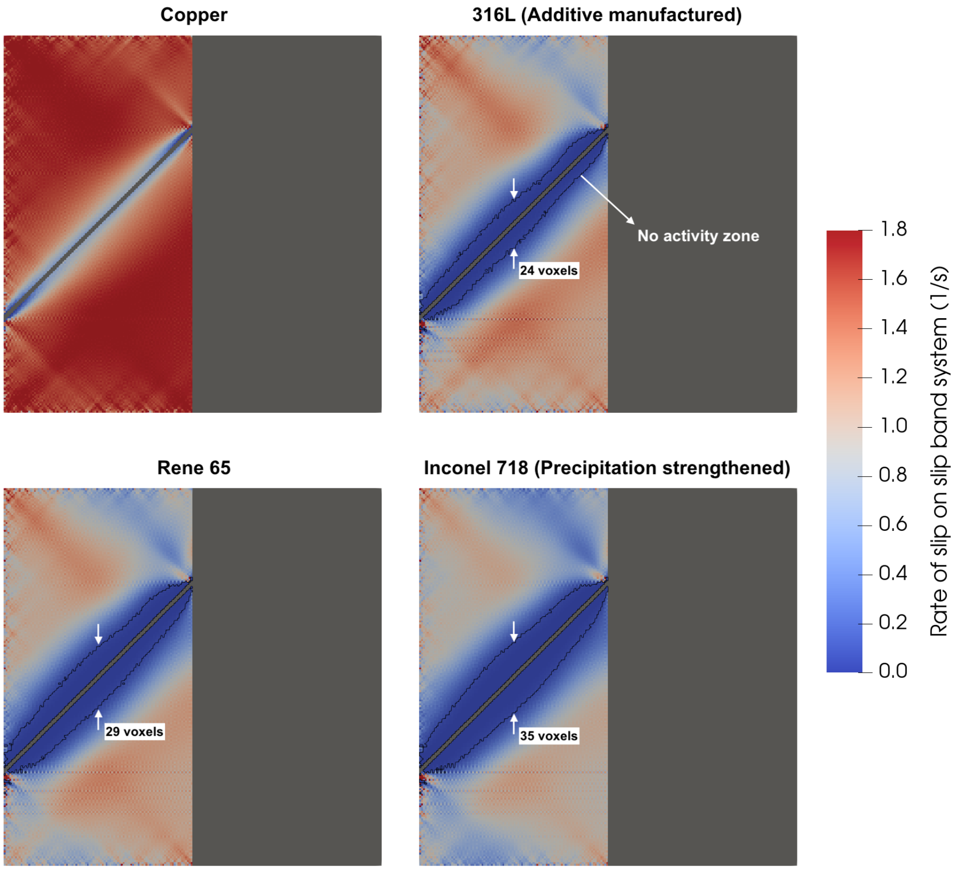

Figure 5.9: Rate of slip on the SB system for copper, stainless steel 316L additive manufactured, René 65, and Inconel 718 precipitation strengthened at 1.0% macroscopic plastic strain, all with the same neighboring grain orientation. The fields in the neighboring grain and SB domain are colored gray to put the emphasis on the slip rate around the band in the parent matrix. In copper, a no activity zone does not develop as no areas around the band have slip rates lower than 5% of that far from the band in the parent matrix. In the maps for the remaining three materials, the black outlines show the boundaries of the no activity zone.

areas within the parent grain far from the SB, unaffected by the reaction-stress. The no activity zone can be seen as a domain near an active SB within which the SB prohibits any slip to accumulate. The outlines in Figure 5.9 show the boundaries of the no activity zone for stainless steel 316L, René 65, and Inconel 718. Although there is a noticeable reduction in the slip rate around the SB in copper, a no activity zone has not developed in this material since the amount of reduction does not meet the criterion set for outlining the no activity zone. To quantify its size in the remaining three materials, the width of the no activity zone around the midpoint of the SB is reported. Accordingly, the size of this zone, when normalized by the SB thickness, increases from 12 in stainless steel 316L to 18 in Inconel 718. Viewing the no activity zone as a domain within which a fully developed SB prevents a new SB from forming, we associate the size of this zone with the SB spacing observed experimentally. That being presumed, Figure 5.9 predicts a larger SB spacing in Inconel 718 than that in stainless steel 316L. Finally, we extend the analysis of the no activity zone to all investigated alloys and average over all neighboring grain orientations. Figure 5.2 shows the numerical results for the SB spacing at 0.2% and 1.0% macroscopic plastic strains, obtained from the size of the no activity zone, and how they compare with the experimentally measured SB spacing in each alloy. At both strain levels and regardless of the crystal structure, the explicit SB model predicts a positive correlation between the SB spacing and material yield strength. This indeed is consistent with the observation that a stronger material tends to localize slip within SBs that are widely spaced across the grain.

5.7 Summary and conclusions

In conclusion, by performing *in-situ* mechanical testing coupled with HR-DIC measurements on a wide range of FCC and HCP materials, we characterize localized SBs in each material and identify SB features including slip amplitude and SB spacing. Our experiments reveal a universal link between the macroscale strength of materials and their microscale strain localization within the SBs. In particular, we show that uniformly across FCC and HCP crystal structures, a material with a higher yield strength has a stronger tendency to accumulate slip in localized, intense SBs that have larger spacing between them. To find out the underlying reasons for such observations, we then employ a micromechanical explicit SB model to simulate slip localization within a discrete SB and its implications on the stress and strain fields. In this model, the SB available domain is allowed to experience strain softening according to the rate-dependent constitutive law in (2.6), while the rest of the parent grain and the grain neighbor are subjected to regular strain hardening as they accumulate slip. Our numerical results find that, uniformly across all materials, the amount of energy required for deforming a grain heterogeneously via localized SBs is lower than that required for the homogeneous deformation of the grain via uniformly distributed slip. This explains why all materials investigated in this work manifested frequent instances of SB as they deformed. Furthermore, we show that the deviation between the levels of energy intensifies as the material becomes stronger, establishing an energetic basis for why a stronger material prefers to accumulate more slip within the SBs than a weaker material does. Our modeling results further reveal that a localizing SB produces a reaction-stress around it which resists further slip in nearby areas. The reaction-stress reduces the slip activity around the band, leaving an area in the close proximity of the band slip-free, which we referred to as the no activity zone. We then associate the size of the no activity zone with the SB spacing, as both indicate a domain in which a new SB is not favored to form. Finally, we demonstrate that the larger SB spacings observed in stronger materials are ensued from the stronger reaction-stress developed around the band, hence the larger size of the no activity zone.

Chapter 6

Role of microstructure on development of microvolumes

6.1 Introduction

Strong alloys, such as Ni-based superalloys, tend to fail by the formation of microcracks, which are localized rare events [198, 199, 200, 201, 202, 23, 203, 204]. Studies have shown that these cracks are preceded by the formation of exceptionally intense slip bands that concentrate on the slip plane of a grain [201, 23, 205, 206, 9, 204, 207]. Identifying the defining characteristics of grains that form such slip localizations have recently received much attention [134, 51]. With the advent of advanced in-situ straining and highly resolved ex-situ techniques, studies on high-performance alloys have revealed that the more fatal slip localizations are tied to intragranular orientation zones that develop ahead of the slip localization. These zones are commonly known as *microvolumes (MVs)*, tend to have a tear-drop shape, and bear crystallographic orientations that are different from the rest of the grain [8, 95, 23, 12, 35, 9]. Compared to other crystalline defects that reorient parts of the grains, such as twins, the orientation gradients in microvolumes are low, appear arbitrary in direction, and short in extent, not yet seen to span the entire grain. Microvolumes form infrequently and have been challenging to detect as well as characterize as a distinct defect. Thanks to recent advances in high-resolution diffraction and microscopy techniques, several experimental works have reported observations of MVs in deformed polycrystalline materials [43, 171, 208, 23, 8, 12, 9, 209].

Due to their connection to microcrack formation, experimental studies have focused on defining the microstructural features that lead to MV formation. Using *in-situ* scanning electron microscopy (SEM) and electron backscattered diffraction (EBSD) analysis, [8] found that MVs in a nickel-based superalloy nucleate at GBs shared by two grains that have a slip activity contrast, with an intense slip band being active in the grain with easier slip and the MV forming within the grain less favorably oriented for slip. It was later reported by [23] that, for the same superalloy, the contrast in Schmid factor across the GB is not a suitable criterion for predicting the formation of MVs when slip transmission across the GB is difficult, nor is the angle between the surface slip traces (tilt angle) for most favorable slip systems on either side of the GB. Instead, the formation of MVs was reported to be related to the angle between the projection on the GB plane of slip plane on either side of the boundary (twist angle), with MVs only appearing for twist angles larger than 55°, irrespective of the tilt angle. Later, [12] analyzed over a few hundred MVs formed in the same material and concluded that MVs are just as likely to form for low twist angles as they are for high twist angles. It was further shown while slip transmission follows geometric criteria to some extent, formation of MVs are not directly related to either the tilt angle, the angle between slip directions, or the angle between slip plane normals.

Using high-resolution digital image correlation (HR-DIC) combined with the Heaviside-DIC method, [208] characterized MVs in Inconel-718 (IN718), observing small-scale intense rotations, up to 4°, from the impingement of SB on GBs where direct slip transmission did not occur. The notion that slip transmission and MV formation are mutually exclusive phenomena is not consistently supported by experiments. For instance, [12] found that while most MVs can be considered elastic in that no slip activity is observed within them, some MVs contain either a single SB in continuity of the incoming SB or several short slip traces not connected to the incoming SB. In a more recent study, [9] strategically combined *in-situ* electron and X-ray characterization techniques to identify MVs in IN718 superalloy and the correlation between MV formation within a grain and the grain orientation distribution. It was found that most MV-containing grains manifest an orientation distribution that is highly skewed with a larger density of grain volume being represented in the tail of the distribution, compared to the grains without a MV. However, their results reflect that some grains also manifest an orientation distribution with high skewness with a dense tail, without a MV being characterized in them.

While these experimental observations have provided a much insight into MVs in polycrystals, a modeling analysis can complement understanding on the origin of MVs by isolating the influence of material parameters, such as orientation, microstructure, and deformation mechanisms. However, there are only a few computational works that have investigated MVs. Many modeling studies focusing on the interaction of SBs and GBs are commonly built around the dislocation pile up model and are not capable of representing the highly localized slip within the SBs. Another reason is that standard full-field numerical methods with intragranular resolution, such as crystal plasticity finite element (CPFE) and fast Fourier transform (CP-FFT), do not model the discrete nature of SBs and the high strain heterogeneity they introduce [210]. Capturing slip localization within discrete SBs has proven important to modeling local phenomena, such as MVs. In a recent study, [35] developed a spatially resolved CPFE framework to explicitly model intense SBs, and MVs associated with them. It was concluded that MVs are more likely to form when the shear induced ahead of an intense SB is dissipated through activation of multiple slip systems at the GB. Furthermore, non-transmissible boundaries were shown not to be directly correlated with the formation of MVs. The calculations in their study, however, were focused on a 2D microstructure comprising only four grains, and only a few neighboring grain orientations were investigated. More importantly, the SB strain was set *a priori*, as in shear-enhanced models, and was not developed based on the applied loading and grain neighborhood.

While the results to date are valuable, many questions concerning MVs still remain. First, the fundamental factors contributing to the formation of MVs need to be identified. Assuming MVs are local phenomena tied with SBs, the scarcity of MVs despite the ubiquity of SBs has not been explained. How a MV modifies the orientation distribution of the host grain, and if those changes can only be a consequence of MVs are also of interest since they would help identify a measurable signature for detecting MVs experimentally. Furthermore, the influence of localization intensity within the SB inside the neighboring grain as well as the orientation relationships between the SB grain and MV grain have yet to be researched. Finally, the variability among experimental studies and their reports in terms of a potential correlation between the formation of MVs and existing geometric factors call for further investigation.

The chapter aims to address these questions by applying the explicit slip band fast Fourier transforms (SB-FFT) technique on 3D microstructures. SB-FFT is used to evaluate the local mechanical fields developed within a polycrystalline nickel-based superalloy IN718. The computational framework is unique in that it allows for a discrete SB to localize slip constitutionally, based on the grain properties, far-field loading, and neighborhood, in contrast to prior studies in which a fixed amount of shear was imposed within the SB domain. This feature enables study of the influence of the neighbor orientations on SB intensity and its subsequent effect on the potential formation of a MV at the SB/GB junction. Modeling a 3D microstructure, furthermore, provides the opportunity to study a more realistic system with more grains and to obtain intragranular orientation distributions for comparison with experiments. We evaluate the local stress, strain, and orientation fields within and ahead of the SB to capture the formation of a MV and identify its contributing factors. Our results first verify that the localization of slip, to a certain level, within the SB in one grain can cause a MV with intensities detectable by characterization techniques at the SB/GB junction. We further demonstrate that the SB localization is not a sufficient factor as the MV grain orientation also influences whether or not a MV would form, contributing to its scarcity. Additionally, we show that MVs are equally likely to form within grains with orientations that accommodate the shear induced by the incoming SB through activation of a single or multiple slip systems at the grain boundary. In the case where a MV forms, we show that it changes the orientation distribution of the MV grain such that the new distribution is skewed with a tail, when displayed in Rodrigues space. We also reveal that a skewed orientation distribution may not be appropriately established as a signature of MV in the grain, as it can ensue from other local phenomena such as development of a large orientation deviation zone near the GB plane that has no interaction with a SB. Finally, our results find that the geometric, stress-based, or residual Burgers vector parameters proposed in the literature for the GB slip transmission are not applicable to explain the formation of MVs.

6.2 Constitutive modeling and model set-up

The evolution of SBs and MVs in polycrystalline IN718 under deformation are simulated using the SB-FFT model described in Chapter 2. The model is applied to the polycrystal aggregate shown in Figure 6.1f. This model is generated with DREAM.3D [211] and comprises 40 grains. The polycrystal is discretized into 100 × 100 × 100 ($x \times y \times z$) voxels and a narrow SB-available domain is preselected in the "SB grain".

The polycrystal setup is then strained along the x-axis, up to a macroscopic total strain of 5%. To replicate uniaxial loading, the normal stress components along the y- and z-axis are enforced to be zero. The orientation of the SB grain is set to those seen experimentally in [9], Bunge Euler angles of either (257.0°, 41.2°, 125.7°) or (348.1°, 39.0°, 17.0°) with (x = tensile axis, y = transverse, z = sample normal), depending on the microstructure model. The orientation of the MV grain is varied to study the role of grain orientation on the formation of MVs. GB sliding is not allowed in the model as we enforce continuity in the displacement field along GBs throughout the polycrystal.

The softening and hardening parameters, along with the single crystal elastic constants at room temperature [190] used in this work are listed in Table 6.1. The softening and hardening material parameters are characterized and rationalized in Chapter 5 for IN718. The few hardening parameters, such as $\tau_c^{s,0}$, are fitted from matching the simulated response with the experimental stress-strain data obtained. To allow for a reasonable amount of softening, material softening in the SB-available domain is limited to 90% of the initial CRSS, i.e., $\min_t \tau_{\mathrm{c}}^{\mathrm{s,t}}(\mathbf{x}) = 0.1\tau_{\mathrm{c}}^{\mathrm{s,0}}(\mathbf{x})$.

Table 6.1: Softening coefficient, elastic constants, critical resolved shear stress (CRSS), and hardening parameters for IN718.

	Elastic constants (GPa) [190]			**CRSS for slip modes ($\tau_c^{s,0}$, MPa)**	**Hardening parameters**		
D_0	C_{11}	C_{12}	C_{44}	$\{1\bar{1}1\} < 110 >$	τ_1^s	θ_0^s	θ_1^s
70	259.6	179.0	109.6	495	0	800	600

6.3 Localization of slip within slip bands

Taken from recent studies of [9] and [43], Figure 6.1e presents an orientation map of IN718 material deformed in tension with a few MVs, differing in size, appearing to emanate into the same grain (Grain A) from a GB between Grain A and Grains B and C. The MVs possess different orientations compared to the parent grain and cause strong orientation gradients. Closer analysis with the Heaviside-DIC method in Figure 6.1a reveals that these two MVs are connected to junctions where slip localization on the $\{111\}$ plane in the neighboring grain (Grain C) impinge on the shared GB. The map of the orientation difference between a material point and the grain average, the *grain reference orientation deviation (GROD)* map, in Figure 6.1c,d exposes the extent and intensity of these two MVs. For both, the GROD intensity is highest at the junction and reduces moving farther into the grain interior.

Figure 6.1f,g shows the 3D model microstructure representation of the grain neighborhood of interest (MV-1), with orientations provided by the SEM-EBSD data. We use a 3D structure, as opposed to a 2D columnar one, to include more grain neighbors and better capture the local material behavior. Figures 6.1g,h show the location of Grains A and C within the polycrystal, and the narrow domain preselected within Grain C based on H-DIC observations, for the development of the SB. As in the experiment, the polycrystal is subjected to uniaxial strain along the x-axis with increments of 0.01% per time step.

First, we focus on the model Grain C, the orientation that was seen experimentally to contain the intense SB. Figure 6.2 shows the calculated evolution of the ϵ_{xx} strain field in Grains A and C as the far-field strain increases. The graph in Figure 6.2 tracks the strain accommodated within the SB and matrix of Grain C. The strain in the SB evolves faster than that accommodated by the matrix. The amplitude of SB strain is 4%

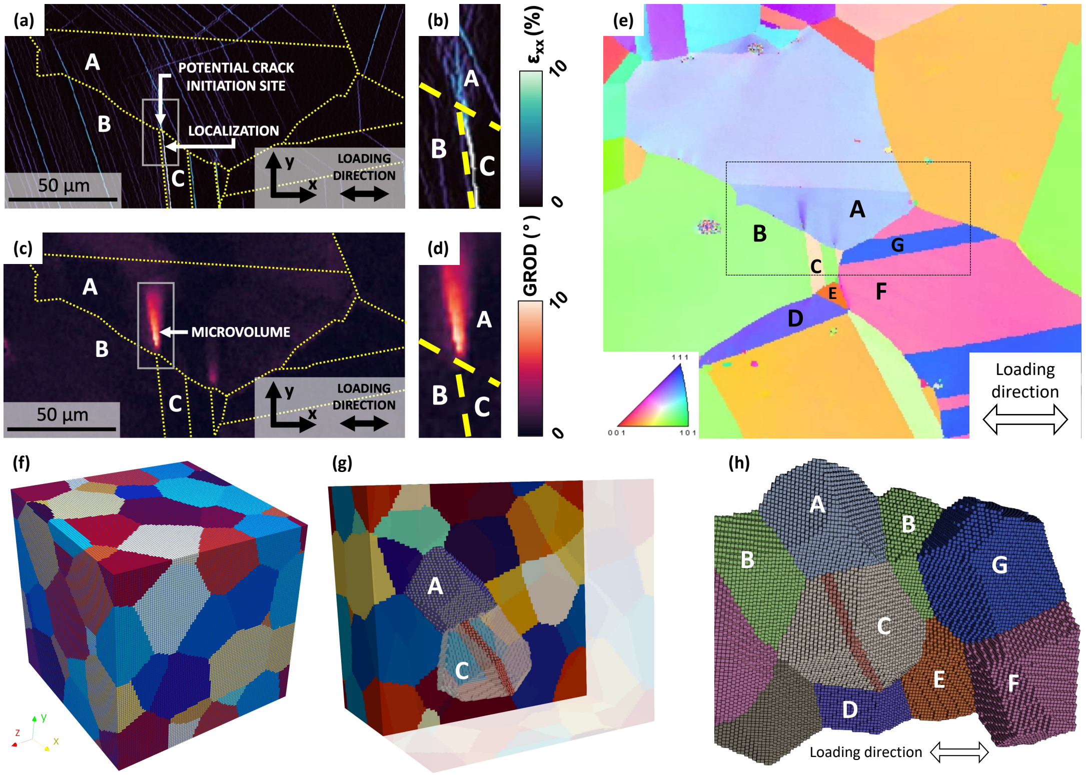

Figure 6.1: (a) Surface strain field of IN718 deformed in tension to a macroscopic plastic strain of 1.26%, captured by high-resolution Heaviside-DIC (H-DIC) technique. An intense slip localization (SB) is evident in Grain C. Grain boundaries (GBs) are outlined in yellow. (b) A field of view (FOV) indicated by a grey box in (a) shows the intensity of slip localized within the SB in Grain C, as well as the intersection of SB with the GB of Grain A. (c) Distribution of the grain reference orientation deviation (GROD), obtained from the 2D-EBSD orientation field of the same neighborhood, reveals the formation of a MV at the SB/GB junction. (d) FOV indicated by a grey box in (c) shows the intensity of GROD ahead of the SB in Grain A. (e) 2D-EBSD image of an extended neighborhood shows Grain A through Grain F, and the orientation data used in modeling. (f) Polycrystalline model (MV-1) to simulate the development of a SB in Grain C and MV in Grain A. The microstructure consists of 40 grains and is discretized into 100 × 100 × 100 ($x \times y \times z$) voxels. (g) The microstructure is cropped along the z-axis to show the location of Grains A and C within the polycrystal. (h) The SB domain is depicted as a red narrow volume in Grain C. The orientation information for the labeled neighboring grains are obtained from the EBSD analysis, and random orientations are used for the remaining grains in the microstructure. Sub-figures (a) through (d) are reproduced with permission from [9].

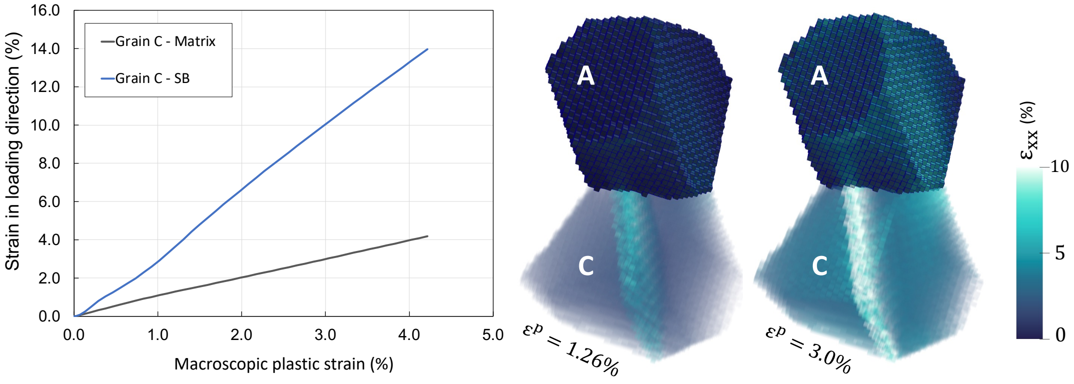

Figure 6.2: Evolution of the SB strain in Grain C as the far-field strain applied to the polycrystal increases. The two strain maps on the right show the distribution of strain along the loading direction at two macroscopic plastic strain levels of 1.26% and 3.0%. The SB strain field at $\epsilon^p = 3.0\%$ agrees with the field measured by DIC shown in Figure 6.1b. Cloud contours are used for Grain C to present the field in the interior of the grain as well.

at 1.26% macroscopic plastic strain. Increasing the macroscopic plastic strain to 3.0% produces a higher amplitude of strain within the model SB that is similar to the amount of strain measured in the SB in grain C in Figure 6.1b. The difference in applied strain can be expected due to differences in the topology of the grains that lie between the far field where the strain is applied and the SB and MV grains. Although this applied strain is higher than that used experimentally, it is preferable to identify the applied strain with local slip accumulated within the SB than with the actual far-field applied strain. Hereinafter for all other microstructures simulated, the maximum macroscopic plastic strain applied to the polycrystal is 3.0%.

6.4 Association of slip bands and microvolumes

Next, we study the orientation distribution in Grain A, the orientation in which the MV is seen to form experimentally. Figure 6.3 shows the calculated GROD distribution for Grain A at different applied strain levels. The GROD is selected here to represent the spatial variation in crystallographic orientation within an individual grain. Alongside the GROD map, we show the distribution of normal strain in loading direction, ϵ_{xx}, in the neighboring Grain C with the developing SB. At an applied strain of 1.2%, the SB in Grain C has already accumulated 3X more strain than the grain average but still only an embryonic, potentially experimentally undetectable, MV has formed in Grain A. At a higher strain level of 2.0%, the strain in the SB has intensified and the MV has grown in size and intensity. At the same time, a planar region of high GROD forms parallel to the GB facet with the neighboring grain (not shown for visualization). Such plumes from triple junction lines have been reported in prior experimental work [212, 213], and presumed to develop due to the incompatible interaction among the adjoining grains [214]. At 3.0%, the SB has localized even more and the MV extended. The plume has intensified as well and spanned the GB plane. To confirm that the MV forms as a result of the SB, Figure 6.3d shows the hybrid GROD/strain maps for the same pair of grains at the same strain level, in the case where a SB is not permitted to develop in Grain C. A MV does not form but the plume prevailing in the GB plane does. Thus, Grain A is predicted to form a MV at the SB/GB junction site. Not only is a SB required to form the MV, but the SB needs to accumulate a threshold amount of strain in order for the MV to emerge (nearly 4X in this case). In the followings, we address the orientation distribution and slip accumulation within the developed MV.

To examine the evolution of orientations in Grain A and isolate the contributions of the MV, we replot the calculated "grain texture" of Grain A using a metric called *discrete single grain orientation distribution (DSGOD)* [215, 216], which is a 3D representation of the weighted distribution of all orientations in the grain. Figure 6.4 shows the DSGOD of Grain A plotted in Rodrigues space at the onset of MV formation ($\epsilon^p = 1.2\%$), as well as a higher macroscopic strain of $\epsilon^p = 3.0\%$. The DSGOD for the SB-free case, which did not produce a MV, is also shown for comparison. Further, we identify by color the

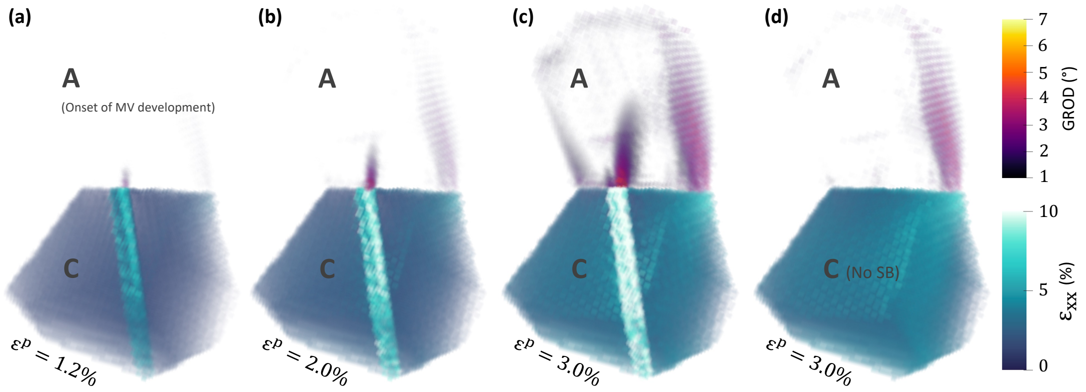

Figure 6.3: (a) Early stage of MV formation at the SB/GB junction after the intensity of the SB reaches a certain level (3X more strain than the grain average in this case). (b, c) Intensity and size of the MV in Grain A grows larger as the SB in Grain C accumulates more strain. (d) A SB-free model predicts homogeneous deformation in Grain C and no MV in Grain A, even after 3.0% macroscopic plastic strain. The plume, the zone with a high GROD near the GB of Grain A to its right, develops near a triple junction as the grain undergoes deformation, with or without the SB. In all sub-figures, the distribution of GROD and strain in the loading direction x are presented for Grain A and Grain C, respectively. The range for GROD maps starts at 1° to provide a better visualization by filtering out the bulk of Grain A with GROD $< 1^\circ$.

parts of the DSGOD that correspond to the SB tip zone at the SB/GB junction (red), the area near the GB of Grain A with its neighbor to its right (blue), and the remaining bulk of Grain A (yellow). Comparing Figure 6.4a and c indicates how the MV, even in its embryonic stage, changes the DSGOD such that the new distribution involves a tail that asymmetrically extends the bulk of the orientation cloud. Figure 6.4d further exhibits how the intensified MV extends the tail further away from the bulk of the cloud, while simultaneously increasing the density of the tail. This is consistent with the recent experimental observations of [9] in IN718 superalloy. The DSGOD of Grain A at the macroscopic plastic strain of $\epsilon^p = 3.0\%$ and for a SB-free model in Figure 6.4b suggests that while no MV forms at the GB/SB junction in this case, the orientation distribution is still relatively skewed, when compared with the distribution in part (a). This is in fact an indication of the orientation deviation zone that developed within the GB mantle near the GB with which the incoming SB would have no interaction.

Next, we analyze another grain neighborhood within the polycrystal where a MV was detected experimentally, shown in Figure 6.5c. We refer to this case as MV-2 hereinafter. Figures 6.5a and b respectively show the GROD and strain in loading direction maps for a neighborhood that contains an intense SB in Grain F and a MV formed at the SB/GB junction in Grain E. A large 3D polycrystal was built, like the one for MV-1. Figure 6.5d presents only the portion of the microstructure model created that contains Grain E and F and a few of their immediate neighbors. The several other grains surrounding the grain aggregate shown to make up the entire polycrystal are not displayed.

The model predicts formation of a sizable MV in Grain E and SB development in Grain F. The calculations indicate that when the applied plastic strain is approximately 1.1%, a MV starts to form at the GB/SB junction. Figure 6.5f presents the calculated strain field and GROD maps at 3.0%. At this point, the SB has evolved to accumulate 4.8X more strain than the matrix. Unlike the MV-1 case, no plume forms in the grain at any triple junction. For comparison, the calculation is repeated without a SB domain in Grain F and the analogous maps are shown in Figure 6.5e. Without a SB in Grain F, Grain E undergoes homogeneous deformation and no MV forms. Finally, we analyze the DSGODs of grain E resulting from the SB-free and discrete SB case. As shown in Figures 6.5g and h, the material within the MV has reoriented to different orientations than the rest of the grain, as indicated by the asymmetry and skewness of the distribution with the SB. Formation of the extreme tail in the DSGOD is a sign of MV formation.

Overall, the results obtained for MV-2 further confirm the conclusions made earlier for MV-1. MVs form at the SB/GB junction and require a SB in the neighboring grain to be sufficiently intense. The SB and MV evolve in tandem and MVs are indeed signs of extreme slip localization. Analysis of the grain texture indicates that the MV orientations are distinct from those of the grain average.

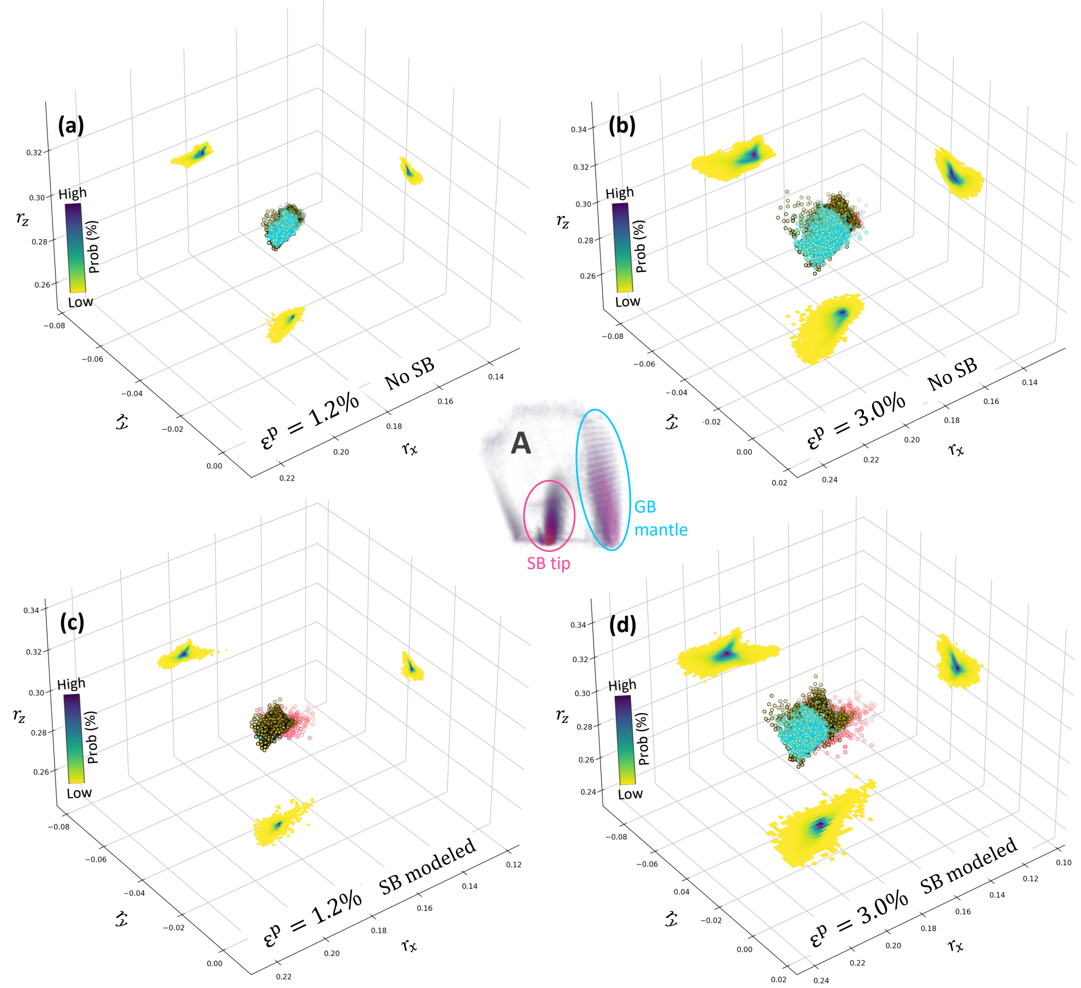

Figure 6.4: Discrete single grain orientation distribution (DSGOD) of Grain A at the onset of MV formation (c), and a later stage of deformation where a macroscopic plastic strain of 3.0% is applied (d). To show the effect of MV on DSGOD, the orientation distributions of Grain A obtained at similar strain levels from the SB-free model are presented in (a) and (b). Red data-points show the orientations at the SB tip zone and blue data-points correspond to the GB mantle far from the SB/GB junction. All DSGODs are plotted in Rodrigues space.

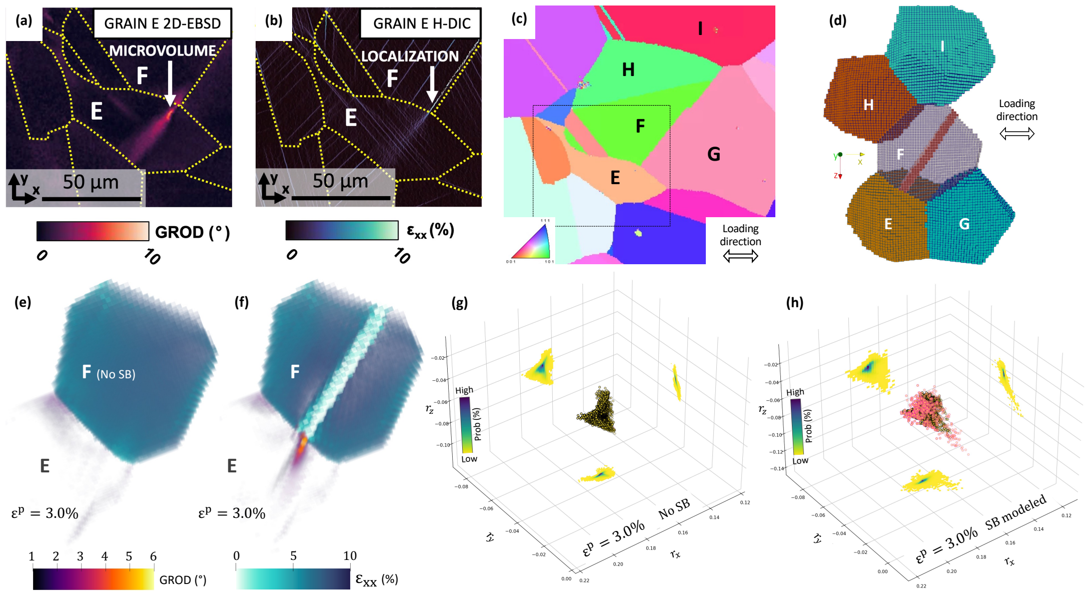

Figure 6.5: (a) Distribution of the GROD obtained from a 2D-EBSD analysis of a neighborhood containing an intense SB in Grain F tied with a MV in Grain E. (b) Surface strain field at a macroscopic plastic strain of 1.26%, captured by HR heaviside-DIC technique. (c) 2D-EBSD image of the extended neighborhood shows Grain E through Grain I, orientation data used to build the model microstructure. (d) The SB domain is depicted as a red narrow volume in Grain F. The orientation information for the these grains are obtained from the EBSD analysis, and random orientations are used for the surrounding grains in the microstructure. (e) The SB-free model predicts homogeneous deformation in Grain F and no MV in Grain E, after 3.0% macroscopic plastic strain. (f) Association of the intense SB in Grain F and the MV in Grain E at the GB/SB junction. In parts (e, f), the distribution of GROD and strain in loading direction are presented for Grain E and Grain F, respectively. The range for GROD maps starts at 1° for better visualization by filtering out the bulk of Grain E with GROD < 1°. (g) DSGOD of Grain E at a macroscopic plastic strain of 3.0% obtained from a SB-free model shows a homogeneous orientation distribution. (h) DSGOD of Grain E with SB that has developed in Grain F signifies a skewed distribution with tail. Red data-points in parts (g, h) show the orientations at the SB tip zone. Sub-figures (a, b) are reproduced with permission from [9].

6.5 Role of grain orientation

Thus far, in simulation, we have used grain orientations from grains experimentally seen to develop MVs. In agreement with experiment, the model predicts that MVs develop at the GB/SB junction. The question arises whether a MV would always form at such junctions provided the SB accumulated sufficient intensity. Indeed, in experiment, several intense SBs are observed to interact with the GBs but not cause a MV in the neighboring grain. We address this question via simulation and test the role of neighboring grain orientation, replacing the orientations of the MV grain, that is, Grain A and Grain E in MV-1 and MV-2 models, respectively. The sets of orientations for these grains are selected such that they represent an even distribution in orientation space, e.g., across stereographic triangle for a face centered cubic (FCC) material. This will ensure the inclusion of different orientations that favor different numbers of slip systems to activate in the grain under investigation. Sixteen cases are selected to replace Grain A, and since they share the same SB grain, this set is hereinafter refer to as “SB1” group. Eight orientations are selected to replace Grain E, and this set is denoted the “SB2” group.

Figure 6.6 shows the hybrid strain/GROD maps ahead of the SB at 3.0% macroscopic plastic strain for four representative orientations in group SB1. For all orientations, a SB develops in the SB grain, the localized slip within which imposes an intense shear strain on the GB. The neighboring grain dissipates the shear by deforming plastically within a zone at the SB/GB junction, consistent with the findings in other studies [35, 12]. Nevertheless, not all orientations are tied with a MV developing in this plastic zone. Orientation O1 in Fig. 6.6a, with Bunge angles (322.3°, 171.9°, 187.2°), allows for a strong MV to form at the SB/GB junction. Similar to the case shown earlier for model MV-1, a plume also develops near the other GB far from the SB tip. When the neighboring grain has the orientation O2 (Bunge angles (0°, 65°, 0°)), no MV forms at the GB/SB junction. This is in spite of the full development of the SB in the SB grain. Figure 6.6c for orientation O3 shows formation of a MV. This example especially demonstrates that not only the formation of a MV is orientation-dependent, but whether the areas near the other GB develop orientation deviations also varies from one orientation to another. Finally, orientation O4:(294.4°, 78.1°, 175.9°) manifests a unique GROD distribution in which no MV forms at the SB/GB junction. Instead, two other GBs, different than the one shared with the SB grain, develop plumes. A similar evaluation of the other orientations in groups SB1 and SB2 demonstrates that grain orientation is one grain property that directly influences whether a MV forms at the SB/GB junction, and if a MV were to form, the degree of reorientation and its size.

The influence of grain orientation is likely to originate from the dependence of deformation mechanisms on the grain orientation. In the present material, the only deformation mechanism is slip and texture development and the amount of reorientation is tied to the slip activity. We are thus led to ask which characteristics of the grain orientation control the formation of a MV, in the region ahead of an intense SB. Several studies have attempted to find an orientation-dependent metric that governs the propensity of MVs [12, 8, 23]. Yet, as pointed out in the Introduction, the correlations suggested in these works are either proven ineffective in later studies or not uniformly applicable to explain all observed MVs or justify why some MVs did not form under certain circumstances. We continued the search for an effective measure to explain MVs by trying different criteria proposed for slip transmission across the GBs. These criteria ranged from purely geometric factors to those that involve the orientation of the GB plane, those that include stress and strain measurements on different slip systems on either side of the GB, and those that are based on the calculation of the residual Burgers vector [13, 11, 217]. Nevertheless, virtually none of these criteria correlated with the intensity of the GROD

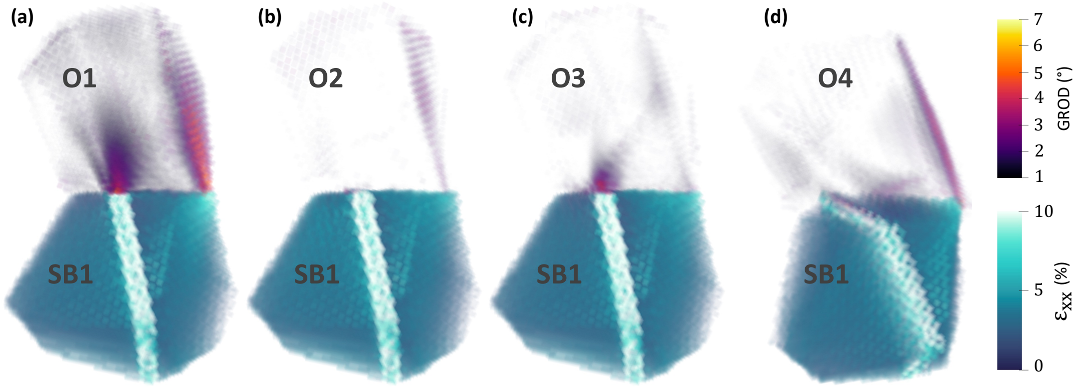

Figure 6.6: Effect of grain orientation on the formation of a MV at the SB/GB junction. Grain orientations in (a) and (c) allow for a MV to develop, while orientations in (b) and (d) do not favor MV formation, despite the full development of the SB in the SB grain. Parts (c) and (d) demonstrate the grain-orientation dependency of highly disoriented zones near other GBs far from the SB tip. The loading direction is horizontal in all parts except for part (d) in which the two grains are rotated to visualize the high GROD area on the GB plane closer to the viewer. The range for GROD maps starts at 1° for better visualization by filtering out the bulk of the grain with GROD $< 1^\circ$.

ahead of the SB tip at the SB/GB junction, as shown in Figure 6.7. From the geometric factors included in Figure 6.7a, $\hat{N}_{mod}$ accounts for slip system orientations, $\hat{M}$ additionally accounts for GB orientation, and $\hat{\chi}$ considers a threshold for slip system and GB angles [11]. Furthermore, η and δ are the angle between slip plane normal vectors, and between slip directions, respectively [12]. In Figure 6.7b, the criteria m'_γ, S_y, and LRB consider sums of geometric factors weighted by plastic slip on different slip systems on either side of the boundary [11], and $|\vec{b_r}|$ approximates the magnitude of the residual Burgers vector [13]. Further details on transmission factors can be found in Table C.1 in Appendix C.

In a recent CPFE study, [35] suggested that MVs are associated with grain orientations that accommodate the shear ahead of the SB by activating multiple slip systems. To examine this premise, we study the individual slip systems activated within the MV grain in the case of MV-1 and MV-2 where the experiments detected a MV, as well as

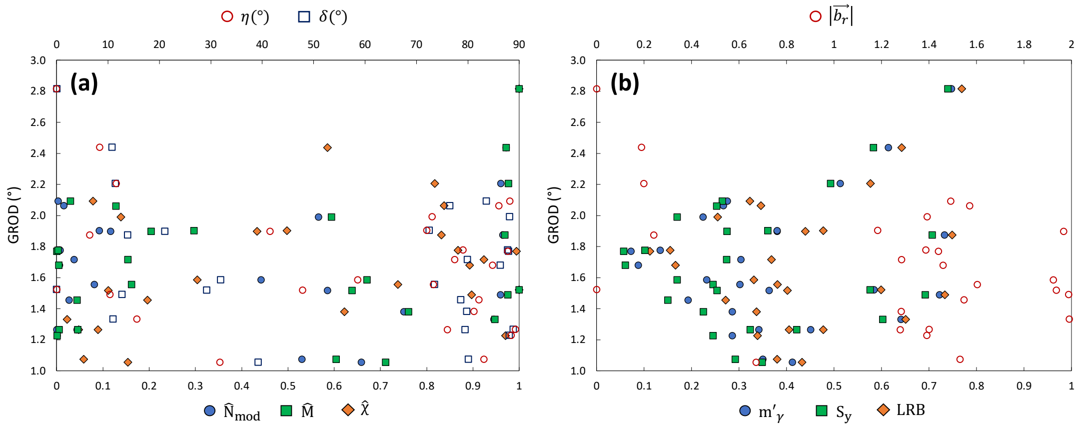

Figure 6.7: The relationship between the intensity of GROD ahead of the SB and different transmission criteria including (a) geometric factors and (b) residual Burgers vector and geometric factors weighted by plastic slip on different slip systems. No strong correlation is apparent between GROD intensity, as a signature of MV formation, and slip transmission factors. Detailed definition of these criteria can be found in [11, 12, 13].

in the case of orientation O2 shown in Figure 6.6b, where no MV formed. Figure 6.8a-c displays the distribution of slip accumulated in the MV grain for model MV-1. Simultaneous activation of three different slip systems at the SB tip confirms the said premise. Figure 6.8d considers the case of MV-2 in which a single slip system, different from the primary system in the grain, is predominantly activated at the SB/GB junction within the MV grain, concurrent with the formation of a strong MV within the same region. This may classify this MV as a plastic MV [12], within which the material undergoes plasticity. Such classification is further supported by the noticeable slip traces measured experimentally at the SB/GB interaction site, as shown in Figure 6.5b. Similarly, the slip traces indicated for systems S4 and S7 (or alternatively S8) in Figure 6.8a-c match with the short slip traces measured experimentally at the SB/GB junction, as shown in Figure 6.1b, classifying the MV formed in model MV-1 also a plastic MV. The Schmid factor for system S4 is high and this slip plane is favorably oriented with respect to the incoming SB ($m' = 0.96$). Yet, slip transfer is incomplete from the incoming SB to system S4 within the MV grain. Instead, several slip traces are seen to initiate at the GB, subsiding as they extend further from the boundary.

An example contradicting the notion that multiple slip systems are associated with a MV is presented in Figure 6.8e-g for grain orientation O2. This orientation accommodates the shear at the SB tip through activation of several slip systems at the GB. The orientation of these slip systems with respect to the incoming SB is not ideally oriented (relatively low m'), which would make it more prone for formation of a MV, under the proposed inverse relationship between slip transfer and MV formation. Yet, as indicated in Figure 6.6b, a MV does not develop in this case. These results suggest that a MV may potentially form regardless of the number of active slip systems at the SB/GB junction, and activation of multiple systems does not necessarily contribute to the formation of a MV.

What is found to be a determining factor in this phenomenon, however, is the grain average stress level compared to that for its neighborhood. For the four orientations presented in Figure 6.6 and the case of model MV-1, Figure 6.8h shows the average stress in loading direction of the MV grain as well as its neighborhood. The term neighborhood here refers to all grains that share a boundary with the MV grain. For orientations that allow a MV to form, the MV grain has a higher stress level than its neighborhood. This higher stress level is either a consequence of SB activity in the neighboring grain or exists in the SB-free model as well. On the contrary, the orientations that were not associated with a MV (O2 and O4) bear a lower stress level than their neighbors, even when an intense SB is modeled. This finding is aligned with the experimental measurements of [9] for a grain with a MV, in which it manifested a larger magnitude of stress in loading direction when compared to its neighborhood.

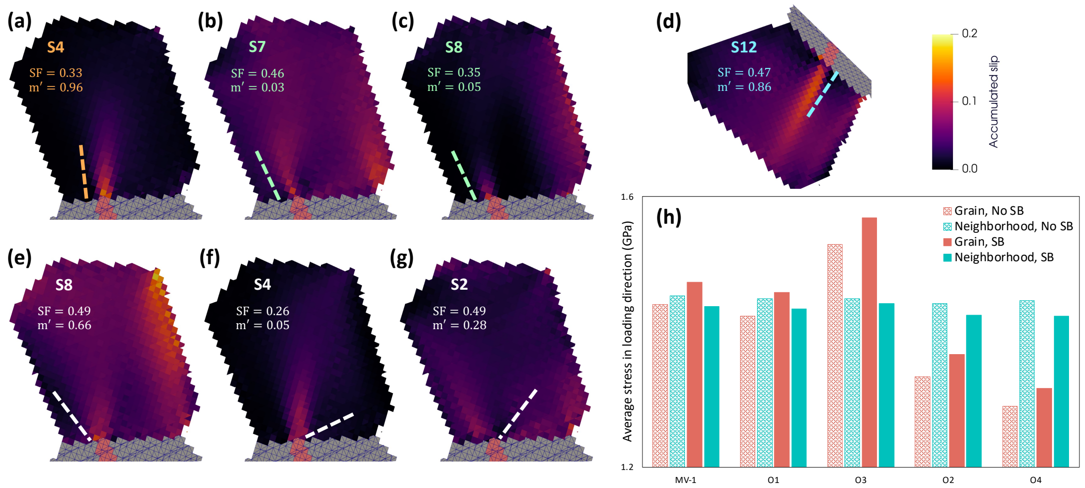

Figure 6.8: (a)-(c) Distribution of accumulated slip in the MV grain indicates the activation of three slip systems at SB/GB junction in the case of MV-1. (d) A single slip system is dominantly activated ahead of the SB in model MV-2, contradicting the speculation that MVs are associated with the activation of multiple slip systems. (e)-(g) Activation of three different slip systems in the grain with orientation O2 and no MV, contests the idea that slip accommodation via multiple slip systems lead to the formation of MVs. (h) Stress in loading direction at 3.0% macroscopic plastic strain, averaged for the MV grain and its neighboring grains, suggest that the grain needs to be sufficiently stressed before it forms a MV. Dashed and solid bars correspond to the results from the SB-free and discrete SB models, respectively. In parts (a) through (g), SF indicates the Schmid factor and m' is a geometric factor that measures the alignment of incoming and outgoing slip systems on either side of the GB to predict the propensity of a slip transfer event [14].

6.6 Discussion

Compared to other microstructural defects such as deformation twinning, MVs are rare events, with a minute chance of forming at any place and at any time in the material, but with an impactful result if they do occur. Contributing to understanding why this is, we show that a MV requires a set of conditions to be met before it forms at the SB/GB junction. First, Figure 6.3 indicates that the SB in the neighboring grain needs to localize slip to a certain extent before it can trigger a MV at its intersection with the GB, i.e., the SB must be exceptionally intense. Second, an intense SB is necessary but not sufficient. The host grain needs to have an orientation favorable for the formation of a MV. Third, we find that a higher stress level in the host grain compared to the average stress level among its nearest neighborhood is correlated with the propensity of the host grain to form a MV. Achieving all three lowers the chances MVs form in the first place. The results encourage development towards newer criteria for MV formation.

Towards that end, for all cases investigated in this work, Figure 6.9a maps all cases simulated here, with the role of the far-field loading, SB strain intensity, and grain orientation on MV formation identified. The MV is quantified by the GROD only within a region at the SB/GB junction and designated by a star symbol on the map. Each data point corresponds to a unique grain orientation in which the GROD is being calculated. First, at the lower applied strain level, no MV has yet formed. The map further exposes that an intense slip band is needed and the more intense the SB, the higher is the propensity for MV formation. Secondly, for the same SB-grain and even for similar amounts of accumulated strain within the SB, not all grain neighbor orientations form MVs. Moreover, the neighbor orientation can also influence the amount of SB strain that develops in the adjoining SB grain. This is realized by the spread in SB strains among the neighbor orientations for the same SB-grain and applied strain. Finally, the data points in Figure 6.9a are colored such that they distinguish the orientations that manifest a higher stress than their neighbors on average (red data points) from the orientations that take on lower stresses. These highly stressed grains develop intense MV, which could serve as a signature for MV formation.

Modeling and experimental studies have associated MVs with certain patterns of slip that develop ahead of the SB. Some ideas are analogous to one proposed for slip transmission. Prior modeling studies show that transmission of a SB is likely if the slip activity that develops ahead of SB is composed on single slip [51, 50]. The notion that MVs and slip transfer are mutually exclusive events would support that multi-slip patterns produce MVs. In agreement, a CPFE SB modeling study associated the likelihood for MV with multiple slip, when considering a few host orientations [35]. In contrast, an experimental study reported that MVs may be associated by dominant single slip [12]. With a crystal plasticity-based technique used here, the slip patterns associated with SBs and MVs were assessed for a wide range of orientations covering the orientation space. We find that the MV is not associated with a type of slip. Both multi-slip and single slip patterns were predicted, corroborating all prior studies. As a major finding of this work, what controls MV formation is the activation of different slip system(s) in the region at the GB/SB junction than that/those activated in the bulk of the grain.

Our modeling results reaffirm the conclusion, recently made by [9], that a MV alters the intragranular texture of the parent grain. Material in the MV reorient in different directions and amounts than those of the rest of the grain. The differing slip activity would explain the differing reorientation tendencies between the MV and the rest of the grain. Further, we study the evolution of DSGOD with straining and show that MV formation results in faster rates of reorientation than those of the grain. Consequently, a MV asymmetrically extends the intragranular orientation distribution into an skewed one with a tail that extends as the MV grows in size. We demonstrate that plumes of

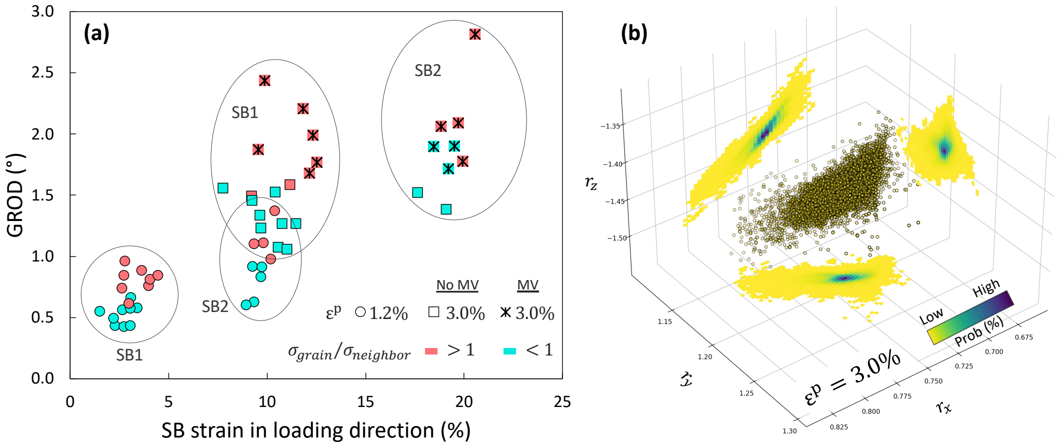

Figure 6.9: (a) A summary of the effect of macroscopic strain, slip localization, and grain orientation on propensity of MVs. A larger slip localized within the SB leads to a more intense MV at the band tip. However, this relationship is not uniformly valid as the orientation of the grain containing the MV also influences the intensity of the GROD at the SB tip. Red and blue datapoints respectively correspond to orientations with a higher and lower stress level when compared to the stress level carried by their neighbors on average. This data indicates the necessity for the host grain to be highly stressed for it to form a MV. (b) The DSGOD of the grain with orientation O4, shown in Figure 6.6d, manifests a distribution with high skewness despite the fact that a MV did not form at the SB tip in that grain.

orientation gradient can form from triple junctions and extend near the grain boundaries and these plumes may also cause the DSGOD to become skewed. As an example, Figure 6.9b shows the skewed DSGOD of the grain with orientation O4 that did not form a MV (see Figure 6.6d) even after 3.0% plastic strain and with a fully developed SB. The formation of plumes may explain the grains that manifested a high skewness-high kurtosis DSGOD but lacked a detectable MV in [9].

The relationship to MV formation and transmission of the slip localization at the GB/SB junction has been examined in several previous works, with a majority of them concluding little correlation [8, 23, 12]. Our application of many previously proposed slip transmission factors suggests that the propensities for MV and slip transmission are unrelated (Figure 6.7). This conclusion may not come as a surprise. Our study affirms that MVs are complex phenomena controlled by the coupling of several subgranular microstructural features, such as grain and neighbor orientations and local stress states. Available slip transmission criteria are based solely on the geometric parameters of two candidate slip systems. The findings here identify that differences in the stress intensity between the grain and its neighbor and local slip activity between the region ahead of the slip localization and rest of the grain are important features of MV-prone grains. Any measure of MV propensity would need to take these non-geometric features into account.

Lastly, experimental observations have revealed that the localization in SBs can become intense enough to physically shear the GB at the SB/GB junction [8, 23, 218]. Continuum dislocation pile-up models, however, cannot project the intense slip activity that is typically observed within these SBs. Furthermore, being built around the assumption that the deformation ahead of a SB in the neighboring grain is purely elastic, dislocation pile-up models are not capable of accurately predicting the interaction between slip band and grain boundary, and fail to model complex phenomena at the GB, such as MVs. The use of an explicit SB modeling technique that allows for intense slip localization within a discrete SB imparts the heterogeneous stress fields, as a result of both elastic and plastic deformations, ahead of the SB. As suggested by our results, such a technique can capture a region of high stress and orientation deviation ahead of an intense SB, and therefore model a MV.

6.7 Conclusions

In this study, we employ a crystal plasticity model, called SB-FFT, to investigate the microstructure and micromechanical features controlling microvolume (MV) formation. The model allows for incremental localization of slip within a slip band (SB), based on the far-field load and grain neighborhood. The 3D microstructure polycrystal models based on experimental ones and the applied deformation are designed to simulate potential formation of SBs and MVs at the intersection of intense SBs with grain boundaries. The model was first validated against two experimental observations in Inconel-718 and subsequently applied to probe a broader range of grain orientations. Our analysis examines the evolution of the intragranular local strain and/or orientation fields within and outside of the SB and MV. The findings of this study provide significant insights into the mechanics of microvolumes and have implications for the design and development of materials that can resist micro-crack initiation. The main conclusions of this study are as follows:

- MVs form at grain boundary/slip localization (GB/SB) junctions provided that the slip strain in the SB is sufficiently intense. SB and MV evolve in tandem, and weak slip bands do not form MVs.
- Orientation of the host grain influences the likelihood of MV formation.
- A MV is more likely to develop within a grain that bears higher stresses compared

to the average stress level of its nearest grain neighborhood.

- Requiring the right orientation, intense slip localization, and relatively high stresses can explain the scarcity of MVs despite the ubiquity of SBs in plastically deforming polycrystalline materials.
- Comparison of several available slip transmission with simulation results suggests that MV formation is not related to the propensity of the SB to transmit.
- The material in the MV has different reorientation tendencies and faster rates of reorientation than the rest of the grain with applied strain. The intragranular orientation distribution containing a MV becomes skewed.
- Slip activity in the MV can be single slip or multi-slip. The distinctive feature is that MV slip activity is different than the rest of the grain.

Chapter 7

Designing Ti-6Al-4V microstructure for strain delocalization using neural networks

7.1 Introduction

As the most common wrought titanium alloy, Ti-6Al-4V finds extensive applications in industries such as aerospace, energy, biomedical, and chemical processing [219, 220]. Like many other titanium alloys, plastic deformation in Ti-6Al-4V is mainly realized via formation of localized slip bands [33, 4, 169, 221]. Unlike pure titanium, however, the alloy does not readily twin unless subjected to very high strain levels during severe plastic deformation processes [222, 223]. At low and moderate strain levels, different slip systems including prismatic, basal, and pyramidal are commonly observed in Ti-6Al-4V [4, 169].

Although the formation of slip bands is the main underlying mechanism warranting polycrystalline materials' ductility and formability, the same phenomenon is believed to be responsible for crack initiation and propagation and, ultimately, the material failure. Ti-6Al-4V titanium alloy is not excluded from this trade-off between strength and toughness. While several theories have been proposed to explain it, a recent experiment on a wide range of polycrystalline materials with several crystal structures revealed that the trade-off has its root in microscopic strain localization within slip bands [3]. It was discovered that the reason why toughness of a material does not scale with its macroscopic strength is that stronger materials – those with a higher yield strength – show a higher tendency to localize strain within intense slip bands. This discovery is in line with our findings in Chapter 5. As presented and discussed in Chapter 3, 4, and 6, the stress/strain concentration associated with these highly-localized slip bands promote either slip transmission across the grain boundary or the development of microvolumes at the slip band/grain boundary junction, both events contributing to crack initiation which is the first step in compromising material toughness.

Over the past few decades, an extensive number of experimental studies have characterized slip bands in Ti-6Al-4V titanium alloy [4, 169, 221, 224]. Most relevant to our work, *in situ* high-resolution scanning electron microscope, digital image correlation (HR SEM-DIC) was employed to investigate the relationship between strain localization and the microstructure of a rolled Ti-6Al-4V plate [4]. It was found that not only did slip bands form before the macroscopic yield point, but they serially transmitted from one grain to another within micro-textured zones, creating a long-range plastic strain localization phenomenon. Such a chain of intense localized slip bands has been correlated with a high frequency of crack initiation events in low cycle fatigue of the alloy [225, 24]. A separate *in situ* SEM investigation of slip transfer in Ti-6Al-4V also confirmed that slip transfer occurs well below the conventional 0.2% yield stress, and further revealed that the likelihood of slip transmission in the alloy significantly increases if there is a good alignment between the incoming and outgoing slip systems, and a high resolved shear stress on the outgoing slip system [169]. The first condition emphasizes the role of grain orientation or texture, while the second manifests the critical role of the grain neighborhood on slip localization and transmission in Ti-6Al-4V. In conclusion, experimental studies confirm that the development and connectivity of slip bands in titanium alloys, including Ti-6Al-4V, adversely affect their mechanical properties [4, 168, 53]. Motivated by these studies, a key question is what combination of microstructural features promote slip localization in Ti-6Al-4V and, perhaps more importantly, what ideal set of features would give rise to a delocalized accommodation of the applied strain in this alloy?

Aside from experimental works, a few computational studies investigated the development of slip bands in Ti-6Al-4V, presenting an acceptable agreement between simulation and experimental results [33, 51]. However, they were limited to a single microstructure and did not explore the effect of microstructure on slip localization in the alloy. Given that there are many parameters involved, such as material parameters, microstructural features, loading conditions, etc., the space of contributing factors to material properties is extremely high dimensional that pure computational exploration would not be practical. In light of this, data-driven and machine learning approaches have recently been used to predict polycrystalline materials properties based on their microstructure characteristics [226, 227, 228, 229, 230, 231, 232, 233, 234]. Most relevant to our work, a heterogeneous grain graph attention model (HGGAT) capable of realizing high-order feature embedding of the microstructure was employed to mine the relationship between the structure and elongation in magnesium alloys [230]. Using a graph neural network (GNN) model trained on simulation results from crystal elasticity finite element method (CEFEM), grain-scale elastic response of polycrystalline Ti-7Al titanium alloy was predicted [231]. Retaining fundamental features of grains including their crystallographic orientation, size, and neighborhood, a similar GNN model was used in a separate study to predict overall stiffness and strength of $\alpha-$Ti microstructures with varying textures [233].

Finally, random forest based machine learning models were used to predict stress hot-spot formation in 2D hexagonal close-packed (HCP) microstructures [234]. It was found that both the crystallography, i.e., texture, and geometry based features are required to predict stress hot-spots.

While these machine learning models have demonstrated promising accuracy levels in predicting mechanical properties, they mainly focus on the overall material properties, such as average stress, and overlook the local plastic deformation events that play a critical role in material's response and its failure. In case of slip bands, the shortcoming has been due partly to the lack of a robust computational tool that can model these localized events in 3D microstructure settings. Furthermore, most relevant machine learning studies to date are limited to predicting material properties from its microstructure, leaving the microstructure optimization for superior properties unaddressed.

In this chapter, we aim to identify the microstructural features that would minimize strain localization in Ti-6Al-4V titanium alloy. Figure 7.1 shows the workflow for the data-driven microstructure design approach used in this chapter. We combine explicit slip band micromechanical simulations on 3D polycrystals with neural network (NN) models to design an optimal Ti-6Al-4V microstructure featuring strain delocalization. We first generate a dataset of 3D polycrystals with different microstructural characteristics and perform crystal plasticity simulations to calculate the mechanical response of each polycrystal, from a localization perspective. We then formulate a set of localization-based properties to optimize, aligning with our goal of delocalizing strain. Subsequently, we design and tune separate NN models to predict these properties for a microstructure, given its characteristics such as texture, grain size and shape. With the high accuracy of these models established, we employ them to generate additional data to enhance our initial dataset of 3D microstructures. Finally, utilizing the expanded dataset, we perform a grid search optimization to identify optimal microstructures, each contributing to the

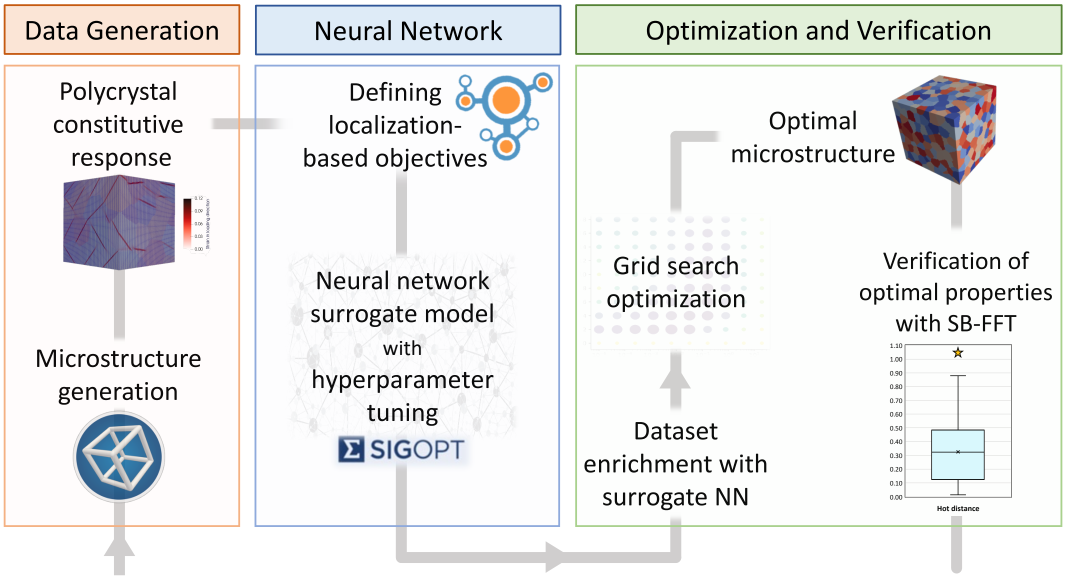

Figure 7.1: Flowchart for design of a microstructure with limited slip localization and transmission likelihood. The workflow consists of data generation using DREAM3D and explicit slip band micromechanical calculations, design of surrogate neural network for predicting localization-based properties, and microstructure optimization via simple grid search.

improvement of a specific localization-based property.

7.2 Data generation and model set-up

Our dataset comprises a total of 360 polycrystalline microstructures, each generated in DREAM3D [211] with a set of unique microstructural features. The first two features included are the mean (μ) and standard deviation (σ) of the grain size distribution calculated from all grains within the microstructure. To accommodate a wide range of grain sizes, we consider $\mu = [2, 2.33, 2.66, 3, 3.5]$. Furthermore, any value from $[0.001, 0.01, 0.1, 0.3]$ can be assigned to σ, introducing very small to significant variations in grain size within the microstructure. It should be noted that the parameter μ does not represent the actual grain size mean but the average value of the log-normal grain size distribution. Similarly, σ is the standard deviation of the log-normal distribution,

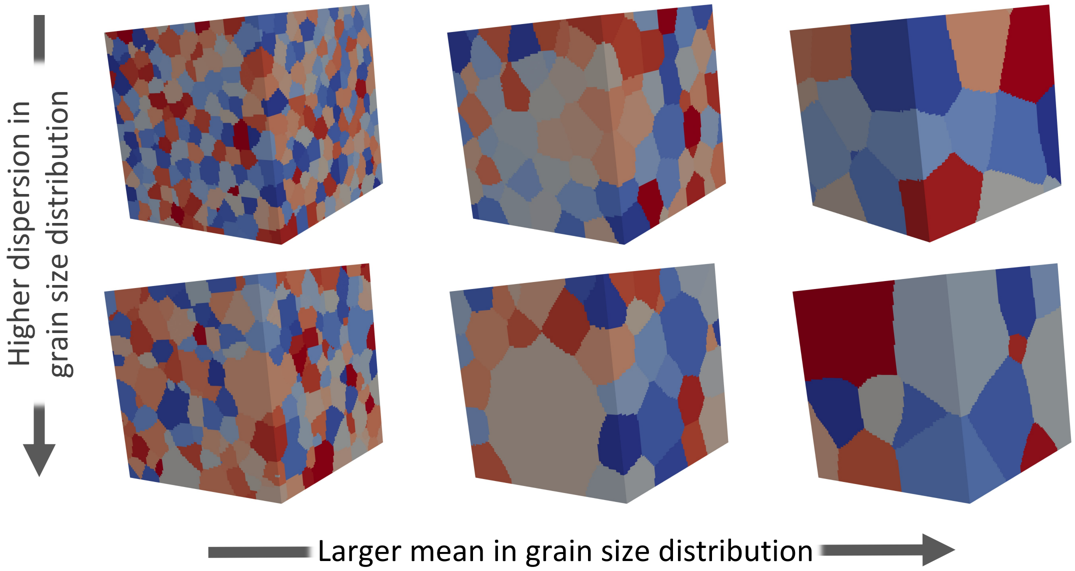

Figure 7.2: Variations in the mean and standard deviation of the grain size distribution within a few example microstructures. Columns from left to right correspond to $\mu = 2$, 2.66, and 3.5, while the top and bottom rows show polycrystals with $\sigma = 0.001$ and 0.1, respectively.

i.e.,

$$\mathrm{ESD}_{\mathrm{ave}} = \exp(\mu + \sigma^2/2) \tag{7.1}$$

where ESD_{ave} can be deemed as the actual grain size in terms of equivalent sphere diameter. The set of possible values for μ, therefore, yields grains that may have an ESD of approximately 7.4, 10.3, 14.3, 20.1, and 33.1 voxels. Figure 7.2 shows how μ and σ control to the overall size and dispersion in size of the grains within the microstructure.

Next, we include in our features the morphology of the grains by allowing either equiaxed or rolled grains comprise the microstructure. This feature is controlled by the aspect ratio (AR) of the grains, to which any value from [1, 3, 8] can be assigned. Figure 7.3 manifests example microstructures with equiaxed (AR = 1) and elongated grains ($\mathrm{AR} = 3, 8$). Although larger values of AR can be considered, they may introduce

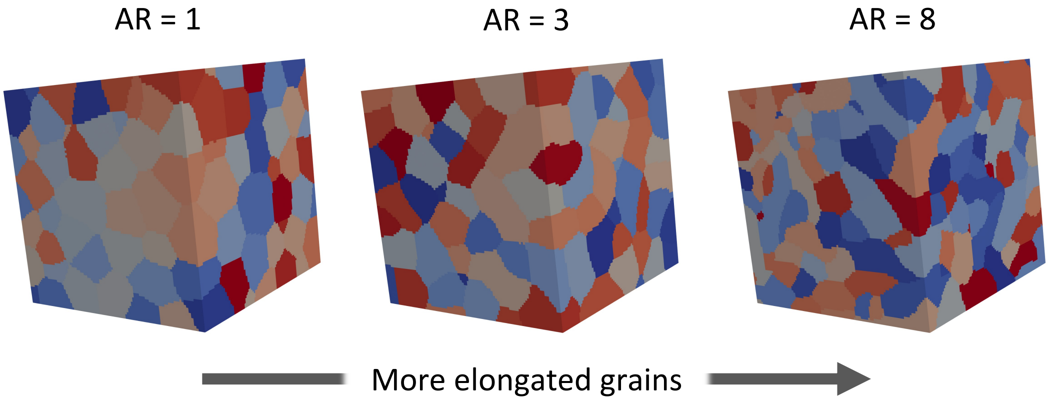

Figure 7.3: Variation in grain shape is manifested by a few example microstructures. From left to right, polycrystals are generated with a grain aspect ratio of AR = 1 (equiaxed), 3 (rolled), and 8 (severely rolled).

problems during the compilation and packing of grains in DREAM3D.

The fourth and last microstructural feature included is the texture. Figure 7.4 presents the pole figures for six unique textures from which the orientation of the grains is sampled. Among them, texture C is an experimentally rolled titanium texture [15] and texture F is a uniformly random (no) texture. The remaining textures are synthetic and inspired by the literature on titanium alloys [235, 236, 237, 238, 239].

Each 3D polycrystal generated by DREAM3D is then discretized into 100 × 100 × 100 ($x \times y \times z$) voxels, as shown in Figure 7.5a. A narrow volume serving as the slip band domain is manually added to each grain within the microstructure. The designated slip plane in each grain is located at the grain centroid, spatially oriented such that it aligns with the grain's most favorable slip system. Material parameters for Ti-6Al-4V including the elastic constants and critical resolved shear stress (CRSS) for different slip modes are listed in Table 3.1. Considering that prismatic slip has the lowest CRSS value, the slip plane in each grain lies on the prismatic plane with the highest Schmid factor, as shown in Figure 7.5b. The microstructure is surrounded by a 20-voxel-thick homogeneous layer with uniformly distributed crystal orientations in all directions to

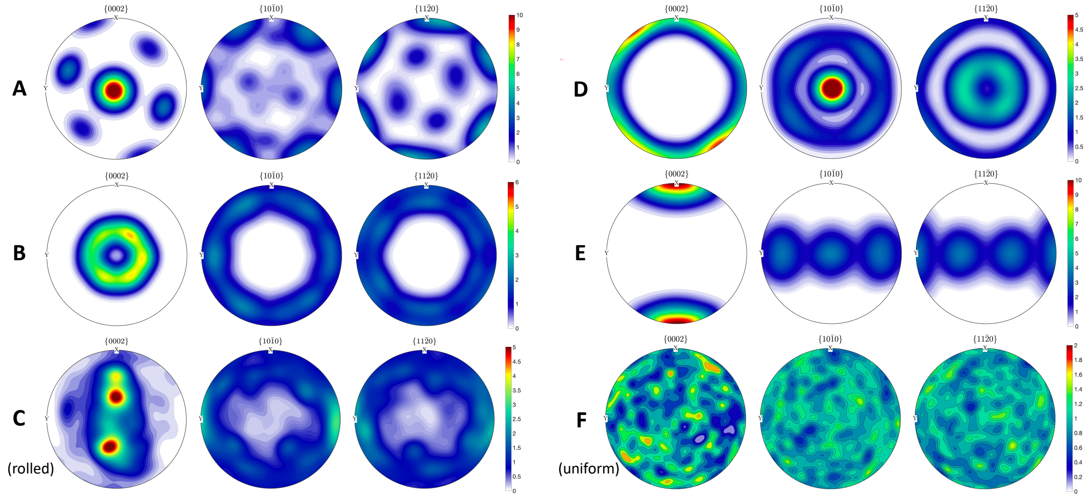

Figure 7.4: Pole figures for textures A through F used for the assignment of orientation to the grains within each microstructure. Textures C and F are experimentally rolled and uniformly random (no) textures, respectively. Intensities are plotted as multiples of random distribution (MRD).

ensure that the spatially resolved micromechanical fields are unaffected by the periodic nature of the imposed boundary conditions (Figure 7.5c). We apply the rate-dependent softening constitutive law described in (2.6) to the polycrystalline model, allowing for incremental localization of slip within slip band domains based on the far-field load and grain neighborhood. The softening coefficient D_0 is set to 64, consistent with the model calibration performed for Ti-6Al-4V alloy in Chapter 3. The polycrystal setup is strained along the y-axis, up to a macroscopic strain of 1%, while the normal stress components along the x- and z-axis are enforced to be zero.

7.3 Defining localization-based property objectives

We begin this section by presenting results of the micromechanical simulations with SB-FFT model from which we define three objectives related to the localization behavior of the material to achieve in our optimization process. Figure 7.6a shows the distribution of the normal strain along the loading direction resolved on two surfaces of an example

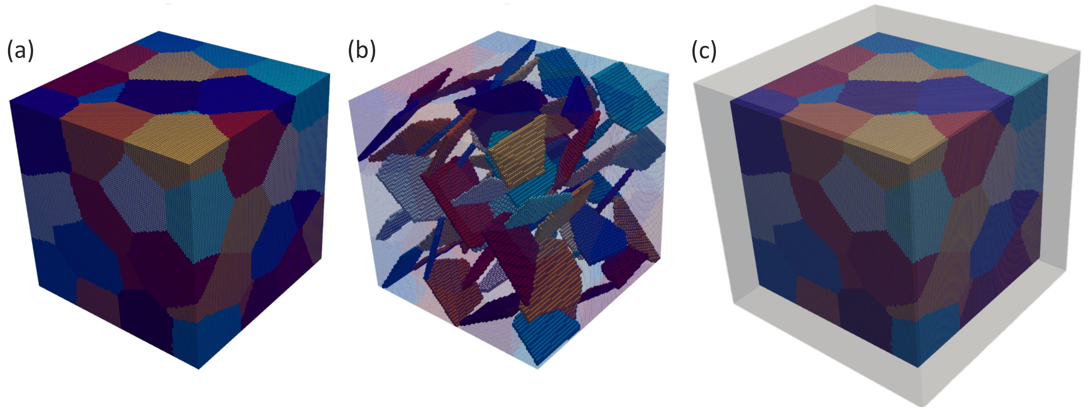

Figure 7.5: (a) An example 3D polycrystal is generated by DREAM3D and discretized into 100 × 100 × 100 ($x \times y \times z$) voxels. (b) A narrow slip band domain is added to each grain, aligned with the most favorable prismatic slip system in the grain. (c) The polycrystal is surrounded by a 20-voxel-thick buffer layer in all directions. This layer is homogeneous and comprised of uniformly distributed crystal orientations.

microstructure subjected to 1% total strain. While strain localization within slip band domains is evident throughout the sample, localization intensity varies from one grain to another and, more interestingly, some grains did not develop significant localization. Considering the 1.0% far-field strain applied to the polycrystal, the simulated range for strain in slip band domains is consistent with the experimental observations from the same alloy [4]. Furthermore, in agreement with the results presented in Chapter 3 on local stress concentration ahead of an active slip band, the strain map in Figure 7.6a demonstrates spike in strain within some grains where the slip band active in a neighboring grain impinged on the shared grain boundary. Such a stress/strain concentration can trigger a new slip/twin band in the grain, as extensively discussed in Chapter 4, contributing to the formation of a long chain of bands evidenced to eventually lead to material's failure [4].

To better understand and compare different localization responses, Figure 7.6b and c shows the histogram of the strain in loading direction across all grains from two microstructures, one sampled from texture D and the other from texture E. In these plots,

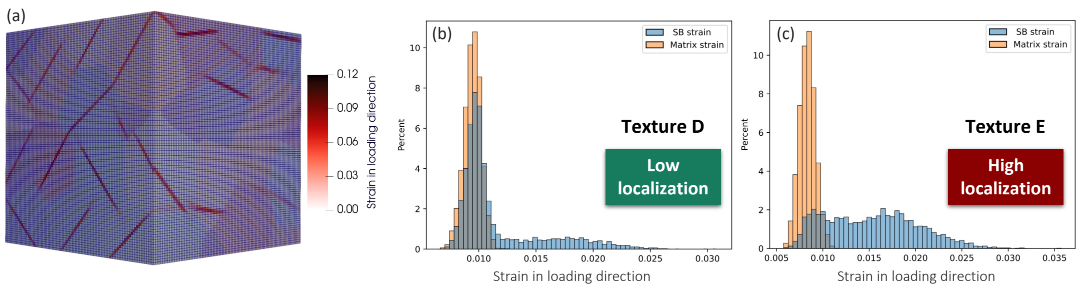

Figure 7.6: (a) Distribution of the normal strain along the loading direction for an example microstructure subjected to 1% total strain. Localization intensity varies from one grain to another throughout the microstructure. (b) Histogram of the strain in loading direction across all grains within a microstructure sampled from texture D shows a delocalized strain state. (c) A same histogram for a microstructure sampled from texture E indicates a high degree of localization of slip within slip band domains.

orange and blue bars represent the strain accommodated by the matrix and slip band domain, respectively. Figure 7.6b indicates that most grains within the polycrystal accommodate a strain level approximately equal to the 1.0% far-field strain. Furthermore, in a large fraction of grains, both the matrix and the slip band domain experience the same strain levels, manifesting this case as a microstructure with low localization or *delocalized* strain state. In stark contrast to this, Figure 7.6c presents a microstructure in which most grains accommodate less than 1.0% strain in their matrix and significantly larger strains in their slip band domains. We consider this case a polycrystal with a high degree of localization. Now, the key question is what combination of microstructural features lead to a localized strain response and, more importantly, what would be an ideal set of features that gives rise to the accommodation of the applied strain in a delocalized manner?

To address this question, we define and formulate a set of property objectives associated with the localization response of the polycrystal. Intuitively, the first quantity to consider is the *slip ratio (SR)*, which evaluates the ratio of the strain accommodated by the slip band domain to that accommodated by the parent matrix in a given grain. A case of perfectly homogeneous deformation yields $\mathrm{SR} = 1$, while $\mathrm{SR} > 1$ indicates some extents of localization. Figure 7.7a shows the cloud distribution of the strain in loading direction in two grains within the same microstructure. The top grain manifests a strong, pronounced slip localization within its band domain, hence a high SR, while the bottom grain accommodates the imposed strain homogeneously with $\mathrm{SR} \simeq 1$. Similar to the comparison made in Figure 7.6, the histograms in Figure 7.7b and c distinguish a microstructure with a delocalized strain state ($\mathrm{SR}_{\mathrm{ave}} = 1.21$) from a highly localized strain response ($\mathrm{SR}_{\mathrm{ave}} = 5.8$). Motivated by these results, we therefore define our first objective to design a microstructure with minimal slip ratio when averaged over all grains, i.e.,

$$\mathrm{minimize}_{\mathbf{f}\in\{\mu,\sigma,\mathrm{AR},\mathrm{Tex}\}}\ \mathrm{SR}_{\mathrm{ave}} = \frac{1}{\mathrm{N}}\sum_{\mathrm{N}} \frac{\varepsilon_{\mathrm{SB}}}{\varepsilon_{\mathrm{M}}}, \tag{7.2}$$

where $\mathbf{f}$ is the feature vector including grain size average (μ), its standard deviation (σ) and shape (AR), and the texture (Tex) of the microstructure encompassing N grains. Furthermore, $\varepsilon_{\mathrm{SB}}$ and ε_{M} are respectively the strain in loading direction within the slip band domain and the matrix of each grain. For simplicity, we hereinafter drop the subscript 'ave' and refer to the average slip ratio for a microstructure as 'SR'.

Next, we define as our second localization-based property the fraction of total applied strain that is accommodated within all slip band domains throughout the microstructure, and denote it by $\mathrm{E}_{\mathrm{inSB}}$. While this property was anticipated to be closely correlated with the SR defined earlier, our statistical analysis revealed that it is not entirely the case as the correlation between SR and $\mathrm{E}_{\mathrm{inSB}}$ is not monotonically increasing. For instance, within the dataset there is a microstructure with $\mathrm{SR} < 2$ and $\mathrm{E}_{\mathrm{inSB}} \simeq 0.5$ while another microstructure accommodates a significantly lower fraction of the applied strain within its slip bands ($\mathrm{E}_{\mathrm{inSB}} \simeq 0.2$) with a SR value of 4. The key distinction between these two cases is that the former tends to accumulate a larger share of the applied strain

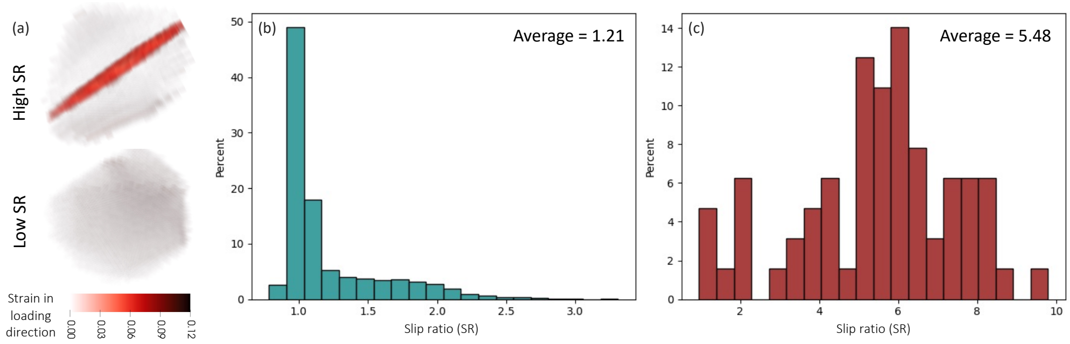

Figure 7.7: (a) Distribution of the strain in loading direction contrasts the slip ratios in two grains within the same microstructure. (b) Histogram of the slip ratio (SR) across all grains within a microstructure shows a delocalized strain state. (c) A same histogram for a different microstructure indicates a high degree of localization evidenced by a majority of the bars at SR > 1.

within its many activated slip bands such that each band is only moderately localizing. On the contrary and perhaps due to the lack of enough active slip bands, the latter microstructure accommodates the imposed deformation via its few, yet highly intense slip bands. A similar phenomenon within a different context was studied and discussed in Chapter 5. Considering that a lower $\mathrm{E}_{\mathrm{inSB}}$ would mean that a larger share of the applied strain is accommodated homogeneously within the matrix, we can define the second objective to design a microstructure that minimizes the fraction of strain in slip bands, i.e.,

$$\text{minimize}_{\mathbf{f}\in\{\mu,\sigma,\mathrm{AR},\mathrm{Tex}\}}\ \mathrm{E}_{\mathrm{inSB}} = \frac{\sum_{\mathrm{N}} \varepsilon_{\mathrm{SB}}}{\sum_{\mathrm{N}} \varepsilon_{\mathrm{M}} + \varepsilon_{\mathrm{SB}}}. \qquad (7.3)$$

Finally, we consider as our third localization-based property the spatial connectivity of the slip bands activated throughout the microstructure. As mentioned in the Introduction, serial transmission and connection of slip bands across the polycrystal has been experimentally evidenced to be the primary cause for initiation, easy coalescence, and growth of micro-cracks in Ti-6Al-4V titanium alloy [4, 24]. Therefore, an intuitive approach to delay crack formation and ultimate failure of the material is to have slip bands activated far from one another within the microstructure. This will minimize the risk of intense slip bands coalescing to form detrimental long-range plastic strain localization. A simple approach for defining a relevant property is to consider the Euclidean distance between any two slip bands in the microstructure. Nevertheless, doing so would fail to take account of grain connectivity within the microstructure. We extensively demonstrated in previous chapters that the stress concentration ahead of an active slip band can trigger a new set of bands in the grain neighbor in a transmission event across the shared grain boundary. Experimental observations from Ti-6Al-4V also emphasize the role of grain connectivity in the formation of long-range strain localization [4]. In order for a slip band to link with another, it needs to serially transmit from one grain to the nearest neighbor, naturally following the grain connectivity within the microstructure. Therefore, using Euclidean distance between two grains is clearly not ideal. To circumvent this and to account for natural progression of slip bands through the microstructure, we apply a 3D graph network to each polycrystal, using the Python package NetworkX [240]. Figure 7.8a shows a simplified version of such a graph, including only surface-visible grains in the polycrystal. Each grain is represented by a node located at the grain's centroid, and there is an edge between two nodes if the two corresponding grains are nearest neighbors. Now, a more reasonable approach to account for the spatial distance between two grains within the microstructure is to evaluate the shortest path between their corresponding nodes in the graph.

We further incorporate into our third localization-based property the intensity of the slip bands being investigated, in order to put a higher emphasis on intense localization events within the microstructure. In Figure 7.8a grains within which a more intense slip band is activated are visualized by larger nodes with darker shades of red. Each node also retains the grain's slip ratio (SR) as its attribute. When calculating the distance between the two most intense slip bands, SR_1 and SR_2 in this example, the shortest path

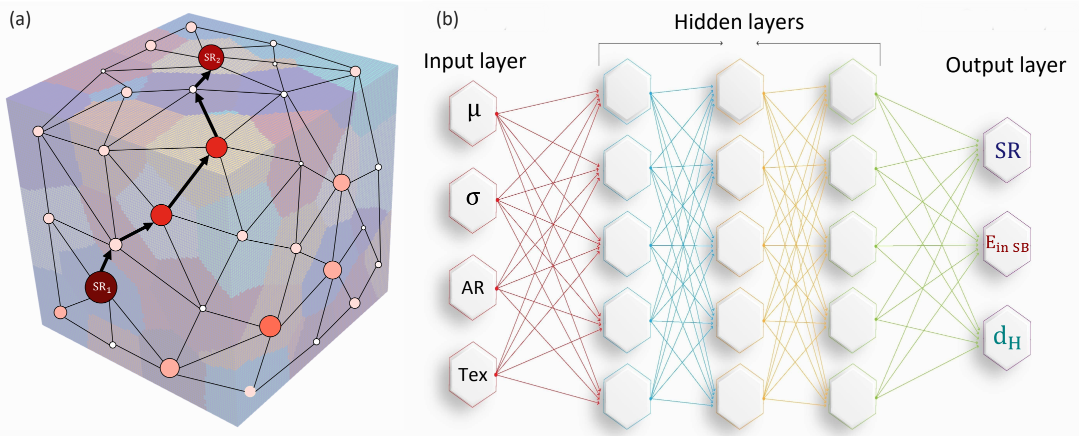

Figure 7.8: (a) A simplified version of 3D graph including only surface-visible grains in the polycrystal. Each node represents a grain, with its size and color intensity proportional to the grain's slip ratio. An edge between two nodes indicates that two grains are nearest neighbors. Considering the grain neighborhood, bold arrows show the shortest path between two grains with intense slip bands. (b) Overall architecture of the neural network model developed here, which includes an input layer, multiple fully-connected hidden layers with ReLU activation function, and an output regression layer. The output layer has only one neuron to predict any of the three properties.

indicated by bold arrows is divided by the product of slip ratio of the two grains. This approach yields a lower adjusted distance between two intense slip bands, and therefore rating them more alarming, compared to two slip bands with the same physical distance but lower intensities. Finally, the adjusted distance is normalized by the average grain size to obtain a quantity that is comparable across fine and coarse grain polycrystals. In a sense, the normalized quantity indicates the number of grains across which one slip band needs to traverse to connect to the other band. We thus define the third objective to design a microstructure that maximizes the *hot distance* (d_H), the average normalized, adjusted distance between slip bands, as in the following,

$$\text{maximize}_{\mathbf{f}\in\{\mu,\sigma,\mathrm{AR},\mathrm{Tex}\}}\ \mathrm{d_H} = \frac{1}{\mathrm{ESD_{ave}N}}\sum_{\mathrm{i,j}\in[\mathrm{N}]}\frac{\text{shortest path between grains i and j}}{\mathrm{SR_i}*\mathrm{SR_j}}. \tag{7.4}$$

7.4 Neural network model and microstructure optimization

With the four microstructural features considered as input parameters and three localization-based properties introduced in (7.2), (7.3), and (7.4) as labels, this section describes the design and optimization of three separate neural network (NN) models to predict the localization response of a polycrystal based on its microstructures.

7.4.1 NN architecture and hyper-parameter tuning

Figure 7.8b shows the overall architecture of the NN we employ to predict a polycrystal's localization response. The NN developed here is a simple multi-layer perceptron (MLP) consisting of an input layer with four neurons, multiple fully-connected hidden layers with rectified linear unit (ReLU) activation function, and a post-processing regression layer. Parameters of the model associated with fully-connected layers are trained with the Adam adaptive learning rate optimization algorithm [241], using mean-squared error (MSE) as the loss function. We assign 70% of the data for training, with the remaining 30% are kept unseen by the model for testing. From the training data, 10% is reserved for cross-validation to assess the generalization capability of the model.

In order to optimize the performance of our neural network model, we conduct hyper-parameter tuning, focusing on all parameters except the base architecture of the model. These parameters include number of layers, learning rate, number of epochs, batch size, and number of neurons in each layer. We employ SigOpt [242] and choose the MSE as our loss metric. SigOpt is an optimization tool that explores a grid of potential values for each hyper-parameter, attempting to minimize the loss via Bayesian optimization. Table 7.1 provides a summary of the parameters and their respective potential values.

Table 7.1: Hyper-parameters of the neural network optimized for predicting each localization-based property. Listed are sets of possible values for each as well as the optimal values determined via Bayesian optimization using SigOpt.

Hyper-parameter	Possible values	Optimal values		
		SR	$\mathrm{E_{inSB}}$	$\mathrm{d_H}$
Number of layers	$[2,3,4,5,6]$	5	2	6
Learning rate	$[1,5,10,50,100]*10^{-4}$	$5*10^{-3}$	$5*10^{-3}$	10^{-3}
Number of epochs	$[64,128,256,512,1024,2048]$	2048	2048	256
Batch size	$[8,16,32,64]$	64	16	32
Size of layer 1	$[8,16,32,64]$	8	16	64
Size of layer 2	$[16,32,64,128,256]$	128	256	256
Size of layer 3	$[16,32,64,128,256]$	128	-	128
Size of layer 4	$[16,32,64,128,256]$	128	-	256
Size of layer 5	$[16,32,64,128]$	16	-	32
Size of layer 6	$[8,16,32,64]$	-	-	16

For each NN, we perform a total of 300 separate experiments, each employing a unique hyper-parameter combination. Upon the completion of all experiments, we select the top candidate model to continue our analysis with the prediction of the localization response of a polycrystal. Listed in Table 7.1 are also the optimal values of hyper-parameters that produce a NN model with the lowest error for predicting each property.

7.4.2 Surrogate NN and grid search optimization

With the basics of the NN model established and its hyper-parameters optimized to produce the lowest error, we train each model on a subset of our dataset of 3D polycrystalline microstructures. To reiterate, each model receives four features as input, including the average and standard deviation of the grain size distribution, grain shape, and texture. The output for each model is one property among slip ratio (SR), strain in slip bands ($\mathrm{E_{inSB}}$), or hot distance ($\mathrm{d_H}$). Once each NN is trained, we apply it to the test portion of the dataset kept unseen by the model, to evaluate its accuracy in predicting the

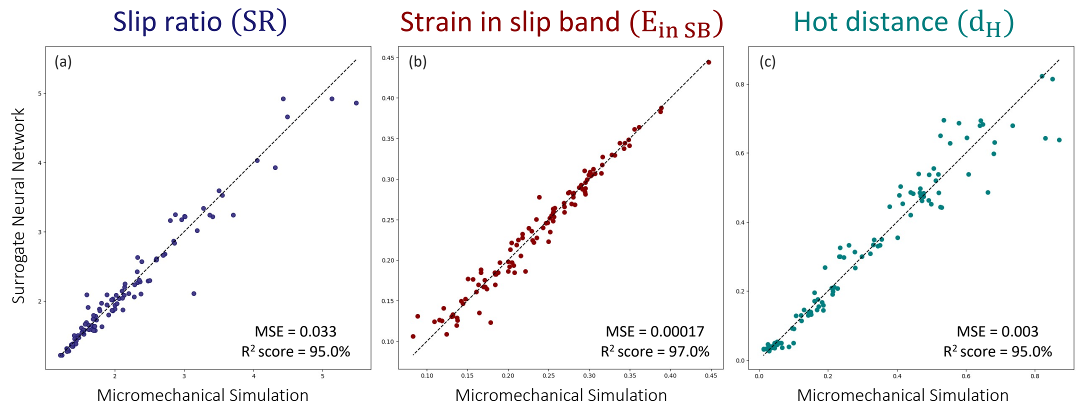

Figure 7.9: Ground truth calculated by micromechanical simulation versus NN predicted values of three localization-based material properties, (a) average ratio of the strain accommodated by slip bands to that accommodated by grain matrices, (b) fraction of the total strain that is accommodated by slip bands, and (c) average normalized, adjusted distance between slip bands within the microstructure.

localization-based property based on the characteristics of the microstructure. As listed in Table 7.1, each NN model is optimized in performance with a unique hyper-parameter configuration. Nevertheless, we use the same approach for training, evaluation, and testing all models. Figure 7.9 shows how NN model predictions compare with the true values calculated via SB-FFT micromechanical simulations for the test data. Overall, all three models exhibit an acceptable performance, with an R^2 score of at least 95% and MSE of $\sim$ 3% at highest. Not only does such a high accuracy rate qualify these models as reliable tools for predicting localization-based material properties given the characteristics of a microstructure, but it provides the opportunity to rapidly enrich our dataset by generating additional pairs of features and labels, typically required for most optimization techniques. This advantage is more acknowledged when comparing the time it takes to run a micromechanical simulation on a 3D microstructure with a size of 100 × 100 × 100 voxels ($\sim$ 36 hours) with the time it takes for a NN model to do the same task in seconds.

Having separate models trained and successfully tested for each property, we then use these surrogate models to generate a large dataset of microstructural features and their corresponding material properties. The enriched dataset comprises 1.5M sample microstructures, compared to our initial limited dataset of 360 microstructures generated with DREAM3D and SB-FFT simulations. The available range for each microstructural feature is extended in the enriched dataset, except for the texture for which we still use the six textures presented in Figure 7.4. We therefore create a fine grid of available values for our features, providing an applicable dataset for conducting a simple grid search for optimal material properties.

For each localization-based property, box and whisker plots in Figure 7.10 present the distribution of the 360 datapoints from our initial dataset. The optimal values obtained from the grid search are also indicated by yellow stars. To obtain each of these three values, we perform a micromechanical simulation on a 3D polycrystal we create using the optimal combination of microstructural features suggested by the grid search. This additional step verifies whether our data-driven optimization scheme produces a truthfully optimal localization response in Ti-6Al-4V. As shown in Figure 7.10a, the optimal solution manifests a superior response, i.e., lower degree of localization. However, given that our initial dataset already contains samples with very low slip ratios and that the SR is lower-bound to 1.0, the gain from the optimal microstructure is not drastic. For the fraction of total strain accommodated by slip bands shown in Figure 7.10b, the gain from the optimal microstructure is more pronounced, but still not significant. It should be noted, however, that a perfectly homogeneous distribution of deformation does not yield $\mathrm{E}_{\mathrm{inSB}} = 0$, as the slip band domains naturally occupy a few percent of the total microstructure. The most significant improvement in localization response is offered by the optimal solution that maximizes the hot distance. Figure 7.10c demonstrates the remarkable increase in the adjusted distance between intense slip bands in the polycrystal, achieved by the optimization scheme developed here.

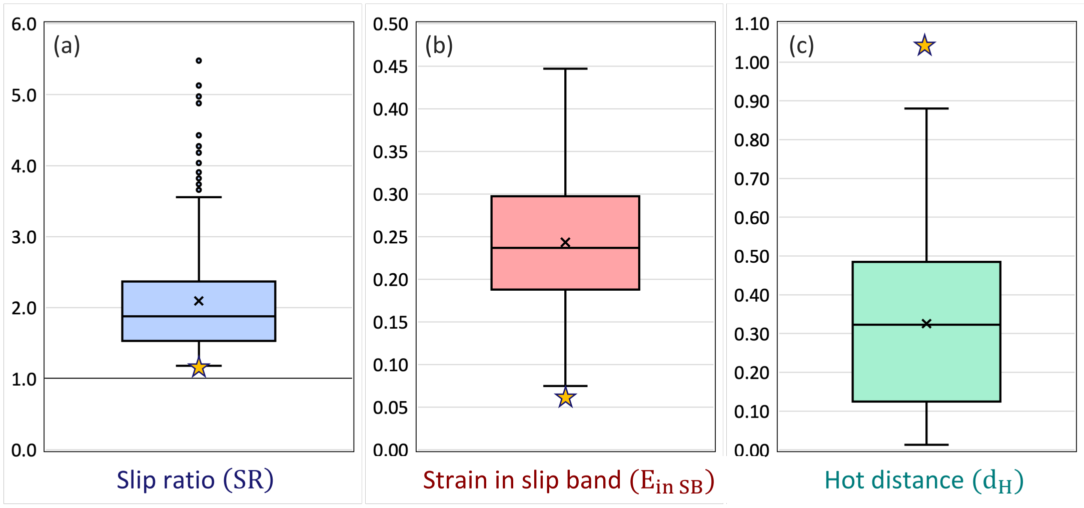

Figure 7.10: Distribution of three localization-based material properties for 360 datapoints from our initial dataset, as well as three datapoints obtained from micromechanical simulations on optimal solutions predicted by the data-driven optimization scheme.

Interestingly, we obtain a uniquely different optimal microstructure when considering each material property. That is to say, the microstructure configuration that maximizes the hot distance does not necessarily minimize the strain in slip bands. The polycrystal that minimizes the slip ratio (SR) has medium-sized, highly elongated grains with very small deviation in their size, and their orientation sampled from texture A. On the other hand, a polycrystal with texture F that comprises large grains that are highly dispersed in their size and elongated in their shape would minimize the fraction of the total strain localized within slip bands (E_{inSB}). Finally, the microstructure that maximizes the hot distance (d_H) is sampled from texture C, has small, yet again highly elongated, grains with small deviation in their size. In the next section, we further discuss these results.

7.5 Discussion and conclusions

The development, long-range transmission, and connectivity of slip bands in polycrystalline materials including Ti-6Al-4V titanium alloy are experimentally evidenced to contribute to crack initiation and propagation, playing a significant role in the failure mechanisms of these materials [4, 24]. Intuitively, a polycrystal that accommodates the imposed deformation more homogeneously is anticipated to possess superior mechanical properties, such as strength and toughness. In this chapter, we combined explicit slip band micromechanical simulations on 3D polycrystals with neural network models to design a Ti-6Al-4V microstructure that features strain delocalization to some extents. We first generated a dataset of 3D polycrystals with different microstructural characteristics and ran crystal plasticity simulations to calculate the mechanical response of each polycrystal, from a localization standpoint. Motivated by the simulation results, we then formulated a set of localization-based properties to optimize, all in line with strain delocalization. Separate neural network (NN) models were designed and tuned to predict these properties for a microstructure, given its characteristics such as texture, grain size and shape. Once the high accuracy of these models was established, we employed them to generate additional data to enrich our initial, relatively limited dataset of 3D microstructures. Finally, we performed a grid search optimization on the new dataset to find optimal microstructures, each improving one localization-based property.

To represent the microstructure and create labels in our framework, we used the combination of a graph network and a simple neural network model. The graph network was used to account for grain neighborhood and connectivity throughout the polycrystal. Using this approach, we presented each microstructure with a total of four key features. Therefore, the input dimensionality was significantly reduced compared to voxel-based machine learning models such as convolutional neural networks (CNN) [243, 244, 245, 246, 228] and graph neural network (GNN) models [229, 230, 231, 247, 233], leading to improved efficiency in terms of computation and memory requirements. While extracting the value of hot distance (d_H) in our approach is accomplished by applying a graph network to the polycrystal, the time required for training our NN models is significantly reduced compared to CNN and GNN models, for which the training time exponentially increases with the number of voxels and grains in the microstructure.

Another advantage of the model developed here is the interpretability of the features and labels, rendering our results readily applicable, from a manufacturing perspective. Although voxel-based CNNs retain the microstructural features for each voxel within the polycrystal, they fail to account for grain neighborhood, a critical aspect for determining macroscopic properties of polycrystalline materials. Furthermore, since the solution would include features, such as orientation, optimized for each voxel, an optimal microstructure one would get from a CNN is not manufacturable. Recently, application of GNNs for predicting mechanical properties of polycrystalline materials have shown promising results in circumventing the first issue. Nevertheless, the problem with the interpretability of optimal solutions still persists. With the current manufacturing capacities, creating a set of grains with orientations, morphology, and connectivity exactly as prescribed by the GNN is unfeasible. The optimal solution provided by our approach, on the other hand, is easy to interpret and feasible to manufacture as many experimental works have successfully developed techniques to control grain size, morphology, and texture in titanium alloys [248, 249, 250, 251, 252].

We showed that the optimal microstructure designed for each localization-based property is unique with a set of microstructural features that does not optimize other properties. Surprisingly, one solution recommended texture F (uniformly random or no texture) with large grains to minimize the total strain localized within slip bands, while the solution that maximized the hot distance featured a rolling texture with small grains. Since the latter include both the intensity of and distance between intense slip bands within the microstructure, we may consider the optimal solution for hot distance more preferable. Ti-6Al-4V microstructures with smaller grains have also been experimentally associated with superior fatigue properties [248, 253, 254], arguably due to the fact that slip length and intensity is smaller in fine-grained materials.

Remarkably, a feature that was common in all optimal microstructures is the elongated shape of grains. This result suggests that higher aspect ratios of grains morphology lead to an improvement in localization-based properties, or equivalently, a more delocalized strain distribution in the material. A plausible argument here is that the smaller dimension in elongated grains can drastically reduce the likelihood of slip band formation and localization, if the orientation of the grain favors a slip band that spans along that direction. Therefore, not only will no slip band form in that grain which contributes to strain delocalization, but the grain will undergo either homogeneous or no deformation at all, breaking the potential chain of long-range localization in the microstructure.

As a final remark, give the close relationship between microscopic localization response and macroscopic material properties, and thanks to the current advances in novel manufacturing techniques, it is envisioned that the findings of this work provide valuable target features for designing optimal Ti-6Al-4V polycrystals to overcome the strength-toughness trade-off. Incorporating more possible textures and microstructural features, allowing slip bands to develop on multiple slip systems, and inclusion of the β phase in the microstructure can provide further insights in future works.

Chapter 8

Data-driven texture design for reducing elastic and plastic anisotropy in titanium alloys

8.1 Introduction

Hexagonal close packed (HCP) titanium-based materials, are continually being researched and designed for high-performance applications, due to a combination of superior properties, such as high specific-strength, corrosion resistance, fatigue resistance, and biocompatibility. However, the strong directional dependencies in the elastic and plastic properties, or anisotropy, reduce their ductility and formability [255, 256]. This anisotropy originates from the inherent low symmetry in their HCP crystal structure. The effective Young's modulus along the $< c >$ axis of a single HCP crystal is greater than that its $< a >$ direction. Small numbers of easy $< a >$ slip systems and large differences in slip strengths among available $< a >$ and $< c + a >$ slip modes, compared to those of cubic crystal structures, lead to a highly anisotropic plastic response.

Extensive research has suggested several ways to reduce the mechanical anisotropy of polycrystalline titanium, including texture control during deformation [250, 251, 252], alloying techniques [257, 258, 259], and application of thermal processes [260, 261, 262]. Nevertheless, the problem of anisotropy via one or a combination of these techniques remains a challenge. First, the elastic and plastic anisotropy in titanium do not generally align crystallographically. The elastic and plastic anisotropy produced by the same texture will not be the same. Consequently, a solution that minimizes the anisotropy of one does not necessarily minimize the anisotropy of the other. Second, considering crystals with highly anisotropic properties has intuitively suggested that a polycrystal consisting of randomly distributed crystal orientations, known as a random or no texture, would give rise to nearly isotropic elastic and plastic responses. However, such an ideal texture has already proven hard to produce in titanium. Further, computational polycrystal plasticity models have shown that compared to typical textures from metal forming techniques, ideal random leads to a weaker material, while still retaining some, albeit lower anisotropy [258]. Third, most conventional manufacturing methods, such as rolling and extrusion, fabricate non-uniform, sharp titanium textures [15, 263, 264, 265]. Experiment and modeling show that these polycrystals exhibit anisotropic plastic responses among two or more orthogonal directions [265, 266, 267, 268, 269]. For instance, cold rolling of titanium and its alloys tend to produce textures with c-axis tilted ±20–40° away from the normal direction toward the transverse direction and the prismatic plane normals aligned with the rolling direction, while samples produced by extrusion typically manifest a texture with c-axis perpendicular to the extrusion direction [265]. Such strong textures give rise to properties, such as yield and ultimate tensile strengths, varying along different directions as high as 20%, even after multiple rounds of heat treatments [269]. Last, the parameter space associated with texture/property relationships is enormous. Complete control of texture can be unfeasible as the texture evolution depends on several variables, such as temperature, material, and processing history, in unknown ways. Reducing anisotropy via alloying techniques and texture control during the deformation involves conducting a prohibitive number of tests within a vast parameter space that consists of different compositions and deformation paths. With thermal processing and with respect to the case study mentioned earlier, it was found that while subsequent heat treatments can reduce anisotropic behavior, they also diminish other mechanical properties [269]. Even pure computational exploration would not be practical due to the high dimensionality of the space of crystallographic orientation.

In light of this, data-driven approaches have recently been used to uncover microstructure property relationships in a wide range of materials [270, 271, 226, 227, 272]. Several studies have employed data-driven reduced-order optimization procedures for the design of a process sequence to control the texture and texture-dependent properties, such as Young's modulus [273, 274, 275, 276]. These studies focus on face-centered cubic (FCCs) materials. Due to the symmetry of this class of materials, anisotropy reduction was not a concern and either an elastic or plastic property in only one direction was optimized. This was accompanied by loss of the same property in other directions [226, 277]. More recently, optimal textures that manifest minimal elastic anisotropy in HCP titanium were explored [278]. While the anisotropy in elastic moduli was minimized, the moduli themselves were not necessarily maximized. Although it is recognized that experimental testing of the proposed optimal textures meets its own challenges, large-scale polycrystalline deformation simulations starting with these textures were not employed as a means of validation.

In this chapter, we aim to identify computationally the microstructural textures that would reduce anisotropy in elastic and plastic properties of titanium alloys, including Ti-6Al-4V, CP-Ti, and Ti-7Al. This approach is a new data-driven optimization method that combines two kinds of modeling techniques. One is combinatorial optimization formulation over the orientation space of single crystals when given a set of property constraints of the polycrystal, and the other is a 3D crystal plasticity constitutive model for the large datasets required for the deformation response of single crystals over the full orientation space. The deformation calculations account for plasticity in the common slip modes of Ti based alloys, basal $\langle a \rangle$, prismatic $\langle a \rangle$, and pyramidal $\langle c + a \rangle$ slip. To verify that the textures achieve the target property, separate, large-scale, 3D polycrystal deformation calculations are performed for several realizations of the same designed texture. First, it is revealed that textures that minimize anisotropy, while maximizing either stiffness or strength, are possible. This set of textures are strong, containing only several orientations, and unlike those found in familiar rolled or extruded Ti textures. Further, the orientations comprising these elastic and plastic anisotropy reducing (AR) textures are not alike, a consequence of the difference between the mechanisms controlling the elastic and plastic anisotropy in titanium. Significantly, these optimized textures decrease the level of both elastic and plastic anisotropy when compared to an ideal uniformly random texture, while not compromising stiffness or strength. We extend the data-driven approach to solve for AR textures that are constrained to be similar to another texture. Using this method, AR textures that are close to the more familiar deformation textures of Ti, such as rolling, are found. Last, we demonstrate that the textures designed for one Ti alloy are transferable to other Ti alloys, without the need to generate additional datasets or repeat the optimization process.

This chapter is structured as follows. We first present the general optimization formulation for the texture-property relationships for a polycrystal. Next, the set of primary and secondary objectives that the textures need to achieve are described. We then discuss the single crystal plasticity model and material data that will drive the optimization model. We dedicate a section to introducing an appropriate sampling method for instantiating a 3D polycrystal microstructure with designed textures. We follow with results on

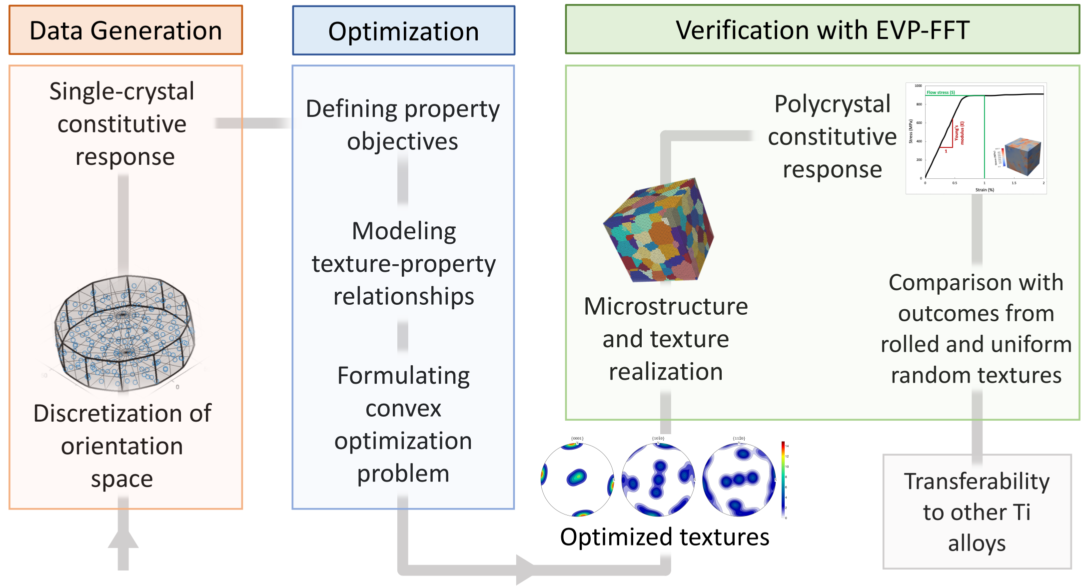

Figure 8.1: Flowchart of the data-driven approach used in this work to minimize elastic and plastic anisotropy in Ti-based materials through texture optimization. The workflow consists of data generation from material's single crystal response, convex optimization methods, and microstructure-sensitive constitutive modeling of optimized textures.

the AR textures that simultaneously maximize elastic and plastic properties, including texture analysis and predictions of stiffness and strength. Designed textures that closely resemble a rolling texture while simultaneously reducing elastic and plastic anisotropy are presented. We conclude with demonstration of transferability of these textures to achieving similar outstanding properties in other Ti alloys, and a discussion on the manufacturability of these design textures.

8.2 Analytic formulation of optimization problems

The goal of the data-driven optimization methodology is to identify a set of orientations, denoted as vector $\boldsymbol{\pi}$, that lead to a target Young's modulus and flow stress or a combination of the two for the polycrystal. We show that this end can be achieved using an optimization scheme when certain assumptions are met. The chief assumption is that for any crystal i, its elastic and plastic properties are independent of the morphology of the crystal and its location within the polycrystal. Equivalently, any two distinct crystals with like orientations will exhibit the same properties.

Figure 8.1 shows the workflow for the data-driven texture design approach used in this study. First, the optimization formulation, parameters, and objectives are presented. Second, the input data required are identified and crystal plasticity approach to generate them described. Third, the designed anisotropy reducing (AR) textures are predicted and validated by polycrystal constitutive response calculations. The selections made for each are described in turn below.

Consider a polycrystal containing N crystals (also called grains) with known orientations and volume fractions. The global coordinate system is $a \in \{x, y, z\}$. Each crystal $i \in \{1, 2, \ldots, N\} =: [N]$ has a volume v_i and a unique orientation with respect to the global system. The orientation space is discretized into d nodes, as shown in Figure 8.2b. The orientation of crystal i is then described by a vector $\boldsymbol{x}_i \in \mathcal{O}_d := \{\boldsymbol{e}_1, \boldsymbol{e}_2, \ldots, \boldsymbol{e}_d\}$, where $\boldsymbol{e}_j, j \in [d]$ corresponds to the j^{th} orientation. The $\boldsymbol{x}$ is a set of grain orientations in the polycrystal.

The properties of interest are denoted by $P_a(\boldsymbol{x})$ along the a-direction for the individual crystals in the polycrystal. The two properties considered in this study are the Young's modulus $E_a(\boldsymbol{x})$ and flow stress $S_a(\boldsymbol{x})$ at a given strain level along the global a-axis. With this, $E_a(\boldsymbol{x}_i)$ is the Young's modulus in the a-direction of crystal i. While isotropy means strictly no directional dependence in material properties, the several tens of distinct loading test directions needed to prove this level of isostropy are rarely carried out in the laboratory, and showing similarity in properties along two to three orthogonal or similarly distinct loading directions is common practice to establish low anisotropy. Without loss of generality, we use, as a basis for identifying reduced anisotropic behavior, the similarity in the stiffness and/or strength along the three orthogonal directions. Accordingly $E_x(\boldsymbol{x}_i)$,

$E_y(\boldsymbol{x}_i)$ and $E_z(\boldsymbol{x}_i)$ are the Young's moduli of a single crystal i in the x, y and z axis, respectively, of the global system. Similarly, $S_x(\boldsymbol{x}_i)$, $S_y(\boldsymbol{x}_i)$, and $S_z(\boldsymbol{x}_i)$ denote the flow stresses of a single crystal i in the x, y, and z axis, respectively, at a given strain.

The Young's modulus E_a of the polycrystal along the a-axis, $a \in \{x, y, z\}$, is the volume-weighted average over the Young's modulus $E_a(\boldsymbol{x}_i)$, $i \in [N]$ of each crystal in the polycrystal, that is:

$$E_a = \frac{1}{V} \sum_{i \in [N]} v_i \cdot E_a(\boldsymbol{x}_i), \tag{8.1}$$

where v_i is the volume of the i^{th} crystal and $V = \sum_{i \in [N]} v_i$ is the total volume of the polycrystal. In the notation for the polycrystal, the $(\boldsymbol{x}_i)$ is dropped. Similarly, the flow stress S_a, $a \in \{x, y, z\}$ of the polycrystal is calculated as follows:

$$S_a = \frac{1}{V} \sum_{i \in [N]} v_i \cdot S_a(\boldsymbol{x}_i), \tag{8.2}$$

With the polycrystalline properties denoted as $P_a \in \{E_a, S_a\}$, we specify a function $\mathcal{I}_p(P_x, P_y, P_z)$, $p \in \{e, s\}$ to serve as a measure of anisotropy. We can consider the following two measures,

$$\mathcal{I}_p(P_x, P_y, P_z) = (P_x - P_y)^2 + (P_x - P_z)^2 + (P_y - P_z)^2 \tag{8.3}$$

and

$$\mathcal{I}_p(P_x, P_y, P_z) = \sum_{a \in \{x,y,z\}} (P_a - \overline{P})^2. \tag{8.4}$$

with $\overline{P} = (P_x + P_y + P_z)/3$.

The general optimization problem of designing a texture $\boldsymbol{x}_i$, $i \in [N]$ of the polycrystal with reduced anisotropy with respect to either the Young's modulus or the flow stress or both is stated by:

$$\text{minimize}_{\mathrm{x_i \in \mathcal{O}_d, i \in [N]}} \ \mathcal{I}_{\mathrm{p}}(P_{\mathrm{x}}, P_{\mathrm{y}}, P_{\mathrm{z}}). \tag{8.5}$$

Solving (8.5) requires two more steps, where the first indicates the nature of the individual crystal properties as a function of orientation $P_a(\boldsymbol{x}_i)$, $a \in \{x, y, z\}$, and the second specifies the constraints. The former is discussed below and latter in the next section.

When the properties of a crystal i, $P_a(\boldsymbol{x}_i)$, $a \in \{x, y, z\}$, depend only on its crystallographic orientation $\boldsymbol{e}_j$ within the polycrystal, then we have that

$$P_a(\boldsymbol{x}_i) = P_a(\boldsymbol{e}_j) \tag{8.6}$$

for all $i \in [N]$ such that $\boldsymbol{x}_i = \boldsymbol{e}_j$, for some $j \in [d]$.

As mentioned at the outset, this is a key assumption and here we expound on a few of its conveniences for solving the problem in hand. First, the objective $\boldsymbol{\pi} := \frac{1}{V} \sum_{i \in [N]} v_i \cdot \boldsymbol{x}_i$ becomes the ideal set of orientations, or simply texture, that leads to a target polycrystalline property. The optimal texture $\boldsymbol{\pi}$ is a collection of non-negative orientations u in orientation space $\mathbb{R}^d$ and must contain at least one orientation and thus the size of $\boldsymbol{\pi}$ is $d-1$, i.e., $\boldsymbol{\pi} \in \Delta_{d-1} := \{\boldsymbol{u} \in \mathbb{R}^d \ : \ u_j \geq 0, j \in [d] \text{ and } \sum_{j \in [d]} u_j = 1\}$.

Second, $E_a(\boldsymbol{x}_i)$, $S_a(\boldsymbol{x}_i) : \mathcal{O}_d \to \mathbb{R}_+$, $a \in \{x, y, z\}$ can be defined as a linear function of the single crystal properties. This permits separately collecting the single crystal properties in a vector $\theta^p_{a,j} := P_a(\boldsymbol{e}_j)$, $p \in \{e, s\}$, where $\theta^p_{a,j}$ are the properties for orientation

j, along the a-axis. This linear relationship is expressed as

$$E_a(\boldsymbol{x}_i) = \boldsymbol{x}_i^T \boldsymbol{\theta}_a^e, \quad S_a(\boldsymbol{x}_i) = \boldsymbol{x}_i^T \boldsymbol{\theta}_a^s, \tag{8.7}$$

With this, $\boldsymbol{\theta}_a^p = \begin{bmatrix} \theta_{a,1}^p & \theta_{a,2}^p & \cdots & \theta_{a,d}^p \end{bmatrix}^T \in \mathbb{R}_+^d, \quad a \in \{x, y, z\}$ and $p \in \{e, s\}$ are single crystal properties, referred to as optimization parameters, which will be calculated by simulations of the single-crystal constitutive response.

We then simplify the problem (8.5) by expressing (8.1) and (8.2) in view of (8.7) as follows:

$$P_a = \frac{1}{V} \sum_{i \in [N]} v_i \cdot \boldsymbol{x}_i^T \boldsymbol{\theta}_a^p = \Big(\frac{1}{V} \sum_{i \in [N]} v_i \cdot \boldsymbol{x}_i \Big)^T \boldsymbol{\theta}_a^p = \boldsymbol{\pi}^T \boldsymbol{\theta}_a^p. \tag{8.8}$$

With this, the AR textures then become the solution to a quadratic optimization program.

Third, the advantage of this linear formulation is that the data driving the optimization are the single crystal Young's moduli and the flow stresses along three orthogonal axes, $\theta_{a,j}^p$, $\forall(a, p)$, $a \in \{x, y, z\}$, $p \in \{e, s\}$ for all orientations $j \in [d]$. We emphasize that this dataset is a separate list, transcending the polycrystal, its number of grains and texture. We will use a 3D crystal plasticity model for a given alloy to generate the data, but these data sets can be obtained by other means.

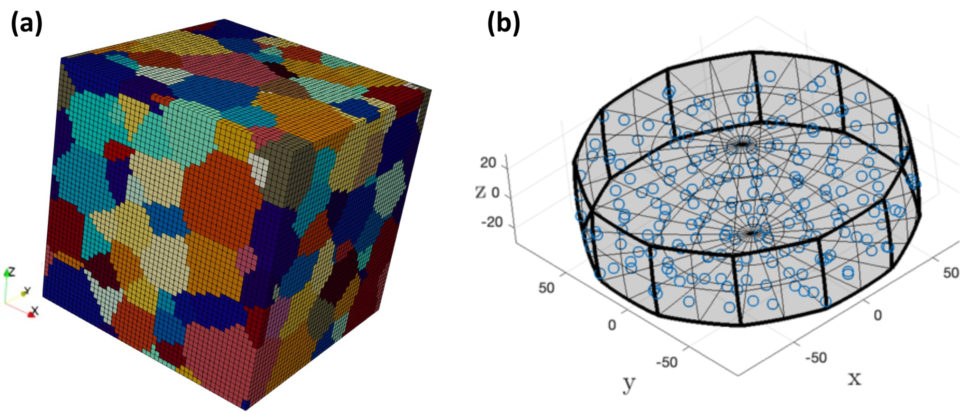

Figure 8.2: (a) A microstructure realization consisting of 125,000 voxels and $N = 198$ crystals. The morphology and location of crystals remain constant throughout this work and different microstructure realizations vary from one another through different assignments of orientations to the N crystals. (b) Fundamental zone for hexagonal symmetry discretized into $d = 201$ orientation nodes.

8.3 Secondary objectives, data generation, and validation

8.3.1 Polycrystal property targets for textures to achieve

Under the linear model in (8.7) and recalling the texture $\boldsymbol{\pi}$ as the optimization variable, the anisotropy reduction problem (8.5) becomes:

$$\min_{\boldsymbol{\pi}\in\Delta_{\mathrm{d}-1}} \mathcal{I}_{\mathrm{p}}(\boldsymbol{\pi}^{\mathrm{T}}\boldsymbol{\theta}^{\mathrm{p}}_{\mathrm{x}}, \boldsymbol{\pi}^{\mathrm{T}}\boldsymbol{\theta}^{\mathrm{p}}_{\mathrm{y}}, \boldsymbol{\pi}^{\mathrm{T}}\boldsymbol{\theta}^{\mathrm{p}}_{\mathrm{z}}). \tag{8.9}$$

where we recall that $\mathcal{I}_p$, $p \in \{e, s\}$ is the anisotropy measure. Since the $\boldsymbol{\theta}^p_a$, $\forall(a,p)$, $a \in \{x, y, z\}$ are fixed and known, $\mathcal{I}_p$ is a function of only $\boldsymbol{\pi}$, i.e.,

$$\min_{\boldsymbol{\pi}\in\Delta_{\mathrm{d}-1}} \mathcal{I}_{\mathrm{p}}(\boldsymbol{\pi}). \tag{8.10}$$

The optimization problem (8.10) is convex as long as $\mathcal{I}_p$ is convex. In particular, for the two anisotropy measures mentioned earlier, (8.10) is a convex quadratic program with linear constraints. With this, the combinatorial problem of searching for the optimal orientation for each of the N crystals from the set of all possible d orientations essentially transforms into a convex one of finding the best texture, $\boldsymbol{\pi} \in \Delta_{d-1}$, that achieves target structural properties of the polycrystal.

The primary objective is to find a texture that minimizes anisotropy in a polycrystal property $p \in \{e, s\}$, which corresponds to the texture that solves (8.10). We will term a texture that minimizes anisotropy $\mathcal{I}_e$ as anisotropy-reducing (AR) textures. However, due to the nature of its objective function, the optimization problem in (8.10) does not have a unique solution (see Appendix D for proof). Thus advantageously in addition to considering anisotropy reduction by minimizing $\mathcal{I}_p(\boldsymbol{\pi})$, we can include secondary objectives, which are any other functions of E_a and S_a, $a \in \{x, y, z\}$, that the texture aims to also fulfill.

In this study, we will consider separately several secondary objectives. The first set of them include predicting AR textures that simultaneously maximizing an elastic and/or plastic properties. While *both* $\mathcal{I}_e(\boldsymbol{\pi})$ and $\mathcal{I}_s(\boldsymbol{\pi})$ will be constrained to be zero, either the Young's modulus or the flow stress, or both will also be maximized. These textures are referred to as "maxE", "maxS", and "max(E+S)", respectively.

Another set of cases aim to design AR textures that are accessible via conventional manufacturing pathways. To this end, we modify (8.10) to include an additional constraint that enforces some degree of similarity between the AR texture and a Ti texture produced via conventional manufacturing processes. As an example, we choose an experimental rolling texture and one of two different measures of similarity between two textures, either the ℓ_1-norm or the KL-divergence measure, the latter of which is a specialized measure between probability distributions (see Appendix D for background). These AR textures are respectively named the "Rolled-like Norm" and "Rolled-like KL" textures.

The last set of cases considers designing highly oriented AR textures. Such strong, sparse textures can be interesting and potentially desirable solutions to (8.10). The common belief is that nominally near isotropic properties can be achieved in polycrystals with "no texture", that is, comprising orientations evenly distributed over orientation space [279, 280]. For highly anisotropic crystals with low symmetry crystal structures, such as Ti, it can be shown that a uniformly random (or no) textured polycrystal of such crystals do not lead to isotropic properties. Thus, counter to the common perception of polycrystals lacking texture, we aim to identify textures that exhibit reduced anisotropic properties, while consisting of only a few distinct orientations. To enforce sparsity, we add a regularizer that penalizes non-sparse solutions. Further details on the design of strong but AR textures can be found in Appendix D.

8.3.2 Data generation of single crystal properties from a crystal plasticity constitutive model

The data that need be supplied to the texture design optimization scheme are the properties in $\theta^p_{a,j}$, $\forall(a,p)$, $a \in \{x,y,z\}$, $p \in \{e,s\}$. For this work, these single crystal properties will be determined by 3D crystal plasticity model for a given Ti alloy; however, they can be obtained by other means, such as experimental measurement. We employ the elasto-viscoplastic fast Fourier transform (EVP-FFT) model described in Chapter 2 to calculate the effective Young's modulus and plastic flow stress of a single crystal of a given orientation j when loaded along the global a-direction. This calculation is repeated for each orientation j, within the set of d orientations spanning the full orientation space, and each loading direction of the global coordinate system, x, y, and z.

The EVP-FFT model was developed in [67] and has since been extensively used to predict micromechanical deformation behavior of a vast range of single crystalline and polycrystalline materials [68, 73, 75, 76], including HCP crystals [281, 282, 70, 51, 50, 283], as studied here. It is a 3D computational micromechanical model for constitutive response of a given crystalline microstructure. The microstructure of the single crystal is discretized into a regular 3D grid of points. Deformation at every material point occurs via elasticity, according to the linear elasticity theory, and plasticity according to crystal plasticity theory. The model accounts for the anisotropic response in the elastic regime through taking in the measured anisotropic elastic constants as an input. It also incorporates plastic anisotropy as it originates from substantial differences in slip resistance among the available slip modes in titanium.

8.3.3 Property generation of the titanium alloys

The texture design optimization formulation is applied to Ti-6Al-4V for an example. The EVP-FFT calculations require the five independent elastic constants, C_{11}, C_{22}, C_{13}, C_{33}, and C_{44}, for an HCP crystal and CRSS values $\tau_c^s(\mathbf{x})$ for the available slip modes in Ti-6Al-4V, which are prismatic $< a >$, basal $< a >$, and pyramidal $< c+a >$ slip. Table 8.1 lists the values used for Ti-6Al-4V. The elastic constants originate from experimental measurements. Polycrystal EVP-FFT calculations using these CRSS values were able to reproduce the macroscopic experimental response of Ti-6Al-4V [284]. The Euler angles corresponding to the orientation j are also needed input. In the calculations that follow, $d = 201$ distinct orientations spanning the full orientation space are determined by discretizing the fundamental zone for hexagonal symmetry, as shown in Figure 8.2b.

The crystal is subjected to a uniaxial tension in that direction, up to 1% total strain. This strain level was selected such that the microstructure experiences some amount of plastic deformation, with several different slip systems being activated among the crystals in the material.

Table 8.1: Elastic constants, anisotropy index (A^L), and the critical resolved shear stress (CRSS) values for different plastic modes used in the crystal plasticity calculations for Ti-6Al-4V, CP-Ti, and Ti-7Al.

Material	Elastic constants (GPa)					A^L	CRSS values of slip modes (MPa)		
	C_{11}	C_{22}	C_{13}	C_{33}	C_{44}		prismatic $< a >$	basal $< a >$	pyramidal $< c + a >$
Ti-6Al-4V [285, 20]	168.0	95.0	69.0	191.0	48.0	0.086	370	420	590
CP-Ti [16, 15]	162.4	92.0	69.0	180.7	46.7	0.075	69	128	180
Ti-7Al [286, 287]	175.4	80.5	66.8	184.8	46.0	0.022	220	245	388

8.3.4 Validation of properties from predicted anisotropy reducing textures: Sampling from the optimized textures

To verify that the designed textures lead to the target properties, we generate polycrystalline microstructure realizations of the optimized texture and simulate is stress-strain response when loading in one of the three global axes, x y, and z. As an example problem, we use the 3D polycrystalline microstructure shown in Figure 8.2a, which consists of $N = 198$ distinct grains, each with a known crystallographic orientation and volume fraction. For a polycrystal, EVP-FFT advantageously accounts for interactions among all the grains in this polycrystal during deformation, including their location and changes in morphologies and crystallographic orientation. Note that none of these features are taken into account in the theoretical optimzation formulation presented earlier. In each EVP-FFT simulation, the model polycrystal is subjected to a uniaxial tension in a given a-direction, up to 1% total strain. From this response, the Young's modulus E and flow stress S can be determined.

In each realization, the starting texture of the model polycrystal needs to approximate the optimized one. Assigning orientations to a finite number of crystals, such that the realized volume fraction, π_j, of the j^{th} orientation in the polycrystal, exactly matches its volume fraction, $\hat{\pi}_j$ in the optimal texture, however, is unattainable. In Appendix D, an ideal approach to assigning orientations to crystals under these conditions is presented. We prove that following it would require solving another combinatorial optimization problem, which is beyond the scope of this study.

With this in mind, we employ an alternative approach. The underlying assumption is that the properties of polycrystals can be approximated as the average (instead of the volume-weighted average) over the properties of each individual crystal; that is:

$$P_a \approx \frac{1}{N} \sum_{i \in [N]} P_a(\boldsymbol{x}_i) \approx \hat{\boldsymbol{\pi}}^T \boldsymbol{\theta}_a^p. \tag{8.11}$$

The $\hat{\boldsymbol{\pi}}$ is a probability mass function, with its j^{th} element, $\hat{\pi}_j$, representing the probability that any given crystal, regardless of its volume, is oriented according to the j^{th} discretized orientation. We can then obtain orientation vectors $\boldsymbol{x}_i$ for each crystal $i \in [N]$, by independently sampling $X_i \sim \hat{\boldsymbol{\pi}}$ (i.e., $\mathbb{P}(X_i = \boldsymbol{e}_j) = \hat{\pi}_j,\ j \in [d]$).

For any microstructure realization, its texture, $\boldsymbol{\pi} := \frac{1}{V} \sum_{i \in [N]} v_i \cdot \boldsymbol{x}_i$, is the observed value of a random vector $\Pi := \frac{1}{V} \sum_{i \in [N]} v_i \cdot X_i$, since the orientations of its individual crystals, $\boldsymbol{x}_i,\ i \in [N]$, are vectors drawn from a probability distribution themselves. Utilizing the property of linearity of expectation and the fact that $\mathbb{E}\big[X_i\big] = \hat{\boldsymbol{\pi}},\ \forall i \in [N]$, we can find the expectation of Π as:

$$\mathbb{E}\big[\Pi\big] = \frac{1}{V} \sum_{i \in [N]} v_i \cdot \mathbb{E}\big[X_i\big] = \Big(\frac{1}{V} \sum_{i \in [N]} v_i\Big) \hat{\boldsymbol{\pi}} = \hat{\boldsymbol{\pi}}. \tag{8.12}$$

Using this approach, we sample $M = 30$ microstructure realizations for each designed textures. If $\boldsymbol{\pi}_q,\ q \in \{1, 2, \ldots, M\} =: [M]$ is the texture of the q^{th} realization, then according to the law of large numbers, for reasonably large M:

$$\frac{1}{M}\sum_{q\in[M]}\boldsymbol{\pi}_q \approx \mathbb{E}\big[\Pi\big] = \hat{\boldsymbol{\pi}}\,. \tag{8.13}$$

In view of (D.4), it becomes evident that (8.11) consists of a reasonable approximation for (8.8) when averaging the results over multiple microstructure realizations. We validate approximation (8.11), using the EVP-FFT simulations, and show that the average properties of the M realizations fall very close to the predicted, while exhibiting low variance among them (see Appendix D).

8.4 Anisotropy reducing textures

The data-driven texture design model is used to predict AR textures with additional structural benefits, given the properties of single crystals of Ti-6Al-4V alloy and various objectives. We will term the texture that only minimizes the measure of elastic anisotropy $\mathcal{I}_e$ as “isoE” texture. We first examine the isoE texture that minimizes elastic anisotropy, which corresponds to that which solves (8.10). The resulting AR texture is shown in Figure 8.3a in the form of three pole figures, [0001], $[10\bar{1}0]$, and $[11\bar{2}0]$. The isoE texture comprises $k = 106$ distinct orientations and conventionally would be considered a weak texture. It is, however, clearly far from a uniformly random texture.

Figure 8.3b shows the pole figures for the optimized maxE texture that maximizes the Young’s modulus in one direction, or equivalently in all directions since the elastic anisotropy is constrained to be zero. The number of distinct orientations present in this texture is only five, clearly distinguishing it as a strong texture. Such a strong, sparse texture would not be conventionally anticipated to reduce the elastic anisotropy. It is also unfamiliar, that is, unlike the textures typically attained by conventional metal forming

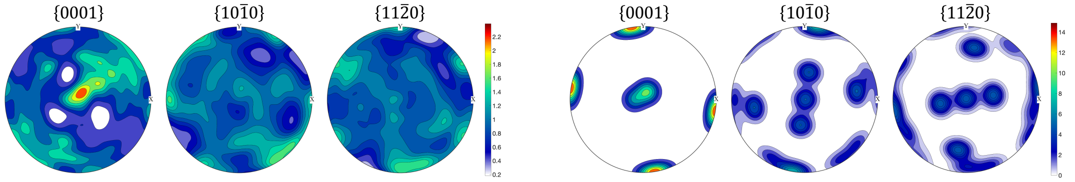

(a) isoE (b) maxE

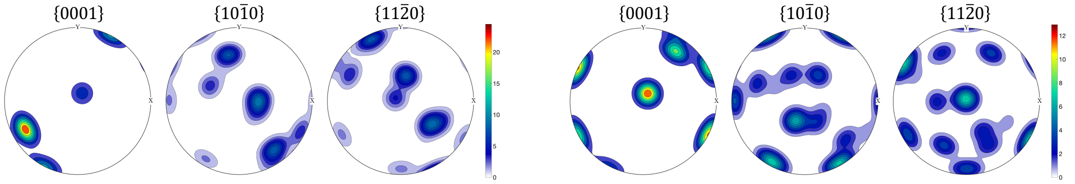

(c) maxS (d) max(E+S)

Figure 8.3: Pole figures for optimized textures (a) isoE, (b) maxE, (c) maxS, and (d) max(E+S). The isoE texture comprises 106 distinct orientations and minimizes the elastic anisotropy with no further objectives implemented. Other three textures, consisting of five distinct orientations, minimize both elastic and plastic anisotropy, while maximizing the effective Young's modulus or flow stress, respectively. Intensities are plotted as multiples of random distribution (MRD).

processes, such as rolling and extrusion [265, 15].

Figure 8.3c displays the pole figures for the maxS texture, the optimized texture expected to maximize the flow stress at 1.0% total strain while simultaneously minimizing elastic and plastic anisotropy. Like the maxE texture, the maxS texture consists of five distinct orientations and would therefore also be deemed a strong texture. Having only one orientation in common, the optimized textures for these two targets are, however, not the same, a consequence of the difference in the directionality of the deformation mechanisms responsible for the elastic and plastic deformation. The final texture shown in Figure 8.3d is the max(E+S) texture, which maximizes both the Young's modulus and flow stress, while simultaneously minimizing elastic and plastic anisotropy. Like the maxE and maxS textures, max(E+S) is composed of five orientations, one in common with the maxE texture and three with the maxS texture, although with varying volume fractions. These optimized textures are also strikingly distinct from deformation textures resulting from bulk metal forming manufacturing processes.

For each texture, $M = 30$ different realizations are generated and the effective Young's moduli (E_x, E_y, E_z) and plastic flow stresses (S_x, S_y, S_z) at 1.0% total strain are calculated in each direction for each polycrystalline microstructure realization. Figure 8.4 shows the results for the isoE, maxE, maxS, and max(E+S) textures. For comparison, also shown are the corresponding moduli and strength predictions from the same EVP-FFT model for a Ti-6Al-4V polycrystal starting with a uniformly random (no) texture and a rolled Ti texture from experimental measurement [15].

To quantify the extent to which the mechanical anisotropy has been reduced, Figure 8.4a provides corresponding $\mathcal{I}_{\mathrm{e}}$ and $\mathcal{I}_{\mathrm{s}}$, the elastic and plastic measures of anisotropy, given by 8.4. The elastic anisotropy reducing texture, isoE, produces a material that exhibits very low elastic anisotropy. The experimentally rolled texture has by far the highest elastic and plastic anisotropy, by an order of magnitude compared to any of the designed textures. In fact, the maxE, maxS, and max(E+S) have very low levels of anisotropy close to that of the uniform texture. By the measures alone, these AR textures appear to have achieved their target.

To verify that these designed AR textures, despite containing a low number of orientations, achieved their target properties, Figure 8.4b,c shows the predicted polycrystal Young's moduli and flow stresses in the three orthogonal directions. The rolled material exhibit significant differences among the properties in each direction, with two of the lowest stiffnesses among all cases studied. The uniform texture exhibits minimal anisotropy especially in flow stress, as expected, compared to the rolled texture. The Young's moduli and flow stresses lie nearly at a median value to those of the rolled texture. While the anisotropy is reduced, the concomitant reduction in mechanical properties are usually not desirable. In contrast, the maxE texture not only maximizes the Young's modulus to a level greater than the uniform texture, but it also substantially minimizes the elastic and plastic anisotropy to a level comparable with the uniform texture, and leads to flow stresses almost as large as that offered by the rolled texture in its strongest direction. Similarly, the optimized texture maxS maximizes the flow stress, reaching as high as that in the rolling direction of the rolled textured material, while simultaneously achieving reasonably low measures of elastic and plastic anisotropy, lower than those offered by a uniform texture. With the most stringent objectives of simultaneously maximizing Young's moduli and flow stresses, the max(E+S) also leads to remarkable properties. For instance, Young's moduli for this texture are not as large as those offered by maxE, but larger than those offered by maxS. Compared to the uniformly random texture, it produces higher Young's moduli and flow stresses and compared to the rolled texture, significantly lower elastic and plastic anisotropy.

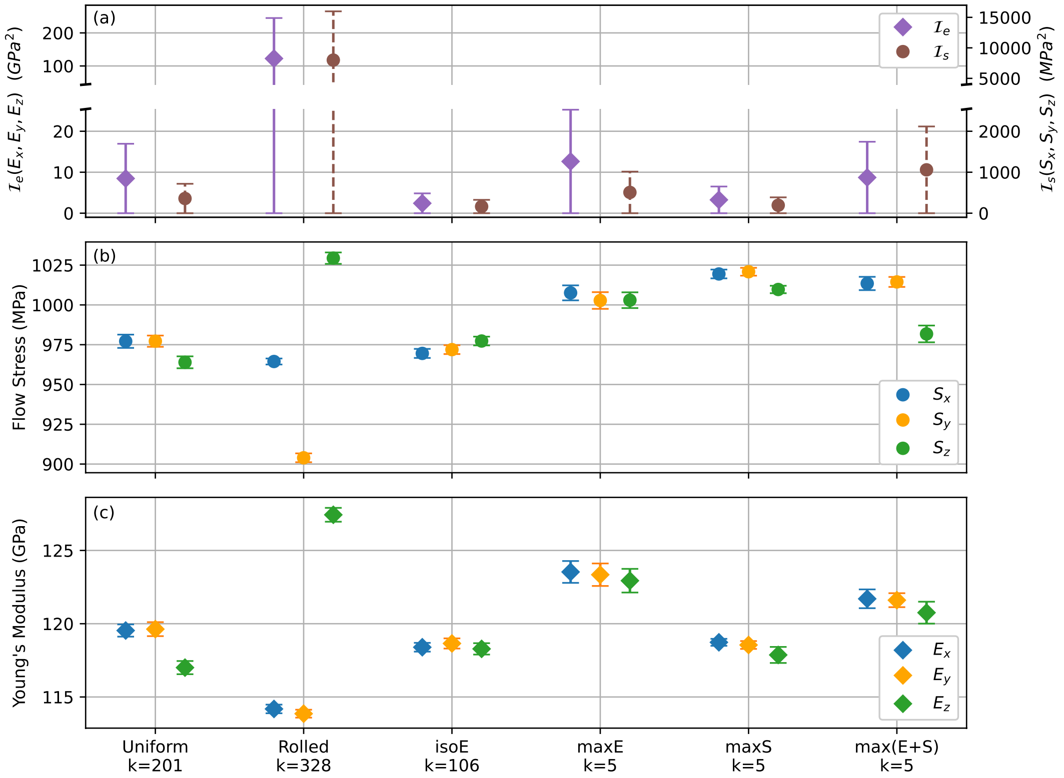

Figure 8.4: (a) Measures of anisotropy ($\mathcal{I}_\mathrm{e}$, $\mathcal{I}_\mathrm{s}$), (b) flow stress at 1.0% total strain, and (c) effective Young's modulus calculated from crystal plasticity simulations applied to $M = 30$ microstructure realizations sampled from two baseline and four optimized textures. Error bars represent the 95% confidence intervals (CI) for the true mean.

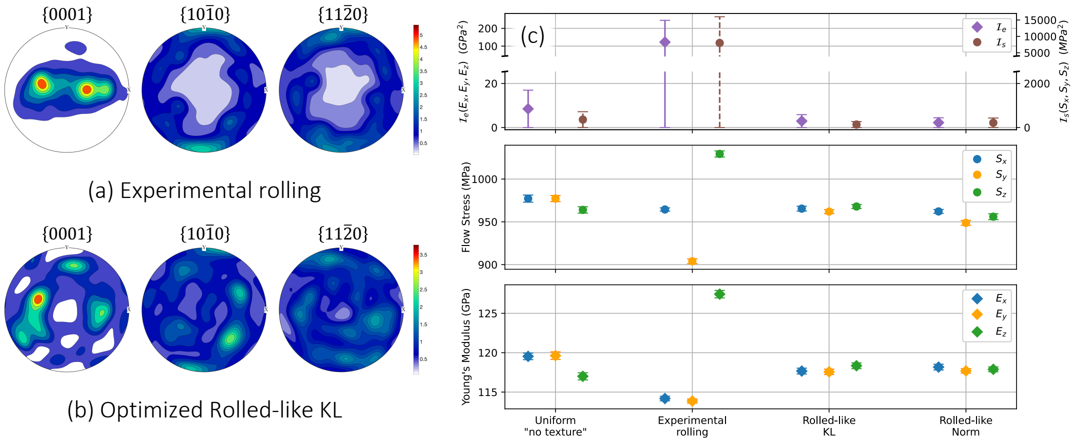

(a) Experimental rolling

(b) Optimized Rolled-like KL

Figure 8.5: (a) Pole figures for experimental rolling texture [15]. (b) Pole figures for the optimized rolled-like texture which minimizes the KL divergence to the rolling texture. Intensities are plotted as multiples of random distribution (MRD). (c) Measures of anisotropy ($\mathcal{I}_{\mathrm{e}}$, $\mathcal{I}_{\mathrm{s}}$), flow stress at 1.0% total strain, and effective Young's modulus calculated from crystal plasticity simulations applied to $M = 30$ microstructure realizations sampled from two baseline and two optimized textures, Rolled-like KL and Rolled-like Norm. Error bars represent the 95% confidence intervals (CI) for the true mean. Optimized Rolled-like textures manifest a significant reduction in anisotropy in both elastic and plastic responses.

8.5 Familiar yet anisotropy-reducing textures

Toward identifying optimized textures that can potentially be attained via conventional manufacturing pathways, the calculations involve minimizing a similarity measure to drive the optimized texture to resemble a rolled texture. Figure 8.5a shows the pole figures for a CP-Ti sample manufactured by conventional rolling [15]. Figure 8.5b presents the designed texture, Rolled-like KL, which is calculated by minimizing the KL divergence to the rolling texture (see Appendix D). Comparing their {0001} pole figures readily shows an acceptable similarity in terms of the location and intensity of orientation distribution.

Figure 8.5c shows the performance of the optimized textures Rolled-like Norm and Rolled-like KL, which are expected to resemble the experimentally rolled texture, while simultaneously minimizing elastic and plastic anisotropy. Results from the EVP-FFT micromechanical calculations confirm the minimal elastic and plastic anisotropy achieved in the polycrystals when starting with these AR textures. While they do not offer large Young's moduli and flow stresses like those textures optimized for maximum properties, they provide much smaller measures of anisotropy than the experimentally rolled texture. Advantageously, the properties of these near-rolled-like textures are comparable to those of a uniform texture, but with the advantage of being potentially more accessible via conventional rolling techniques.

8.6 Strong yet anisotropy-reducing textures

Table 8.2 presents, in the form of Euler angles and pole figures, two highly oriented, yet elastic anisotropy reducing textures, denoted as "Sparse" and "MaxAve". These textures aimed to minimize the elastic anisotropy, while promoting sparsity in the optimized solution. The first texture "Sparse" is distinguished from any other AR texture discussed thus far since it was not confined to maximize any one property or achieve similarity with another texture. This texture only contains $k = 3$ distinct orientations, one of which is dominant (see (D.18) for more details). The other two non-dominant orientations are the single crystal orientations that each maximizes the Young's modulus in x or y direction.

To determine the extent to which this texture minimizes elastic anisotropy, Figure 8.6a presents the measure $\mathcal{I}_{\mathrm{e}}$ calculated from crystal plasticity deformation simulations of polycrystals bearing this texture. Remarkably, the Sparse texture achieves even lower levels of elastic anisotropy than the isoE and uniformly random textures. Yet again, it is shown that an exceedingly strong texture can achieve near isotropic properties.

The elastic moduli in all three directions calculated from the polycrystal simulations are compared in Figure 8.6b. The Sparse texture produces low elastic moduli, comparable to those presented by the isoE texture. Thus, while it is remarkable that such a sparse

Table 8.2: Number of distinct orientations (k) present in each sparse AR texture, and corresponding Bunge Euler angles (°). The textures are also shown in the form of three pole figures, [0001], $[10\bar{1}0]$, and $[11\bar{2}0]$.

Texture	k	Bunge Euler angles $(\phi_1^\circ, \Phi^\circ, \phi_2^\circ)$	Pole figures
Sparse	3	$(189, 90, 181), (81, 90, 269), (126, 50, 224)^*$	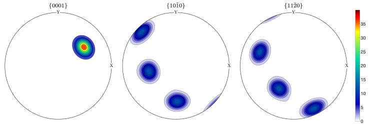
MaxAve	3	$(30, 10, 300), (189, 90, 181), (81, 90, 269)$	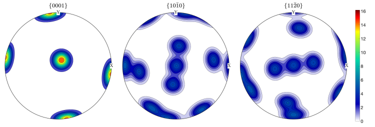

* dominant orientation.

texture can minimize anisotropy, the Sparse texture achieves this attribute at the expense of reduced stiffness.

In light of this trade-off, an alternative set of secondary objectives in texture design was considered. In the convex optimization problem, we set the objective to maximizing the *average* Young's modulus, $\overline{E}$, while maintaining $\mathcal{I}_e(\boldsymbol{\pi}) = 0$ as a constraint. The orientations and pole figures for the resulting texture "MaxAve" are given in Table 8.2. With calculation of the elastic properties of a MaxAve polycrystal, the corresponding $\mathcal{I}_\mathrm{e}$ is much larger than that of the isoE and slightly larger than the uniformly random (no) texture case (Figure 8.6a). This can be expected since, as we have already seen, the uniform texture (or equivalently, equally distributing orientations) does not lead to the lowest anisotropy in mechanical properties. The MaxAve texture, however, leads to a material that is outstandingly stiff (as seen in Figure 8.6b). Its Young's modulus is even greater than that arising from the maxE texture. Thus, the MaxAve material outstandingly breaks the trade-off between elastic anisotropy and stiffness, achieving an anisotropy level similar to no texture case but with a much higher stiffness.

It is worth noting from Table 8.2 that the c-axes of the crystals in MaxAve are nearly equally distributed along the three orthogonal axes of the polycrystal. To ex-

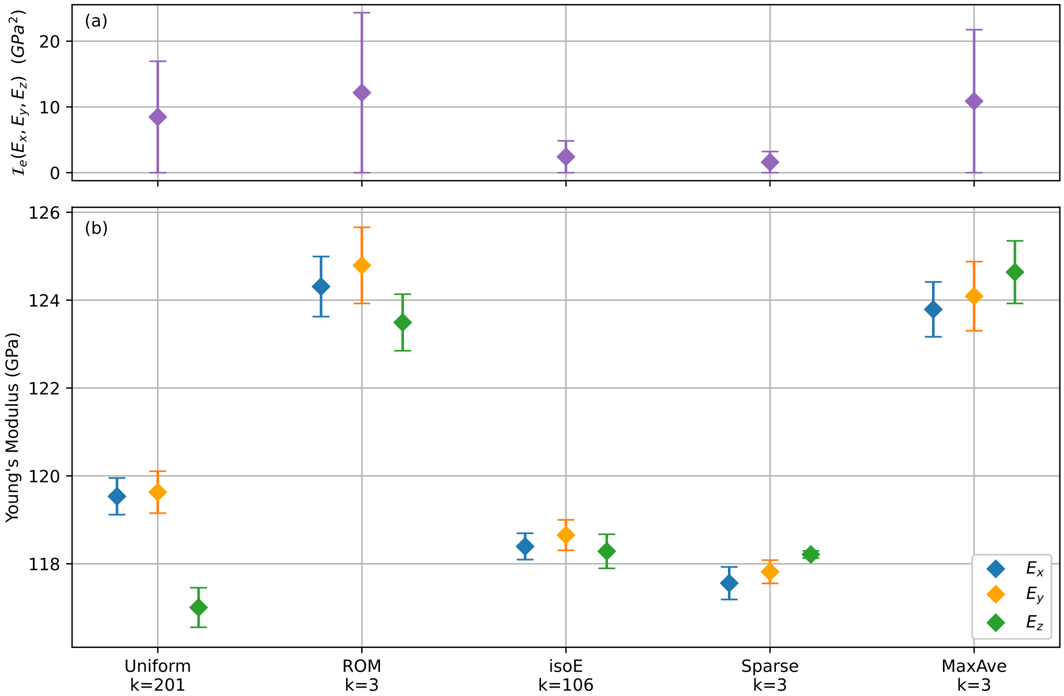

Figure 8.6: (a) Measure of elastic anisotropy $\mathcal{I}_e$, and (b) flow stress at 1.0% total strain calculated from crystal plasticity simulations applied to $M = 30$ microstructure realizations sampled from the rule of mixtures (ROM) texture, the non-sparse AR texture isoE, and two sparse textures. The texture MaxAve is intended to maximize the average Young's modulus, while remaining a sparse texture and minimizing elastic anisotropy. Error bars represent the 95% confidence intervals (CI) for the true mean.

plain MaxAve, we consider a strong, hypothetical texture composed of three, equally weighted orientations, corresponding to the single crystal orientation that maximizes E_a along the x, y, or z axis. This "rule of mixtures" (ROM) texture presumes that a sparse, yet anisotropy reducing texture can be achieved by simply including the three orthogonal crystals equally distributed. Formally, we define this ROM texture as $\boldsymbol{\pi} = \frac{1}{3}\sum_{a\in\{x,y,z\}} \boldsymbol{e}_{j_a^p}$, where $j_a^p = \mathrm{argmax}_{\mathrm{j}\in[\mathrm{d}]}\theta^{\mathrm{p}}_{\mathrm{a,j}}$. Figure 8.6 shows that the ROM polycrystal achieves an overall Young's modulus equal to that of the MaxAve texture, albeit with a slightly higher $\mathcal{I}_\mathrm{e}$. Therefore, the MaxAve texture can be explained as simply one composed of three equally-weighted orientations, each of which maximizes that property in a single direction.

8.7 Transferability and manufacturability of anisotropy-reducing textures

8.7.1 Transferability of the AR textures to other Ti alloys

In this section, we address the question whether the optimal textures calculated by the convex optimization scheme when driven by data for the Ti-6Al-4V alloy would decrease the elastic and plastic anisotropy in other Ti-based materials, such as CP-Ti and Ti-7Al. To this end, we apply the EVP-FFT model to textures optimized for Ti-6Al-4V, but with the intrinsic materials properties of CP-Ti and Ti-7Al, presented in Table 8.1. We neither repeat the data generation process nor solve the optimization problem again.

The single crystals of these three alloys differ in their degree of elastic and plastic anisotropy. To compare the intrinsic level of elastic anisotropy, the universal index of elastic anisotropy A^L [101] is determined for each. This is a non-negative measure for which ideal isotropy is zero. CP-Ti is similar to Ti-6Al-4V but Ti-7Al is evidently naturally lower in elastic anisotropy. As before, the CRSS values for CP-Ti and Ti-7Al are characterized using polycrystal EVP-FFT calculations fit to experimental stress-strain responses [284]. Comparing the CRSS values among the slip modes for the same alloy shows that CP-Ti has the greatest differences and is likely the most plastically anisotropic alloy.

Figure 8.7 shows the mechanical response obtained from an experimentally rolled texture, as well as the two optimized textures, maxE and maxS. Overall, these results confirm that the optimized textures successfully reduce elastic and plastic anisotropy for CP-Ti and Ti-7Al. The small differences between the optimized textures for Ti-6Al-4V and other Ti-based materials can be explained by the variations in the inherent elastic and plastic anisotropy among these materials. For instance, the measure of plastic anisotropy for the maxS texture in Ti-6Al-4V and Ti-7Al are comparable, both smaller than that in CP-Ti. A plausible explanation for such behavior is the larger inherent plastic anisotropy in CP-Ti, i.e., the greater differences among the critical resolved shear stresses required to activate distinct slip modes, when compared to the other two alloys (see Table 8.1).

The maxE texture for Ti-7Al, furthermore, remarkably shows outstanding properties beyond minimizing its anisotropic response. As indicated by the relatively small $\mathcal{I}_{\mathrm{e}}$ in Figure 8.7b, the rolled texture in Ti-7Al polycrystal is associated with low elastic anisotropy. The optimized texture maxE, however, reduces the elastic anisotropy in Ti-7Al, while increasing its effective Young's modulus to a level much higher than that offered by the rolled texture in its strongest direction. Moreover, while not explicitly optimized for maximum flow stress, this texture offers a very low plastic anisotropy and high strength, again almost as high as the strongest direction of the rolled texture. Evidently, the AR textures driven by single crystal data for one Ti-based material can achieve similar properties in other Ti-based materials as well, without the need to repeat the data generation and optimization processes. Put another way, the data-driven convex optimization approach can be used to efficiently generate anisotropy reducing textures for multiple Ti-based materials at once, for which single crystal data can be generated or is available.

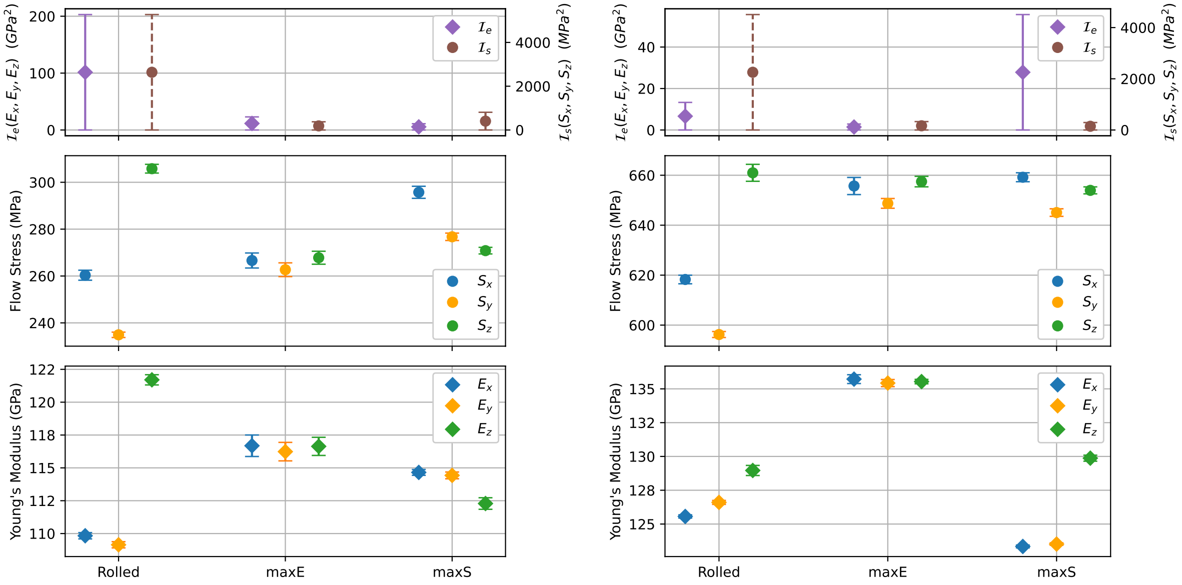

(a) CP-Ti (b) Ti-7Al

Figure 8.7: Effective Young's modulus, flow stress at 1.0% total strain, and measures of anisotropy ($\mathcal{I}_\mathrm{e}$, $\mathcal{I}_\mathrm{s}$) calculated from crystal plasticity simulations applied to $M = 30$ microstructure realizations sampled from the conventionally rolled, optimized maxE, and maxS ODFs for CP-Ti (a) and Ti-7Al (b). Error bars represent the 95% CI for the true mean.

8.7.2 Manufacturability of the AR textures

Using a convex optimization formulation driven by single crystal data, a set of textures that manifest minimal elastic and plastic anisotropy have been predicted. The performance of these textures for Ti-based materials was further verified using micromechanical simulations of a 3D polycrystal microstructure with the EVP-FFT technique, as opposed to experimentation. Over the years, polycrystal models have been advanced to predict the elastic and plastic properties of a polycrystal based on the same properties of the individual crystals and the starting texture, or distribution of the orientation of the constituent grains. 3D spatially resolved models, such as EVP-FFT, further take into account the granular structure, including the location and morphology of the grains and the evolution in the crystallographic and morphological orientation of all grains during deformation. Such polycrystal models have demonstrated the ability to replicate experimental stress-strain responses with given initial texture. Here, polycrystal calculations of the constitutive response starting with the optimized textures were used to determine the influence of textures on material response and demonstrate that these textures successfully achieved their target property. Thus, it seems that textures found here via data-driven optimization might prove useful candidates in producing Ti alloys with reduced anisotropy.

Nevertheless, the feasibility of producing some of the AR textures remains to be addressed. Considering that no current manufacturing technique has yet to make textures with a near-isotropic response, it can be easily anticipated that if any theoretical formulation succeeded in demonstrating an AR texture or textures, these textures would likely not be familiar. The pole figures in Figure 8.3 of the isoE, maxE, maxS, and max(E+S) textures confirm such premise.

While these textures appear uncommon, their manufacturability should not be ruled out. Here, we provide some examples from the literature in which varied, uncommon textures are produced using currently available manufacturing techniques, such as asymmetric rolling, equal-channel angular pressing (ECAP), and additive manufacturing. In [288], laser powder bed fusion (LPBF) technique along with a subsequent annealing process was used to fabricate Ti-6Al-4V samples with a texture fairly similar to the maxE texture presented in this work. Using a die with 120° angle between intersecting channels, initial cylindrical billets made of CP-Ti were subjected to eight ECAP passes with a unique route, which involved 180° rotation of a billet around its longitudinal axis between each consecutive pass [289]. This manufacturing path fabricated samples with textures similar to the optimal texture maxS presented in Figure 8.3.

Since some of the most effective AR textures were uncommon, we incorporated additional constraints to the optimization formulation, such that the texture aimed to reduce anisotropy while still remaining similar to one that is manufactureable via conventional synthesis pathways. We envision that, in practice, producing these AR textures may only entail relatively small modifications to the conventional process. Nevertheless, producing some of the AR textures discovered here in the laboratory might entail challenges. But thanks to the current advances in novel manufacturing techniques, we are confident that the findings in this work provide valuable target textures for designing Ti and Ti alloys with near isotropic behavior.

8.8 Conclusions and final remarks

In this study, we used a combination of 3D microstructure-sensitive crystal plasticity modeling and convex optimization theory to identify optimal textures that minimize elastic and plastic anisotropy while maximizing the effective Young's modulus or strength of multiple Ti-based materials. Anisotropy reducing textures were proposed by a rigorous data-driven approach with reasonably convenient data generation requirements, as straightforward as HCP single crystal directional responses. Multiple additional constraints and objectives were implemented within this approach, tailoring it based on the design problem at hand. The effectiveness of each proposed texture in reducing anisotropy was verified by the EVP-FFT model applied to a polycrystal whose texture approximated the optimized one.

Despite the common association between a strong texture and highly anisotropic elastic and/or plastic response, our approach revealed several highly oriented textures, consisting of as few as five orientations, that show nearly-isotropic elastic and plastic responses. When specifically compared to the results from a typical rolling texture, the optimal textures significantly reduced the elastic and plastic anisotropy, while offering

Young's moduli and strength almost as high as those exhibited by the rolled material along the rolling direction.

To improve practicality, further specifications were implemented into the optimization algorithm to design anisotropy reducing textures that visually resemble a rolled Ti texture. These optimal rolled-like textures featured manufacturability, presented a significant reduction in the anisotropic response of the material, and offered overall elastic and plastic properties superior to those of a typical rolled texture loaded in transverse directions.

Finally, the optimal textures introduced in our work featured transferability. A texture optimized for one Ti-based material through data-generation and optimization processes can be used to minimize anisotropy in other Ti-based materials, without the need to repeat the optimization processes.

Most of the optimal textures introduced in this work do not seem readily manufacturable via conventional pathways. However, recent advances in innovative manufacturing techniques offer a promising prospect for utilizing these optimal textures as desirable target textures when designing Ti-based materials with minimal anisotropy.

Last, the target was to explore optimal crystallographic textures and, therefore, the optimal design of grain structure, such as grain morphology and topological arrangement, is not within the scope of this work. It could be envisioned, however, that the formulation developed here could be extended to include these other important microstructural features.

Chapter 9

Conclusions and recommendations for future work

9.1 Summary and conclusions

Predicting the behavior of metallic materials is vital for identification of potential failure modes and enhancing structural integrity. However, achieving this requires a thorough understanding of the microstructure–property relationships. Polycrystalline materials often possess complex microstructures that have long posed challenges in accurately predicting their overall properties. A notable factor contributing to this complexity is the localized nature of slip within slip bands in these materials. Despite recent advancements in experimental techniques for characterizing slip bands, these methods are often costly and time-consuming to efficiently explore localization behavior of materials under varying conditions. Therefore, there exists a pressing demand for a reliable computational framework that can rigorously model slip bands.

The overarching objective of this dissertation is to develop a meso-scale computational tool based on the theory of crystal plasticity to explicitly model slip bands and the heterogeneous stress and strain fields associated with them, thereby enhancing our understanding of the formation and consequences of slip localization in polycrystalline materials.

Inspired by previous research that revealed the multiplication of mobile dislocations destroying the short-range order and facilitating subsequent dislocation glide, we proposed a rate-dependent softening mechanism to model discrete slip bands in crystalline solids. By incorporating this mechanism, we expanded the capabilities of the EVP-FFT approach by developing the SB-FFT model, which is capable of modeling slip localization. Once the efficacy of the proposed model was verified and validated, we exploited the calculated stress field ahead of the slip band to propose a slip band tip stress-based criterion for identifying slip transmission paths. We showed that the nearest neighbor grain orientation affects slip band development and its potential transmission. Particularly, our results for Mg and Ti indicated that the type of transmitted slip system is correlated with the misorientation between two grains.

Next, we applied the SB-FFT model to experimentally observed slip-twin and slip-slip transmission instances in pure Ti showed that the orientation and curvature of the grain boundary exert a significant influence on the local stress fields at the grain boundary, consequently affecting the slip/twin transmission across the boundary. We further demonstrated that the deformation mechanisms within each grain are not solely dictated by the properties of the host grain, but are also heavily influenced by neighboring grain properties, such as the presence of heterogeneities like slip bands and twins. Finally, in situations where geometric factors were ineffective, the local stress field calculated by our model was capable of determining whether a transmission has occurred in an observed co-located pair, and also the direction of the transmission.

To find the underlying reasons for the recent experimental observation of the positive association between macroscopic yield strength and microscopic slip intensity and slip band spacing, we applied the SB-FFT model to a wide range of FCC and HCP materials. Our results found that, uniformly across all materials, the amount of energy required for deforming a grain heterogeneously via localized slip bands is lower than that required for the homogeneous deformation of the grain via uniformly distributed slip. Furthermore, we showed that the deviation between the levels of energy intensifies as the material becomes stronger, establishing an energetic basis for why stronger materials tend to accumulate more slip within their slip bands. Our simulation results also revealed that a localizing slip band produces a reaction-stress which resists further slip in nearby areas, developing a no activity zone. With this, we demonstrated that the larger slip band spacings observed in stronger materials are ensued from the stronger reaction-stress, and hence the larger no activity zone, associated with slip bands.

Additionally, the simulation of slip localization in one grain and potential microvolume in the neighboring grain revealed that several conditions need to be met simultaneously for microvolumes to form, offering an explanation for their scarcity. These conditions entailed the localization of slip to a sufficient high intensity in the slipping grain, the microvolume grain experiencing higher stress levels than the average stress of its nearest grain neighborhood, and a crystallographic orientation suitable for activating secondary slip under the stress field produced by the slip localization. Analysis of the 3D orientation distributions as they evolve with strain further indicated that microvolumes cause the distribution to become highly skewed, with the extreme tails extending further as strain increases. Lastly, comparison of simulation results with several previously proposed slip transmission criteria suggested that, contrary to current belief, microvolume formation is not related to the propensity of slip transmission.

Next, to design a Ti-6Al-4V microstructure that features strain delocalization, we combined SB-FFT simulations on 3D polycrystals with neural network models, and accounted for grain neighborhood and connectivity throughout the polycrystal through a graph representation of the microstructure. Our results yielded an acceptable performance of the surrogate neural network models in predicting localization-based properties. Furthermore, we demonstrated that while each material property is optimized via a unique microstructure solution, elongated shape of the grains is a common feature among all solutions, proposing a valuable target feature for designing Ti-6Al-4V polycrystals that may overcome the strength-toughness trade-off.

Finally, we combined data-driven methods and crystal plasticity calculations to propose a theoretical framework to derive textures that minimize anisotropy while maximizing Young's modulus or flow stress in titanium alloys. Deformation crystal plasticity simulations of 3D polycrystal microstructure realizations of the optimized textures demonstrated the achievement of target properties. Counterintuitively, our findings revealed that appropriate fractions of a relatively small number of select orientations can reduce elastic or plastic anisotropy. We also derived anisotropy-reducing textures constrained to achieve similarity to those from common metal forming processes like rolling. Lastly, we showed that anisotropy-reducing textures obtained for one alloy can be effectively used for minimizing anisotropy in other Ti alloys, without the need to repeat the data-collection and optimization processes.

9.2 Recommendations for future work

In this dissertation, we implemented the SB-FFT modeling framework to provide insight into the development and implications of slip bands in polycrystalline materials. It is envisioned that the capabilities of this model can be further exploited to advance our understanding of slip bands. The followings are a few research topics recommended for future investigation:

1. Slip reversibility in crystalline materials subjected to cyclic loading: Nucleation

of fatigue cracks in crystalline materials is known to be due to localized, intense slip bands. During a load cycle, reverse slip may differ from slip in the forward direction in precipitation-hardened materials. A recent study [171] used Heaviside-DIC method to directly measure slip irreversibility at the scale of discrete slip bands in a nickel-based superalloy. An investigation of slip bands during the first fatigue cycle revealed that slip bands developed during tension may undergo one of the following configurations during compressive loading: (a) full recovery such that their slip amplitude is zero at the end of the first cycle, (b) partial or no recovery, in which the slip amplitude is in the direction of forward accumulated slip, and (c) a reversal in the direction of slip after tensile and compressive loads. It was further observed that intense slip bands with low-moderate recovery developed in the first cycle are nuclei for cracks that form later in cycling. Now, a critical question worthy of investigation is to identify the microstructural conditions that cause limited recovery of slip bands in cyclic loading. The SB-FFT model with cyclic loading can be used to address this question and provide new insights into the requirements for preventing incipient slip bands from turning into crack-susceptible persistent slip bands.

2. Slip localization in nanolayered, bimetallic composites: A common observation from nanostructured metals is that they succumb to the usual strength-ductility trade-off, rendering the simultaneous yield and ultimate tensile strengths, ductility, and strain hardening unattainable. A recent study on duplex-phase Zr, however, presented a nanolayered, bimetallic composite exhibiting a unique hierarchical 3D structure that yielded high strain hardening, high strength, and high ductility [290]. TEM analysis of dislocations accumulated within the α phase indicated several dislocation lines, on a preferred crystallographic plane, creating pile ups along the

interface. With the macroscopic strain increases, dislocation activity transitioned from single slip to multi-slip and eventually to multi-modal slip. Accordingly, the high strain hardening and ductility of the material were attributed to the increasing dislocation accumulation and the dispersive nature of slip. While slip bands in nanostructured metals are not conventionally considered due to the insufficient space for dislocation accumulation within crystals of nanoscale dimensions [291, 292, 293], this study reveals the relevance of slip bands to the deformation of these materials. Thus, the SB-FFT model developed here is applicable to the problem and capable of providing valuable insights for design of nanolaminates with superior properties.

3. Role of slip bands in the development of stress triaxiality: Several studies have linked high stress triaxiality to faster void growth and crack formation [294, 295]. Slip band stress concentrations can result in a number of instabilities, in both the parent and neighboring crystals. As shown in Appendix A, an example of these instabilities is the heterogeneous, intensified stress triaxiality within and around an active slip band. The SB-FFT method presented here can be used to investigate the role of slip banding in crack or void formation, via analysis of the stress triaxiality maps around and in front of the slip band. Particularly, the dependence of the developed stress triaxiality on crystallographic orientation is to be further studied in future works.

Appendix A

Supplementary materials for Chapter 3

A.1 Role of the stress exponent (n)

To study the effect of the stress exponent (n) on the extent of strain localization within the slip band, the bicrystal setup for which the evolution of localized shear is presented in Figure 3.3 is selected and a set of simulations with different stress exponents have been conducted. In all simulations, the parent crystal has an orientation of (90°, 90°, 45°) and the neighboring grain orientation is (152°, 128°, 136°). Figure A.1 shows the average shear strain accumulated on the slip band system within the band domain ($\bar{\varepsilon}_{\mathrm{SB}}$), normalized by that in the parent matrix ($\bar{\varepsilon}_{\mathrm{M}}$), as the applied strain increases. It is found that a larger stress exponent yields a higher degree of strain localization in the slip band.

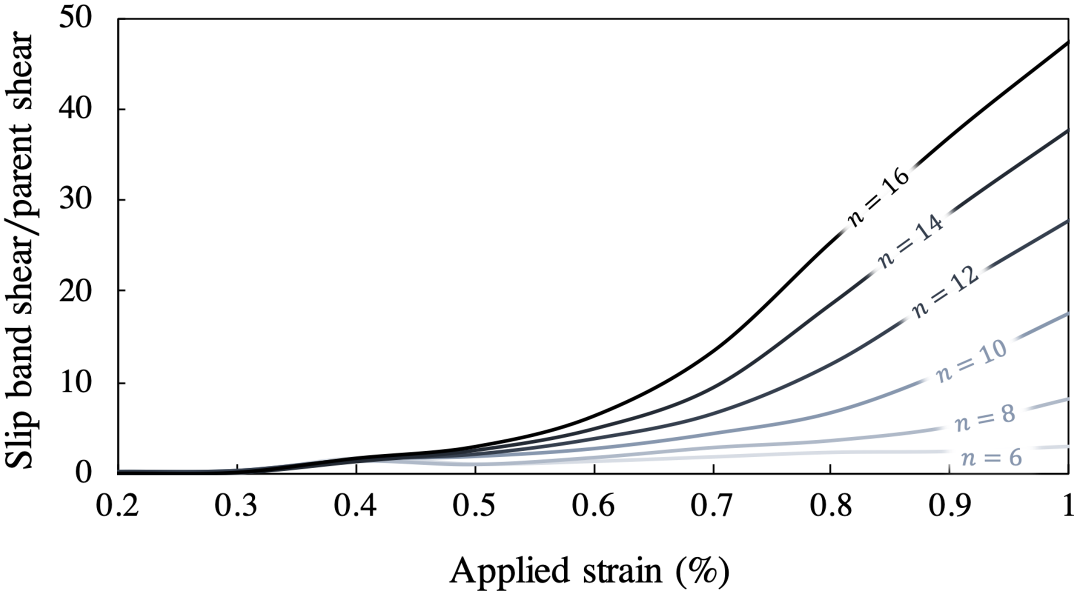

Figure A.1: Average accumulated shear on the slip band system within the band domain normalized by that in the parent grain for different stress exponents exponent (n).

A.2 Contours of equivalent plastic strain

The overall plastic response of the neighboring grain depends on its orientation, i.e., the availability of its slip systems with respect to the far-field strain. As an illustration, Figure A.2 shows the contours of equivalent plastic strain in the three typical cases of soft, moderate, and hard neighbor for CP-Ti bi-crystals subjected to 1% applied strain (properties of grain neighbor orientations for these three cases are listed in Table 3.2). As previously presented in Chapter 3, a harder neighbor promotes faster localization within the band. Furthermore, it is revealed that the neighbor in all three cases has undergone some plasticity, the extent of which varies from one case to another. Plastic strain in the soft neighbor is more uniformly distributed, while in the hard neighbor, it is developed mainly near the grain boundaries, especially at the slip band tip.

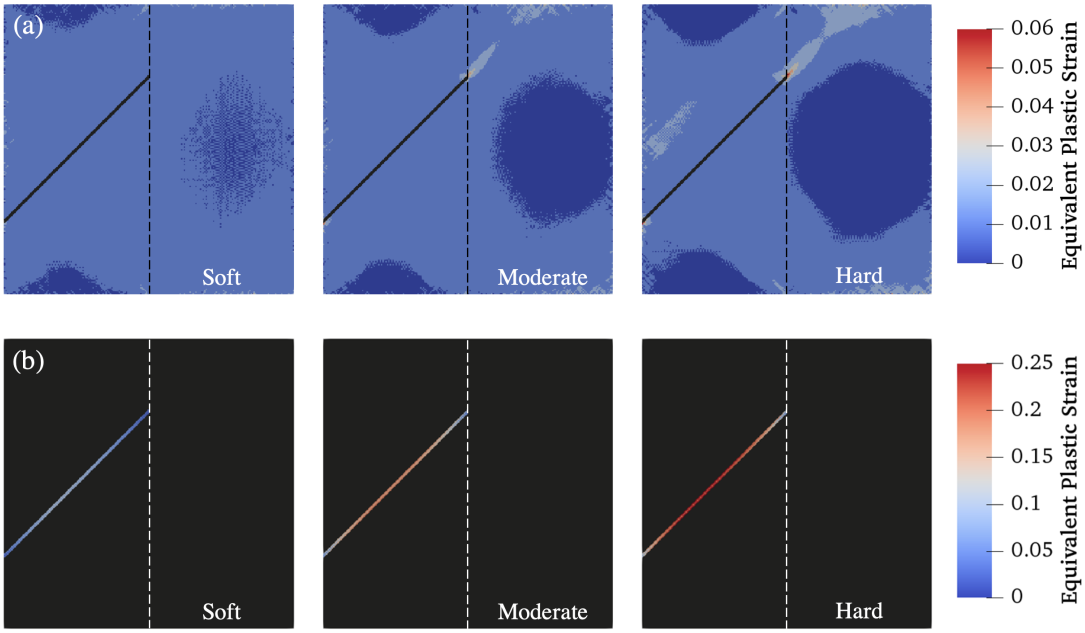

Figure A.2: Distribution of the equivalent plastic strain in (a) parent and neighboring grains, and (b) slip band domain for three cases of soft, moderate, and hard neighbor in CP-Ti bi-crystals subjected to 1% macroscopic strain. Properties of grain neighbor orientations for these three cases are listed in Table 3.2. To represent the heterogeneity better, the slip band in (a) and the two grains in (b) are colored black.

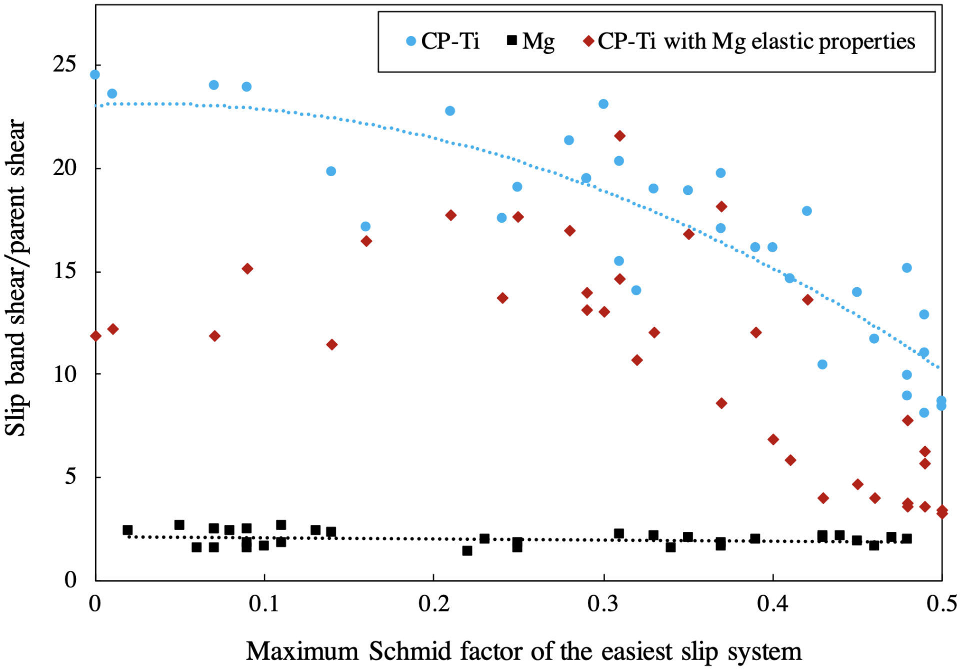

Figure A.3: Average accumulated plastic strain on the slip band system within the slip band normalized by that in the parent grain for CP-Ti, Mg, and a hypothetical material with plastic properties of CP-Ti and elastic properties of Mg at 1% macroscopic applied strain for a broad range of grain neighbor orientations.

A.3 Role of elastic properties on slip localization

To study the effect of elastic properties (e.g., elastic anisotropy) on strain localization within the slip band, in addition to CP-Ti and Mg which were studied in Figure 3.7a, degree of localization is investigated in a hypothetical material with plastic properties of CP-Ti and elastic properties of Mg. Figure A.3 shows the average accumulated shear within the slip band normalized by that in the parent, for a broad range of neighbor orientations. Comparison of the results obtained for these three materials suggests that in addition to plastic properties (e.g., slip strength), elastic properties of HCP materials (e.g., elastic anisotropy) have an effect on strain localization within slip bands. Furthermore, plastic properties appear to have a stronger effect since the results for the hypothetical material are closer to those for CP-Ti than Mg.

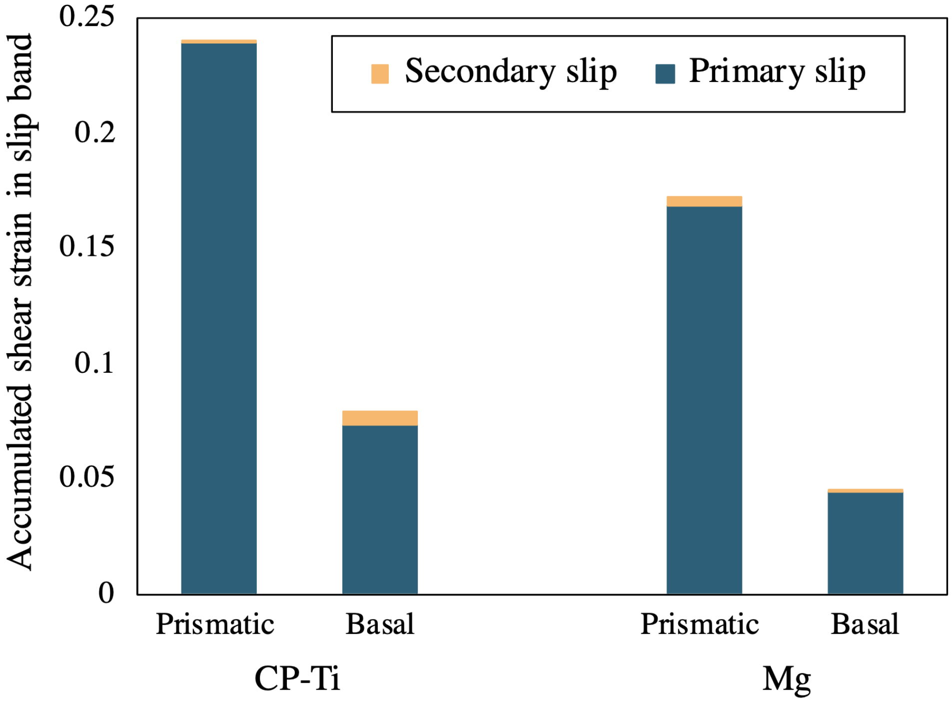

Figure A.4: Extent of secondary slip accumulated within the band domain compared to the primary slip for CP-Ti and Mg with a prismatic/basal slip band subjected to 1% applied strain.

A.4 Secondary slip within the slip band

Figure A.4 shows the extent of primary and secondary slip accumulated in the band domain for CP-Ti and Mg, each with a prismatic or basal slip band. The amount of slip is obtained at 1% applied strain and averaged over 50 different cases, each with a distinct neighbor orientation. Any slip occurred on a system other than slip band system is considered secondary slip. Figure A.4 confirms that, especially for commonly observed situations of basal bands in Mg and prismatic bands in Ti, no significant secondary slip occurs in the band domain.

A.5 Contours of slip on different slip systems

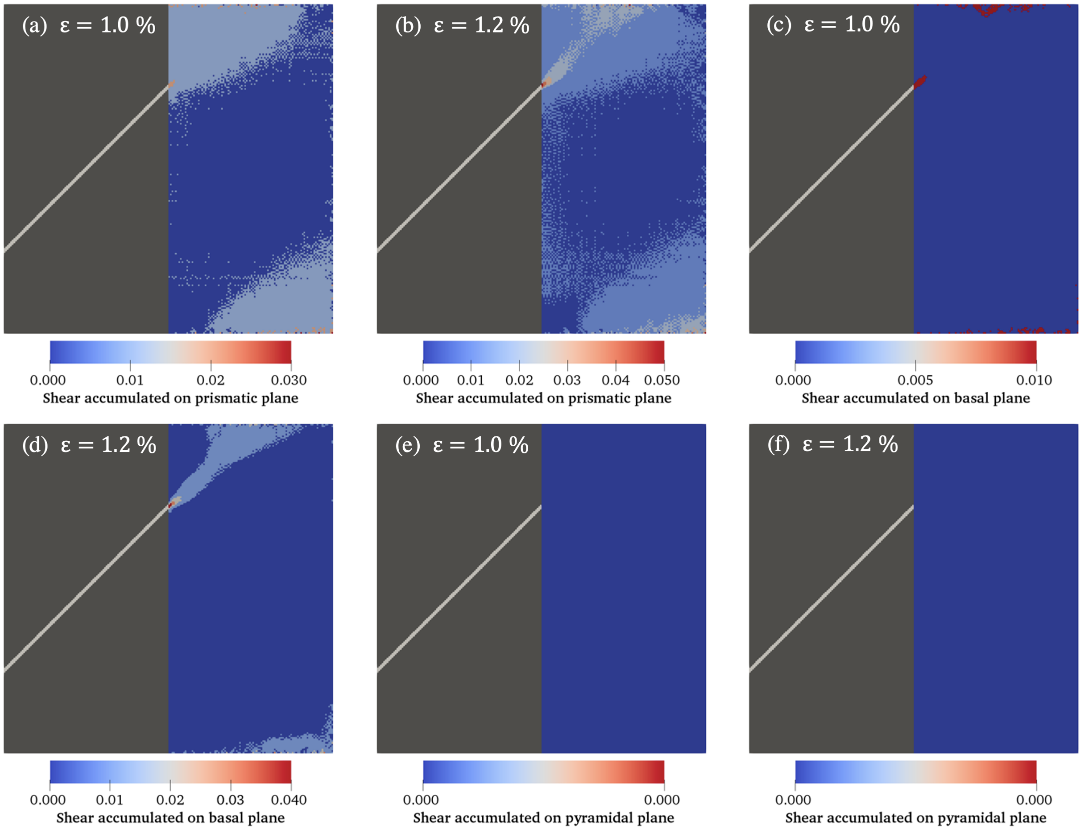

Figure A.5: Accumulated shear strain for slip systems shown in Figure 3.8; prismatic system at (a) 1% and (b) 1.2% applied strain, basal system at (c) 1% and (d) 1.2% applied strain, and pyramidal system at (e) 1% and (f) 1.2% applied strain.

A.6 Contours of stress triaxiality

Figure A.6a, b shows the evolution of stress triaxiality within and around the slip band as the applied strain increases, respectively for a CP-Ti bicrystal with a prismatic band and a Mg bicrystal with a basal band. The Euler angels of the neighboring grain are (22°, 92°, 307°) in CP-Ti and (12°, 58°, 81°) in Mg. With the application of the far-field strain and as the slip band develops in CP-Ti, stress triaxiality in the parent grain starts to become nonuniformly distributed, such that within the band and in some areas around it, a larger triaxiality is formed. At 1% strain, nonuniformity of stress triaxiality is intensified. A strong triaxiality has developed at the intersection of the slip band and the grain boundary. Likewise, in the Mg bicrystal, it is revealed that while some areas in the parent matrix experience a negative triaxiality, material points within the band domain manifest large positive stress triaxialities. While the degree of heterogeneity in and values of triaxiality around the slip band changes from one neighbor orientation to another, this observation holds true for all studied cases. Such increase in stress triaxiality around the band can have implications for formation of voids, especially at the band/GB intersection.

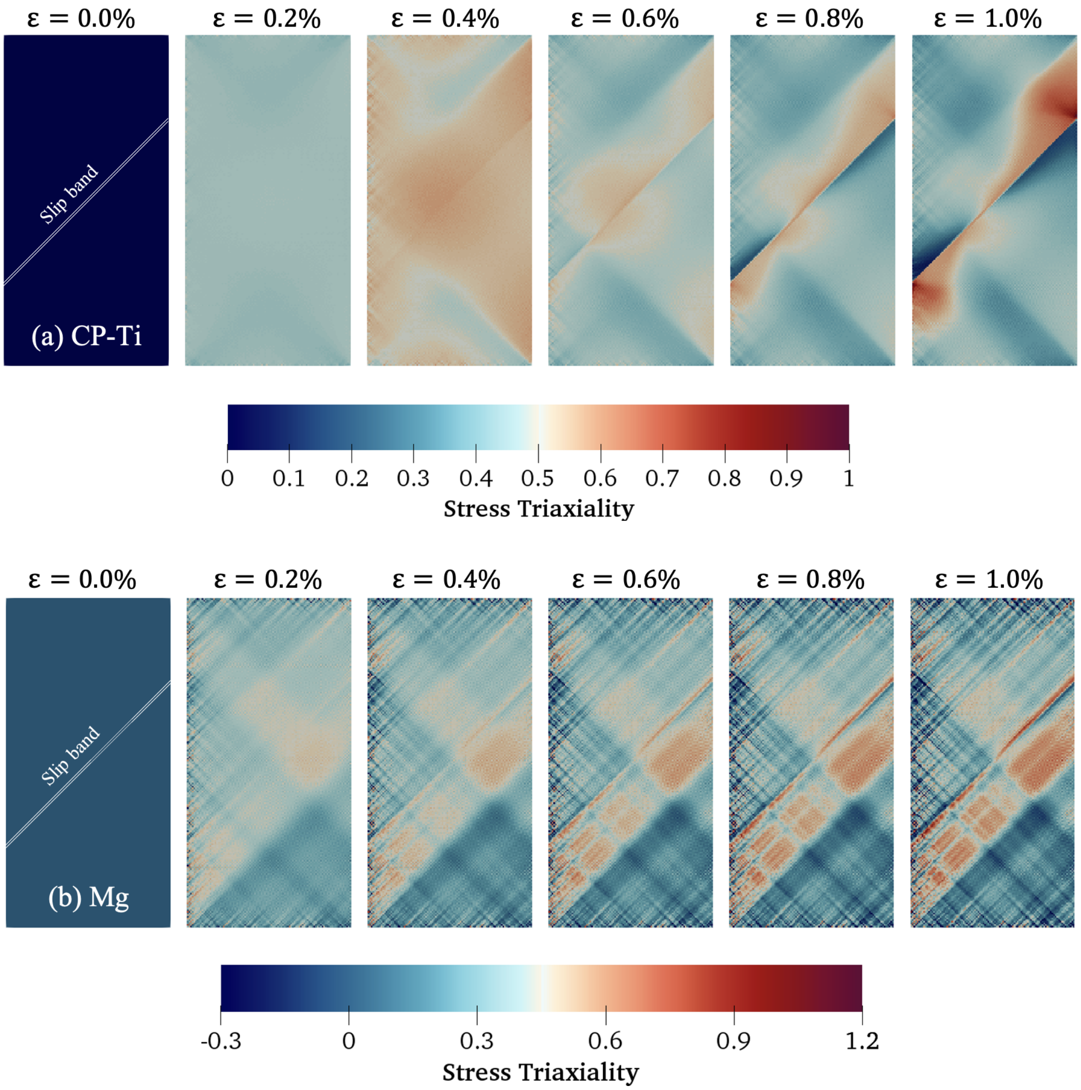

Figure A.6: Distribution of stress triaxiality within and around the slip band as the applied strain increases, for (a) CP-Ti bicrystal with a prismatic band, and (b) Mg bicrystal with a basal band.

Appendix B

Effect of modeling more neighboring grains on local stress fields

In Chapter 4, we investigated how an active SB/twin lamella in one grain influences the local stress field in the neighboring grain by modeling a discrete SB/twin lamella within a bicrystal setup that consists of only the two grains of interest. We did not spatially resolve the stress field in more neighboring grains, relying on the assumption that the local stress field within and around the tip of the slip band or the twin lamella outweighs the stress heterogeneity due to the presence of the next nearest neighboring grains. To check this assumption, we select the pair P2 and repeat our calculations, this time on a model microstructure that contains more neighboring grains. Figure B.1a and b respectively shows the EBSD map of pair P2 and its neighboring grains, and the model microstructure we created for modeling this grain aggregate. Calculated at 2% applied strain, Figure B.1c and d shows the distribution of the resolved shear stress for the experimentally observed twin variant in Grain 2, for the extended model microstructure, respectively without and with a SB modeled in Grain 1. A comparison between Figure B.1c and Figure 4.4c reveals that the direct interaction of neighboring grains slightly changes the stress distribution in Grain 2 in the SB-free models. When a slip band is modeled in Grain 1, the local stress distribution in Grain 2 is heavily influenced by the slip band-induced stress concentration ahead of the band near the grain boundary, as indicated by comparing Figure B.1d and Figure 4.4d. Therefore, the local stress field at the band tip completely outweighs any stress heterogeneities due to the constraint effects from more neighboring grains. This validates our assumption that the local stress fields developed ahead of localized slip/twin bands heavily influence the selection of slip system or twin variant at the GB within the neighboring grain, onto which the transmission is likely to occur. It further demonstrates that resolving more of the neighboring grains does not affect the conclusions made in this work.

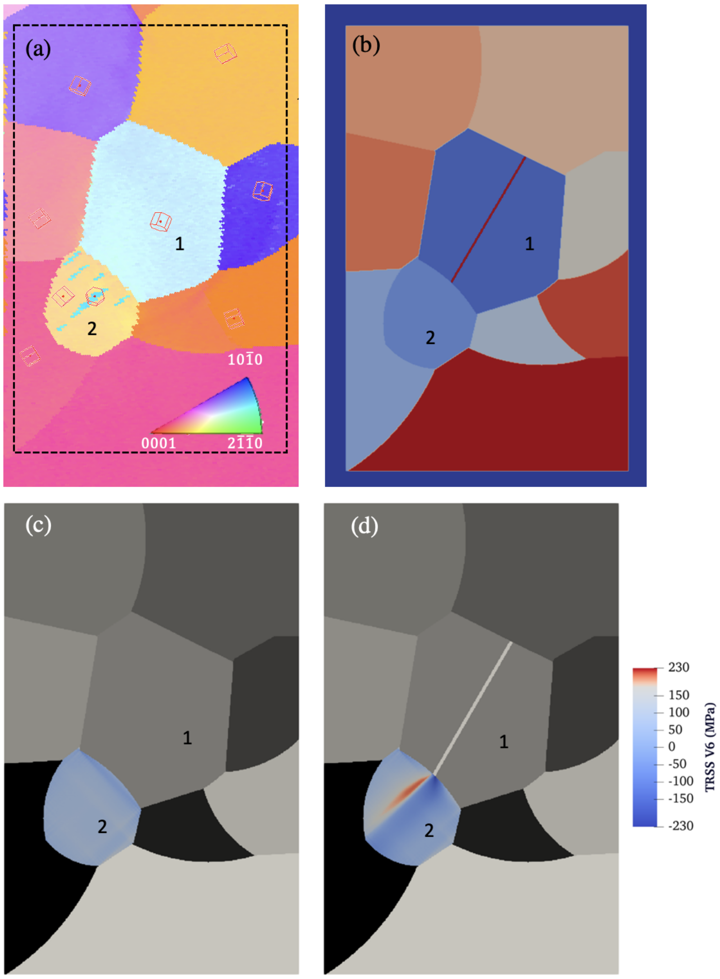

Figure B.1: (a) EBSD map of Grain 1 (slip banded) and Grain 2 (twinned) and their neighboring grains. (b) The microstructure model created for CPFFT calculation of 10 grains contained in the dashed box in (a). (c, d) Calculated field at 2% macroscopic strain of the twin plane resolved shear stress (TRSS) for the $(1\bar{1}02)[\bar{1}101]$ tensile twin variant (V6) (c) without and (d) with an intense slip band in Grain 1

Appendix C

Geometric factors for all orientations investigated in Chapter 6

Table C.1: Values of transmission factors and GROD intensity ahead of the SB for different grain orientations in microstructure models SB1 and SB2. To determine whether a MV forms in each orientation, a threshold of GROD > 1.6° is used. Detailed definition of transmission factors can be found in [11], [13], and [12].

Model	Orientation	Geometric factors								Geometric factors weighted by slip			Residual Burgers vector	GROD (°)	MV
		SF	$\hat{N}$	$\hat{N}_{mod}$	$\hat{M}$	$\hat{M}_{mod}$	$\hat{\chi}$	η (°)	δ (°)	m'_{γ}	S_y	LRB	$\lvert\vec{b_r}\rvert$		
SB1	MV-1	0.18	0.42	0.28	0.35	0.67	0.55	11.6	11.4	0.51	0.49	0.58	1.18	2.21	Y
	O1	0.15	0.41	0.27	0.29	0.59	0.33	8.4	10.8	0.61	0.58	0.64	1.11	2.44	Y
	O2	0.25	0.47	0.28	0.29	0.49	0.35	31.8	39.2	0.41	0.35	0.43	1.34	1.06	N
	O3	0.17	0.37	0.29	0.33	0.63	0.44	73.1	88.1	0.22	0.17	0.26	1.07	1.99	Y
	O4	0.26	0.37	0.25	0.31	0.63	0.45	73.3	73.5	0.30	0.25	0.38	1.07	1.56	N
	O5	0.16	0.39	0.27	0.29	0.57	0.49	10.4	12.7	0.72	0.69	0.73	1.42	1.49	N
	O6	0.25	0.50	0.26	0.30	0.55	0.19	89.3	88.9	0.34	0.32	0.40	1.19	1.27	N
	O7	0.16	0.30	0.25	0.34	0.64	0.32	84.9	86.3	0.09	0.06	0.17	1.02	1.68	Y
	O8	0.24	0.37	0.25	0.29	0.56	0.31	15.7	11.0	0.64	0.60	0.65	1.72	1.33	N
	O9	0.28	0.52	0.28	0.37	0.66	0.48	88.4	88.1	0.29	0.24	0.34	1.39	1.23	N
	O10	0.26	0.50	0.29	0.34	0.58	0.59	83.1	80.1	0.35	0.29	0.38	1.61	1.07	N
	O11	0.24	0.44	0.28	0.34	0.66	0.49	0.1	0.0	0.58	0.58	0.60	1.15	1.52	N
	O12	0.27	0.47	0.29	0.39	0.69	0.41	82.2	78.6	0.19	0.15	0.27	1.12	1.46	N
	O13	0.14	0.41	0.27	0.29	0.58	0.38	6.5	13.8	0.73	0.71	0.75	1.07	1.87	Y
	O14	0.14	0.31	0.24	0.32	0.59	0.34	87.8	88.0	0.07	0.06	0.11	1.32	1.77	Y
	O15	0.24	0.44	0.28	0.35	0.62	0.32	76.0	79.5	0.45	0.42	0.48	1.51	1.27	N
	O16	0.17	0.35	0.29	0.39	0.71	0.25	58.6	31.9	0.23	0.17	0.33	1.41	1.59	N
SB2	MV-2	0.26	0.46	0.26	0.27	0.62	0.48	77.5	79.9	0.30	0.27	0.37	1.14	1.72	Y
	O1	0.24	0.31	0.29	0.36	0.72	0.29	41.6	21.1	0.38	0.27	0.44	1.69	1.90	Y
	O2	0.18	0.44	0.28	0.31	0.60	0.38	90.0	0.1	0.75	0.74	0.77	1.15	2.82	Y
	O3	0.27	0.48	0.28	0.33	0.64	0.43	81.2	79.8	0.29	0.23	0.34	1.13	1.38	N
	O4	0.14	0.34	0.30	0.34	0.66	0.43	47.9	29.2	0.36	0.25	0.40	1.45	1.52	N
	O5	0.14	0.30	0.26	0.30	0.58	0.36	79.1	87.7	0.13	0.10	0.16	1.47	1.78	Y
	O6	0.24	0.34	0.25	0.31	0.57	0.30	88.2	83.6	0.28	0.26	0.32	1.43	2.09	Y
	O7	0.25	0.42	0.25	0.27	0.63	0.42	72.1	72.5	0.38	0.36	0.48	1.13	1.90	Y
	O8	0.17	0.40	0.28	0.32	0.62	0.54	86.1	76.5	0.27	0.25	0.35	0.98	2.06	Y

Appendix D

Supplementary materials for Chapter 8

D.1 Generating microstructure realizations from an optimized texture

As described in the main text, generating microstructure realizations where the true volume fraction, π_j, the j^{th} orientation represents in the polycrystal, precisely matches the optimized volume fraction, $\hat{\pi}_j$ is not feasible. The reason for that is that, for all polycrystalline microstructures, the number, N, of crystals and their relative volumes are fixed.

With this in mind, even if $\boldsymbol{\pi}$ cannot exactly match $\hat{\boldsymbol{\pi}}$, we can assign orientations to crystals in such a way that the difference between $\boldsymbol{\pi}$ and $\hat{\boldsymbol{\pi}}$ is minimized. In the main text, we claim that this approach requires solving a combinatorial optimization problem, and thus we abandon it in favor of sampling orientations from the optimized texture instead. In the following, we rigorously define the aforementioned problem.

Let $\boldsymbol{v} \in \mathbb{R}^N$ be the vector that contains the volume fractions, $\frac{v_i}{V}$, $i \in [N]$, of all N crystals of the polycrystal. Also, if $\boldsymbol{x}_i \in \mathcal{O}_d$ is the "one-hot encoding" vector that describes the orientation of crystal $i \in [N]$, we define as $X \in \{0,1\}^{Nxd}$ the matrix having $\boldsymbol{x}_i^T$ as it's i^{th} row for all $i \in [N]$. We can now rewrite the ODF vector, $\boldsymbol{\pi}$, that we had previously defined as $\boldsymbol{\pi} := \frac{1}{V}\sum_{i\in[N]} v_i \cdot \boldsymbol{x}_i$, as:

$$\boldsymbol{\pi} = X^T \boldsymbol{v}. \tag{D.1}$$

Given that, we can define the mean square error (MSE) between $\boldsymbol{\pi}$ and $\hat{\boldsymbol{\pi}}$ as:

$$\|\boldsymbol{\pi} - \hat{\boldsymbol{\pi}}\|_2^2 = \boldsymbol{v}^T X X^T \boldsymbol{v} - 2\boldsymbol{v}^T X \hat{\boldsymbol{\pi}} + \hat{\boldsymbol{\pi}}^T \hat{\boldsymbol{\pi}} \tag{D.2}$$

Then, the optimal, in terms of MSE, way to generate a microstructure realization for a given optimized texture, $\hat{\boldsymbol{\pi}}$, is by solving the following problem:

$$\begin{aligned} \min\nolimits_{\mathrm{X}} \quad & \boldsymbol{v}^T X X^T \boldsymbol{v} - 2\boldsymbol{v}^T X \hat{\boldsymbol{\pi}} \\ \text{s.t.} \quad & X \in \{0,1\}^{Nxd}, \quad \boldsymbol{x}_i^T \mathbb{1} = 1,\ \forall i \in [N] \end{aligned} \tag{D.3}$$

The above is an integer programming problem, solving of which would add unnecessary complexity to our method. Besides, minimizing the MSE does not explicitly provide any guarantee about preserving the structure of $\hat{\boldsymbol{\pi}}$ in $\boldsymbol{\pi}$. Thus, it is possible that the solution of (D.3) will have a different sparsity and/or indices of non-zero nodes from the optimized texture. Finally, there is no theoretical guarantee about the maximum value of the solution of (D.3). This means that, for some textures, even the texture, $\boldsymbol{\pi}$, of the microstructure realization that minimizes the MSE might not be sufficiently close to the optimized texture, $\hat{\boldsymbol{\pi}}$.

For these reasons, we follow the alternate approach of simply sampling the orientation of each crystal from the texture. We generate M microstructure realizations for each optimized texture, as detailed in the Sampling from the optimized texture subsection. As stated in the same subsection and repeated here for completeness, for reasonably large M, the sample mean of those textures should converge to the optimized texture, circumventing the problems associated with assigning orientations to crystals in a microstructure with fixed grain morphology and arrangement:

$$\frac{1}{M}\sum_{q\in[M]} \boldsymbol{\pi}_q \approx \mathbb{E}\big[\Pi\big] = \hat{\boldsymbol{\pi}}\,. \tag{D.4}$$

A caveat of this new approach is that, because of the way that we sample orientations from the texture, we are implicitly making the assumption that the overall properties of the polycrystal are calculated as the unweighted average over the properties of the individual crystals (see (8.11)). In Figure D.1, we verify that this assumption is reasonable, as long as M is large enough. Specifically, we sample $M = 30$ microstructure realizations for each one of the three selected textures and show that the sample means of the effective Young's modulus and flow stress fall very close to those predicted by the averaging scheme introduced in (8.11), while exhibiting low variance among them. Note that the low variance indicates that even a single realization is likely to have a property value closed to the desired one.

D.2 Detailed formulation of optimization problems

Here, we provide further details on the optimization problems presented in Section 7.2. We select our measure of anisotropy with respect to property P to be $\mathcal{I}_p = \mathcal{I}(P_x, P_y, P_z) =$

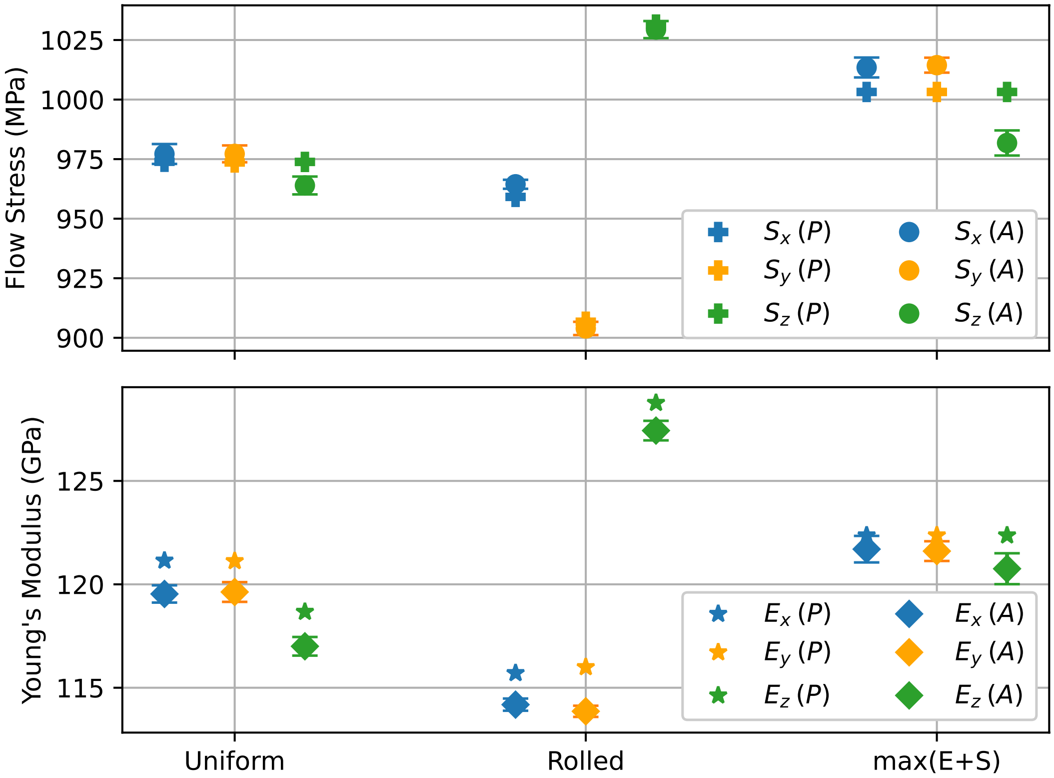

Figure D.1: Predicted (P) and actual (A) Young's modulus and flow stress at 1.0% total strain calculated from crystal plasticity simulations applied to $M = 30$ microstructure realizations sampled from two baseline textures, uniformly random and conventionally rolled textures, as well as one anisotropy reducing texture, max(E+S). Error bars represent the 95% CI for the true mean.

$\sum_{s\in\{x,y,z\}}(P_s - \overline{P})^2$. In view of (8.8), we can expand this as:

$$\mathcal{I}_p(\boldsymbol{\pi}) = \boldsymbol{\pi}^T H_p \boldsymbol{\pi}, \tag{D.5}$$

where

$$H_p = (\boldsymbol{\theta}_x^p - \boldsymbol{\mu}_p)(\boldsymbol{\theta}_x^p - \boldsymbol{\mu}_p)^T + (\boldsymbol{\theta}_y^p - \boldsymbol{\mu}_p)(\boldsymbol{\theta}_y^p - \boldsymbol{\mu}_p)^T + (\boldsymbol{\theta}_z^p - \boldsymbol{\mu}_p)(\boldsymbol{\theta}_z^p - \boldsymbol{\mu}_p)^T, \tag{D.6}$$

$$\boldsymbol{\mu}_p = \frac{1}{3}(\boldsymbol{\theta}_x^p + \boldsymbol{\theta}_y^p + \boldsymbol{\theta}_z^p). \tag{D.7}$$

It now becomes clear that we can constrain the feasible region to include only strictly isotropic solutions (i.e. $\mathcal{I}_p(\boldsymbol{\pi}) = 0$) by enforcing d linear constraints, $H_p\boldsymbol{\pi} = 0$. Then, considering the following for maximizing the average property $\overline{P}$,

$$\begin{aligned} \max_{\boldsymbol{\pi}} \quad & \overline{P}(\boldsymbol{\pi}) \\ \text{s.t.} \quad & \boldsymbol{\pi} \in \Delta_{d-1}, \quad \mathcal{I}_e(\boldsymbol{\pi}) = 0, \quad \mathcal{I}_s(\boldsymbol{\pi}) = 0 \end{aligned} \tag{D.8}$$

we can rigorously define the following optimization problems, each of which maximizes one or both of Young's modulus and plastic flow stress, while constraining the solution to be both elastically and plastically isotropic:

1a. **Maximizing the average Young's modulus, $\overline{E}$:**

$$\begin{aligned} \max_{\boldsymbol{\pi}} \quad & \boldsymbol{\mu}_e^T\boldsymbol{\pi} \\ \text{s.t.} \quad & \boldsymbol{\pi} \in \Delta_{d-1}, \quad H_e\boldsymbol{\pi} = 0, \quad H_s\boldsymbol{\pi} = 0 \end{aligned} \tag{D.9}$$

1b. **Maximizing the average flow stress, $\overline{S}$:**

$$\begin{aligned} \max_{\boldsymbol{\pi}} \quad & \boldsymbol{\mu}_s^T\boldsymbol{\pi} \\ \text{s.t.} \quad & \boldsymbol{\pi} \in \Delta_{d-1}, \quad H_e\boldsymbol{\pi} = 0, \quad H_s\boldsymbol{\pi} = 0 \end{aligned} \tag{D.10}$$

1c. **Maximizing both $\overline{E}$ and $\overline{S}$:**

$$\begin{aligned} \max_{\boldsymbol{\pi}} \quad & (\boldsymbol{\mu}_e + \boldsymbol{\mu}_s)^T\boldsymbol{\pi} \\ \text{s.t.} \quad & \boldsymbol{\pi} \in \Delta_{d-1}, \quad H_e\boldsymbol{\pi} = 0, \quad H_s\boldsymbol{\pi} = 0 \end{aligned} \tag{D.11}$$

All of the above are linear programs (LP) with linear objective function and linear constraints that can be solved computationally efficiently to high accuracy by standard

LP solvers. These solvers are widely available and use algorithms such as simplex method and interior-point method [296]. This is in stark contrast to the original combinatorial optimization problem over $\mathcal{O}_d^N$ which can have prohibitively large, in fact, exponential, computational complexity in the worst-case. In Chapter 8, we refer to the solutions of (D.9), (D.10), and (D.11) as maxE, maxS, and max(E+S), respectively. The pole figures for these textures are shown in Figure 8.3 and their effective properties and anisotropy measures are presented in Figure 8.4.

Furthermore, constraining the optimization vector to live in the $(d-1)$-dimensional simplex instead of the combinatorial space $\mathcal{O}_d^N$, provides even more flexibility. That is, when given an ODF, $\boldsymbol{\pi}' \in \Delta_{d-1}$, that corresponds to some texture of interest, optimization of any convex function $g(\boldsymbol{\pi}, \boldsymbol{\pi}') : \Delta_{d-1} \times \Delta_{d-1} \to \mathbb{R}$, either as part of the objective or as part of a constraint, can be readily included. This conveniently enables the design of accessible textures, as proposed earlier. Specifically, if $\boldsymbol{\pi}' = \boldsymbol{\pi}_{rol}$ is the ODF of a known texture manufactured via rolling and $g(\cdot)$ is a similarity measure between probability distributions, we can obtain an accessible texture by minimizing its distance to the rolled texture,

$$\begin{aligned} \min_{\boldsymbol{\pi}} \quad & g(\boldsymbol{\pi}, \boldsymbol{\pi}_{rol}) \\ \text{s.t.} \quad & \boldsymbol{\pi} \in \Delta_{d-1}, \quad \mathcal{I}_e(\boldsymbol{\pi}) = 0, \quad \mathcal{I}_s(\boldsymbol{\pi}) = 0 \end{aligned} \tag{D.12}$$

Then we explore the use of two similarity measures. First, we consider the ℓ_1-norm, $g(\boldsymbol{\pi}, \boldsymbol{\pi}') = \|\boldsymbol{\pi} - \boldsymbol{\pi}'\|_1$, using which (D.12) becomes:

2a. **Minimizing the ℓ_1-norm to a rolled texture:**

$$\begin{aligned} \min_{\boldsymbol{\pi}} \quad & \|\boldsymbol{\pi} - \boldsymbol{\pi}_{rol}\|_1 \\ \text{s.t.} \quad & \boldsymbol{\pi} \in \Delta_{d-1}, \quad H_e\boldsymbol{\pi} = 0, \quad H_s\boldsymbol{\pi} = 0 \end{aligned} \tag{D.13}$$

The ℓ_1-norm is not only convex but also allows for (D.13) to be rewritten as a linear program and solved effortlessly. However, when it comes to comparing probability distributions, there exist more suitable measures, such as the KL divergence, $g(\boldsymbol{\pi}, \boldsymbol{\pi}') = \sum_{j\in[d]} f_{KL}(\pi_j, \pi'_j)$, where f_{KL} is a function of two scalars defined as:

$$f_{KL}(x,y) = \begin{cases} x\log(\frac{x}{y}), & \text{if } x, y > 0 \\ 0, & \text{if } x = y = 0 \\ +\infty, & \text{otherwise} \end{cases} \tag{D.14}$$

Technically, the KL divergence is not a distance as $g(\boldsymbol{\pi}, \boldsymbol{\pi}') \neq g(\boldsymbol{\pi}', \boldsymbol{\pi})$. However, here this is not a problem as we keep one of the arguments fixed, $\boldsymbol{\pi}' = \boldsymbol{\pi}_{rol}$, and only optimize over $\boldsymbol{\pi}$. Moreover, KL divergence, like the ℓ_1-norm, is convex, albeit using it on the objective results in a geometric program in convex form [297]. These problems are in general harder to solve than linear programs; yet efficient algorithms exist [298]. Thus, we can modify (D.12) and use an appropriate solver to find a solution to:

2b. **Minimizing the KL divergence to a rolled texture:**

$$\begin{aligned} \min_{\boldsymbol{\pi}} \quad & \sum_{j\in[d]} f_{KL}(\pi_j, \pi_{rol,j}) \\ \text{s.t.} \quad & \boldsymbol{\pi} \in \Delta_{d-1}, \quad H_e\boldsymbol{\pi} = 0, \quad H_s\boldsymbol{\pi} = 0 \end{aligned} \tag{D.15}$$

Now, by looking at (D.14) we immediately notice an obvious benefit of using the KL divergence in the place of the ℓ_1-norm. That is, for KL divergence to be finite, orientation nodes that have zero probability to appear in the baseline rolled texture, must also be assigned zero probability on the orientation distribution of the optimized texture. Conversely, the optimized orientation distribution cannot have zero weights at the indices where the orientation distribution of the baseline texture has non-zero values. Intuitively, this means that the location of the poles of the solution to (D.15), obtained with the KL divergence, must coincide with the location of the poles of the baseline rolled texture. We visually confirm this similarity by looking at the pole figures in Figure 8.5. Furthermore, the plot in Figure 8.5 shows that the solutions to (D.13) and (D.15), respectively referred to as Rolled-like Norm and Rolled-like KL textures, produce nearly isotropic mechanical properties, with the KL divergence method offering slightly higher values of strength.

D.3 Sparsity considerations

As mentioned in Section 7.3, we also explore the design of anisotropy reducing textures with sparse orientation distributions, by modifying $\min_{\boldsymbol{\pi}\in\Delta_{\mathrm{d}-1}} \mathcal{I}_{\mathrm{p}}(\boldsymbol{\pi})$ to add a regularizer that penalizes non-sparse solutions as:

$$\begin{aligned} \min_{\boldsymbol{\pi}} \quad & \mathcal{I}_p(\boldsymbol{\pi}) + \lambda\|\boldsymbol{\pi}\|_0 \\ \text{s.t.} \quad & \boldsymbol{\pi} \in \Delta_{d-1}, \end{aligned} \tag{D.16}$$

where $\lambda > 0$ is a regularization parameter and $\|\boldsymbol{\pi}\|_0$ denotes the number of nonzero elements of $\boldsymbol{\pi}$.

However, the ℓ_0-“norm”, $\|\boldsymbol{\pi}\|_0$, is not convex and (D.16) cannot be solved efficiently. Also, for any $\boldsymbol{\pi} \in \Delta_{d-1}$, the ℓ_1-norm is fixed to one, i.e., $\|\boldsymbol{\pi}\|_1 = \sum_{j\in[n]} |\pi_j| = 1$. Thus, the commonly used approach of using the ℓ_1-norm as a sparsity promoting measure is not applicable here. Instead, we explore two alternative approaches. First, we use an algorithm which was specifically designed and analyzed as a surrogate for cardinality penalized optimization over probability vectors [299]. Additionally, we develop a problem-specific approach, in which, by examining the structure of the H_p matrix, we reveal that there exists a class of problems, for whose solutions, if unique, we establish a strict upper bound on their cardinality, i.e., the number of unique orientations that constitute them.

D.3.1 Sparse probability measure recovery schemes

The original cardinality constrained problem in (D.16) has been shown to be efficiently approximated by the following optimization problem [299]:

3a. **Sparse orientation distribution recovery scheme:**

$$\begin{aligned} &\min\nolimits_{\mathrm{j}\in[\mathrm{d}]}\{\min\nolimits_{\boldsymbol{\pi},\tau}\ \boldsymbol{\pi}^T H_p \boldsymbol{\pi} + \tau\} \\ &\qquad\qquad \text{s.t.}\quad \boldsymbol{\pi}\in\Delta_{d-1}, \tau\geq 0, \pi_j \geq\ \lambda/\tau \end{aligned} \tag{D.17}$$

In (D.17), we first solve d inner convex quadratically constrained quadratic minimization programs and then select the solution of the one with the minimum objective value. We also consider a variation, where after solving the d inner programs, we instead pick the solution with the minimum cardinality, i.e.:

3b. **Sparse orientation distribution recovery scheme with minimum cardinality selection:**

$$\begin{aligned} &\min\nolimits_{\mathrm{j}\in[\mathrm{d}]}\ \|\boldsymbol{\pi}_{\mathrm{j}}\|_0, \quad \text{where} \\ &\boldsymbol{\pi}_j\ :=\ \operatorname{argmin}_{\boldsymbol{\pi},\tau}\ \boldsymbol{\pi}^T H_p \boldsymbol{\pi} + \tau \\ &\qquad\qquad \text{s.t.}\quad \boldsymbol{\pi}\in\Delta_{d-1}, \tau\geq 0, \pi_j \geq\ \lambda/\tau \end{aligned} \tag{D.18}$$

Solving (D.17) results in a sparse texture with $k = 9$ distinct orientations. While this solution is not as sparse as the maxE and maxS textures, it is significantly sparser than the solution of $\min_{\boldsymbol{\pi}\in\Delta_{\mathrm{d}-1}} \mathcal{I}_{\mathrm{p}}(\boldsymbol{\pi})$, referred to as the isoE texture. Furthermore, solving (D.18) for $p = e$ and $\lambda = 5 * 10^{-6}$ produces a texture with the minimum number of orientations $k = 3$. In Figure 8.6, we refer to this solution as the texture Sparse. As expected, the texture Sparse, along with the ROM texture, consists of the fewest number of orientations.

D.3.2 Exploiting the structure of the constraints

In addition to the regularization-based methods described in the previous, we devise another, fundamentally different, approach for the discovery of strong, yet anisotropy reducing textures. We achieve this by exploiting the structure of the optimization problem's constraints. To see this, suppose that we simply want to solve the problem of designing a texture that maximizes the average Young's modulus or flow stress, $\overline{P}$, while being nearly isotropic with respect to that same property:

3c. **Sparse orientation distribution recovery by optimizing a linear function:**

$$\begin{aligned} \max_{\boldsymbol{\pi}} \quad & \boldsymbol{\mu}_p^T \boldsymbol{\pi} \\ \text{s.t.} \quad & \boldsymbol{\pi} \in \Delta_{d-1}, \quad H_p \boldsymbol{\pi} = 0 \end{aligned} \tag{D.19}$$

This problem has $d+1$ equality constraints ($H_p\boldsymbol{\pi} = 0$ and $\boldsymbol{\pi}^T \mathbb{1} = 1$) and d inequality constraints ($\pi_j \geq 0$, $\forall j \in [d]$). We start by making a key observation about the rank of the matrix H_p, which is used to define d of the equality constraints. After calculating the parameter vectors $\boldsymbol{\theta}_a^p$, $a \in \{x, y, z\}$, $p \in \{e, s\}$, we notice that $\boldsymbol{\theta}_x^p, \boldsymbol{\theta}_y^p$ and $\boldsymbol{\theta}_z^p$ are linearly independent $\forall p \in \{e, s\}$. However, the vectors $\boldsymbol{\theta}_x^p - \boldsymbol{\mu}_p, \boldsymbol{\theta}_y^p - \boldsymbol{\mu}_p$ and $\boldsymbol{\theta}_z^p - \boldsymbol{\mu}_p$ are only pairwise linearly independent as:

$$\begin{aligned} \boldsymbol{\theta}_x^p - \boldsymbol{\mu}_p &= \boldsymbol{\theta}_x^p - \frac{1}{3}(\boldsymbol{\theta}_x^p + \boldsymbol{\theta}_y^p + \boldsymbol{\theta}_z^p) \\ &= -[\boldsymbol{\theta}_y^p - \frac{1}{3}(\boldsymbol{\theta}_x^p + \boldsymbol{\theta}_y^p + \boldsymbol{\theta}_z^p)] - [\boldsymbol{\theta}_z^p - \frac{1}{3}(\boldsymbol{\theta}_x^p + \boldsymbol{\theta}_y^p + \boldsymbol{\theta}_z^p)] \\ &= -(\boldsymbol{\theta}_y^p - \boldsymbol{\mu}_p) - (\boldsymbol{\theta}_z^p - \boldsymbol{\mu}_p). \end{aligned} \tag{D.20}$$

Now, let us define the matrix $\Theta \in \mathbb{R}^{d \times 3}$ as:

$$\Theta = [\boldsymbol{\theta}_x^p - \boldsymbol{\mu}_p, \quad \boldsymbol{\theta}_y^p - \boldsymbol{\mu}_p, \quad \boldsymbol{\theta}_z^p - \boldsymbol{\mu}_p]. \tag{D.21}$$

As the columns of Θ are pairwise linearly independent, but not linearly independent, we have that $\text{rank}(\Theta) = 2$. Now, note that $H_p = \Theta\Theta^T$ and, therefore, $\text{rank}(H_p) = \text{rank}(\Theta\Theta^T) = \text{rank}(\Theta) = 2$.

Additionally, let us denote $F \subset \mathbb{R}^d$ the polyhedron which comprises the feasible region of (D.19). For some vector $\boldsymbol{\pi} \in F$, let $J(\boldsymbol{\pi}) = \{j : \boldsymbol{e}_j^T \boldsymbol{\pi} = 0\} = \{j : \pi_j = 0\}$ be the set of the inequalities that are active on $\boldsymbol{\pi}$. Then, $\boldsymbol{\pi}$ is a vertex of F if and only if the set of vectors that consists of the rows of H_p, the $\mathbb{1}$ vector and the vectors $\boldsymbol{e}_j$, $\forall j \in J(\boldsymbol{\pi})$ linearly spans the vector space $\mathbb{R}^d$ [300]. However, as $\text{rank}(H_p) = 2$, for the above set of vectors to span $\mathbb{R}^d$, it must contain at least $d-3$ of the d basis vectors $\boldsymbol{e}_j$, $j \in [d]$. Equivalently, for $\boldsymbol{\pi} \in F$ to be a vertex of F at least $d-3$ inequalities of the form $\pi_j \geq 0$, $j \in [d]$ must be satisfied with equality. In terms of (D.19), this implies that for an orientation distribution to be a vertex of F, its sparsity must be $k \leq 3$.

Now, suppose that (D.19) has a unique solution. Then, because we have a linear objective function which has a unique minimum over a polyhedron, the minimum must occur on a vertex of the polyhedron. Thus, if the solution to (D.19) is unique, its sparsity must be $k \leq 3$. Of course, we cannot know if the solution to the optimization program is unique in advance. However, given its simplicity compared to (D.17) and (D.18), along with the added benefit that it maximizes Young's modulus or flow stress, (D.19) can become our first recourse when designing strong, but anisotropy reducing textures. In Figure 8.6, we refer to the solution of (D.19) for $p = e$ as MaxAve texture. This texture has only $k = 3$ distinct orientations present, exactly matching the upper bound we established for unique solutions. Similarly, observe that in Figure 8.4, the solutions of (D.9), (D.10) and (D.11) have sparsity $k = 5$, matching the rank of the matrix of linear equality constraints, $[H_e, H_s, \mathbb{1}]^T$.

Bibliography

[1] Z. Zheng, D. S. Balint, and F. P. Dunne, *Rate sensitivity in discrete dislocation plasticity in hexagonal close-packed crystals*, *Acta Materialia* **107** (2016) 17–26.

[2] Y. Huang and J. Jiang, *A critical review of von mises criterion for compatible deformation of polycrystalline materials*, *Crystals* **13** (2023), no. 2 244.

[3] J. Stinville, M. Charpagne, A. Cervellon, S. Hemery, F. Wang, P. Callahan, V. Valle, and T. Pollock, *On the origins of fatigue strength in crystalline metallic materials*, *Science* **377** (2022), no. 6610 1065–1071.

[4] M. P. Echlin, J. C. Stinville, V. M. Miller, W. C. Lenthe, and T. M. Pollock, *Incipient slip and long range plastic strain localization in microtextured Ti-6Al-4V titanium*, *Acta Materialia* **114** (2016) 164–175.

[5] L. Wang, Y. Yang, P. Eisenlohr, T. Bieler, M. Crimp, and D. Mason, *Twin nucleation by slip transfer across grain boundaries in commercial purity titanium*, *Metallurgical and Materials Transactions A* **41** (2010), no. 2 421.

[6] Y. Guo, D. M. Collins, E. Tarleton, F. Hofmann, A. J. Wilkinson, and T. B. Britton, *Dislocation density distribution at slip band-grain boundary intersections*, *Acta Materialia* **182** (2020) 172–183.

[7] Y. Guo, D. Collins, E. Tarleton, F. Hofmann, J. Tischler, W. Liu, R. Xu, A. Wilkinson, and T. Britton, *Measurements of stress fields near a grain boundary: Exploring blocked arrays of dislocations in 3d*, *Acta Materialia* **96** (2015) 229–236.

[8] P. Villechaise, J. Cormier, T. Billot, and J. Mendez, *Mechanical behaviour and damage processes of udimet 720li: influence of localized plasticity at grain boundaries*, in *12th International symposium on superalloys*, vol. 15, Superalloys2012, 2012.

[9] D. Shadle, K. Nygren, J. Stinville, M. Charpagne, T. Long, M. Echlin, C. Budrow, A. Polonsky, T. Pollock, and M. Miller, *Combining signature discovery with in-situ multimodal characterizations to investigate rare material response phenomena*, *Nature Communications* (2022).

[10] B. Zhou, L. Wang, P. Jin, H. Jia, H. J. Roven, X. Zeng, and Y. Li, *Revealing slip-induced extension twinning behaviors dominated by micro deformation in a magnesium alloy*, *International Journal of Plasticity* **128** (2020) 102669.

[11] E. Bayerschen, A. McBride, B. Reddy, and T. Böhlke, *Review on slip transmission criteria in experiments and crystal plasticity models*, *Journal of materials science* **51** (2016) 2243–2258.

[12] J. Genée, L. Signor, and P. Villechaise, *Slip transfer across grain/twin boundaries in polycrystalline ni-based superalloys*, *Materials Science and Engineering: A* **701** (2017) 24–33.

[13] W. Z. Abuzaid, M. D. Sangid, J. D. Carroll, H. Sehitoglu, and J. Lambros, *Slip transfer and plastic strain accumulation across grain boundaries in hastelloy x*, *Journal of the Mechanics and Physics of Solids* **60** (2012), no. 6 1201–1220.

[14] J. Luster and M. Morris, *Compatibility of deformation in two-phase ti-al alloys: Dependence on microstructure and orientation relationships*, *Metallurgical and Materials Transactions A* **26** (1995) 1745–1756.

[15] J. Wang, M. Zecevic, M. Knezevic, and I. J. Beyerlein, *Polycrystal plasticity modeling for load reversals in commercially pure titanium*, *International Journal of Plasticity* **125** (2020) 294–313.

[16] G. Simmons and H. Wang, *A handbook of single crystal elastic constants and calculated aggregate properties*, 1971.

[17] M. Yoo, *Slip, twinning, and fracture in hexagonal close-packed metals*, *Metallurgical Transactions A* **12** (1981) 409–418.

[18] I. Beyerlein, R. McCabe, and C. Tomé, *Effect of microstructure on the nucleation of deformation twins in polycrystalline high-purity magnesium: A multi-scale modeling study*, *Journal of the Mechanics and Physics of Solids* **59** (2011), no. 5 988–1003.

[19] J. Wang, X. Wang, K. Yu, T. J. Rupert, S. Mahajan, E. J. Lavernia, J. M. Schoenung, and I. J. Beyerlein, *Manipulating deformation mechanisms with y alloying of mg*, *Materials Science and Engineering: A* **817** (2021) 141373.

[20] F. Bridier, D. L. McDowell, P. Villechaise, and J. Mendez, *Crystal plasticity modeling of slip activity in Ti-6Al-4V under high cycle fatigue loading*, *International Journal of Plasticity* **25** (2009), no. 6 1066–1082.

[21] L. Wang, Z. Zheng, H. Phukan, P. Kenesei, J.-S. Park, J. Lind, R. Suter, and T. R. Bieler, *Direct measurement of critical resolved shear stress of prismatic and basal slip in polycrystalline ti using high energy x-ray diffraction microscopy*, *Acta Materialia* **132** (2017) 598–610.

[22] J. Stinville, M. Charpagne, R. Maaß, H. Proudhon, W. Ludwig, P. Callahan, F. Wang, I. Beyerlein, M. Echlin, and T. Pollock, *Insights into plastic localization by crystallographic slip from emerging experimental and numerical approaches*, *Annual Review of Materials Research* **53** (2023) 275–317.

[23] B. Larrouy, P. Villechaise, J. Cormier, and O. Berteaux, *Grain boundary–slip bands interactions: Impact on the fatigue crack initiation in a polycrystalline forged ni-based superalloy*, *Acta Materialia* **99** (2015) 325–336.

[24] K. Le Biavant, S. Pommier, and C. Prioul, *Local texture and fatigue crack initiation in a Ti-6Al-4V titanium alloy*, *Fatigue & Fracture of Engineering Materials & Structures* **25** (2002), no. 6 527–545.

[25] S. Joseph, T. C. Lindley, and D. Dye, *Dislocation interactions and crack nucleation in a fatigued near-alpha titanium alloy*, *International Journal of Plasticity* **110** (2018) 38–56.

[26] C. Lavogiez, S. Hémery, and P. Villechaise, *On the mechanism of fatigue and dwell-fatigue crack initiation in Ti-6Al-4V*, *Scripta Materialia* **183** (2020) 117–121.

[27] S. Hémery, J. Stinville, F. Wang, M. Charpagne, M. Emigh, T. Pollock, and V. Valle, *Strain localization and fatigue crack formation at (0001) twist boundaries in titanium alloys*, *Acta Materialia* **219** (2021) 117227.

[28] N. R. Barton, A. Arsenlis, and J. Marian, *A polycrystal plasticity model of strain localization in irradiated iron*, *Journal of the Mechanics and Physics of Solids* **61** (2013), no. 2 341–351.

[29] T. Erinosho and F. Dunne, *Strain localization and failure in irradiated zircaloy with crystal plasticity*, *International Journal of Plasticity* **71** (2015) 170–194.

[30] J. Hure, S. El Shawish, L. Cizelj, and B. Tanguy, *Intergranular stress distributions in polycrystalline aggregates of irradiated stainless steel*, *Journal of Nuclear Materials* **476** (2016) 231–242.

[31] A. Patra and D. L. McDowell, *Crystal plasticity-based constitutive modelling of irradiated bcc structures*, *Philosophical Magazine* **92** (2012), no. 7 861–887.

[32] A. Patra and D. L. McDowell, *Crystal plasticity investigation of the microstructural factors influencing dislocation channeling in a model irradiated bcc material*, *Acta Materialia* **110** (2016) 364–376.

[33] M. Zhang, F. Bridier, P. Villechaise, J. Mendez, and D. McDowell, *Simulation of slip band evolution in duplex Ti–6Al–4V*, *Acta Materialia* **58** (2010), no. 3 1087–1096.

[34] S. Forest, *Modeling slip, kink and shear banding in classical and generalized single crystal plasticity*, *Acta materialia* **46** (1998), no. 9 3265–3281.

[35] M. I. Latypov, J. M. Hestroffer, J.-C. Stinville, J. R. Mayeur, T. M. Pollock, and I. J. Beyerlein, *Modeling lattice rotation fields from discrete crystallographic slip bands in superalloys*, *Extreme Mechanics Letters* **49** (2021) 101468.

[36] A. Marano, L. Gélébart, and S. Forest, *Intragranular localization induced by softening crystal plasticity: Analysis of slip and kink bands localization modes from high resolution FFT-simulations results*, *Acta Materialia* **175** (2019) 262–275.

[37] A. Marano and L. Gélébart, *Non-linear composite voxels for FFT-based explicit modeling of slip bands: application to basal channeling in irradiated Zr alloys*, *International Journal of Solids and Structures* **198** (2020) 110–125.

[38] A. Akhtar and A. Teghtsoonian, *Plastic deformation of zirconium single crystals*, *Acta Metallurgica* **19** (1971), no. 7 655–663.

[39] M. Ardeljan, M. Knezevic, T. Nizolek, I. J. Beyerlein, N. A. Mara, and T. M. Pollock, *A study of microstructure-driven strain localizations in two-phase polycrystalline hcp/bcc composites using a multi-scale model*, *International Journal of Plasticity* **74** (2015) 35–57.

[40] N. Barton and P. Dawson, *On the spatial arrangement of lattice orientations in hot-rolled multiphase titanium*, *Modelling and Simulation in Materials Science and Engineering* **9** (2001), no. 5 433.

[41] O. Diard, S. Leclercq, G. Rousselier, and G. Cailletaud, *Evaluation of finite element based analysis of 3d multicrystalline aggregates plasticity: Application to crystal plasticity model identification and the study of stress and strain fields near grain boundaries*, *international Journal of Plasticity* **21** (2005), no. 4 691–722.

[42] D. Solas and C. Tomé, *Texture and strain localization prediction using a n-site polycrystal model*, *International Journal of Plasticity* **17** (2001), no. 5 737–753.

[43] J. Stinville, M. Echlin, D. Texier, F. Bridier, P. Bocher, and T. Pollock, *Sub-grain scale digital image correlation by electron microscopy for polycrystalline materials during elastic and plastic deformation*, *Experimental mechanics* **56** (2016) 197–216.

[44] K. Hagihara, N. Yokotani, and Y. Umakoshi, *Plastic deformation behavior of mg12yzn with 18r long-period stacking ordered structure*, *Intermetallics* **18** (2010), no. 2 267–276.

[45] M. Lentz, M. Risse, N. Schaefer, W. Reimers, and I. Beyerlein, *Strength and ductility with {1011}—{1012} double twinning in a magnesium alloy*, *Nature communications* **7** (2016), no. 1 11068.

[46] B.-Y. Liu, J. Wang, B. Li, L. Lu, X.-Y. Zhang, Z.-W. Shan, J. Li, C.-L. Jia, J. Sun, and E. Ma, *Twinning-like lattice reorientation without a crystallographic twinning plane*, *Nature communications* **5** (2014), no. 1 3297.

[47] E. Vasilev, N. C. Ferreri, R. Decker, I. J. Beyerlein, and M. Knezevic, *Strain-rate sensitivity, tension-compression asymmetry, r-ratio, twinning, and texture evolution of a rolled magnesium alloy mg-1.3 zn-0.4 ca-0.4 mn*, *Metallurgical and Materials Transactions A* **51** (2020) 3858–3868.

[48] J. Williams, R. Baggerly, and N. Paton, *Deformation behavior of hcp ti-al alloy single crystals*, *Metallurgical and Materials Transactions A* **33** (2002) 837–850.

[49] M. Wronski, M. A. Kumar, L. Capolungo, R. J. McCabe, K. Wierzbanowski, and C. N. Tome, *Deformation behavior of cp-titanium: experiment and crystal plasticity modeling*, *Materials Science and Engineering: A* **724** (2018) 289–297.

[50] B. Ahmadikia, L. Wang, M. A. Kumar, and I. J. Beyerlein, *Grain boundary slip–twin transmission in titanium*, *Acta Materialia* **244** (2023) 118556.

[51] B. Ahmadikia, M. A. Kumar, and I. J. Beyerlein, *Effect of neighboring grain orientation on strain localization in slip bands in hcp materials*, *International Journal of Plasticity* **144** (2021) 103026.

[52] L. Wang, P. Eisenlohr, Y. Yang, T. Bieler, and M. Crimp, *Nucleation of paired twins at grain boundaries in titanium*, *Scripta Materialia* **63** (2010), no. 8 827–830.

[53] S. Hémery, A. Nait-Ali, M. Guéguen, J. Wendorf, A. Polonsky, M. Echlin, J. Stinville, T. Pollock, and P. Villechaise, *A 3D analysis of the onset of slip activity in relation to the degree of micro-texture in Ti-6Al-4V*, *Acta Materialia* **181** (2019) 36–48.

[54] K. S. Chan and D. L. Davidson, *Evidence of void nucleation and growth on planar slip bands in a nb-cr-ti alloy*, *Metallurgical and Materials Transactions A* **30** (1999) 579–585.

[55] Z. Zhang and Z. Wang, *Dependence of intergranular fatigue cracking on the interactions of persistent slip bands with grain boundaries*, *Acta Materialia* **51** (2003), no. 2 347–364.

[56] M. T. Andani, A. Lakshmanan, M. Karamooz-Ravari, V. Sundararaghavan, J. Allison, and A. Misra, *A quantitative study of stress fields ahead of a slip band blocked by a grain boundary in unalloyed magnesium*, *Scientific reports* **10** (2020), no. 1 3084.

[57] J. Livingston and B. Chalmers, *Multiple slip in bicrystal deformation*, *Acta Metallurgica* **5** (1957), no. 6 322–327.

[58] Z. Shen, R. Wagoner, and W. Clark, *Dislocation pile-up and grain boundary interactions in 304 stainless steel*, *Scripta metallurgica* **20** (1986), no. 6 921–926.

[59] T. Lee, I. Robertson, and H. Birnbaum, *Prediction of slip transfer mechanisms across grain boundaries*, *Scripta metallurgica* **23** (1989), no. 5 799–803.

[60] T. Lee, I. Robertson, and H. Birnbaum, *Tem in situ deformation study of the interaction of lattice dislocations with grain boundaries in metals*, *Philosophical Magazine A* **62** (1990), no. 1 131–153.

[61] F. Bridier, P. Villechaise, and J. Mendez, *Analysis of the different slip systems activated by tension in a α/β titanium alloy in relation with local crystallographic orientation*, *Acta Materialia* **53** (2005), no. 3 555–567.

[62] T. Bieler, P. Eisenlohr, C. Zhang, H. Phukan, and M. Crimp, *Grain boundaries and interfaces in slip transfer*, *Current Opinion in Solid State and Materials Science* **18** (2014), no. 4 212–226.

[63] Y. Brechet, G. Canova, and L. Kubin, *Strain softening, slip localization and propagation: from simulations to continuum modelling*, *Acta materialia* **44** (1996), no. 11 4261–4271.

[64] M. Sauzay, K. Bavard, and W. Karlsen, *Tem observations and finite element modelling of channel deformation in pre-irradiated austenitic stainless steels–interactions with free surfaces and grain boundaries*, *Journal of nuclear materials* **406** (2010), no. 1 152–165.

[65] L. Sluys and Y. Estrin, *The analysis of shear banding with a dislocation based gradient plasticity model*, *International journal of solids and structures* **37** (2000), no. 46-47 7127–7142.

[66] D. Zhou, J. Moosbrugger, and D. Morrison, *Finite element simulation of psb macroband nucleation and propagation in single crystal nickel cycled at low plastic strain amplitudes*, *International journal of plasticity* **22** (2006), no. 7 1336–1366.

[67] R. A. Lebensohn, A. K. Kanjarla, and P. Eisenlohr, *An elasto-viscoplastic formulation based on fast fourier transforms for the prediction of micromechanical fields in polycrystalline materials*, *International Journal of Plasticity* **32** (2012) 59–69.

[68] P. Eisenlohr, M. Diehl, R. A. Lebensohn, and F. Roters, *A spectral method solution to crystal elasto-viscoplasticity at finite strains*, *International Journal of Plasticity* **46** (2013) 37–53.

[69] M. A. Kumar and I. J. Beyerlein, *Influence of plastic properties on the grain size effect on twinning in Ti and Mg*, *Materials Science and Engineering: A* **771** (2020) 138644.

[70] M. A. Kumar, I. J. Beyerlein, R. A. Lebensohn, and C. N. Tome, *Role of alloying elements on twin growth and twin transmission in magnesium alloys*, *Materials Science and Engineering: A* **706** (2017) 295–303.

[71] R. A. Lebensohn, M. I. Idiart, P. P. Castañeda, and P.-G. Vincent, *Dilatational viscoplasticity of polycrystalline solids with intergranular cavities*, *Philosophical Magazine* **91** (2011), no. 22 3038–3067.

[72] R. A. Lebensohn, R. Brenner, O. Castelnau, and A. D. Rollett, *Orientation image-based micromechanical modelling of subgrain texture evolution in polycrystalline copper*, *Acta Materialia* **56** (2008), no. 15 3914–3926.

[73] R. A. Lebensohn and A. D. Rollett, *Spectral methods for full-field micromechanical modelling of polycrystalline materials*, *Computational Materials Science* **173** (2020) 109336.

[74] M. Montagnat, O. Castelnau, P. Bons, S. Faria, O. Gagliardini, F. Gillet-Chaulet, F. Grennerat, A. Griera, R. A. Lebensohn, H. Moulinec, *et. al.*, *Multiscale modeling of ice deformation behavior*, *Journal of Structural Geology* **61** (2014) 78–108.

[75] J. S. Nagra, A. Brahme, R. A. Lebensohn, and K. Inal, *Efficient fast fourier transform-based numerical implementation to simulate large strain behavior of polycrystalline materials*, *International Journal of Plasticity* **98** (2017) 65–82.

[76] M. Upadhyay, L. Capolungo, V. Taupin, C. Fressengeas, and R. Lebensohn, *A higher order elasto-viscoplastic model using fast fourier transforms: Effects of lattice curvatures on mechanical response of nanocrystalline metals*, *International Journal of Plasticity* **83** (2016) 126–152.

[77] M. A. Kumar, I. J. Beyerlein, and C. N. Tomé, *Effect of local stress fields on twin characteristics in HCP metals*, *Acta Materialia* **116** (2016) 143–154.

[78] M. A. Kumar and I. J. Beyerlein, *Local microstructure and micromechanical stress evolution during deformation twinning in hexagonal polycrystals*, *Journal of Materials Research* **35** (2020), no. 3 217–241.

[79] A. Rovinelli, R. A. Lebensohn, and M. D. Sangid, *Influence of microstructure variability on short crack behavior through postulated micromechanical short crack driving force metrics*, *Engineering Fracture Mechanics* **138** (2015) 265–288.

[80] A. Melander, *Work hardening and softening in a dislocation glide plane with precipitates*, *Materials Science and Engineering* **34** (1978), no. 3 235–240.

[81] J. Olfe and H. Neuhäuser, *Dislocation groups, multipoles, and friction stresses in α-cuzn alloys*, *physica status solidi (a)* **109** (1988), no. 1 149–160.

[82] T. Alden, *Microstructural interpretation of work softening in aluminum*, *Metallurgical Transactions A* **7** (1976), no. 8 1057–1063.

[83] R. Armstrong, H. Ammon, W. Elban, and D. Tsai, *Investigation of hot spot characteristics in energetic crystals*, *Thermochimica acta* **384** (2002), no. 1-2 303–313.

[84] L. Dai, L. Liu, and Y. Bai, *Formation of adiabatic shear band in metal matrix composites*, *International journal of solids and structures* **41** (2004), no. 22-23 5979–5993.

[85] M. Bapna and M. Meshii, *Deformation of quench-hardened gold single crystals*, *Materials Science and Engineering* **16** (1974), no. 1-2 181–191.

[86] T. Byun, N. Hashimoto, K. Farrell, and E. Lee, *Characteristics of microscopic strain localization in irradiated 316 stainless steels and pure vanadium*, *Journal of nuclear materials* **349** (2006), no. 3 251–264.

[87] M. Lai, C. C. Tasan, and D. Raabe, *Deformation mechanism of ω-enriched ti–nb-based gum metal: Dislocation channeling and deformation induced ω–β transformation*, *Acta Materialia* **100** (2015) 290–300.

[88] T. Mori and M. Meshii, *Plastic deformation of quench-hardened aluminum single crystals*, *Acta Metallurgica* **17** (1969), no. 2 167–175.

[89] T. Neeraj, D.-H. Hou, G. Daehn, and M. Mills, *Phenomenological and microstructural analysis of room temperature creep in titanium alloys*, *Acta materialia* **48** (2000), no. 6 1225–1238.

[90] J. Sharp, *Correlation between cleared channels and surface slip steps in neutron irradiated copper crystals*, *Radiation effects* **14** (1972), no. 1-2 71–75.

[91] D. Ulmer and C. Altstetter, *Hydrogen-induced strain localization and failure of austenitic stainless steels at high hydrogen concentrations*, *Acta Metallurgica et Materialia* **39** (1991), no. 6 1237–1248.

[92] L. Xiao and Y. Umakoshi, *Cyclic deformation behaviour and dislocation structure of ti-5 at.% al single crystals oriented for double prism slip*, *Philosophical Magazine A* **82** (2002), no. 12 2379–2396.

[93] L. Xiao and Y. Umakoshi, *Cyclic deformation behaviour and saturation bundle structure in ti–5 at.% al single crystals deforming by single prism slip*, *Philosophical Magazine* **83** (2003), no. 30 3407–3426.

[94] L. Xiao and Y. Umakoshi, *Cyclic deformation behavior and dislocation structure of ti-2 at. pct al single crystals oriented for double prism slip*, *Metallurgical and Materials Transactions A* **35** (2004), no. 9 2845–2852.

[95] Y. Guo, T. Britton, and A. Wilkinson, *Slip band–grain boundary interactions in commercial-purity titanium*, *Acta Materialia* **76** (2014) 1–12.

[96] Y. Estrin and L. Kubin, *Local strain hardening and nonuniformity of plastic deformation*, *Acta metallurgica* **34** (1986), no. 12 2455–2464.

[97] X. Xiao, D. Song, J. Xue, H. Chu, and H. Duan, *A size-dependent tensorial plasticity model for fcc single crystal with irradiation*, *International Journal of Plasticity* **65** (2015) 152–167.

[98] C. Tome, G. Canova, U. Kocks, N. Christodoulou, and J. J. Jonas, *The relation between macroscopic and microscopic strain hardening in FCC polycrystals*, *Acta metallurgica* **32** (1984), no. 10 1637–1653.

[99] G. Proust, C. N. Tomé, A. Jain, and S. R. Agnew, *Modeling the effect of twinning and detwinning during strain-path changes of magnesium alloy az31*, *International Journal of Plasticity* **25** (2009), no. 5 861–880.

[100] Y. Jeong, B. Jeon, and C. N. Tomé, *Finite element analysis using an incremental elasto-visco-plastic self-consistent polycrystal model: Fe simulations on zr and low-carbon steel subjected to bending, stress-relaxation, and unloading.*, *International Journal of Plasticity* **147** (2021) 103110.

[101] C. M. Kube, *Elastic anisotropy of crystals*, *AIP Advances* **6** (2016), no. 9 095209.

[102] H. Neuhäuser, *Slip-line formation and collective dislocation motion*, *Dislocations in solids* **6** (1983) 319–440.

[103] M. Bapna, T. Mori, and M. Meshii, *The observation of slip channels in quenched gold*, *The Philosophical Magazine: A Journal of Theoretical Experimental and Applied Physics* **17** (1968), no. 145 177–184.

[104] T. B. Britton and A. J. Wilkinson, *Stress fields and geometrically necessary dislocation density distributions near the head of a blocked slip band*, *Acta Materialia* **60** (2012), no. 16 5773–5782.

[105] C. Wejdemann and O. Pedersen, *Atomic force microscopy of the intense slip localization causing fatigue crack initiation in polycrystalline brass*, *Materials Science and Engineering: A* **387** (2004) 556–559.

[106] A. Weidner, R. Beyer, C. Blochwitz, C. Holste, A. Schwab, and W. Tirschler, *Slip activity of persistent slip bands in polycrystalline nickel*, *Materials Science and Engineering: A* **435** (2006) 540–546.

[107] L. Brown, *Constant intermittent flow of dislocations: central problems in plasticity*, *Materials Science and Technology* **28** (2012), no. 11 1209–1232.

[108] P. Hirsch and J. Lally, *The deformation of magnesium single crystals*, *Philosophical Magazine* **12** (1965), no. 117 595–648.

[109] T. Kehagias, P. Komninou, G. Dimitrakopulos, J. Antonopoulos, and T. Karakostas, *Slip transfer across low-angle grain boundaries of deformed titanium*, *Scripta metallurgica et materialia* **33** (1995), no. 12.

[110] W. Abuzaid, M. D. Sangid, H. Sehitoglu, J. Carroll, and J. Lambros, *The role of slip transmission on plastic strain accumulationacross grain boundaries*, *Procedia IUTAM* **4** (2012) 169–178.

[111] A. Tatschl and O. Kolednik, *On the experimental characterization of crystal plasticity in polycrystals*, *Materials Science and Engineering: A* **356** (2003), no. 1-2 447–463.

[112] R. R. Boyer, *An overview on the use of titanium in the aerospace industry*, *Materials Science and Engineering: A* **213** (1996), no. 1-2 103–114.

[113] M. Niinomi, *Mechanical properties of biomedical titanium alloys*, *Materials Science and Engineering: A* **243** (1998), no. 1-2 231–236.

[114] M. Koike and H. Fujii, *The corrosion resistance of pure titanium in organic acids*, *Biomaterials* **22** (2001), no. 21 2931–2936.

[115] X. Liu, P. K. Chu, and C. Ding, *Surface modification of titanium, titanium alloys, and related materials for biomedical applications*, *Materials Science and Engineering: R: Reports* **47** (2004), no. 3-4 49–121.

[116] I. Inagaki, T. Takechi, Y. Shirai, and N. Ariyasu, *Application and features of titanium for the aerospace industry*, *Nippon steel & sumitomo metal technical report* **106** (2014), no. 106 22–27.

[117] N. Yi, T. Hama, A. Kobuki, H. Fujimoto, and H. Takuda, *Anisotropic deformation behavior under various strain paths in commercially pure titanium grade 1 and grade 2 sheets*, *Materials Science and Engineering: A* **655** (2016) 70–85.

[118] M. E. Nixon, O. Cazacu, and R. A. Lebensohn, *Anisotropic response of high-purity α-titanium: Experimental characterization and constitutive modeling*, *International Journal of Plasticity* **26** (2010), no. 4 516–532.

[119] L. Wang, R. Barabash, T. Bieler, W. Liu, and P. Eisenlohr, *Study of twinning in α-ti by ebsd and laue microdiffraction*, *Metallurgical and Materials Transactions A* **44** (2013), no. 8 3664–3674.

[120] S. Nemat-Nasser, W. Guo, and J. Cheng, *Mechanical properties and deformation mechanisms of a commercially pure titanium*, *Acta materialia* **47** (1999), no. 13 3705–3720.

[121] D. H. Shin, I. Kim, and J. Kim, *Deformation mechanisms of pure ti during equal channel angular pressing*, *Metals and Materials International* **8** (2002) 513–518.

[122] K. E. K. Amouzou, T. Richeton, A. Roth, M. Lebyodkin, and T. Lebedkina, *Micromechanical modeling of hardening mechanisms in commercially pure α-titanium in tensile condition*, *International Journal of Plasticity* **80** (2016) 222–240.

[123] J. Ren, Q. Wang, X. Lu, W. Liu, P. Zhang, and X. Zhang, *Effect of oxygen content on active deformation systems in pure titanium polycrystals*, *Materials Science and Engineering: A* **731** (2018) 530–538.

[124] B. Barkia, V. Doquet, J.-P. Couzinie, I. Guillot, and E. Héripré, *In situ monitoring of the deformation mechanisms in titanium with different oxygen contents*, *Materials Science and Engineering: A* **636** (2015) 91–102.

[125] N. Benmhenni, S. Bouvier, R. Brenner, T. Chauveau, and B. Bacroix, *Micromechanical modelling of monotonic loading of cp α-ti: Correlation between macroscopic and microscopic behaviour*, *Materials Science and Engineering: A* **573** (2013) 222–233.

[126] T. R. Bieler, L. Wang, A. J. Beaudoin, P. Kenesei, and U. Lienert, *In situ characterization of twin nucleation in pure ti using 3d-xrd*, *Metallurgical and Materials Transactions A* **45** (2014) 109–122.

[127] M. A. Kumar, M. Wroński, R. J. McCabe, L. Capolungo, K. Wierzbanowski, and C. N. Tomé, *Role of microstructure on twin nucleation and growth in hcp titanium: A statistical study*, *Acta Materialia* **148** (2018) 123–132.

[128] X. Guan, L. Lu, S. Luo, and D. Fan, *In situ observations of detwinning and strain localization in pure titanium*, *Materials Science and Engineering: A* **813** (2021) 141073.

[129] M. D. Sangid, H. J. Maier, and H. Sehitoglu, *The role of grain boundaries on fatigue crack initiation–an energy approach*, *International Journal of Plasticity* **27** (2011), no. 5 801–821.

[130] C. Guo, R. Xin, C. Ding, B. Song, and Q. Liu, *Understanding of variant selection and twin patterns in compressed mg alloy sheets via combined analysis of schmid factor and strain compatibility factor*, *Materials Science and Engineering: A* **609** (2014) 92–101.

[131] D. Culbertson, Q. Yu, and Y. Jiang, *In situ observation of cross-grain twin pair formation in pure magnesium*, *Philosophical Magazine Letters* **98** (2018), no. 4 139–146.

[132] Y. Su, S. Han, P. Eisenlohr, and M. A. Crimp, *Predicting shear transmission across grain boundaries with an iterative stress relief model*, *Acta Materialia* **215** (2021) 116992.

[133] S. Han, P. Eisenlohr, and M. A. Crimp, *Ecci based characterization of dislocation shear in polycrystalline arrays during heterogeneous deformation of commercially pure titanium*, *Materials Characterization* **142** (2018) 504–514.

[134] S. Han and M. A. Crimp, *Ecci analysis of shear accommodations at grain boundaries in commercially pure alpha titanium*, *International Journal of Plasticity* **131** (2020) 102731.

[135] Y. Yang, L. Wang, T. Bieler, P. Eisenlohr, and M. Crimp, *Quantitative atomic force microscopy characterization and crystal plasticity finite element modeling of heterogeneous deformation in commercial purity titanium*, *Metallurgical and Materials Transactions A* **42** (2011) 636–644.

[136] L. Wang, R. Barabash, Y. Yang, T. Bieler, M. Crimp, P. Eisenlohr, W. Liu, and G. E. Ice, *Experimental characterization and crystal plasticity modeling of heterogeneous deformation in polycrystalline α-ti*, *Metallurgical and Materials Transactions A* **42** (2011) 626–635.

[137] M. A. Kumar, I. Beyerlein, R. McCabe, and C. Tomé, "Grain neighbour effects on twin transmission in hexagonal close-packed materials, nat. commun. 7 (2016) 13826."

[138] J. Hirth, J. Wang, and C. Tomé, *Disconnections and other defects associated with twin interfaces*, *Progress in Materials Science* **83** (2016) 417–471.

[139] S. Chen and Q. Yu, *The role of low angle grain boundary in deformation of titanium and its size effect*, *Scripta Materialia* **163** (2019) 148–151.

[140] Z. Zheng, D. S. Balint, and F. P. Dunne, *Investigation of slip transfer across hcp grain boundaries with application to cold dwell facet fatigue*, *Acta Materialia* **127** (2017) 43–53.

[141] Z. Tong, L. Wang, G. Zhu, and X. Zeng, *Predicting twin nucleation in a polycrystalline mg alloy using machine learning methods*, *Metallurgical and Materials Transactions A* **50** (2019) 5543–5560.

[142] S. Keshavarz and S. Ghosh, *Hierarchical crystal plasticity fe model for nickel-based superalloys: Sub-grain microstructures to polycrystalline aggregates*, *International Journal of Solids and Structures* **55** (2015) 17–31.

[143] Y. Tadano, Y. Yoshihara, and S. Hagihara, *A crystal plasticity modeling considering volume fraction of deformation twinning*, *International Journal of Plasticity* **84** (2016) 88–101.

[144] N. Grilli, A. C. Cocks, and E. Tarleton, *A phase field model for the growth and characteristic thickness of deformation-induced twins*, *Journal of the Mechanics and Physics of Solids* **143** (2020) 104061.

[145] S. Hu, C. H. Henager Jr, and L. Chen, *Simulations of stress-induced twinning and de-twinning: a phase field model*, *Acta Materialia* **58** (2010), no. 19 6554–6564.

[146] J. D. Clayton and J. Knap, *A phase field model of deformation twinning: nonlinear theory and numerical simulations*, *Physica D: Nonlinear Phenomena* **240** (2011), no. 9-10 841–858.

[147] C. Liu, P. Shanthraj, M. Diehl, F. Roters, S. Dong, J. Dong, W. Ding, and D. Raabe, *An integrated crystal plasticity–phase field model for spatially resolved twin nucleation, propagation, and growth in hexagonal materials*, *International Journal of Plasticity* **106** (2018) 203–227.

[148] M. A. Kumar, L. Capolungo, R. McCabe, and C. Tomé, *Characterizing the role of adjoining twins at grain boundaries in hexagonal close packed materials*, *Scientific Reports* **9** (2019), no. 1 3846.

[149] Y. Sun, K. Zhou, H. Qiao, R. Xin, H. Wang, and P. Wu, *Crystal plasticity-based finite element modeling of twin transmission across grain boundaries in magnesium*, *Materials Today Communications* **30** (2022) 102998.

[150] B. Wagenknecht, D. Libiran, S. Poon, and K. Sztykiel, *In-situ four-point bending apparatus for scanning electron micro-scopes*, *Senior Design Project, Mechanical Engineering, Michigan State University* (2008).

[151] M. A. Kumar, I. J. Beyerlein, and C. N. Tome, *Grain size constraints on twin expansion in hexagonal close packed crystals*, *Journal of Applied Physics* **120** (2016), no. 15 155105.

[152] R. Li and H. B. Chew, *Grain boundary traction signatures: Quantifying the asymmetrical dislocation emission processes under tension and compression*, *Journal of the Mechanics and Physics of Solids* **103** (2017) 142–154.

[153] Y. B. Chun, S.-H. Yu, S. Semiatin, and S.-K. Hwang, *Effect of deformation twinning on microstructure and texture evolution during cold rolling of cp-titanium*, *Materials Science and Engineering: A* **398** (2005), no. 1-2 209–219.

[154] B. Wang, H. Liu, Y. Zhang, B. Zhou, L. Deng, C. Wang, J. Chen, and Y. Zhang, *Effect of grain size on twinning behavior of pure titanium at room temperature*, *Materials Science and Engineering: A* **827** (2021) 142060.

[155] J. Sun, P. Trimby, F. Yan, X. Liao, N. Tao, and J. Wang, *Grain size effect on deformation twinning propensity in ultrafine-grained hexagonal close-packed titanium*, *Scripta Materialia* **69** (2013), no. 5 428–431.

[156] A. Ghaderi and M. R. Barnett, *Sensitivity of deformation twinning to grain size in titanium and magnesium*, *Acta materialia* **59** (2011), no. 20 7824–7839.

[157] E. Cerreta, G. Gray, A. Lawson, T. Mason, and C. Morris, *The influence of oxygen content on the α to ω phase transformation and shock hardening of titanium*, *Journal of applied physics* **100** (2006), no. 1.

[158] Y. Xu and B. Zhang, *Effects of hydrogen as a solid solution element on the deformation behavior of a near-alpha titanium alloy*, *Materials Science and Engineering: A* **815** (2021) 141269.

[159] F. Roters, P. Eisenlohr, L. Hantcherli, D. D. Tjahjanto, T. R. Bieler, and D. Raabe, *Overview of constitutive laws, kinematics, homogenization and multiscale methods in crystal plasticity finite-element modeling: Theory, experiments, applications*, *Acta materialia* **58** (2010), no. 4 1152–1211.

[160] J. Clayton and J. Knap, *Phase field modeling of directional fracture in anisotropic polycrystals*, *Computational Materials Science* **98** (2015) 158–169.

[161] H. Abdolvand, J. Wright, and A. J. Wilkinson, *Strong grain neighbour effects in polycrystals*, *Nature communications* **9** (2018), no. 1 171.

[162] C. Zhang, H. Li, P. Eisenlohr, W. Liu, C. Boehlert, M. Crimp, and T. Bieler, *Effect of realistic 3d microstructure in crystal plasticity finite element analysis of polycrystalline ti-5al-2.5 sn*, *International Journal of Plasticity* **69** (2015) 21–35.

[163] S. Sun and V. Sundararaghavan, *A probabilistic crystal plasticity model for modeling grain shape effects based on slip geometry*, *Acta Materialia* **60** (2012), no. 13-14 5233–5244.

[164] Z. Zhang, D. Lunt, H. Abdolvand, A. J. Wilkinson, M. Preuss, and F. P. Dunne, *Quantitative investigation of micro slip and localization in polycrystalline materials under uniaxial tension*, *International Journal of Plasticity* **108** (2018) 88–106.

[165] J. M. Hestroffer, M. I. Latypov, J.-C. Stinville, M.-A. Charpagne, V. Valle, M. P. Miller, T. M. Pollock, and I. J. Beyerlein, *Development of grain-scale slip activity and lattice rotation fields in inconel 718*, *Acta Materialia* **226** (2022) 117627.

[166] V. Wan, M. Cuddihy, J. Jiang, D. MacLachlan, and F. Dunne, *An hr-ebsd and computational crystal plasticity investigation of microstructural stress distributions and fatigue hotspots in polycrystalline copper*, *Acta Materialia* **115** (2016) 45–57.

[167] M. Yaghoobi, Z. Chen, V. Sundararaghavan, S. Daly, and J. E. Allison, *Crystal plasticity finite element modeling of extension twinning in we43 mg alloys: calibration and validation*, *Integrating Materials and Manufacturing Innovation* **10** (2021) 488–507.

[168] P. R. Dawson, M. P. Miller, T. M. Pollock, J. Wendorf, L. H. Mills, J. C. Stinville, M. A. Charpagne, and M. P. Echlin, *Mechanical metrics of virtual polycrystals (mechmet)*, *Integrating Materials and Manufacturing Innovation* **10** (2021) 265–285.

[169] S. Hémery, P. Nizou, and P. Villechaise, *In situ sem investigation of slip transfer in Ti-6Al-4V: Effect of applied stress*, *Materials Science and Engineering: A* **709** (2018) 277–284.

[170] B. Poole and F. P. Dunne, *Slip band interactions and gnd latent hardening in a galling resistant stainless steel*, *Materials Science and Engineering: A* **813** (2021) 141176.

[171] J. Stinville, P. Callahan, M. Charpagne, M. Echlin, V. Valle, and T. Pollock, *Direct measurements of slip irreversibility in a nickel-based superalloy using high resolution digital image correlation*, *Acta Materialia* **186** (2020) 172–189.

[172] R. Sperry, A. Harte, J. Q. da Fonseca, E. R. Homer, R. H. Wagoner, and D. T. Fullwood, *Slip band characteristics in the presence of grain boundaries in nickel-based superalloy*, *Acta Materialia* **193** (2020) 229–238.

[173] G. Po, M. S. Mohamed, T. Crosby, C. Erel, A. El-Azab, and N. Ghoniem, *Recent progress in discrete dislocation dynamics and its applications to micro plasticity*, *JOM* **66** (2014) 2108–2120.

[174] M. Huang, L. Zhao, and J. Tong, *Discrete dislocation dynamics modelling of mechanical deformation of nickel-based single crystal superalloys*, *International Journal of Plasticity* **28** (2012), no. 1 141–158.

[175] L. Capolungo, I. Beyerlein, and Z. Qwang, *The role of elastic anisotropy on plasticity in hcp metals: a three-dimensional dislocation dynamics study*, *Modelling and Simulation in Materials Science and Engineering* **18** (2010), no. 8 085002.

[176] J. Wang, I. Beyerlein, and C. Tomé, *Reactions of lattice dislocations with grain boundaries in mg: implications on the micro scale from atomic-scale calculations*, *International Journal of Plasticity* **56** (2014) 156–172.

[177] M. d. Koning, R. Miller, V. Bulatov, and F. F. Abraham, *Modelling grain-boundary resistance in intergranular dislocation slip transmission*, *Philosophical Magazine A* **82** (2002), no. 13 2511–2527.

[178] J. Wang, *Atomistic simulations of dislocation pileup: grain boundaries interaction*, *JOM* **67** (2015) 1515–1525.

[179] Y. Gao and Z. Jin, *Interaction between lattice dislocations and low-angle grain boundaries in ni via molecular dynamics simulations*, *Molecular Simulation* **43** (2017), no. 13-16 1172–1178.

[180] A. Kammers and S. Daly, *Self-assembled nanoparticle surface patterning for improved digital image correlation in a scanning electron microscope*, *Experimental Mechanics* **53** (2013), no. 8 1333–1341.

[181] C. B. Montgomery, B. Koohbor, and N. R. Sottos, *A robust patterning technique for electron microscopy-based digital image correlation at sub-micron resolutions*, *Experimental Mechanics* **59** (Sep, 2019) 1063–1073.

[182] A. Kammers and S. Daly, *Digital image correlation under scanning electron microscopy: Methodology and validation*, *Experimental Mechanics* **53** (2013), no. 9 1743–1761.

[183] J. Stinville, M. Echlin, D. Texier, F. Bridier, P. Bocher, and T. Pollock, *Sub-grain scale digital image correlation by electron microscopy for polycrystalline materials during elastic and plastic deformation*, *Experimental Mechanics* (2015) 1–20.

[184] W. C. Lenthe, J. C. Stinville, M. P. Echlin, Z. Chen, S. Daly, and T. M. Pollock, *Advanced detector signal acquisition and electron beam scanning for high resolution sem imaging*, *Ultramicroscopy* **195** (2018) 93 – 100.

[185] V. Valle, L. Laou, I. Léandry, S. Yotte, S. Rossignol, and S. Hedan, *Crack analysis in mudbricks under compression using specific development of stereo-digital image correlation*, *Experimental Mechanics* **58** (12, 2017).

[186] J. Stinville, M. Charpagne, F. Bourdin, P. Callahan, Z. Chen, M. Echlin, D. Texier, J. Cormier, P. Villechaise, T. Pollock, and V. Valle, *Measurement of elastic and rotation fields during irreversible deformation using heaviside-digital image correlation*, *Materials Characterization* **169** (2020) 110600.

[187] F. Bourdin, J. Stinville, M. Echlin, P. Callahan, W. Lenthe, C. Torbet, D. Texier, F. Bridier, J. Cormier, P. Villechaise, T. Pollock, and V. Valle, *Measurements of plastic localization by heaviside-digital image correlation*, *Acta Materialia* **157** (2018) 307 – 325.

[188] M. Charpagne, J. Stinville, P. Callahan, D. Texier, Z. Chen, P. Villechaise, V. Valle, and T. Pollock, *Automated and quantitative analysis of plastic strain localization via multi-modal data recombination*, *Materials Characterization* **163** (2020) 110245.

[189] X. Du and J.-C. Zhao, *First measurement of the full elastic constants of ni-based superalloy rené 88dt*, *Scripta Materialia* **152** (2018) 24–26.

[190] G. Martin, N. Ochoa, K. Sai, E. Hervé-Luanco, and G. Cailletaud, *A multiscale model for the elastoviscoplastic behavior of directionally solidified alloys: Application to fe structural computations*, *International Journal of Solids and Structures* **51** (2014), no. 5 1175–1187.

[191] C. A. Stewart, S. P. Murray, A. Suzuki, T. M. Pollock, and C. G. Levi, *Accelerated discovery of oxidation resistant coni-base γ/γ'alloys with high l12 solvus and low density*, *Materials & Design* **189** (2020) 108445.

[192] C. A. Bronkhorst, J. R. Mayeur, V. Livescu, R. Pokharel, D. W. Brown, and G. T. Gray III, *Structural representation of additively manufactured 316l austenitic stainless steel*, *International Journal of Plasticity* **118** (2019) 70–86.

[193] G. Simmons, H. Wang, *et. al.*, *Single crystal elastic constants and calculated aggregate properties*, .

[194] M. Yoo, *Slip, twinning, and fracture in hexagonal close-packed metals*, *Metallurgical Transactions A* **12** (1981), no. 3 409–418.

[195] F. Bridier, D. L. McDowell, P. Villechaise, and J. Mendez, *Crystal plasticity modeling of slip activity in Ti-6Al-4V under high cycle fatigue loading*, *International Journal of Plasticity* **25** (2009), no. 6 1066–1082.

[196] V. Doquet and B. Barkia, *A micromechanical model of the viscoplastic behaviour of titanium accounting for its anisotropic and strain-rate-dependent viscosity*, *Mechanics of Time-Dependent Materials* **19** (2015), no. 2 153–166.

[197] V. Tari, R. A. Lebensohn, R. Pokharel, T. J. Turner, P. A. Shade, J. V. Bernier, and A. D. Rollett, *Validation of micro-mechanical fft-based simulations using high energy diffraction microscopy on ti-7al*, *Acta materialia* **154** (2018) 273–283.

[198] M. Bache, *A review of dwell sensitive fatigue in titanium alloys: the role of microstructure, texture and operating conditions*, *International journal of fatigue* **25** (2003), no. 9-11 1079–1087.

[199] K. O. Findley and A. Saxena, *Low cycle fatigue in rene 88dt at 650 c: crack nucleation mechanisms and modeling*, *Metallurgical and Materials Transactions* **37** (2006), no. 5 1469.

[200] D. Davidson, R. Tryon, M. Oja, R. Matthews, and K. Ravi Chandran, *Fatigue crack initiation in waspaloy at 20 c*, *Metallurgical and materials transactions A* **38** (2007) 2214–2225.

[201] F. Dunne, A. Wilkinson, and R. Allen, *Experimental and computational studies of low cycle fatigue crack nucleation in a polycrystal*, *International Journal of Plasticity* **23** (2007), no. 2 273–295.

[202] J. Miao, T. M. Pollock, and J. W. Jones, *Microstructural extremes and the transition from fatigue crack initiation to small crack growth in a polycrystalline nickel-base superalloy*, *Acta Materialia* **60** (2012), no. 6-7 2840–2854.

[203] S. Griffiths, H. G. Tabasi, T. Ivas, X. Maeder, A. De Luca, K. Zweiacker, R. Wróbel, J. Jhabvala, R. Logé, and C. Leinenbach, *Combining alloy and process modification for micro-crack mitigation in an additively manufactured ni-base superalloy*, *Additive Manufacturing* **36** (2020) 101443.

[204] F. León-Cázares, F. Monni, T. Jackson, E. Galindo-Nava, and C. Rae, *Stress response and microstructural evolution of nickel-based superalloys during low cycle fatigue: Physics-based modelling of cyclic hardening and softening*, *International Journal of Plasticity* **128** (2020) 102682.

[205] A. Pineau, *Crossing grain boundaries in metals by slip bands, cleavage and fatigue cracks*, *Philosophical Transactions of the Royal Society A: Mathematical, Physical and Engineering Sciences* **373** (2015), no. 2038 20140131.

[206] A. W. Mello, A. Nicolas, and M. D. Sangid, *Fatigue strain mapping via digital image correlation for ni-based superalloys: The role of thermal activation on cube slip*, *Materials Science and Engineering: A* **695** (2017) 332–341.

[207] Z. Liu, R. Li, D. Chen, Y. Sun, B. He, and Y. Zou, *Enhanced tensile ductility of an additively manufactured near-α titanium alloy by microscale shear banding*, *International Journal of Plasticity* **157** (2022) 103387.

[208] J. Stinville, M. Charpagne, F. Bourdin, P. Callahan, Z. Chen, M. Echlin, D. Texier, J. Cormier, P. Villechaise, T. Pollock, *et. al.*, *Measurement of elastic and rotation fields during irreversible deformation using heaviside-digital image correlation*, *Materials Characterization* **169** (2020) 110600.

[209] C. Bean, F. Wang, M. Charpagne, P. Villechaise, V. Valle, S. Agnew, D. Gianola, T. Pollock, and J. Stinville, *Heterogeneous slip localization in an additively*

manufactured 316l stainless steel, *International Journal of Plasticity* **159** (2022) 103436.

[210] M. Knezevic and I. J. Beyerlein, *Multiscale modeling of microstructure-property relationships of polycrystalline metals during thermo-mechanical deformation*, *Advanced Engineering Materials* **20** (2018), no. 4 1700956.

[211] M. A. Groeber and M. A. Jackson, *DREAM. 3D: a digital representation environment for the analysis of microstructure in 3D*, *Integrating Materials and Manufacturing Innovation* **3** (2014) 56–72.

[212] T. R. Bieler, R. Alizadeh, M. Peña-Ortega, and J. Llorca, *An analysis of (the lack of) slip transfer between near-cube oriented grains in pure al*, *International Journal of Plasticity* **118** (2019) 269–290.

[213] J. Chen, J. Lu, W. Cai, Y. Zhang, Y. Wang, W. Jiang, M. Rizwan, and Z. Zhang, *In-situ study of adjacent grains slip transfer of inconel 718 during tensile process at high temperature*, *International Journal of Plasticity* (2023) 103554.

[214] M. Charpagne, J. Hestroffer, A. Polonsky, M. Echlin, D. Texier, V. Valle, I. Beyerlein, T. Pollock, and J. Stinville, *Slip localization in inconel 718: A three-dimensional and statistical perspective*, *Acta Materialia* **215** (2021) 117037.

[215] P. C. Hansen, H. O. Sørensen, Z. Sükösd, and H. F. Poulsen, *Reconstruction of single-grain orientation distribution functions for crystalline materials*, *SIAM Journal on Imaging Sciences* **2** (2009), no. 2 593–613.

[216] T. J. Long and M. P. Miller, *Statistical characterization of intragrain misorientations at large strains using high-energy x-ray diffraction: Application to hydrogen embrittlement*, *Integrating Materials and Manufacturing Innovation* **8** (2019) 423–439.

[217] M. D. Sangid, T. Ezaz, and H. Sehitoglu, *Energetics of residual dislocations associated with slip–twin and slip–gbs interactions*, *Materials Science and Engineering: A* **542** (2012) 21–30.

[218] J. Genée, *Etude statistique et numérique des interactions bandes de glissement-joints de grains: application aux superalliages de nickel.* PhD thesis, Chasseneuil-du-Poitou, Ecole nationale supérieure de mécanique et d . . . , 2017.

[219] R. Boyer, *Attributes, characteristics, and applications of titanium and its alloys*, *JOM* **62** (2010) 21–24.

[220] J. C. Williams and R. R. Boyer, *Opportunities and issues in the application of titanium alloys for aerospace components*, *Metals* **10** (2020), no. 6 705.

[221] D. Lunt, J. Q. d. Fonseca, D. Rugg, and M. Preuss, *Slip band characterisation in Ti-6Al-4V with varying degrees of macrozones*, in *Proceedings of the 13th World Conference on Titanium*, pp. 1129–1134, Wiley Online Library, 2016.

[222] Q. Wang and Z. Liu, *Plastic deformation induced nano-scale twins in Ti-6Al-4V machined surface with high speed machining*, *Materials Science and Engineering: A* **675** (2016) 271–279.

[223] G. G. Yapici, I. Karaman, and Z.-P. Luo, *Mechanical twinning and texture evolution in severely deformed Ti-6Al-4V at high temperatures*, *Acta Materialia* **54** (2006), no. 14 3755–3771.

[224] C. Lavogiez, S. Hémery, and P. Villechaise, *Concurrent operation of $< c + a >$ slip and twinning under cyclic loading of Ti-6Al-4V*, *Scripta Materialia* **157** (2018) 30–33.

[225] F. Bridier, P. Villechaise, and J. Mendez, *Slip and fatigue crack formation processes in an α/β titanium alloy in relation to crystallographic texture on different scales*, *Acta Materialia* **56** (2008), no. 15 3951–3962.

[226] R. Liu, A. Kumar, Z. Chen, A. Agrawal, V. Sundararaghavan, and A. Choudhary, *A predictive machine learning approach for microstructure optimization and materials design*, *Scientific Reports* **5** (2015), no. 1 1–12.

[227] A. Mangal and E. A. Holm, *Applied machine learning to predict stress hotspots ii: Hexagonal close packed materials*, *International Journal of Plasticity* **114** (2019) 1–14.

[228] C. Herriott and A. D. Spear, *Predicting microstructure-dependent mechanical properties in additively manufactured metals with machine-and deep-learning methods*, *Computational Materials Science* **175** (2020) 109599.

[229] M. Dai, M. F. Demirel, Y. Liang, and J.-M. Hu, *Graph neural networks for an accurate and interpretable prediction of the properties of polycrystalline materials*, *npj Computational Materials* **7** (2021), no. 1 103.

[230] C. Shu, J. He, G. Xue, and C. Xie, *Grain knowledge graph representation learning: A new paradigm for microstructure-property prediction*, *Crystals* **12** (2022), no. 2 280.

[231] D. C. Pagan, C. R. Pash, A. R. Benson, and M. P. Kasemer, *Graph neural network modeling of grain-scale anisotropic elastic behavior using simulated and measured microscale data*, *npj Computational Materials* **8** (2022), no. 1 259.

[232] B. Ahmadikia, O. Paraskevas, W. Van Hyning, J. Hestroffer, I. J. Beyerlein, and C. Thrampoulidis, *Data-driven texture design for reducing elastic and plastic anisotropy in titanium alloys*, *Acta Materialia* **(In review)**.

[233] J. M. Hestroffer, M.-A. Charpagne, M. I. Latypov, and I. J. Beyerlein, *Graph neural networks for efficient learning of mechanical properties of polycrystals*, *Computational Materials Science* **217** (2023) 111894.

[234] A. Mangal and E. A. Holm, *Applied machine learning to predict stress hotspots ii: Hexagonal close packed materials*, *International Journal of Plasticity* **114** (2019) 1–14.

[235] M. W. Priddy, S. R. Kalidindi, D. McDowell, and N. Paulson, *Synthetic alpha-Ti microstructures and associated elastic stiffness and yield strength properties-extended*, *matin.gatech.edu/resources/187* (2017).

[236] M. Peters, G. Lütjering, and G. Ziegler, *Control of microstructures of* $(\alpha+\beta)$*-titanium alloys*, *International Journal of Materials Research* **74** (1983), no. 5 274–282.

[237] M. Peters, A. Gysler, and G. Lütjering, *Influence of texture on fatigue properties of Ti-6Al-4V*, *Metallurgical and Materials Transactions A* **15** (1984) 1597–1605.

[238] G. Lütjering, *Influence of processing on microstructure and mechanical properties of* $(\alpha+\beta)$ *titanium alloys*, *Materials Science and Engineering: A* **243** (1998), no. 1-2 32–45.

[239] B. D. Smith, *Microstructure-sensitive plasticity and fatigue of three titanium alloy microstructures*. PhD thesis, Georgia Institute of Technology, 2013.

[240] A. Hagberg, P. Swart, and D. S Chult, *Exploring network structure, dynamics, and function using networkx*, tech. rep., Los Alamos National Lab.(LANL), Los Alamos, NM (United States), 2008.

[241] D. P. Kingma and J. Ba, *Adam: A method for stochastic optimization*, *arXiv preprint arXiv:1412.6980* (2014).

[242] S. Clark and P. Hayes, “SigOpt Web page.” `https://sigopt.com`, 2019.

[243] C. Rao and Y. Liu, *Three-dimensional convolutional neural network (3D-CNN) for heterogeneous material homogenization*, *Computational Materials Science* **184** (2020) 109850.

[244] X. Li, Z. Liu, S. Cui, C. Luo, C. Li, and Z. Zhuang, *Predicting the effective mechanical property of heterogeneous materials by image based modeling and deep learning*, *Computer Methods in Applied Mechanics and Engineering* **347** (2019) 735–753.

[245] A. Cecen, H. Dai, Y. C. Yabansu, S. R. Kalidindi, and L. Song, *Material structure-property linkages using three-dimensional convolutional neural networks*, *Acta Materialia* **146** (2018) 76–84.

[246] Z. Yang, Y. C. Yabansu, R. Al-Bahrani, W.-k. Liao, A. N. Choudhary, S. R. Kalidindi, and A. Agrawal, *Deep learning approaches for mining structure-property linkages in high contrast composites from simulation datasets*, *Computational Materials Science* **151** (2018) 278–287.

[247] N. N. Vlassis, R. Ma, and W. Sun, *Geometric deep learning for computational mechanics part i: Anisotropic hyperelasticity*, *Computer Methods in Applied Mechanics and Engineering* **371** (2020) 113299.

[248] C. Stubbington and A. Bowen, *Improvements in the fatigue strength of Ti-6Al-4V through microstructure control*, *Journal of Materials Science* **9** (1974) 941–947.

[249] C. Ng, M. Bermingham, and M. Dargusch, *Controlling grain size, morphology and texture in additively manufactured β-titanium alloy with super transus hot isostatic pressing*, *Additive Manufacturing* **59** (2022) 103176.

[250] D. Ao, J. Gao, X. Chu, S. Lin, and J. Lin, *Formability and deformation mechanism of Ti-6Al-4V sheet under electropulsing assisted incremental forming*, *International Journal of Solids and Structures* **202** (2020) 357–367.

[251] Z. Zhu, R. Liu, M. Yan, C. Cao, J. Gu, and N. Chen, *Texture control and the anisotropy of mechanical properties in titanium sheet*, *Journal of Materials Science* **32** (1997), no. 19 5163–5167.

[252] K. L. Murty and I. Charit, *Texture development and anisotropic deformation of zircaloys*, *Progress in Nuclear Energy* **48** (2006), no. 4 325–359.

[253] M. Peters and G. Lutjering, *P183 of titanium and titanium alloys, report cs-2933*, *Electric Power Research Institute* (1983).

[254] H. Kimura and O. Izumi, *Titanium'80, Science and Technology, vol. 1, Kyoto, Japan, 19-22 May 1980* (1980) 1980.

[255] E. Rennhack and D. Crooks, *Elevated temperature plastic anisotropy of ti-6ai-4v plate*, *Metallurgical Transactions A* **10** (1979), no. 4 457–462.

[256] F. H. Froes and I. L. Caplan, *Titanium'92, Science and Technology: Proceedings of a Symposium Sponsored by the Titanium Committee of the Minerals Metals & Materials, Structural Metals Division Held at the Seventh World Titanium Conference, June 29-July 2, 1992 in San Diego, California*, vol. 2. Minerals, Metals and Materials Society, 1993.

[257] M. A. Kumar, I. Beyerlein, R. Lebensohn, and C. Tome, *Modeling the effect of alloying elements in magnesium on deformation twin characteristics*, in *Magnesium Technology 2017*, pp. 159–165. Springer, 2017.

[258] M. A. Kumar, I. J. Beyerlein, and C. N. Tome, *A measure of plastic anisotropy for hexagonal close packed metals: Application to alloying effects on the formability of mg*, *Journal of Alloys and Compounds* **695** (2017) 1488–1497.

[259] S. Agnew, M. Yoo, and C. Tome, *Application of texture simulation to understanding mechanical behavior of Mg and solid solution alloys containing Li or Y*, *Acta Materialia* **49** (2001), no. 20 4277–4289.

[260] N. Kouraytem, J. Varga, B. Amin-Ahmadi, H. Mirmohammad, R. A. Chanut, A. D. Spear, and O. T. Kingstedt, *A recrystallization heat-treatment to reduce deformation anisotropy of additively manufactured inconel 718*, *Materials & Design* **198** (2021) 109228.

[261] X. Chen, G. Zhao, X. Xu, and Y. Wang, *Effects of heat treatment on the microstructure, texture and mechanical property anisotropy of extruded 2196 al-cu-li alloy*, *Journal of Alloys and Compounds* **862** (2021) 158102.

[262] C.-L. Li, J. W. Won, S.-W. Choi, J.-H. Choe, S. Lee, C. H. Park, J.-T. Yeom, and J. K. Hong, *Simultaneous achievement of equiaxed grain structure and weak texture in pure titanium via selective laser melting and subsequent heat treatment*, *Journal of Alloys and Compounds* **803** (2019) 407–412.

[263] S. Suwas, B. Beausir, L. Tóth, J.-J. Fundenberger, and G. Gottstein, *Texture evolution in commercially pure titanium after warm equal channel angular extrusion*, *Acta Materialia* **59** (2011), no. 3 1121–1133.

[264] L. Zeng and T. Bieler, *Effects of working, heat treatment, and aging on microstructural evolution and crystallographic texture of α, α', α'' and β phases in ti-6al-4v wire*, *Materials Science and Engineering: A* **392** (2005), no. 1-2 403–414.

[265] Y. Wang and J. Huang, *Texture analysis in hexagonal materials*, *Materials Chemistry and Physics* **81** (2003), no. 1 11–26.

[266] J. W. Won, K.-T. Park, S.-G. Hong, and C. S. Lee, *Anisotropic yielding behavior of rolling textured high purity titanium*, *Materials Science and Engineering: A* **637** (2015) 215–221.

[267] W. Schillinger, B. Lorenzen, and A. Bartels, *Anisotropic mechanical behavior of textured γ-tial caused by the directionality of twinning*, *Materials Science and Engineering: A* **329** (2002) 644–648.

[268] T. Yasmeen, B. Zhao, J.-H. Zheng, F. Tian, J. Lin, and J. Jiang, *The study of flow behavior and governing mechanisms of a titanium alloy during superplastic forming*, *Materials Science and Engineering: A* **788** (2020) 139482.

[269] M. Nakai, M. Niinomi, J. Hieda, K. Cho, Y. Nagasawa, T. Konno, Y. Ito, Y. Itsumi, and H. Oyama, *Reduction in anisotropy of mechanical properties of coilable (α+ β)-type titanium alloy thin sheet through simple heat treatment for use in next-generation aircraft applications*, *Materials Science and Engineering: A* **594** (2014) 103–110.

[270] J. Jung, J. I. Yoon, H. K. Park, J. Y. Kim, and H. S. Kim, *An efficient machine learning approach to establish structure-property linkages*, *Computational Materials Science* **156** (2019) 17–25.

[271] A. Agrawal and A. Choudhary, *Perspective: Materials informatics and big data: Realization of the "fourth paradigm" of science in materials science*, *Apl Materials* **4** (2016), no. 5 053208.

[272] W. Fu and B. Ahmadikia, *Optimizing knitted fiber-reinforced composite carabiners*, in *IOP Conference Series: Materials Science and Engineering*, vol. 1044, p. 012008, IOP Publishing, 2021.

[273] V. Sundararaghavan and N. Zabaras, *On the synergy between texture classification and deformation process sequence selection for the control of texture-dependent properties*, *Acta materialia* **53** (2005), no. 4 1015–1027.

[274] V. Sundararaghavan and N. Zabaras, *Linear analysis of texture–property relationships using process-based representations of rodrigues space*, *Acta materialia* **55** (2007), no. 5 1573–1587.

[275] V. Sundararaghavan and N. Zabaras, *A statistical learning approach for the design of polycrystalline materials*, *Statistical Analysis and Data Mining: The ASA Data Science Journal* **1** (2009), no. 5 306–321.

[276] V. Sundararaghavan and N. Zabaras, *A multi-length scale sensitivity analysis for the control of texture-dependent properties in deformation processing*, *International Journal of Plasticity* **24** (2008), no. 9 1581–1605.

[277] A. Paul, P. Acar, W.-k. Liao, A. Choudhary, V. Sundararaghavan, and A. Agrawal, *Microstructure optimization with constrained design objectives using machine learning-based feedback-aware data-generation*, *Computational Materials Science* **160** (2019) 334–351.

[278] M. Hasan and P. Acar, *Microstructure-sensitive stochastic design of polycrystalline materials for quasi-isotropic properties*, *AIAA Journal* **60** (2022), no. 12 6869–6880.

[279] L. Anand, *Single-crystal elasto-viscoplasticity: application to texture evolution in polycrystalline metals at large strains*, *Computer methods in applied mechanics and engineering* **193** (2004), no. 48-51 5359–5383.

[280] D. Steglich and Y. Jeong, *Texture-based forming limit prediction for mg sheet alloys ze10 and az31*, *International Journal of Mechanical Sciences* **117** (2016) 102–114.

[281] B. Leu, M. A. Kumar, and I. J. Beyerlein, *The effects of free surfaces on deformation twinning in hcp metals*, *Materialia* **17** (2021) 101124.

[282] P. Liu, Z. Wang, Y. Xiao, R. A. Lebensohn, Y. Liu, M. F. Horstemeyer, X. Cui, and L. Chen, *Integration of phase-field model and crystal plasticity for the prediction of process-structure-property relation of additively manufactured metallic materials*, *International Journal of Plasticity* **128** (2020) 102670.

[283] B. Ahmadikia, D. Shadle, J. C. Stinville, K. E. Nygren, M. A. Kumar, T. M. Pollock, M. P. Miller, and I. J. Beyerlein, *Role of microstructure on the development of microvolumes in polycrystals*, *International Journal of Plasticity* (2023).

[284] B. Ahmadikia, J. C. Stinville, T. M. Pollock, and I. J. Beyerlein, *Modelling slip localization in metals for mechanical properties prediction*, *Nature Communications* (2023).

[285] W. Petry, A. Heiming, J. Trampenau, M. Alba, C. Herzig, H. Schober, and G. Vogl, *Phonon dispersion of the bcc phase of group-iv metals. i. bcc titanium*, *Physical Review B* **43** (1991), no. 13 10933.

[286] K. Chatterjee, A. Venkataraman, T. Garbaciak, J. Rotella, M. Sangid, A. Beaudoin, P. Kenesei, J. Park, and A. Pilchak, *Study of grain-level deformation and residual stresses in ti-7al under combined bending and tension using high energy diffraction microscopy (hedm)*, *International Journal of Solids and Structures* **94** (2016) 35–49.

[287] V. Tari, R. A. Lebensohn, R. Pokharel, T. J. Turner, P. A. Shade, J. V. Bernier, and A. D. Rollett, *Validation of micro-mechanical fft-based simulations using high energy diffraction microscopy on ti-7al*, *Acta materialia* **154** (2018) 273–283.

[288] M. T. Hasib, H. E. Ostergaard, X. Li, and J. J. Kruzic, *Fatigue crack growth behavior of laser powder bed fusion additive manufactured ti-6al-4v: Roles of post heat treatment and build orientation*, *International Journal of Fatigue* **142** (2021) 105955.

[289] J. Kawałko, M. Wroński, M. Bieda, K. Sztwiertnia, K. Wierzbanowski, D. Wojtas, M. Łagoda, P. Ostachowski, W. Pachla, and M. Kulczyk, *Microstructure of titanium on complex deformation paths: Comparison of ecap, kobo and he techniques*, *Materials Characterization* **141** (2018) 19–31.

[290] J.-W. Zhang, I. J. Beyerlein, and W.-Z. Han, *Hierarchical 3d nanolayered duplex-phase zr with high strength, strain hardening, and ductility*, *Physical Review Letters* **122** (2019), no. 25 255501.

[291] X. Wu, M. Yang, F. Yuan, G. Wu, Y. Wei, X. Huang, and Y. Zhu, *Heterogeneous lamella structure unites ultrafine-grain strength with coarse-grain ductility*, *Proceedings of the National Academy of Sciences* **112** (2015), no. 47 14501–14505.

[292] X. Wu and Y. Zhu, *Heterogeneous materials: a new class of materials with unprecedented mechanical properties*, *Materials Research Letters* **5** (2017), no. 8 527–532.

[293] C. Huang, Y. Wang, X. Ma, S. Yin, H. Höppel, M. Göken, X. Wu, H. Gao, and Y. Zhu, *Interface affected zone for optimal strength and ductility in heterogeneous laminate*, *Materials Today* **21** (2018), no. 7 713–719.

[294] Y. Bao, *Dependence of ductile crack formation in tensile tests on stress triaxiality, stress and strain ratios*, *Engineering fracture mechanics* **72** (2005), no. 4 505–522.

[295] P. G. Christodoulou, S. Dancette, R. A. Lebensohn, E. Maire, and I. J. Beyerlein, *Role of crystallographic orientation on intragranular void growth in polycrystalline fcc materials*, *International Journal of Plasticity* **147** (2021) 103104.

[296] D. Bertsimas and J. N. Tsitsiklis, *Introduction to linear optimization*, vol. 6. Athena Scientific Belmont, MA, 1997.

[297] S. Boyd, S. P. Boyd, and L. Vandenberghe, *Convex optimization*, ch. 4. Cambridge university press, 2004.

[298] M. Grant, S. Boyd, and Y. Ye, *Cvx users' guide*, in *Tech. Rep. Build*, ch. D, p. 711. Cambridge Univ., 2009.

[299] M. Pilanci, L. Ghaoui, and V. Chandrasekaran, *Recovery of sparse probability measures via convex programming*, *Advances in Neural Information Processing Systems* **25** (2012) 2420–2428.

[300] A. Barvinok, *A course in convexity*, vol. 54, ch. II. American Mathematical Soc., 2002.